Thermal and Water Management of Evaporatively Cooled Fuel Cell Vehicles

by

Ashley Fly

A Doctoral Thesis

Submitted in partial fulfilment of the requirements for the award of Degree of Doctor of Philosophy of Loughborough University

November 2015

Abstract

Proton Exchange Membrane Fuel Cells (PEMFCs) present a promising alternative to the conventional internal combustion engine for automotive applications because of zero harmful exhaust emissions, fast refuelling times and possibility to be powered by hydrogen generated through renewable energy. However, several issues need to be addressed before the widespread adoption of PEMFCs, one such problem is the removal of waste heat from the fuel cell electrochemical reaction at high ambient temperatures. Automotive scale fuel cells are most commonly liquid cooled, evaporative cooling is an alternative cooling method where liquid water is added directly into the fuel cell flow channels. The liquid water evaporates within the flow channel, both cooling and humidifying the cell. The evaporated water, along with some of the product water, is then condensed from the fuel cell exhaust, stored, and re-used in cooling the fuel cell.

This work produces a system level model of an evaporatively cooled fuel cell vehicle suitable for the study of water balance and heat exchanger requirements across steady state operation and transient drive cycles. Modelling results demonstrate the ability of evaporatively cooled fuel cells to self regulate temperature within a narrow region ($\pm 2^{\circ}$C) across a wide operating range, provided humidity is maintained within the flow channels through sufficient liquid water addition. The heat exchanger requirements to maintain a self sufficient water supply are investigated, demonstrating that overall heat exchange area can be reduced up to 40% compared to a liquid cooled system due to the presence of phase change within the vehicle radiator improving heat transfer coefficients. For evaporative cooling to remain beneficial in terms of heat exchange area, over 90% of the condensed liquid water needs to be extracted from the exhaust stream.

Experimental tests are conducted to investigate the condensation of water vapour from a saturated air stream in a compact plate heat exchanger with chevron flow enhancements. Thermocouples placed within the condensing flow allow the local heat transfer coefficient to be determined and an empirical correlation obtained. The corresponding correlation is used to produce a heat exchanger model and study the influence different heat exchanger layouts have on the overall required heat transfer area for an evaporatively cooled fuel cell vehicle.

A one-dimensional, non-isothermal model is also developed to study the distribution of species, current density and temperature along the flow channel of an evaporatively cooled fuel cell using different methods of liquid water addition. Results show that good performance can be achieved with cathode inlet humidities as low as 20%, although some anode liquid water addition may be required at high current densities due to increased electro-osmotic drag. It is also demonstrated that both good membrane hydration and temperature regulation can be managed by uniform addition of liquid water across the cell to maintain a target exhaust relative humidity.

Acknowledgements

I would like to express my up most thanks to Professor Rob Thring for his support, advice and supervision throughout the project and for providing the opportunity to carry out this research. This work would also not have been possible without the financial support of the Doctoral Training Centre in Hydrogen Fuel Cells and Their Applications, provided through the Engineering and Physical Sciences Research Council (EPSRC).

Thank you to everyone who has helped in some way with my research. Thank you to all those in the Department of Aeronautical and Automotive Engineering at Loughborough University who have been a part of my education since I started as an undergraduate student almost nine years ago. Thank you to Intelligent Energy, particularly to Dr. Pratap Rama and Dr. Chris Gurney, for their continued advice and support throughout this work. I would like to thank my fellow research students in the Fuel cell research group for making the past few years enjoyable. Especially to Michael Whiteley for introducing me to rock climbing and helping me discover the wonders of Norebang and Soju in South Korea.

I would also like to thank my family for all their support, particularly to my parents for the encouragement they have given me over the years in pursuing my education. Thank you to my dog Newton, so many of the best ideas for this project occurred whilst out walking him, given time to think things through away from any distractions. Thank you for your undying loyalty and love.

Finally, I am most grateful to my wife Arraminta for her continued loving support and companionship throughout everything I do in my studies and beyond. I could not ask for anything more, thank you for being there and for tolerating me.

Contents

List of Figures

List of Tables

Nomenclature

A	Area (m^2)
a, b	Empirical constants
b_h	Blowing parameter
C	Heat capacity (J/K)
C_d	Drag coefficient
C_n	Nozzle discharge coefficient
C_p	Specific heat (J/kgK)
c	Colburn factor
D	Diffusivity (cm^2/s)
D_λ	Membrane diffusivity (cm^2/s)
d_h	Hydraulic diameter (m)
E_c	Cathode activation energy (kJ/mol)
E_n	Reversible cell voltage (V)
F	Faraday constant (C/mol)
F_T	Tractive effort (N)
f	Friction factor
G	Mass transfer coefficient (kg/m^2s)
g	Gravitational constant (m/s^2)
H	Enthalpy (J/kg)
h	Heat transfer coefficient (W/m^2K)
I	Current (A)
i	Current density (A/cm^2)
i_{oc}	Exchange current density (A/cm^2)
i_n	Internal current density (A/cm^2)
J	Mass flux across the membrane (mol/cm^2s)

Ja	Jakob number
j	Leverett J function
K	Permeability (m^2)
k	Thermal conductivity (W/mK) / Nozzle pressure coefficient (kg/Ns)
L	Length (m)
M	Molar mass (kg/mol)
m	Mass (kg)
N	Molar flow rate (mol/s)
N_{fan}	Radiator fan speed (rpm)
NTU	Number of transfer units
Nu	Nusselt number
n	Number of cells in stack / section number
n_{drag}	Electro osmotic drag coefficient
n_{drag}^{sat}	Electro osmotic drag coefficient at saturation
n_{tubes}	Number of cooling tubes in stack / radiator
P	Pressure (Pa)
Pr	Prandtl number
Q	Energy (J)
q	Heat transfer (W/m^2)
R_0	Universal gas constant (J/molK)
RH	Relative humidity
Re	Reynolds number
Sc	Schmidt number
St	Stanton number
s	GDL water void fraction
T	Temperature (K)
t	Time (s) / Thickness (m)
U	Overall heat transfer coefficient (W/m^2K)
V	Voltage (V) / Volume (m^3) / Velocity (m/s)
v	Volume flow rate (l/s)
W	Work (W)
W_{nc}	Mass fraction non-condensable gas
W_v	Mass fraction vapour

x	Volume fraction / Distance from channel inlet (m)
z	Thickness (m)

Subscript

0	Value at STP
a	Ambient
act	Activation
an	Anode
b	Bulk fluid
CSA	Cross sectional area
c	Cold side
ca	Cathode
cd	Condensation
$cell$	Single cell
$comp$	Compressor
$coolant$	Liquid coolant
c_r	Critical value
cv	Convection
$drag$	Electro osmotic drag
e	Entrance
em	Exit manifold
$elec$	Electrical power
f	Condensate film
fc	Fuel crossover
h	Hot side
hum	Humidifier
ht	Heat transfer
i	Condensate layer interface
inj	Injected / added
l	Liquid water
$loss$	Loss from stack to environment
m	Manifold
mem	Membrane

mt	Mass transfer
N	Nusselt value (pure condensation)
ohm	Ohmic
$reac$	Electrochemical reaction
rad	Radiator
s	Fuel cell stack
sat	Saturation
sec	Value for a single section
t	Total
$tube$	Coolant / radiator tube
$trans$	Transport (membrane or losses)
v	Water vapour
w	Wall

Greek

α	Charge transfer coefficient
β	Vapour pressure differential constant (mol/sPa)
γ	Specific heat ratio of air
ΔH_v	Enthalpy of vapourisation (J/kg)
Δh_l	Higher heating value (HHV) of hydrogen (J/mol)
$\Delta\hat{h}$	Enthalpy change (J/molK)
$\Delta\hat{s}$	Entropy change (J/mol)
δ	Condensate layer thickness (m)
ϵ	Heat exchanger effectiveness / GDL porosity
ϵ_s	Relative roughness
η	Collection efficiency
η_c	Compressor efficiency
η_f	Fin efficiency
θ	Water entrainment constant / GDL contact angle / Road gradient
κ_{rl}	Relative permeability
Λ	Stoichiometry
λ	Membrane water content
μ	Absolute viscosity (Ns/m^2)

ρ	Density (kg/m^3)
ρ_{dry}	Dry membrane density (kg/m^3)
σ	Conductivity (S/m(cm^2)) / Liquid water surface tension (N/m^2)
τ	Water interface addition gain (mol/s) / GDL tortuosity
ϕ	Water vapour activity
ψ	Pressure coefficient (0.5)
Ω	Membrane resistance (Ω/cm^2)
ω	Net water transport (mol/mol)
ζ	Liquid water addition constant (mol/s)

Chapter 1

Introduction

There is a very high confidence (95-100%) that human induced climate change through increased carbon dioxide (CO_2) emissions are linked to increases in the earth's surface temperature [1]. According to the Intergovernmental Panel for Climate Change (IPCC), to prevent global surface temperature increases in excess of 2°C substantial reductions in CO_2 emissions are required over the next few decades, reducing to 'near zero' emissions by the year 2100 [1].

In 2012, CO_2 emissions were 31.7Gton, a 1.2% increase from the previous year and a 58% increase from the year 2000 [2]. Road transport accounted for 5.37Gton (17%) of this total with average global CO_2 emissions of 764kg per capita [2]. Significant attention has therefore been focused on reducing the CO_2 emissions of road transport through replacing the burning of fossil fuels in the internal combustion engine with a more sustainable and less polluting powertrain.

Of the suitable alternative powertrains, hydrogen fuel cells are one of the most promising replacements of the internal combustion engine. The hydrogen fuel can be generated from renewable energy through electrolysis of water and stored on-board the vehicle in high pressure tanks. The fuel cell then uses the hydrogen to generate electrical energy, propelling the vehicle. The only tailpipe emissions from a fuel cell vehicle are water and heat. Prototype hydrogen fuel cell vehicles have been released by several major automotive manufactures, including Ford [3], General Motors [4], Honda [5], Hyundai [6], Toyota [7] and Volkswagen [8] among others. A significant advantage of hydrogen fuel cells compared to other electrical powertrains, such as batteries, are extended range and reduced refuelling times. However several issues such as high cost and performance degradation need to be addressed before widespread adoption.

In this chapter the basics of fuel cell operation are introduced, the novel contributions of this work are outlined and a brief overview of the other chapters in this thesis is given.

1.1 Fuel cell basics

A fuel cell is an energy conversion device which converts chemical energy directly into electrical energy through an oxidising reaction. All fuel cells consist of an anode and cathode separated by an electrolyte, different electrolytes are used for different oxidising reactions across a range of operating conditions. The most common types of fuel cell are listed below:

- Proton Exchange Membrane Fuel Cell
- Alkaline Electrolyte Fuel Cell
- Direct Methanol Fuel Cell
- Phosphoric Acid Fuel Cell
- Molten Carbonate Fuel Cell
- Solid Oxide Fuel Cell

Of the above different types of fuel cell it is widely regarded that the proton exchange membrane fuel cell (PEM fuel cell, PEMFC or PEFC) is the most suitable candidate for use in automotive applications [9]. The main benefits of PEM fuel cells compared to other fuel cell types for use in vehicles are fast start up times, good transient capabilities and ability to cope with vibration.

A proton exchange membrane fuel cell generates electricity through the oxidisation of hydrogen, producing water and heat in the process. Hydrogen is split into a proton and electron using a catalyst at the anode, the protons travel through the proton exchange membrane from anode to cathode whereas the electrons are forced to travel through an external circuit, performing work. The protons and electrons then combine with oxygen at the cathode, forming water and completing the electrochemical reaction equation. Equations 1.1 and 1.2 show the anode and cathode half cell reactions respectively, equation 1.3 shows the full cell reaction of a PEM fuel cell.

$$H_2 \rightarrow 2H^+ + 2e^- \tag{1.1}$$

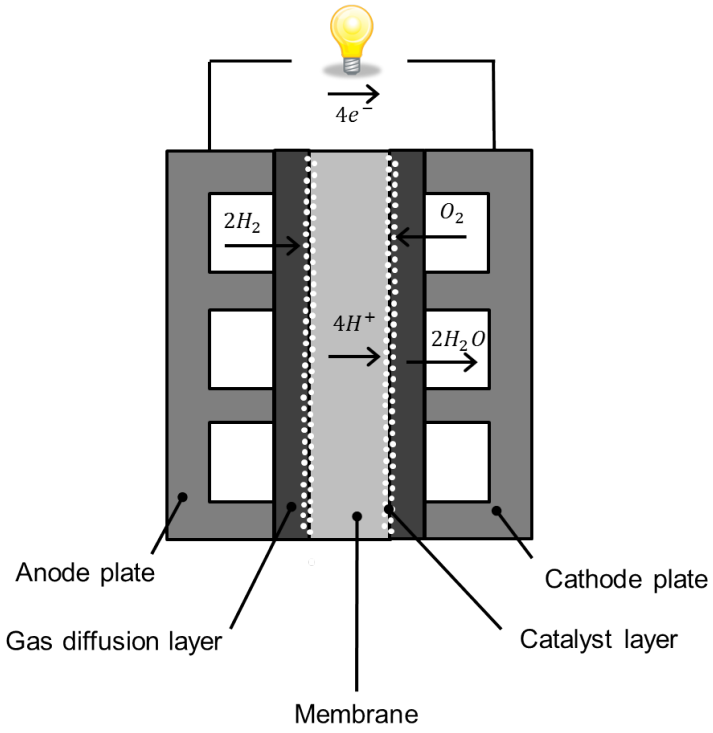

Figure 1.1: Diagram of a single proton exchange membrane (PEM) fuel cell

$$\frac{1}{2}\mathrm{O_2} + 2\mathrm{H^+} + 2\mathrm{e^-} \rightarrow \mathrm{H_2O} \tag{1.2}$$

$$\mathrm{H_2} + \frac{1}{2}\mathrm{O_2} \rightarrow \mathrm{H_2O} \tag{1.3}$$

The proton exchange membrane consists of several sub components, the gas diffusion layer, catalyst layer and electrolyte, figure 1.1 illustrates the construction of a single PEM fuel cell. The purpose of the gas diffusion layer is to allow reactants and products to transfer from the fuel cell flow channels to the catalyst layer whilst providing a high electrical conductivity. Gas diffusion layers are typically constructed of carbon fibre paper or cloth coated with Polytetrafluoroethylene (PTFE). The catalyst layer consists of a catalyst, typically platinum, supported on carbon at the interface of the gas diffusion layer and membrane. It is at this point on the anode and cathode where the respective half cell equations occur. The membrane forms the central component of the fuel cell, allowing protons to travel from anode to cathode whilst being impermeable to both electrons and gas. Membranes are typically made from a perfluorinated-sulphonic acid (PSA) ionomer, the most common

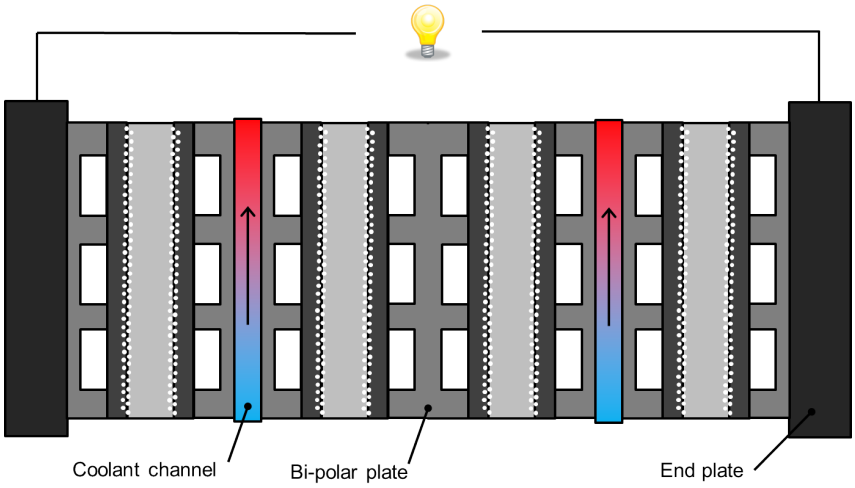

Figure 1.2: Diagram of a proton exchange membrane (PEM) fuel cell stack

commercial material being Nafion®. Proton transport across the membrane is facilitated through the movement of liquid water from anode to cathode, meaning that for a high proton conductivity the membrane should be well hydrated, however excess liquid water will prevent reactants reaching the catalyst layer. Effective water management is therefore critical in the efficient operation of a PEM fuel cell.

Each PEM fuel cell can theoretically generate a maximum voltage of 1.23V at standard temperature and pressure [10]. To achieve more practical voltages for high power applications multiple cells are put together in series, forming a fuel cell stack. Figure 1.2 illustrates a four cell stack, current is collected from either the end plates or a separate current collector positioned at opposite ends of the stack, the anode and cathode of adjacent cells are connected directly by bi-polar plates.

In practice, the voltage of each cell will be lower than the theoretical maximum voltage due to limitations in reaction kinetics, mass transfer resistance and both electronic and protonic resistance. As the operating current increases, losses also increase and the achievable cell voltage will reduce, efficiencies for a PEM fuel cell at part load are typically in the region of 50%, based on the lower heating value of hydrogen [11]. The energy from the fuel not utilised in generating electricity is dissipated as heat energy at the cathode catalyst layer. To prevent overheating of the cell and drying of the membrane, waste heat energy must be effectively dissipated from the cell and rejected to the environment. The most common method of removing waste heat from large scale (>5kW) PEM fuel cells is by passing liquid

coolant through flow channels between cells at selected intervals, illustrated in figure 1.2. Heat is transferred from the catalyst layer to the bi-polar plate through conduction then into the coolant through forced convection. The heated coolant is then cooled through an external heat exchanger, which in an automotive application would typically be the vehicle radiator. An alternative way to remove waste heat from the cell which has been demonstrated in several applications [12, 13] is to add liquid water into the flow channel. The liquid water evaporates and the high enthalpy of vaporisation removes the thermal energy from the electrochemical reaction, both cooling and humidifying the cell. The evaporated water, along with some of the product water is then extracted from the exhaust stream using a condenser. This process is referred to as evaporative cooling.

1.2 Novel contributions

The objective of this work is to further understand how different operating parameters influence the water and thermal management of evaporatively cooled PEM fuel cells at both cell and system level with application to fuel cell vehicles. This has been achieved through the development of a series of validated models for the fuel cell stack and heat exchangers, the key novel contributions of this thesis are listed below:

- The first system level thermal and water management study of an evaporatively cooled fuel cell vehicle over both steady state and transient drive cycles.
- The first quantitative comparison of the temperature regulation abilities and heat exchanger requirements of evaporatively cooled and liquid cooled fuel cell vehicles.
- The first model based study into the distribution of liquid water addition in evaporatively cooled fuel cells.
- The first experimental study on the influence of non-condensable gas on the condensation of water in compact plate heat exchangers.

1.3 Thesis outline

Chapter 2: Literature review. In this chapter, the different methods of thermal and water management in PEM fuel cells are presented. The advantages and disadvantages of each method are considered, looking at system layout and detailing significant results of previous work. Models from the existing literature used to study the water and thermal management of PEM fuel cells are then reviewed. Finally the literature is summarised and important

areas where the current knowledge requires progress are identified.

Chapter 3: Lumped parameter model of an evaporatively cooled fuel cell vehicle. A lumped parameter model of an evaporatively cooled fuel cell and significant balance of plant are presented in this chapter. The validation of the stack model using experimental data and effect of model assumptions are also discussed. The transient vehicle model and under bonnet air flow model are then detailed along with the computational procedures for solving the model.

Chapter 4: Segmented model of an evaporatively cooled fuel cell. In this chapter, a steady state, non-isothermal one dimensional model of an evaporatively cooled fuel cell is presented. The model accounts for both the presence of liquid water in the gas diffusion layer and variation in species concentration along the anode and cathode flow channels. Different methods of liquid water addition are presented and discussed.

Chapter 5: Heat exchanger models and experiments. The heat exchanger models required to complete the thermal system model are presented in this chapter, along with an experimental study on condensation in a compact plate condenser in the presence of a non-condensable gas. Three separate models are obtained and validated, a single phase radiator model along with two models for the condensation of water vapour from the cathode exhaust mixture for different geometries.

Chapter 6: Analysis. The models presented in the previous chapters are used to study the water balance and heat exchanger requirements of evaporatively cooled fuel cell vehicles at different conditions, with direct comparisons being made to liquid cooled fuel cells. Water addition rates for sufficient evaporative cooling across the cell are studied using the segmented model of chapter 4, looking into spatial temperature and humidity profiles and comparing exit conditions to those predicted by the lumped parameter model.

Chapter 7: Conclusions. The results and models from previous chapters are summarised, areas to expand the progress made by this thesis are identified under further work.

Chapter 2

Literature review

2.1 Introduction

In chapter 1, the proton exchange membrane fuel cell (PEMFC) was briefly introduced, along with the generation of waste heat and the most common way to remove it in automotive systems. In this chapter, the thermal management of fuel cell vehicles is covered in detail, presenting the current state of the art and identifying key gaps in the literature where the existing knowledge can be expanded. A review of modelling methods for the study of thermal management in fuel cell vehicles is also presented.

2.2 Heat generation

As indicated in chapter 1, not all of the available energy from the hydrogen fuel is converted into electricity, some of the energy is lost driving the electrochemical reaction and overcoming the resistances of the membrane and electrodes. The energy not converted into electricity is released in the cell as heat. The rate of heat release ($\dot{Q}$) is equal to the difference between the reversible open circuit voltage (E_n) and the actual cell voltage (V_{cell}) multiplied by the cell current (I), shown in equation 2.1. As the cell current increases, so too does the heat generation in the cell, this is illustrated for a typical polarisation curve in figure 2.1. The cell voltage and hence heat release rate will vary with cell operating conditions such as pressure, relative humidity and temperature.

$$\dot{Q} = (E_n - V_{cell})\, I \tag{2.1}$$

The typical operating temperature range of a PEMFC is between 60-80°C [14], at tem-

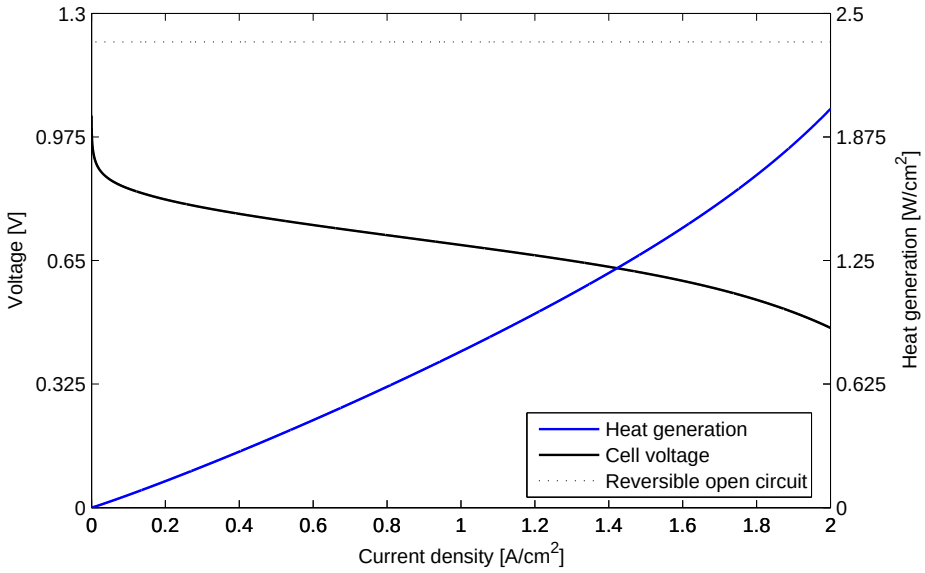

Figure 2.1: Cell voltage and heat generation

peratures lower than this the reaction kinetics are slowed and the cell efficiency reduced [15]. At high temperatures the water vapour required to maintain humidity increases and the membrane is more prone to drying, above 100°C and the liquid water within the membrane boils at atmospheric pressure, significantly increasing the protonic resistance of the membrane and causing irreversible damage [9].

To maintain the fuel cell at a constant temperature, the rate of heat removal from the cell must equal the rate of heat release, this is referred to as thermal balance. To achieve thermal balance, the thermal management of a PEMFC needs to be able to adapt to changes in heat generation, particularly in automotive applications where transient loads are common. Heat generation can vary from zero to in excess of the maximum electrical load, for example in figure 2.1, at the maximum electrical power of 0.98W/cm^2 the rate of heat generation is 1.68W/cm^2.

In a conventional liquid cooled fuel cell system the inlet gas streams will be humidified and possibly preheated close to cell operating temperature prior to the fuel cell inlet for optimum performance across the cell. The increase in enthalpy between the inlet and exit gas flow is therefore small, limiting the amount of waste heat which can be removed from the exhaust. Fronk *et. al* [11] estimated that exhaust heat flow in a PEMFC vehicle accounts for approximately 10% of the total fuel energy, compared to 33% for a 'typical' internal

combustion engine. Assuming the electrical efficiency of a PEMFC at medium to high load is 40% and the thermal efficiency of an internal combustion engine is 33% the heat rejection to coolant can be calculated, shown in figure 2.2. It can be seen that despite the PEMFC having a higher efficiency than the internal combustion engine, the fraction of total fuel energy rejected to the coolant is higher due to a reduced exhaust heat flow [11].

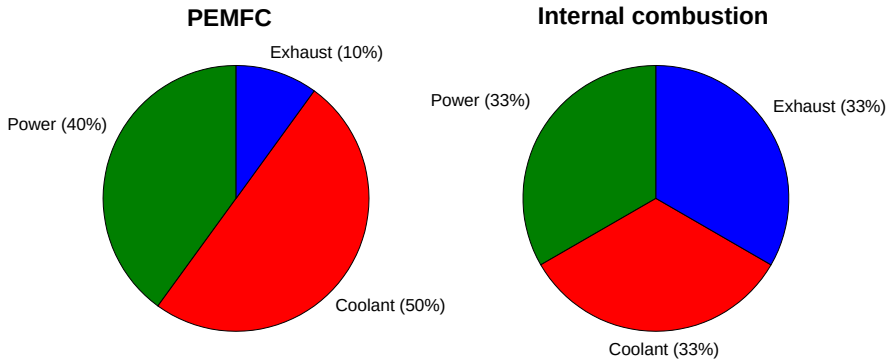

Figure 2.2: Distribution of fuel energy in typical PEMFC and IC powertrains

2.3 Air cooling

In low power fuel cell systems (<100W) which do not require external humidification it is possible to remove heat through a combination of airflow through the cathode and natural convection from the surface, this is the simplest form of thermal management since no additional components are required [10]. As heat generation increases with power, the cathode stoichiometry required to maintain thermal balance also increases, removing more water vapour from the cell and drying the membrane. Eventually it becomes more practical to separate the cooling air flow from the reactant air flow to maintain membrane humidification [16]. The separate cooling air flow passes through channels between the bi-polar plates, removing waste heat through forced convection. An additional fan is required compared to passive cooling, variations in the fan voltage can be used to regulate the stack temperature.

Sasmito *et. al* [17] conducted a numerical study into different cooling strategies for various different power fuel cells, considering both membrane water content and temperature spacial distribution. Fuel cell power and parasitic loads were determined for passive cooling, edge cooling with fins, separate air cooling and also separate liquid cooling. Results showed that the liquid cooled system had the highest limiting current density and provided the

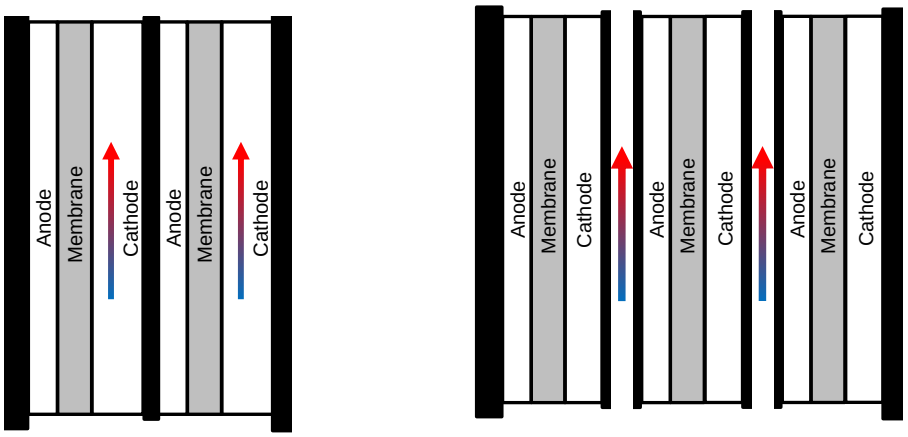

(a) Cathode air flow cooling

(b) Separate air flow cooling

Figure 2.3: Diagrams of air cooling methods

best performance above 4kW, below this both air cooled and edge cooled cooling techniques provided higher system power densities. More recently Odabaee *et. al* [18] used metal foam within the air cooling channels to improve heat transfer efficiency, although at the expense of additional pressure drop.

Air cooled PEMFCs have been demonstrated in vehicle applications by [19] and [20]. Ryan *et. al* [19] used a 3.0kW Horizon fuel cell, cooled through cathode air flow, to power a prototype Microcab H2EV. The authors noted that at high ambient temperatures and demanding driving conditions the fuel cell was required to de-rate power to prevent overheating. Ikeya *et. al* (Suzuki Motor Corporation) [20] produced a prototype Burgmann scooter powered by a 1.6kW stack with a separate cooling air flow. The scooter was the first fuel cell powered vehicle to receive whole vehicle type approval in the European Union.

In both the examples presented, the vehicle power requirements have been small. To power a conventional passenger vehicle a significantly larger fuel cell stack is required, for example the 2007 Hyundai Tuscan fuel cell vehicle utilised a 100kW stack [6]. Using the estimation of Fronk *et. al* [11] (figure 2.2) the heat rejection to the coolant medium would be 125kW; at an operating temperature of 80°C and ambient temperature of 25°C the minimum air flow rate for thermal balance is 2090 litres per second (equation 2.2). Channelling this flow rate of air between the cells of a large stack would induce significant pressure loss and an infeasible parasitic load. Alternatively if the same conditions were used for liquid water the minimum flow rate drops to 0.54 litres per second because of the fluid's significantly

higher density ($\rho = 998\text{kg/m}^3$) and specific heat capacity ($C_p = 4182\text{kJ/kgK}$).

$$v = \frac{10^3}{\rho}\dot{m} = \frac{10^3}{\rho}\frac{\dot{Q}}{C_p\,(T_1 - T_2)} = \frac{10^3}{1.08}\frac{125 \times 10^3}{1007\,(80 - 25)} = 2089.7\text{l/s} \tag{2.2}$$

This simple comparison shows that the reduction in cooling fluid flow rate and parasitic load of liquid cooling significantly offsets the disadvantage of requiring an additional coolant pump and radiator at higher powers. As such air cooled systems are generally not used for fuel cell systems with electrical powers above 5kW [10].

2.4 Liquid cooling

In a liquid cooled PEMFC system the waste heat from the electrochemical reaction is removed by passing a liquid cooling medium through channels in the bi-polar plates, shown in figure 1.2. The heated liquid coolant is then cooled in a separate heat exchanger. For vehicle applications this is usually the vehicle radiator, although for other applications such as combined heat and power (CHP) a liquid to liquid heat exchanger may be used. Once cooled, the coolant returns to a tank where it is then pumped back into the fuel cell stack, completing the coolant loop shown in figure 2.4.

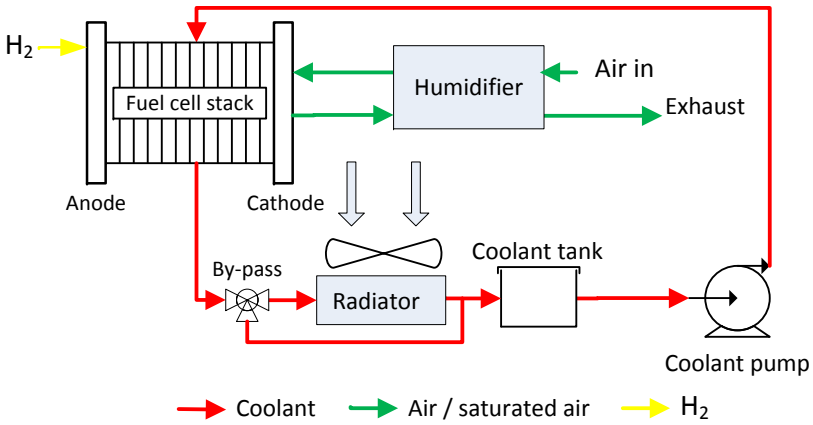

Figure 2.4: Layout A: liquid cooled system

The liquid coolant used should ideally have a high heat capacity, sub-zero freezing temperature (for cold starts) and low electrical conductivity to prevent current leakage through the cooling loop and degradation of the bi-polar plates [16]. The most common cooling medium is a mixture of de-ionized water and ethylene glycol (anti-freeze), with additional

steps taken to maintain a low conductivity [16]. One problem with the use of de-ionized water based coolant is its incompatibility with aluminium heat exchangers, alternative dielectric coolants have been developed, however at the expense of coolant heat capacity [11].

An alternative liquid cooling method was demonstrated by Shyu *et. al* [21], the authors produced a novel fuel cell with a circulating liquid electrolyte loop instead of the conventional solid electrolyte membrane. The liquid electrolyte both removed the need for external humidification and facilitated in removing waste heat from the cell to an electrolyte reservoir. Experimental results were performed on a single cell which did not require external cooling, peak power was low compared to conventional solid electrolyte cells.

The design of liquid cooled fuel cell stacks has received significant attention in the literature, particularly relating to the optimisation of the coolant channel geometry, referred to as the coolant flow field. To promote reaction kinetics and reduce losses the fuel cell should be operated close to the maximum allowable temperature. However, the use of a single phase coolant medium implies some level of temperature profile will be present across the surface of the cell as the coolant changes from inlet to outlet temperature. Figure 2.5 shows the coolant flow field pattern for a PEMFC stack with graphite bi-polar plates. Several authors, including [22–24] among others have conducted numerical studies to evaluate the performance of different coolant plate designs. Chen *et. al* [22] studied six different coolant flow field patterns to observe the temperature distribution across the surface of the cell with constant heat flux, introducing the concept of index of uniform temperature. Kang *et. al* [23] considered how different flow configurations of both the coolant and reactant flow channels influenced the overall cell performance, showing the membrane temperature distribution across the surface of the cell. Sasmito *et. al* [24] also conducted a numerical study on six different gas and coolant flow fields, showing that whilst the conventional serpentine flow channel produced the highest gross fuel cell power the modified parallel serpentine produced the highest net power once parasitics were considered.

The purpose of the thermal management system in a liquid cooled fuel cell is to maintain the stack temperature within acceptable limits, this is achieved by regulating the temperature and flow rate at which the coolant enters the fuel cell stack. A low coolant inlet temperature will remove more heat from the stack although at the expense of increasing the thermal gradient within the stack, conversely a higher coolant inlet temperature will reduce heat transfer from the stack to the coolant but reduce the thermal gradient within the stack. Similarly, an increased coolant flow rate will both improve the heat transfer coefficient and reduce the thermal gradient across the stack but at the expense of increased parasitic load.

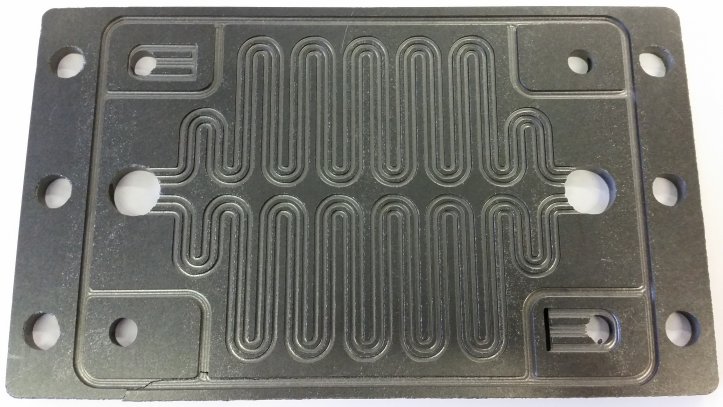

Figure 2.5: Coolant flow field on bi-polar plate

Yu and Jung [25] used a 2D model to determine the optimum stack coolant inlet temperature as a function of current density to minimise both parasitic losses and spacial temperature variation. The optimum coolant inlet temperature reduced from 75-70°C as current density increased from 0-1.5A/cm^2.

Since the current density, and hence heat generation, is dictated by the user demands, the desired coolant inlet temperature must be achieved through controlling the rate of heat rejection through the external heat exchanger. One possible method of achieving this is through regulating the heat exchanger fan speed and coolant flow rate. Yu and Jung [26] varied fan speed using both proportional integral (PI) and pulse width modulation (PWM) control to achieve a desired stack temperature, coolant flow rate was also varied to achieve a desired stack inlet temperature determined from their previous study [25]. Saygili *et. al* [27] used a 3kW PEM fuel cell system to produce a semi-empirical system model, investigating the performance of PI and PWM control of the radiator fan coupled with either constant voltage, compressor tracking or PI control of coolant flow rate pump. Meyer and Yao [28] produced a simplified fuel cell thermal model, creating a μ-synthesis controller to regulate stack temperature through variable fan and pump speeds.

An alternative method of regulating stack temperature is to modify the flow rate of coolant exposed to the external heat exchanger through a variable radiator by-pass valve (shown in figure 2.4). Hu *et. al* [29] compared PI and fuzzy based control of the by-pass valve factor and coolant flow rate, both methods showed good performance, with the fuzzy controller being able to adapt better to changes in the heat exchanger model parameters.

Other authors have taken a wider system level approach to stack temperature regulation and incorporated the thermal management into the reactant flow control. Ahn and Choe [30] compared PI and state feedback control of reactant air flow and radiator by-pass valve position with gain optimisation through a linear quadratic regulator. Panos *et. al* [31] produced an explicit model predictive controller to regulate both coolant flow rate and compressor flow rate simultaneously, although variation in the coolant inlet temperature was not considered.

All of the above studies have managed to regulate stack temperature to within acceptable limits ($\pm 2°C$) across transient current profiles. However, other than [29] the previous studies have not considered the influence changes in ambient conditions will have on system thermal management. This is especially important in automotive applications where variation in ambient temperature will affect heat transfer and vehicle speed can significantly influence radiator air speed [32].

In hot climates the temperature difference between the fuel cell stack and ambient will be significantly reduced. For a fuel cell operating at 70°C at an ambient temperature of 40°C the driving temperature difference for heat rejection is 30°C. In comparison, the coolant temperature at the exit of an internal combustion engine is typically around 100°C [33], giving twice the temperature difference at the same ambient temperature. Several studies have directly compared the thermal management requirements of conventional and PEMFC vehicles. Fronk *et. al* [11] showed that the required air flow rate across the radiator was 3.7 times greater for a PEMFC powertrain than an internal combustion engine of comparative power. Adams *et. al* (Ford motor company) [3] produced a 60kW prototype PEMFC vehicle, showing that for an operating temperature of 80-90°C, 1.5 times the radiator frontal area and 2.5 times the radiator air flow rate was required compared to the standard internal combustion engine vehicle. Rogg *et. al* [34] deduced that the cooling power requirements of a PEMFC vehicle are four times that of a conventional combustion vehicle, the authors then went on the study vehicle cooling modules specifically for fuel cell vehicles.

2.4.1 Water management

For a conventional PEMFC membrane to remain hydrated the gas flow rate into the stack is normally partially hydrated. Ideally this is achieved using a passive vapour exchange device, such as an enthalpy wheel or membrane, between the high humidity exhaust and the low humidity inlet gas [35]. These passive devices have a limited range of control and during transients may not be able to sufficiently hydrate the inlet gas stream [36]. An alternative

method is to condense a small amount of liquid water from the exhaust and inject this into the inlet air flow to achieve a desired humidity. This method gives greater control over inlet humidity and can provide additional cooling to the compressor exit gas, although at the expense of additional system complexity and thermal load of the condenser.

Water balance in liquid cooled fuel cell systems has been studied by [37–41] among others. Ito *et al.* [37] simulated water balance in a 100kW liquid cooled system looking at the thermal load requirements of the condenser, radiator, compressor and intercooler at different operating conditions. Bao *et al.* [38] published a similar study of thermal loads also including a model in which the effect of non-condensable gasses in the condenser were considered. Wan *et. al* [39] conducted an experimental study on water balance of an 84 cell stack at different inlet humidities and condenser fan operations. Results showed that the ability to cool the exhaust below the water balance temperature was highly dependant on fan operation and only weakly dependant on inlet humidities.

Haraldsson and Alvfors [40] and Haraldsson *et al.* [41] both studied water balance across transient drive cycles, using the open-source ADVISOR fuel cell model to investigate how ambient conditions effect fuel cell performance over standard drive cycles. Simulated results showed a reduction in net water flow with an increase in ambient temperature and improved water balance from warm starts opposed to ambient starts. However, the condenser model used in the studies of [40] and [41] does not consider the influence of non-condensable gas (O_2 and N_2) on condensation which has a significant influence on heat transfer (discussed in section 5.3). Additionally, the model does not consider the collection of liquid water present in the gas stream, only the collection of vapour condensed in the heat exchanger. This will influence the water balance during warm up when stack temperature is low and the product water leaving the stack remains in liquid form.

The literature on liquid cooled fuel cells has demonstrated that whilst it is possible to maintain fuel cell temperature within an ideal operating range, the hardware requirements become a limiting factor at higher ambient temperatures. The limitations become particularly apparent in vehicles where increased radiator size may not be permissible due to packaging constraints. This has led to the development of alternative cooling systems which aim to improve heat transfer through utilizing phase change.

2.5 Phase change cooling

The cooling methods discussed previously have involved the sensible (single-phase) heating of a fluid, an alternative method is to use a cooling medium which will change phase as it removes the waste heat. The advantage of two phase cooling is that the thermal energy required to change phase can far exceed the heat capacity of the fluid in sensible heating, which can lead to improved heat transfer and reduced thermal gradients across the cell.

Phase change cooling for low power PEMFC applications can be achieved using heat pipes. Silva et. al [42] used a de-ionized water heat pipe to regulate temperature from a heated graphite plate which was used to represent a single 20W fuel cell. The condensing end of the heat pipe was connected to a capillary pumped loop which used Acetone to transfer heat to the environment via a fin and tube condenser, regulating cell temperature without the need for active cooling. However the volume required for such a system would not be suitable for large scale applications in its current form.

Garrity et. al [43] produced an experimental micro channel cooling plate which removed heat through boiling, the working fluid was HFE-7100. The experimental set-up was shown to remove heat at a maximum rate of 32kW/m^2, far exceeding current cell heat generation rates. Soupremanien *et. al* [15] conducted a similar study on flow boiling within a single flow channel, conducting visualisation studies and comparing single-phase and two-phase cooling with Forane 365 HX as the working fluid. Results showed both increased heat removal rate and reduced pressure drop for the two-phase cooling, although the single phase cooling performance might have been improved with the use of water as the coolant fluid. Both the study by Garrity *et. al* [43] and Soupremanien *et. al* [15] condensed the working fluid using a liquid cooled condenser, in a vehicle application the condensation would ideally take place in a radiator, which may not always be located directly next to the fuel cell.

A disadvantage of using flow boiling as a means of cooling is the potential for overheating if the heat generation flux exceeds the critical heat flux. At this point the boiling regime transitions from nucleate to film boiling. The vapour film prevents contact between the wall and the liquid, reducing the heat flux with further increases in temperature until the Leidenfrost point is achieved as described in the Nukiyama boiling curve (Incropera and DeWitt [44]). This can be avoided by ensuring a sufficient supply of cooling fluid, understanding the point at which the critical heat flux occurs and designing a suitable safety factor.

2.5.1 Evaporative cooling

Another method of phase change cooling is to evaporate liquid water inside the reactant flow channels of the anode and cathode. This has several advantages compared to other cooling methods as the heat is removed directly from the flow channels and the evaporated water can also humidify the cell, removing the need for an external humidifier. The rate at which liquid water is added will have a significant impact on cell performance. Insufficient water will simultaneously overheat and dry the membrane, whereas excess water will cause flooding, preventing reactant and product diffusion and significantly reduce performance. For this reason it is not possible to add the liquid water prior to the cell inlet since flooding would occur in the initial stages of the cell, instead the liquid water is added over the surface of the cell, requiring a modified bi-polar plate. Figure 2.6 illustrates a three cell evaporatively cooled PEMFC stack with liquid water added directly to the cathode flow. In this case the anode is humidified through back diffusion from the cathode, anode liquid water addition is also possible although the potential for heat removal through evaporation is less than the cathode because of a reduced gas flow.

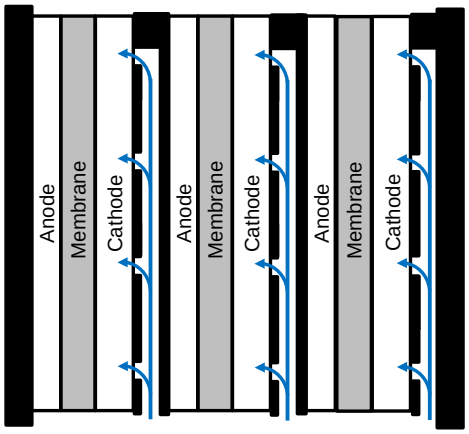

Figure 2.6: Evaporatively cooled stack with cathode liquid water addition

Two separate methods of adding the liquid water to the flow channels have been explored in the literature, a wicking method where liquid water is drawn into the flow channel and an injection method where liquid water is forced into the flow channel. The former uses a water concentration gradient whereas the latter uses a pressure gradient to facilitate transport. Systems achieving liquid water addition through wicking have been demonstrated and patented by UTC power [12, 45] and General Motors [46]. Meyers *et.al* [12] experimentally demonstrated a 30 cell evaporatively cooled stack showing power densities in excess of 0.85W/cm^2. Liquid water was added to the cathode flow channel through the use of a

porous bi-polar plate with water being pulled through with capillary pressure, removing the need for an external water pump. Darling and Perry [45] later patented a similar design using porous bi-polar plates to transport liquid water from cooling channels to the anode flow field with the use of a mechanical water pump, no experimental results were given. Goebel [46] patented an evaporatively cooled fuel cell which used a porous medium to wick water from a liquid flow channel to the cathode gas flow channel. The wicking material is of similar construction to the gas diffusion layer and forms channels across the surface of the cell to increase exposure to the gas channel.

Direct liquid water injection has been developed commercially by Intelligent Energy [13, 47–49]. Matcham *et al.* [47] detailed a method of liquid water injection involving the distribution of liquid water from a single inlet to selected points throughout the cell between two metal foil layers. Even distribution was promoted through the use of a plenum with a baffle pattern etched into the foil around 10 microns thick. For a serpentine flow channel arrangement, liquid water was added at the point where the flow channel doubles back (180° turn) on one side of the cell, water was supplied between 3-6 times the minimum rate required for thermal balance. Adcock *et. al* [48] experimentally demonstrated the technology of [47] in a 12kW 192 cell stack, showing cold start ability from -20°C. Warburton et. al [13] used the same technology to produce a 30kW fuel cell system which were installed in five prototype hybrid vehicles. More recently Hardill *et.al* [49] claimed increased power of 55kW using a 324 cell stack with a volumetric power density of 3.7kW/l.

The water evaporated in cooling the cell is carried out of the stack in vapour phase with the exhaust gas flow. In a system which does not have an indefinite supply of de-ionised water, water vapour from the exhaust stream must be condensed and collected to replenish the amount used in cooling the fuel cell. This is referred to as water balance in an evaporatively cooled fuel cell. A condenser is used to cool the exhaust stream down to a temperature where a suitable amount of liquid water is present to replenish that used in cooling the cell. The liquid water is then separated, typically using a cyclone and the water stored in a tank until it is re-used. The simplest system layout which utilises an air cooled condenser is shown in figure 2.7. This is the preferred system layout described in [48], however such a system may not always be feasible in automotive applications. Conventional aluminium radiators may not be used because the presence of aluminium ions in the collected water will contaminate the fuel cell causing premature degradation [50]. Instead stainless steel radiators should be used, although at added expense, limited availability and reduced thermal conductivity. Furthermore, in certain circumstances, such as range extenders, packaging constraints may mean the fuel cell system does not have access to the frontal area of the vehicle. An alter-

native is to condense the fuel cell exhaust using a liquid coolant loop, the condenser can then form part of the traditional vehicle cooling loop, replacing the combustion engine as the main heat source. This layout can make packaging simpler and also allow conventional aluminium radiators to be used, although at the expense of added complexity and possibly reduced heat transfer due to an intermediate heat exchanger. Such a system is shown in figure 2.8.

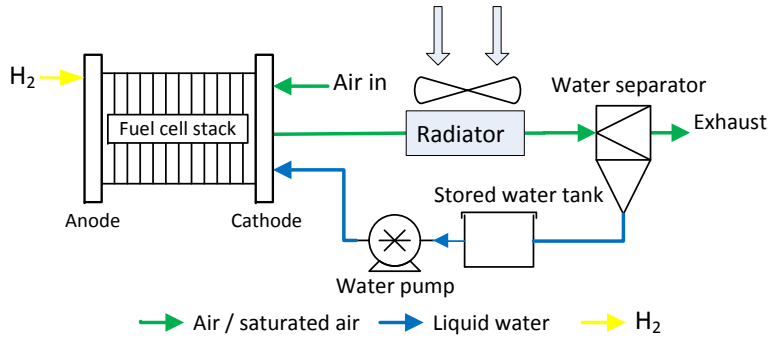

Figure 2.7: Layout B: Evaporatively cooled system with condensing radiator

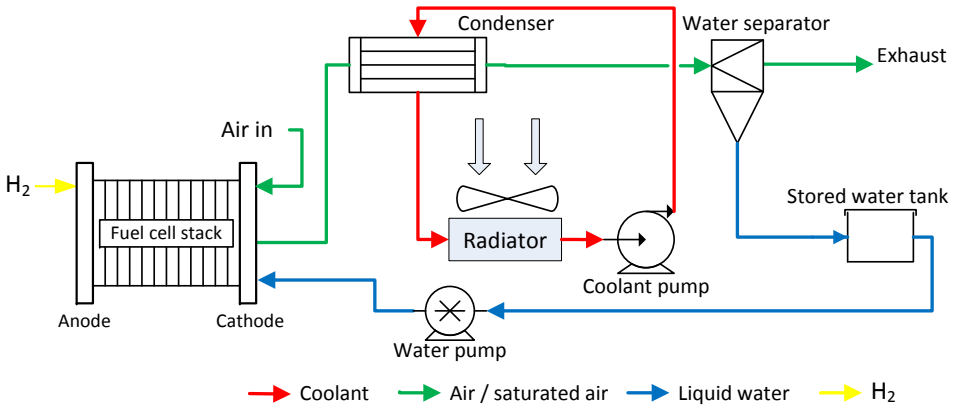

Figure 2.8: Layout C: Evaporatively cooled system with intermediate cooling loop

The presence of a liquid water tank in figures 2.7 and 2.8 acts as a buffer for the water balance of an evaporatively cooled system. During periods of high thermal load the system may be unable to maintain water balance, the net water flow (equation 2.3) will be negative and the stored water volume will be depleted. Conversely, during periods of low thermal load the heat exchanger will be more effective allowing all the added water, along with some of the reaction product water, to be collected. This gives a positive net water flow and replenishes the stored water volume. This implies that over a transient drive cycle an evaporatively cooled system does not need to reject the peak thermal load but only sufficient heat to

achieve water balance over the whole drive cycle provided the tank volume is sufficient for the fluctuations required. This presents a significant advantage compared to liquid cooled systems where the heat rejection profile should closely follow the heat generation profile to regulate temperature within acceptable limits.

$$\textit{Net water flow} = \textit{Liquid collected from exhaust} - \textit{Liquid added to stack} \tag{2.3}$$

Although a large stored water tank allows for greater flexibility in achieving water balance, it also has significant implications on the ability of the system to start-up in sub-zero freezing conditions, since unlike the fuel cell stack the evaporative cooling system cannot be purged of water on shut-down. Ice within the evaporative cooling system must be thawed before the fuel cell stack can operate effectively, failure to do so may result in permanent damage to the cell membranes due to insufficient cooling and low humidity. One way of achieving this is in a battery hybrid powertrain is to use the electrical power of the battery to thaw the stored water tank and pipework leading to the fuel cell stack. Once some liquid water is available to evaporate in the stack, the fuel cell can operate and produce its own heat to facilitate the thawing process. The larger the stored water tank the more energy that will be required to thaw it, increasing the time the vehicle will have to run only on the battery. Furthermore, a large stored water tank increases system volume and mass, restricting vehicle packaging and reducing overall performance. A compromise must therefore be made between a large tank for good transient net water flow and a small tank for reduced mass, simpler packaging and lower thermal inertia for cold starts.

Whilst both thermal balance and system water balance have been studied for liquid cooled systems there are currently no studies available in the existing literature which explore the temperature regulation and water balance behaviour of evaporatively cooled fuel cells. Unlike liquid cooled fuel cells, stack temperature in an evaporatively cooled stack is influenced by the cell operating parameters and liquid water addition. The heat exchanger requirements are also significantly different, the liquid cooled system being single phase and the evaporatively cooled two-phase.

2.6 Fuel cell modelling

The use of models and computer simulations have helped increase the rate of advancement in fuel cell technology by reducing the development time and experimental costs. Many of the studies discussed in this chapter were conducted through the use of models which often offer a useful insight into the behaviour of a fuel cell in areas which are hard to measure

experimentally. When developing a model of any system it is important to understand the assumptions made when developing the model, the models limitations in representing the real system and how the model has been validated against experimental data.

The mathematical modelling of PEMFCs is a significant multidisciplinary research field covering a wide range of different phenomena at different scales. This section will give a brief introduction to macro-scale fuel cell models suitable for single cell study up to vehicle level study. The first significant mathematical models of a PEMFCs were produced in the early 1990s [51]. Springer *et. al* [52] produced a fundamental model of a single fuel cell based on conventional mass transfer relationships and the empirical membrane hydration relationship of [53]. Simultaneously Bernardi and Verbrugge [54] developed a one dimensional through cell model of a flow channel gas diffusion layer and membrane for the cathode side of a single cell. Fuller and Newman [55] published one of the first one dimensional models to consider the change in reactants along the flow channel of the cell. Later on Gurau *et. al* [56] developed one of the first two dimensional flow channel models and as the field of computational fluid dynamics (CFD) has developed increasingly detailed three dimensional models have been published.

One of the first transient models was published by Amphlett *et. al* [57] which considered the variation in temperature with time at a whole cell level. Pukrushpan *et. al* [58] later used a similar method to simulate transient gas flow in the anode and cathode assuming each could be represented by a single isothermal lumped volume. The simplified transient models of [57] and [58] provide the basis for the vast majority of control oriented and system level fuel cell models. Whilst not providing the detail of the three dimensional CFD models, they allow for real time simulation and with sufficient empirical correlations can provide a good prediction of system level behaviour.

There is very little information on the modelling of evaporatively cooled fuel cells in the existing literature. Kells and Jackson [59] and Warburton *et. al* [13] both produced vehicle level models of a prototype evaporatively cooled fuel cell vehicle, both used commercially available software packages but neither gave any information on how the fuel cell was represented. Schultze and Horn [60] developed a lumped parameter model of an evaporatively cooled fuel cell stack using a similar approach to [58] for the flow channel dynamics but without the isothermal assumption. Evaporative cooling was considered using a thermal balance assuming all available liquid water would evaporate up to saturation, normalised temperature and pressure results were presented and validated. Based on the current literature there is significant scope to further develop the understanding in fuel cell modelling

relating to evaporatively cooled fuel cells, both at system level and cell level.

2.7 Literature review summary

The most common way of removing waste heat from large scale PEMFC systems is through liquid cooling. Many studies have shown that by using this method stack temperature can be regulated within a narrow region across transient operations. However, at high ambient temperatures the ability to reject waste heat can prove challenging compared to conventional combustion vehicles. Furthermore, few studies have considered the implication changes in radiator air flow through vehicle speed variation will have on thermal management performance. This is particularly relevant to systems which do not utilise a radiator coolant by-pass.

Evaporative cooling presents a possible alternative to liquid cooling for automotive size fuel cell stacks. Despite several successful prototype stacks producing up to 55kW there have been very few studies on the modelling and performance of such systems. Only one lumped parameter model of an evaporatively cooled fuel cell stack exists, there is yet to be a comprehensive system level model or a model which considers the spacial variation inside the cell. This work seeks to develop the modelling of evaporatively cooled fuel cells in the existing literature and use the new models to study cell and system performance across different operating conditions.

It is also not clear from the current literature which situations favour which cooling method. It is therefore desired to produce a direct quantitative comparison of liquid and evaporatively cooled systems comparing heat exchanger requirements and parasitic loads over both steady state and transient drive cycles in thermally demanding conditions.

The remainder of this thesis seeks to further the knowledge on evaporatively cooled PEMFCs through the development, validation and analysis of different mathematical models.

Chapter 3

Lumped parameter model of an evaporatively cooled fuel cell vehicle

3.1 Introduction

To study water balance of an evaporatively cooled fuel cell system over transient drive cycles and investigate methods of improving water collection rates, a computationally efficient yet sufficiently accurate model is required. In this chapter, the development and validation of a lumped parameter (zero-dimensional) fuel cell stack model and key balance of plant components are detailed. The completed model is combined with the two phase heat exchanger models of chapter 5 and used to quantify water balance in chapter 6.

The full system model consists of the fuel cell stack model described in sections 3.2 to 3.7, the balance of plant models described in section 3.8 and the vehicle model described in section 3.9. The fuel cell stack model is comprised of four separate sub-models; cell voltage, water transport, mass balance and energy balance. The interaction between the different fuel cell stack sub-models is shown in figure 3.1, where the model inputs are requested current density, anode and cathode inlet flow rates (separated into different species) and inlet temperatures. All inputs may be time variant in transient simulations.

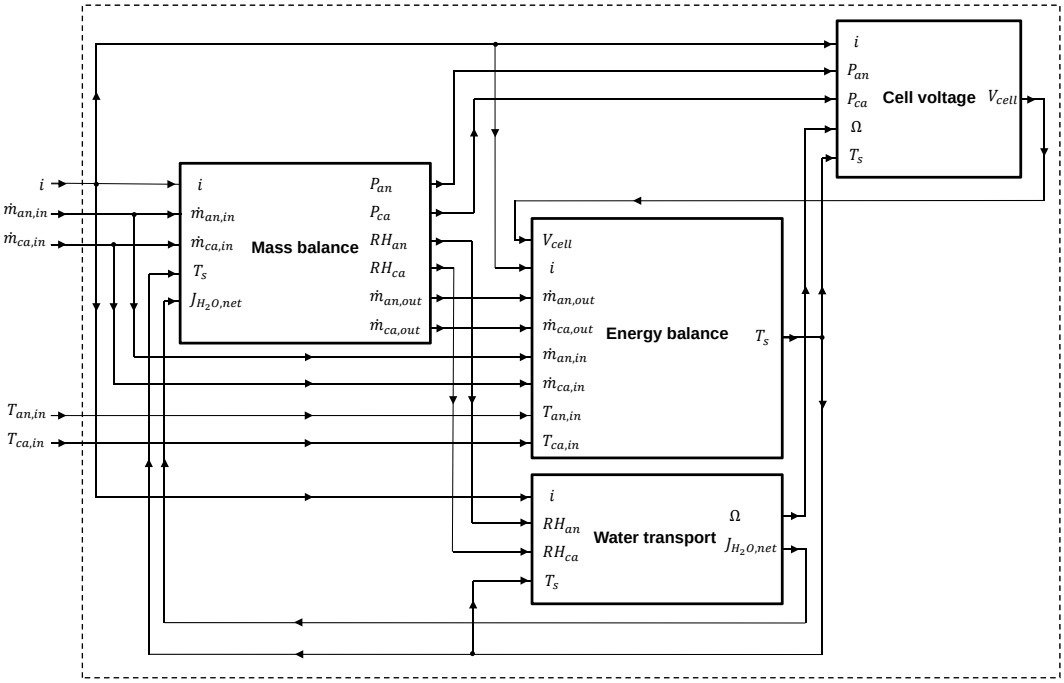

Figure 3.1: Submodel interaction for lumped parameter fuel cell model

3.2 Cell voltage model

The fuel cell converts chemical energy to electrical energy through the oxidation of hydrogen using equation 3.1. The electrical potential of the cell is dependant on the thermodynamic potential (Gibbs free energy) and charge of the electrochemical reaction. In the case of equation 3.1, two electrons pass through the external circuit for each hydrogen molecule oxidised, the reversible open circuit voltage (E_n) is determined using equation 3.2. Since the Gibbs free energy (Δg_f) changes with temperature it is often more useful to express in terms of enthalpy ($\Delta\hat{h}$) and entropy ($\Delta\hat{s}$) of the electrochemical reaction, shown on the right of equation 3.2 where T_s is the stack temperature which will vary with time in transient simulations and F is the Faraday constant.

$$\mathrm{H_2} + \frac{1}{2}\mathrm{O_2} \rightarrow \mathrm{H_2O} \tag{3.1}$$

$$E_n = \frac{-\Delta g_f}{2F} = \frac{\Delta\hat{h} - T_s\Delta\hat{s}}{2F} \tag{3.2}$$

As well as changing with temperature, the Gibbs free energy also changes with the

concentration of the chemical products and reactants. This is commonly expressed using the Nernst equation, which when combined with equation 3.2 gives the reversible open circuit voltage of a hydrogen fuel cell with a liquid water product accounting for changes in temperature and pressure (equation 3.3), where pressure (P) is expressed in bar absolute and can be time variant in transient simulations. The reversible open circuit voltage for such a reaction at 20°C, 1bar.a pressure is 1.23V.

$$E_n = -\frac{\Delta\hat{h} - T_s\Delta\hat{s}}{2F} + \frac{R_0 T_s}{2F} ln\left(\frac{P_{H_2} P_{O_2}^{\frac{1}{2}}}{1}\right) \tag{3.3}$$

The reversible open circuit voltage represents the maximum theoretical potential which can be obtained by the cell, however, as with any real system, there are irreversible losses which reduce the efficiency of the system. In a hydrogen fuel cell the irreversible losses are generally split into four separate causes or 'overvoltages'; activation overvoltage, fuel crossover, mass transport losses and ohmic losses.

3.2.1 Activation overvoltage

Activation overvoltage (V_{act}) is defined as the energy lost to overcome the activation barrier of the electrochemical reaction and has an exponential relationship with current density (i)[61]. The activation overvoltage is expressed using the semi-empirical Tafel equation, shown in equation 3.4 where α and i_{oc} represent the charge transfer coefficient and internal current density respectively.

$$V_{act} = \frac{R_0 T_s}{2\alpha F} ln\left(\frac{i}{i_{oc}}\right) \tag{3.4}$$

The charge transfer coefficient is the proportion of the total electrical energy which is harnessed in changing the rate of the electrochemical reaction [10], in this work an empirically determined value has been used which is shown in table A.2. The exchange current density represents the rate at which the reversible electrochemical reaction occurs when no current is applied. A higher exchange current density represents a more 'active' surface and a lower activation overvoltage. As with the open circuit voltage, the exchange current density changes with reactant pressure and cell temperature which is accounted for using equation 3.5 [9]. Where $i_{oc,0}$ is the experimentally determined exchange current density at standard temperature and pressure and $x_{O_2,0}$ is the volume fraction of Oxygen in air at standard temperature and pressure.

$$i_{oc} = i_{oc,0}\left(\frac{P_{O_2}}{P_0 x_{O_2,0}}\right)^{\psi} exp\left[-\frac{E_c}{R_0 T_s}\left(1 - \left(\frac{T_s}{T_0}\right)\right)\right] \tag{3.5}$$

The oxidation of hydrogen (equation 3.1) is the combination of two half cell reactions, one for the anode (equation 3.6), the other for the cathode (equation 3.7). The rate at which the reversible reaction occurs at each electrode is different, meaning that the anode and cathode each have a different exchange current density. The anode exchange current density is several orders of magnitude higher than the cathode [9], meaning that the cathode activation overpotential is dominant and the anode activation overpotential can be ignored.

$$\mathrm{H_2} \leftrightarrow 2\mathrm{H^+} + 2e^- \tag{3.6}$$

$$\frac{1}{2}\mathrm{O_2} + 2\mathrm{H^+} + 2e^- \leftrightarrow \mathrm{H_2O} \tag{3.7}$$

3.2.2 Fuel crossover

The purpose of the membrane in a proton exchange membrane fuel cell is to be conductive to protons only and prevent transport of electrons and diffusion of reactants across the membrane. In reality a small amount of hydrogen will diffuse across the membrane from the high hydrogen concentration at the anode to the low concentration at the cathode, here it will react with the oxygen producing water and heat but no electrical energy. A similar phenomenon, called internal current density, occurs due to a small number of electrons (relative to the number of protons) being conducted across the membrane, before combining with the protons at the cathode to make hydrogen and oxidising to form water. Since both fuel crossover and internal current density have the same effect they are often treated as one loss [10].

Fuel crossover and internal current density are considered in the model using the Tafel equation, shown in equation 3.8, where i_n is an empirically determined constant to represent both losses. Equation 3.8 is the only voltage loss to effect the cell voltage when no external load is applied, typically reducing the reversible open circuit voltage by around 0.2V [10] to give the actual open circuit voltage.

$$V_{fc} = \frac{R_0 T_s}{2\alpha F} ln\left(\frac{i_n}{i_{oc}}\right) \tag{3.8}$$

3.2.3 Mass transport loss

Mass transport losses represent the voltage loss due to reductions in reactant concentration at the catalyst layer, predominately on the cathode side where the oxygen is supplied from air. As current density increases, the rate at which the oxygen can diffuse from the flow channel, through the gas diffusion layer to the catalyst layer becomes less than the rate at

which oxygen is consumed in the electrochemical reaction. This causes the oxygen concentration and hence voltage to be reduced at high currents.

Mass transport losses can also be caused by a reduction in oxygen partial pressure along the flow channel from cell inlet to outlet as the oxygen is consumed in the electrochemical reaction. The influence of localised mass concentration losses are largely negated in air fed fuel cells by operating at sufficient stoichiometries, values in excess of 2.0 are common [9].

The amount of mass transport loss is dependant on many factors, such as the cell geometry, stoichiometry, gas diffusion layer properties and presence of liquid water. Because of the complexity in analytically predicting mass transport losses, the empirical exponential relationship of equation 3.9 [10] has been used in this model where a_{trans} and b_{trans} are determined from experimental results.

$$V_{trans} = a_{trans} exp\left(b_{trans} i\right) \tag{3.9}$$

3.2.4 Ohmic losses

Both the electrons moving around the external circuit and protons transferring through the membrane experience some resistance to flow which is proportional to the cell current. The resistance to electron flow is due to the resistivity and contact resistance of the gas diffusion layer, bi-polar plates and current collectors. Resistance to proton flow is caused by the properties of the membrane separating the anode and cathode. In practice, the ionic conductivity of the membrane is significantly less than the electronic conductivity of the external circuit meaning that resistance through the membrane dominates [61]. Therefore it is reasonable to assume resistance to electron flow is negligible compared to resistance to proton flow when calculating losses. Voltage drop due to ionic resistance is determined using Ohms law (equation 3.10).

$$V_{ohm} = \Omega i \tag{3.10}$$

The resistance (Ω) of the membrane is highly dependant on its water content, since water acts as a vehicle mechanism for transporting protons from anode to cathode. The ionic conductivity of the membrane is therefore often expressed as an empirical function of water activity. The calculation of ionic conductivity used in the model is discussed in section 3.3.

3.2.5 Cell voltage

Once the reversible open circuit voltage and irreversible voltages have been calculated, the cell voltage is determined using equation 3.11. Substituting equations 3.3 to 3.10 in to equation 3.11, the operational cell voltage can be expressed using equation 3.12.

$$V_{cell} = E_n - V_{act} - V_{fc} - V_{trans} - V_{ohm} \tag{3.11}$$

$$V_{cell} = -\frac{\Delta\hat{h} - T_s\Delta\hat{s}}{2F} + \frac{R_0 T_s}{2F} ln\left(\frac{P_{H_2} P_{O_2}^{\frac{1}{2}}}{1}\right) - \frac{R_0 T_s}{2\alpha F} ln\left(\frac{i + i_n}{i_{oc}}\right) - a_{trans} exp\left(b_{trans} i\right) - \Omega i \tag{3.12}$$

Figure 3.2 shows the reversible open circuit voltage, irreversible voltages and cell voltage as a function of current density for a typical fuel cell. At low current densities (<0.2A/cm^2) the activation and fuel crossover losses account for the main reduction in voltage, this region is referred to as the activation voltage region. Between 0.2-1.2A/cm^2 further reductions in voltage with increase in current is predominantly due to the increase in ohmic loss with only a small increase in activation overvoltage. This middle region is referred to as the ohmic operating region. At high current densities mass transfer begins to dominate causing cell voltage to reduce with further increases in current. This region is referred to as the mass transport or mass concentration region and should be avoided during normal operation because of low cell efficiencies. Because the different irreversible voltages are dominant in different regions of the polarisation curve, the determination of each of the empirical values used in equation 3.12 can be made separately without significantly influencing the behaviour of the other irreversible voltage losses. For example, the section of the internal current density (i_n) primarily effects the voltage at very low loads but does not influence the shape of the polarisation curve. Conversely the mass concentration loss constants (a_{trans}, b_{trans}) only influence the shape of the polarisation curve at high current densities, allowing these constants to be selected in isolation.

3.3 Water transport

The primary method of transporting protons across the membrane from anode to cathode is by using water as a vehicle mechanism. Therefore being able to model the water content and water transport within the membrane is of critical importance. The complexities in analytically modelling the transport of water through the membrane at different operating conditions mean that to retain the goal of simulating thermal transients at a system level

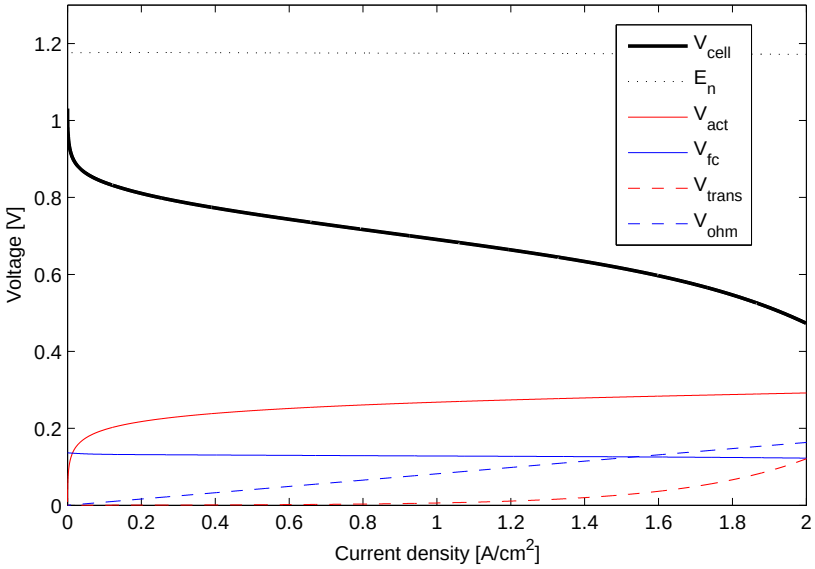

Figure 3.2: Cell voltage polarisation curve

a semi-empirical model must be used. Several such models are available in the literature, with empirical constants obtained for different membranes and operating conditions using a variety of experimental methods, a summary of which are discussed by Dai *et al.* [62]. Experimental analysis performed by Husar *et al.* [63] demonstrated variation by up to an order of magnitude between predicted rates of water transport between different correlations. Of the available semi-empirical water transport models the widely used relationship of Springer *et al.* [52] for a Nafion® 117 membrane has been used in this study to determine the water content, resistance and water flux through the membrane. This method has been chosen since it agrees well with subsequent experimental analysis, is derived from the experimental data of Zawodzinski *et al.* [64] and is based on the widely used Nafion® series of commercial membranes. This relationship has also been used extensively in previous validated fuel cell models, including [25, 60, 65].

The localised water content of a membrane is defined as the ratio of water molecules to the number of charge ($SO_3^-H^+$) sites and can be expressed as a function of the water vapour activity (ϕ), or alternatively relative humidity if an ideal gas is assumed [63]. Equation 3.13 shows the empirical water content for a Nafion® 117 membrane at 30°C as a function of water vapour activity [52].

$$\lambda = \begin{cases} 0.043 + 17.81\phi - 39.85\phi^2 + 36.0\phi^3 & 0 < \phi \leq 1 \\ 14 + 1.4\,(\phi - 1) & 1 < \phi < 3 \end{cases} \tag{3.13}$$

Two different methods of water transport across the membrane need to be considered, these are electro-osmotic drag and back diffusion.

3.3.1 Electro-osmotic drag

Electro-osmotic drag is the flux of water molecules transferred from anode to cathode by protons moving through the membrane. Electro-osmotic drag flux can be expressed using equation 3.14, where n_{drag} is the number of water molecules dragged from anode to cathode for each proton. Zawodzinski *et al.* [64] showed that on average 2.5 water molecules are dragged from anode to cathode for each proton in a fully hydrated Nafion® 117 membrane, giving $n_{drag}^{sat} = 2.5$. Equation 3.15 is then used to compensate for the reduction in electro-osmotic drag coefficient at lower membrane water content [52], where λ is the mean membrane water content.

$$J_{H_2O,drag} = 2n_{drag}\frac{i}{2F} \tag{3.14}$$

$$n_{drag} = n_{drag}^{sat}\frac{\lambda}{22} \tag{3.15}$$

3.3.2 Back diffusion

Back diffusion is the flux of water molecules across the membrane from a higher to a lower concentration. Since water production occurs on the cathode side, the anode tends to have a lower water concentration. Back diffusion therefore usually occurs from cathode to anode, acting in the opposite direction to electro-osmotic drag. Back-diffusion is modelled using Fick's law of diffusion, shown in equation 3.16 where ρ_{dry} and M_{mem} are the membrane dry density and molecular mass respectively, determined from manufacturer specification. λ represents the mean water content in the membrane. The diffusion coefficient (D_λ) at 30°C is expressed as an empirical function of membrane water content for a Nafion® 117 membrane using equation 3.17 for values of λ greater than four. When λ is less than four, the diffusion coefficient is obtained using a look up table of the experimental data from [52]; since this equates to relative humidities less than 30% it is unlikely the look up section will be used in normal operation. The variation in membrane diffusivity with water content is shown in figure 3.3. Equation 3.18 is then used to correct for temperature variations [52].

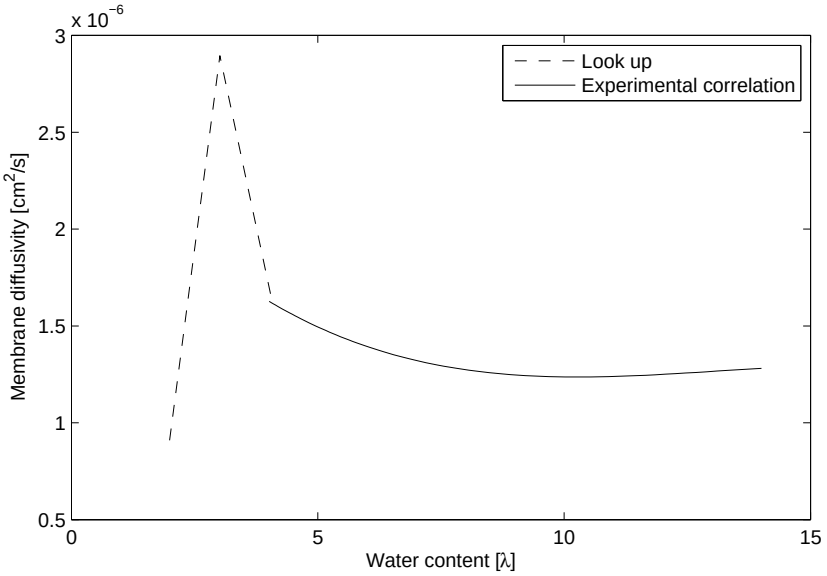

Figure 3.3: Membrane water vapour diffusivity using the method of Springer *et al.* [52]

$$J_{H_2O,back} = -\frac{\rho_{dry}}{M_{mem}} D_\lambda \frac{d\lambda}{dz} \tag{3.16}$$

$$D_{\lambda,30} = \left(2.563 - 0.33\lambda + 0.0264\lambda^2 - 0.000671\lambda^3\right) 10^{-6} \qquad \lambda > 4 \tag{3.17}$$

$$D_\lambda = exp\left(2416\left(\frac{1}{303} - \frac{1}{T_s}\right)\right) D_{\lambda,30} \tag{3.18}$$

Both the water content gradient ($d\lambda/dz$) and membrane diffusivity (D_λ) vary through the thickness of the membrane, the two variables also influence the net water flux through the membrane and in turn the water content distribution. To remove the complexity of having to model the spatial distribution of water content across the membrane, and to maintain the model as lumped parameter, it is assumed that the water content gradient is linear from anode to cathode and the diffusivity is uniform across the membrane. This assumption is deemed reasonable because of the thickness of the membrane is typically less than 100μm. A comparison of the analytical example of [61] (assuming constant diffusivity) to the linear water content gradient assumption is shown in figure 3.4. Water vapour activities are 0.8 and 1.0 on the anode and cathode respectively.

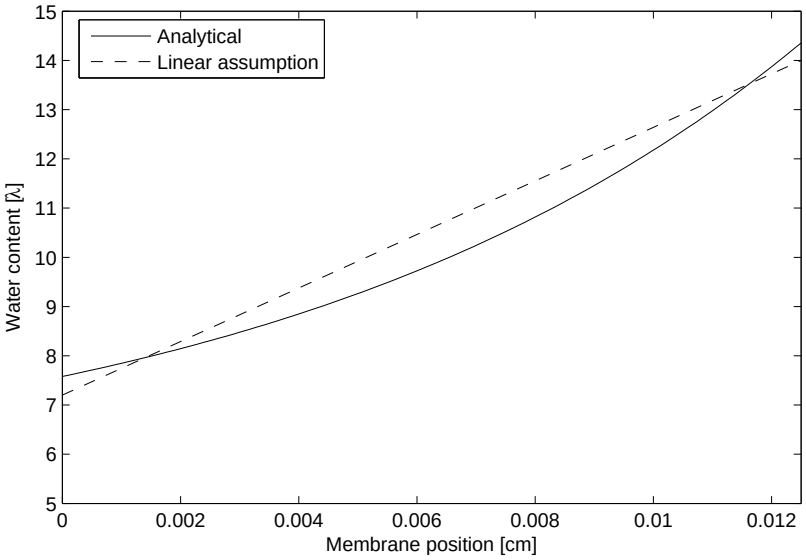

Figure 3.4: Analytical vs. linear water content assumption

Based on this assumption, the water content gradient can be calculated from the water content at the anode and cathode using equation 3.19. The lumped parameter model proposed in this chapter does not consider the effects of the gas diffusion layer, therefore the humidity in the anode or cathode flow channels is equal to the humidity at the membrane interface which is used to determine the membrane water content.

$$\frac{d\lambda}{dz} = \frac{\lambda_{ca} - \lambda_{an}}{t_{mem}} \tag{3.19}$$

The Net water flux across the membrane can then be expressed using equation 3.20 where water flux is positive from anode to cathode. The variation in water flux with current density for a fuel cell model simulating an un-humidified open ended anode with a 1.03 hydrogen stoichiometry and a humidified cathode is shown in figure 3.5. The figure shows that for the simulated case, back diffusion is greater than electro-osmotic drag, giving a net flux from cathode to anode aiding the hydration of the anode. It is important to ensure both electrodes are sufficiently hydrated for efficient operation, especially at high current densities where the increased electro-osmotic drag can cause drying in the anode.

$$J_{H_2O,net} = \frac{n_{drag} i}{F} - \frac{\rho_{dry}}{M_{mem}} D_\lambda \frac{d\lambda}{dz} \tag{3.20}$$

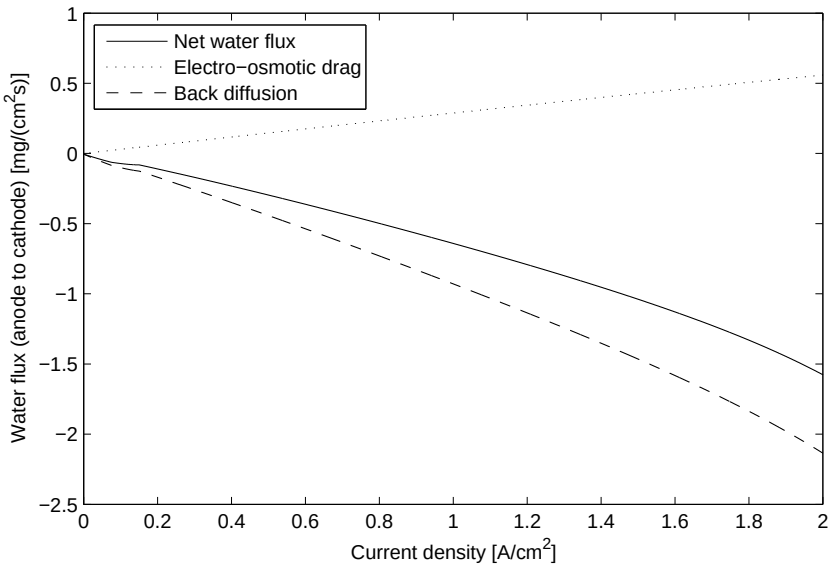

Figure 3.5: Current density vs. steady state membrane water flux

3.3.3 Membrane resistance

The ionic conductivity (σ) of the membrane varies significantly with water content since the water molecules are used to facilitate the transport of protons from anode to cathode. In the model, ionic conductivity is determined using the empirical relationship of [52] for a Nafion® 117 membrane as a function of water content at 30°C (equation 3.21). Corrections for temperature variation are made using equation 3.22 and conductivity is related to resistance using equation 3.23, where the mean membrane water content is used to evaluate the conductivity.

$$\sigma_{30} = 0.005139\lambda - 0.00326 \quad \lambda > 1 \tag{3.21}$$

$$\sigma = exp\left(1268\left(\frac{1}{303} - \frac{1}{T_s}\right)\right)\sigma_{30} \tag{3.22}$$

$$\Omega = \int_0^{t_{mem}} \frac{1}{\sigma}\,\mathrm{d}z \approx \frac{t_{mem}}{\sigma} \tag{3.23}$$

3.4 Mass conservation

The model simulates the fuel cell stack as two single volumes connected by a membrane, the two volumes represent the anode and the cathode flow channels. Mass flux into and out of each volume is considered, as well mass flux of water across the membrane and consumption and production at the membrane surfaces from the electrochemical reaction. The different mass fluxes considered in the fuel cell stack model are shown in figure 3.6, where $\dot{m}_{H_2O,ca,inj}$ represents the liquid water added directly into the cathode flow channel for evaporative cooling and humidification.

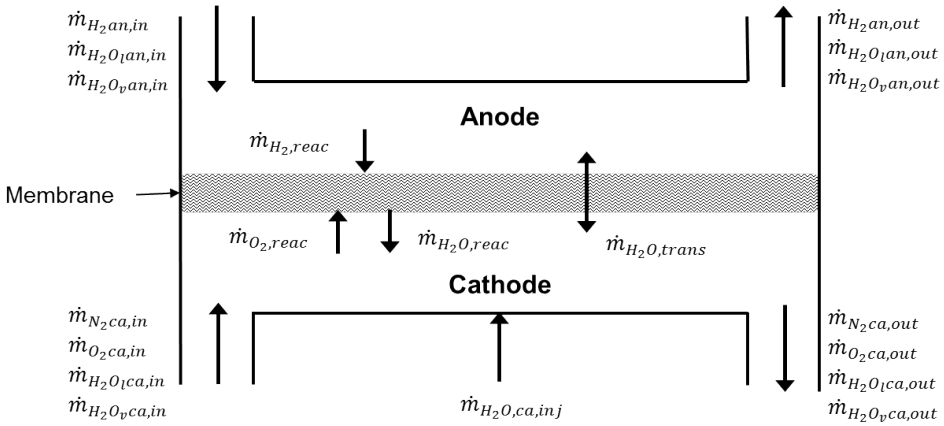

Figure 3.6: Mass conservation of lumped parameter fuel cell stack

3.4.1 Cathode

Conservation of three separate species are considered in the cathode volume, these are nitrogen, oxygen and water. The first order differential mass balance equations for each species are shown in equations 3.24-3.26.

$$\frac{dm_{O_2,ca}}{dt} = \dot{m}_{O_2,ca,in} - \dot{m}_{O_2,ca,out} - \dot{m}_{O_2,reac} \tag{3.24}$$

$$\frac{dm_{N_2,ca}}{dt} = \dot{m}_{N_2,ca,in} - \dot{m}_{N_2,ca,out} \tag{3.25}$$

$$\frac{dm_{H_2O,ca}}{dt} = \dot{m}_{H_2O,ca,in} + \dot{m}_{H_2O,ca,inj} + \dot{m}_{H_2O,reac} - \dot{m}_{H_2O,ca,out} + \dot{m}_{H_2O,trans} \tag{3.26}$$

Where $\dot{m}_{O_2,ca,in}$, $\dot{m}_{N_2,ca,in}$ and $\dot{m}_{H_2O,ca,in}$ are equal to the inlet manifold exit flow,

described in section 3.8.2. $\dot{m}_{H_2O,trans}$ is the net water mass flux across the membrane from the anode, determined using equation 3.27. $\dot{m}_{O_2,reac}$ and $\dot{m}_{H_2O,reac}$ are the rate of oxygen consumption and water production and are described by equations 3.28 and 3.29 respectively.

$$\dot{m}_{H_2O,trans} = M_{H_2O} A_{cell} J_{H_2O,net} \tag{3.27}$$

$$\dot{m}_{O_2,reac} = A_{cell} M_{O_2} \frac{in}{4F} \tag{3.28}$$

$$\dot{m}_{H_2O,reac} = A_{cell} M_{H_2O} \frac{in}{2F} \tag{3.29}$$

The cathode gas exit mass flow rate $\dot{m}_{ca,out}$ is determined using the linearised nozzle equation. Shown in equation 3.30 where k_{ca} and A_{ca} are the nozzle pressure coefficient and cross sectional area respectively. P_{ca} is the cathode pressure, determined from the sum of partial pressures, using the ideal gas law, shown in equation 3.31 where x represents each gas species (N_2,O_2,H_2Ov). P_{em} is the pressure of the exit manifold, calculated in section 3.8.2, V_{ca} is the lumped cathode volume.

$$\dot{m}_{ca,out} = k_{ca} A_{ca} \left(P_{ca} - P_{em} \right) \tag{3.30}$$

$$P_{ca} = \sum_{x=1}^{3} P_x = \sum_{x=1}^{3} \frac{m_x R_0 T_s}{M_x V_{ca}} \tag{3.31}$$

To determine the separate species exit mass flow rates required for equations 3.24-3.26 the cathode gas exit mass flow rate is split into its constituent parts using species mass fractions (equations 3.32-3.34). From which species mass flow rate is found using equations 3.35 to 3.37.

$$x_{N_2} = \frac{m_{N_2}}{m_{N_2} + m_{O_2} + m_{H_2Ov}} \tag{3.32}$$

$$x_{O_2} = \frac{m_{O_2}}{m_{N_2} + m_{O_2} + m_{H_2Ov}} \tag{3.33}$$

$$x_{H_2Ov} = \frac{m_{H_2Ov}}{m_{N_2} + m_{O_2} + m_{H_2Ov}} \tag{3.34}$$

$$\dot{m}_{N_2,ca,out} = x_{N_2} \dot{m}_{ca,out} \tag{3.35}$$

$$\dot{m}_{O_2,ca,out} = x_{O_2}\dot{m}_{ca,out} \tag{3.36}$$

$$\dot{m}_{H_2Ov,ca,out} = x_{H_2Ov}\dot{m}_{ca,out} \tag{3.37}$$

Once the mass of each species has been determined the water mass within the cathode is further split into water vapour mass and liquid water mass within the cathode flow channel. The model makes the simplifying assumption that all water present will evaporate up to the point of saturation, after which any additional water will be in a liquid state. The vapour mass limit within the cathode volume is calculated from the ideal gas law for water vapour with a partial pressure equal to the saturation pressure (equation 3.38). Saturation pressure is found using a look-up table with information gathered from the CRC data book [66].

$$m_{v,max} = \frac{P_{sat}V_{ca}M_{H_2O}}{R_0T_s} \tag{3.38}$$

The logic to determine the composition of vapour and liquid, given the above assumptions, then becomes:

$$\left.\begin{aligned} m_{H_2Ov,ca} &= m_{H_2O,ca} \\ m_{H_2Ol,ca} &= 0 \end{aligned}\right\} \quad if \quad m_{H_2O,ca} \leq m_{v,max} \tag{3.39}$$

$$\left.\begin{aligned} m_{H_2Ov,ca} &= m_{v,max} \\ m_{H_2Ol,ca} &= m_{H_2O,ca,} - m_{v,max} \end{aligned}\right\} \quad if \quad m_{H_2O,ca,} > m_{v,max} \tag{3.40}$$

Once mass of water vapour is found, the partial pressure of water vapour is calculated using the ideal gas law, from which the relative humidity is determined using equation 3.41. The calculated relative humidity is then used in the water transport equations of section 3.3. In transient simulations the relative humidity will change with time due to variations in both the vapour partial pressure and saturation pressure.

$$RH = \frac{P_v}{P_{sat}} \tag{3.41}$$

Liquid water can leave the cathode volume by two means, either by evaporating once the humidity falls below 100% and leaving as water vapour, or alternatively leaving as water droplets entrained within the gas flow. The empirical method described by [60], shown in equation 3.42, has been used to model liquid water entrainment. Liquid water exit flow rate is proportional to the mass flow rate of gas leaving the cathode multiplied by the mass of liquid in the gas channel and a liquid entrainment coefficient (θ). An arbitrary value of 2.0 was chosen for the entrainment factor, variation of this value will influence the amount of water

stored in the fuel cell flow channels. Since the influence of flooding on fuel cell performance is not considered in the current model the selection of the entrainment coefficient will not significantly influence the model response. The inclusion of flooding effects is a key area for further development of the model.

$$\dot{m}_{H_2Ol,out} = \theta \dot{m}_{ca,out} m_{H_2Ol} \tag{3.42}$$

3.4.2 Anode

The mass balance of hydrogen and water are considered in the anode flow channel using two first order differential equations, one for each species. Equations 3.43 and 3.44 show the mass balance equations for Hydrogen and water respectively.

$$\frac{dm_{H_2,an}}{dt} = \dot{m}_{H_2,an,in} - \dot{m}_{H_2,an,out} - \dot{m}_{H_2,reac} \tag{3.43}$$

$$\frac{dm_{H_2O,an}}{dt} = \dot{m}_{H_2O,an,in} - \dot{m}_{H_2O,an,out} - \dot{m}_{H_2O,trans} \tag{3.44}$$

$\dot{m}_{H_2,an,in}$ is the mass flow rate of hydrogen into the anode and is determined from the fuel cell current density and anode stoichiometry (Λ_{an}) using equation 3.45. $\dot{m}_{H_2O,an,in}$ represents the water mass flow rate into the anode, calculated using equation 3.46. The first expression in equation 3.46 represents the water vapour carried into the anode from a humidified inlet, where RH is the inlet fuel humidity at pressure P_{an} and P_{sat} is evaluated at the anode inlet temperature. The second expression in equation 3.46 accounts for any liquid water in the anode inlet, if present. $\dot{m}_{H_2,reac}$ is the rate at which hydrogen is consumed at the anode membrane interface due to the electrochemical reaction, calculated using equation 3.47. $\dot{m}_{H_2O,trans}$ is the net water flux across the membrane expressed in mass flow terms using equation 3.27.

$$\dot{m}_{H_2,an,in} = \Lambda_{an} A_{cell} M_{H2} \frac{in}{2F} \tag{3.45}$$

$$\dot{m}_{H_2O,an,in} = \frac{\dot{m}_{H_2,an,in} P_{sat} RH}{P_{an} - P_{sat} RH} \frac{M_{H_2O}}{M_{H_2}} + \dot{m}_{H_2Ol,an,in} \tag{3.46}$$

$$\dot{m}_{H_2,reac} = A_{cell} M_{H_2} \frac{in}{2F} \tag{3.47}$$

The total gas exit flow rate from the anode is determined using the linearised nozzle equation [65] shown in equation 3.48, where P_{an},P_a,k_{an} and A_{an} are the anode pressure, ambient pressure, linearised nozzle coefficient and nozzle cross sectional area respectively.

To maintain the requested pressure in the anode across a range of flow rates a proportional integral differential (PID) controller is used. The controller input is the error between desired and actual anode pressure and the output is the nozzle cross sectional area (A_n). Changing the nozzle cross sectional area directly simulates the opening and closing of the back pressure valve, actuator dynamics are approximated using a first order transfer function with a one second time constant. The back pressure controller has saturation limits of 0-5$\times 10^{-4}$m^2 for a 50kW stack to prevent both negative and excessive valve areas, along with back-calculation anti-windup to avoid slow response after periods of operating on the limits. Controller gains were tuned manually to both provide adequate transient performance in pressure regulation from low to full load and minimise settling oscillations.

$$\dot{m}_{an,out} = A_{an} k_{an} \left(P_{an} - P_a\right) \tag{3.48}$$

Separate species mass flow out of the anode is determined from the total anode gas flow rate using the water vapour gas mass fraction (equation 3.49). Equations 3.50 and 3.51 show the anode exit mass flow rates for hydrogen ($\dot{m}_{H_2,an,out}$) and water vapour ($\dot{m}_{H_2O,an,out}$) respectively.

$$x_{H_2Ov,an} = \frac{m_{H_2Ov,an}}{m_{H_2a} + m_{H_2Ov,an}} \tag{3.49}$$

$$\dot{m}_{H_2,an,out} = \dot{m}_{an,out} \left(1 - x_{H_2Ov,an}\right) \tag{3.50}$$

$$\dot{m}_{H_2Ov,an,out} = \dot{m}_{an,out} x_{H_2Ov,an} \tag{3.51}$$

Similarly to the cathode, the mass of water is split into water vapour and liquid water, assuming that liquid water will evaporate until the saturation point, after which any additional water will remain in liquid form. The maximum vapour mass in the anode is determined using equation 3.52. The respective liquid and vapour masses in the cathode volume are then found using equation 3.39, anode relative humidity can be found using equation 3.41.

$$m_{v,max} = \frac{P_{sat} V_{an} M_{H_2O}}{R_0 T_s} \tag{3.52}$$

Liquid water can leave the anode by either evaporating when the humidity falls below saturation or as droplets entrained within the gas flow. As with the cathode, the empirical method of [60], shown in equation 3.53, is used to determine the liquid mass flow entrained in the gas flow. A value of 2.0 has been arbitrarily chosen as the entrainment coefficient θ.

$$\dot{m}_{H_2Ol,an,out} = \theta \dot{m}_{an,out} m_{H_2Ol} \tag{3.53}$$

The anode mass conservation model assumes an open ended cathode arrangement and does not consider the diffusion of inert nitrogen from the cathode across the membrane. Several commercial stacks use a dead-ended anode with periodic purging to keep nitrogen and water accumulation below acceptable limits. A dead ended anode can be simulated by time averaging the hydrogen lost during a single purge over the time period between purges, effectively representing the purge as a constant anode stoichiometry. Simulation by Rabbani and Masoud [67] showed that an anode stoichiometry of 1.03 was sufficient to keep nitrogen content to negligible levels.

3.5 Energy conservation

The transient temperature of the stack is determined by performing an energy balance of the fuel cell stack as a single lumped volume. The energy fluxes considered are shown in figure 3.7, stack temperature is modelled using a first order differential shown in equation 3.54.

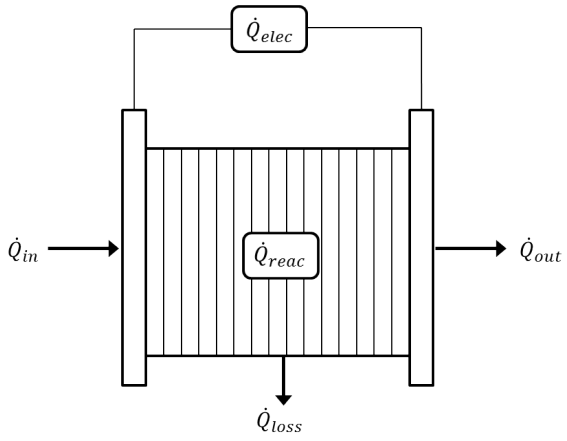

Figure 3.7: Energy balance of fuel cell stack

$$m_s C_{ps} \frac{dT_s}{dt} = \dot{Q}_{reac} - \dot{Q}_{elec} + \dot{Q}_{in} - \dot{Q}_{out} - \dot{Q}_{loss} - \dot{Q}_{coolant} \tag{3.54}$$

$\dot{Q}_{reac}$ represents the total energy rate released into the stack by the hydrogen oxidation reaction with a liquid water product and is determined using equation 3.55, where Δh_l is the higher heating value of hydrogen in J/mol. $\dot{Q}_{elec}$ is the electrical power produced by the

stack and removed for useful work, electrical power is determined from the cell voltage and current using equation 3.56 where n represents the number of cells in the stack.

$$\dot{Q}_{reac} = \frac{\dot{m}_{H_2,an,in}\Delta h_l}{\Lambda_a M_{H_2}} \tag{3.55}$$

$$\dot{Q}_{elec} = V_{cell} n A_{cell} i \tag{3.56}$$

$\dot{Q}_{in}$ and $\dot{Q}_{out}$ represent the enthalpy of the inlet and exit flows into and out of the fuel cell stack respectively, and are determined from the sum of species enthalpies using equation 3.57. The first term on the right hand side of equation 3.57 represents the energy from the vaporisation of liquid water, the second term represents the sensible heat of all the species (including water vapour). The constants for the enthalpy of vaporisation of water (ΔH_v) and specific heat capacity (C_{pj}) are evaluated at different temperatures using a look-up with data from [66]. Equation 3.58 gives the anode inlet enthalpy as an example where hydrogen, water vapour and liquid water are considered, similar equations for anode exit and the cathode side are obtained using equation 3.57.

$$\dot{Q} = \dot{m}_v \Delta H_v + \sum_{j=1}^{n} \dot{m}_j C_{pj} \left(T_s - T_0\right) \tag{3.57}$$

$$\dot{Q}_{an,in} = \left(\dot{m}_{H_2,an,in} C_{pH_2} + \dot{m}_{H_2Ol,an,in} C_{pH_2O,l}\right)\left(T_{in} - T_0\right) + \dot{m}_{H_2Ov,an,in}\left(\Delta H_v + C_{pH_2Ov}\left(T_{in} - T_0\right)\right) \tag{3.58}$$

$\dot{Q}_{loss}$ is the thermal energy transferred from the stack to the surrounding environment through convection and is determined using Newton's law of cooling, shown in equation 3.59 where h_s is the constant convective heat transfer coefficient and A_s the stack external heat transfer area.

$$\dot{Q}_{loss} = h_s A_s \left(T_s - T_a\right) \tag{3.59}$$

$\dot{Q}_{coolant}$ represents the heat removed from liquid cooling channels between cells. In the evaporatively cooled model this is set to zero for all cases, the calculation of $\dot{Q}_{coolant}$ for the liquid cooled model is discussed in section 3.6.2.

3.6 Stack cooling

The difference between the energy release rate of the electrochemical reaction and the electrical energy produced (first two terms on the right hand side of equation 3.54) represents

the waste heat released into the stack. To maintain a constant stack temperature, the cooling system must remove an equal amount of heat from the stack. The different methods for removing this waste heat were discussed in section 2, where it was shown that both evaporative cooling and liquid cooling were both feasible methods of removing heat from large scale (>10kW) fuel cell stacks. To perform a quantitative comparison of the two cooling methods both have been separately implemented into the fuel cell system model using the methods discussed below.

3.6.1 Evaporative cooling

Heat is removed from the evaporatively cooled model by adding liquid water directly to the cathode flow channel. The liquid evaporates and exits the cathode as a vapour, removing the energy taken in changing phase with it. Since heat lost from the stack to its surrounding through convection ($\dot{Q}_{loss}$) is relatively small, the difference between stack inlet and outlet enthalpies ($\dot{Q}_{in} - \dot{Q}_{out}$) must be similar magnitude but opposite sign to the heat energy released into the stack ($\dot{Q}_{reac} - \dot{Q}_{elec}$).

The rate at which liquid water is supplied to the cathode flow channel is determined by a proportional integral (PI) controller to achieve a desired cathode gas channel humidity, usually close to saturation. From the current error and previous errors between the desired and actual cathode humidity the PI controller determines the rate at which liquid water is added to the cathode ($\dot{m}_{H_2O,ca,inj}$ in equation 3.26) which then effects the cathode humidity, completing the feedback loop shown in figure 3.8. To prevent the controller requesting unrealistic liquid water flow rates, upper and lower saturation limits are placed on the controller, the minimum being zero and the maximum varying with the size of the fuel cell stack (3 lpm for a 50kW stack). Controller anti-windup is also used to prevent poor controller performance after operating at the saturation point. The controller gains are tuned manually with the primary objective to prevent membrane drying during transients and secondary objectives to minimise water consumption and provide a smooth response.

There is significant scope for further study on the control of water addition in evaporatively cooled fuel cell stacks. The non-linear behaviour of the fuel cell system means a simplified PI controller may not provide the best response. It may be possible to improve transient stack performance through the use of feed-forward control based on current demand or model based optimal control methods.

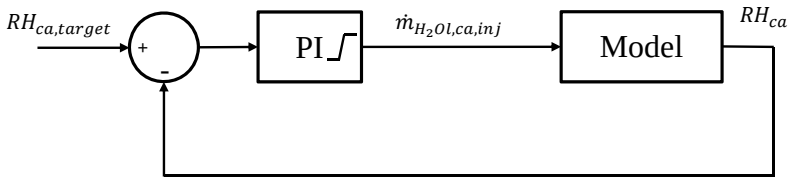

Figure 3.8: Liquid water addition rate control

3.6.2 Liquid cooling

In the liquid cooled model water is not added directly into the flow channels, therefore to achieve a high humidity within the stack for optimum performance the inlet flow must be humidified prior to the inlet. The additional inlet water vapour means the difference between inlet and exit enthalpy is not sufficient to remove all the waste heat and a separate cooling method is required to maintain thermal balance.

In the liquid cooled model waste heat is removed through conduction by passing liquid coolant through multiple circular tubes between cells. Heat transfer is determined using a one-dimensional model stepping along the coolant tube from inlet to outlet, evaluating the heat transfer at ten separate points of equal area to account for changes in coolant properties with temperature. Since stack temperature is assumed uniform across the stack, the tube wall temperature in each section is equal to stack temperature. Assuming all coolant tubes are identical and flow is evenly distributed, heat transfer is calculated for a single tube then scaled up across the stack.

For a given total system coolant flow rate, the mass flow rate through each tube ($\dot{m}_{coolant,tube}$) is found by dividing the total mass flow rate ($\dot{m}_{coolant}$)by the number of cooling tubes in the stack. Next the coolant Reynolds number is found using equation 3.60, where d_h is the tube hydraulic diameter, $A_{CSA,tube}$ the tube cross sectional area, μ the coolant absolute viscosity and V the velocity.

$$Re = \frac{\rho V d_h}{\mu} = \frac{\dot{m}_{coolant,tube} d_h}{A_{CSA,tube}\mu} \tag{3.60}$$

Coolant Nusselt number is then found using the Dittus-Boelter equation for turbulent pipe flow[44], shown in equation 3.61 from which heat transfer coefficient (h) is found using equation 3.62, where k is the thermal conductivity of the coolant.

$$Nu = 0.023 Re^{0.8} Pr^{0.4} \tag{3.61}$$

$$Nu \equiv \frac{hd_h}{k} \tag{3.62}$$

The effectiveness number of transfer units method (ϵ-NTU) method is then used to find the heat transfer in each section [44]. Since a uniform stack temperature is assumed, the hot side (stack) thermal resistance contribution is zero and the only thermal resistance is due to the cold side (coolant). The overall heat transfer coefficient is therefore equal to the convective heat transfer coefficient of the cold side ($UA = hA$). Next the number of transfer units NTU are calculated using equation 3.63, from which the heat exchanger effectiveness is determined from equation 3.64 for a heat exchange with a heat capacity ratio of zero [44]. The heat capacity ratio is zero in this case since the hot side (fuel cell stack) is at a uniform temperature.

$$NTU \equiv \frac{UA}{C_{min}} = \frac{hA}{\dot{m}_{coolant,tube} C_{p,coolant}} \tag{3.63}$$

$$\epsilon = 1 - exp\left(-NTU\right) \tag{3.64}$$

Heat transfer in each section is then determined using equation 3.65, and section outlet temperature using equation 3.66

$$\dot{Q}_{sec,tube} = \epsilon \dot{m}_{coolant,tube} C_{p,coolant} \left(T_s - T_{coolant,in}\right) \tag{3.65}$$

$$T_{sec,out} = T_{sec,in} + \frac{\dot{Q}_{sec,tube}}{\dot{m}_{coolant,tube} C_{p,coolant}} \tag{3.66}$$

This process is then repeated, feeding the exit properties of one section into the inlet of the next until heat transfer in all ten sections has been evaluated. After which heat transfer for the whole tube and hole stack are evaluated using equations 3.67 and 3.68 respectively. The value of $\dot{Q}_{coolant}$ is then used in equation 3.54 when operating as a liquid cooled system.

$$\dot{Q}_{coolant,tube} = \sum_{n=1}^{10} \dot{Q}_{sec,tube,n} \tag{3.67}$$

$$\dot{Q}_{coolant} = n_{tubes} \dot{Q}_{coolant,tube} \tag{3.68}$$

3.7 Stack model validation

The fuel cell stack model brings together data and empirical correlations from multiple sources, each of these has been validated independently but not as part of the whole fuel cell stack model described in this chapter. It is possible that by combining multiple correlations from studies conducted in different conditions that the validity of the model may be reduced. The empirical correlations used in this model have all been obtained from the literature on PEM fuel cells and are applicable over their typical operating ranges. Furthermore, each of the sub-models illustrated in figure 3.1 contain no more than one source of empirical correlation. This means that all interaction between the different correlations is done using physical parameters such as temperature, pressure and relative humidity.

The validation of the whole fuel cell stack model has been performed in two sections; firstly the ability of the evaporatively cooled model to predict a stack temperature at a fixed voltage, then the ability to predict cell voltage at a fixed current density.

3.7.1 Temperature

The model was parametrized to meet the specification of an experimental 15kW evaporatively cooled fuel cell stack produced by an industrial partner. The model was then run at constant current with cell voltage, gas flow rates and inlet temperatures manually specified to match that of the experimental data, the target cathode relative humidity set to 100%. 30 separate steady state tests were conducted at different current densities, stoichiometry, pressure and across different fuel cell stacks. Comparing the experimental stack temperature (measured at the cathode exhaust) to the stack temperature predicted by the model showed a mean absolute error of 1.5°C. The results indicate that the evaporatively cooled model gives a good representation of the experimental stack across a range of steady state operating points.

The experimental tests used in this validation were performed by an industrial partner using proprietary evaporative cooling technology. As such the experimental data used for the validation has not been made publicly available so cannot be displayed in this thesis.

3.7.2 Voltage

Section 3.7.1 showed the ability of the evaporatively cooled model to predict stack temperature with a specified cell voltage. This validated the mass conservation, water transport and energy balance sub models but did not consider the cell voltage sub model discussed in

section 3.2. The polarisation curve of [12] for a 15 cell evaporatively cooled fuel cell stack was used to establish the empirical parameters required in equation 3.12. This was achieved by performing simulations of the evaporatively cooled model across slow polarisation tests (so that a steady state temperature was achieved) and comparing experimental to predicted data. Figure 3.9 compares the experimental and predicted cell voltages across a polarisation curve conducted at a cathode stoichiometry of 1.67, cathode humidity of 80% and 1.06bar.a inlet pressure. The empirical values used are shown in table 3.1, these were obtained by a least squares curve fitting within reasonable limits given in [10].

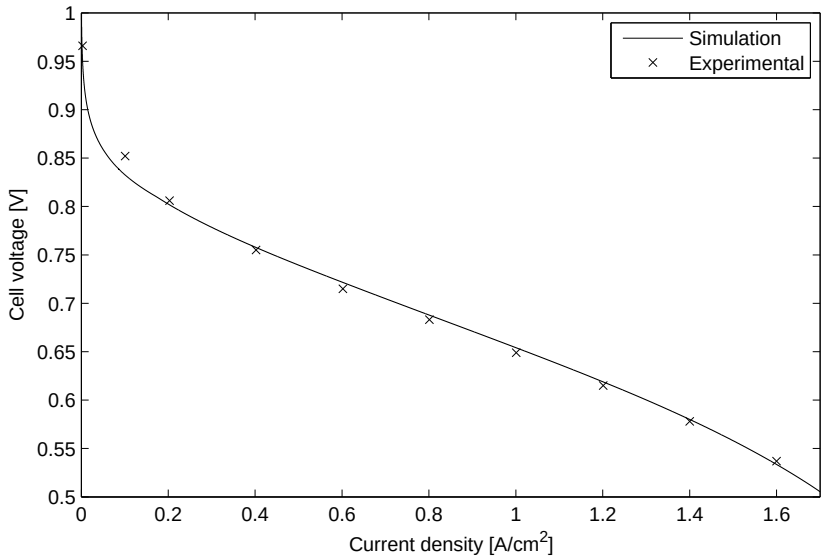

Figure 3.9: Cell voltage validation, experimental data from [12]

Parameter	**Value**
Internal current density (i_n)	1.5×10^{-4}A/cm^2
Mass transport coefficient (a_{trans})	3×10^{-4}
Mass transport coefficient (b_{trans})	3.0
Exchange current density at STP ($i_{oc,0}$)	3.2×10^{-8}A/cm^2

Table 3.1: Lumped parameter model cell voltage parameters

Based on the assumptions and data used the model is valid between 0-100°C, 15-100% gas channel relative humidity and 1-3bar.a operating pressure. Confidence in the model validity is highest in the high humidity 60-80°C range at low operating pressures since this is where the bulk of the validation has been performed. The model may be used at higher pressures where the ideal gas law remains valid, however maximum operating pressure is

usually dictated by the maximum operating temperature, this is discussed further in section 6.

3.8 Balance of plant

To simulate the operation of the fuel cell in a mobile environment it is important to also consider the balance of plant components since these will both effect the operating conditions of the stack and the net power output of the system. This section details the compressor and cathode manifold sub models.

3.8.1 Compressor

A constant efficiency compressor model is included in the simulation to calculate the cathode inlet conditions for the evaporatively cooled fuel cell stack [10]. From known ambient conditions and desired exit pressure, the compressor exit temperature for an isentropic process is calculated using equation 3.69.

$$\frac{T_2'}{T_1} = \left(\frac{P_2}{P_1}\right)^{\frac{\gamma-1}{\gamma}} \tag{3.69}$$

The exit temperature from a non-isentropic process (T_2) can be compared to the exit temperature from an isentropic process (T_2') using the isentropic efficiency (equation 3.70).

$$\eta_c = \frac{Isentropic\ work}{Actual\ work} = \frac{T_2' - T_1}{T_2 - T_1} \tag{3.70}$$

Substituting equation 3.70 into equation 3.69 the exit temperature for a compressor with a constant isentropic efficiency can be found, shown in equation 3.71

$$T_2 = T_1 + \frac{T_1}{\eta_c}\left[\left(\frac{P_2}{P_1}\right)^{\frac{\gamma-1}{\gamma}} - 1\right] \tag{3.71}$$

Air mass flow rate is calculated using the fuel cell current and requested stoichiometry, shown in equation 3.72.

$$\dot{m}_{air} = \frac{M_{air}}{x_{O_2}} \frac{\Lambda_{ca} A_{cell} in}{4F} \tag{3.72}$$

The work required for the non-isentropic compression can then be found using equation 3.73.

$$W_{comp} = \dot{m}_{air} C_{p,air} \left(T_2 - T_1\right) \tag{3.73}$$

The compressor efficiency and stack operating conditions will significantly influence the compressor exit temperature and parasitic loads. Figure 3.10a shows how compressor exit temperature changes with pressure ratio and efficiency for a 20°C inlet temperature, at high pressure ratios the compressor exit may need to be cooled prior to entering the fuel cell stack. Figure 3.10b shows the work required in compressing the air at different stoichiometries for a 70% compressor efficiency, 360 cell stack with a cell active area of 200cm^2 operating at a current density of 0.5A/cm^2. For comparison, the parameters used equate to a gross fuel cell power of 27kW using the polarisation curve of figure 3.9.

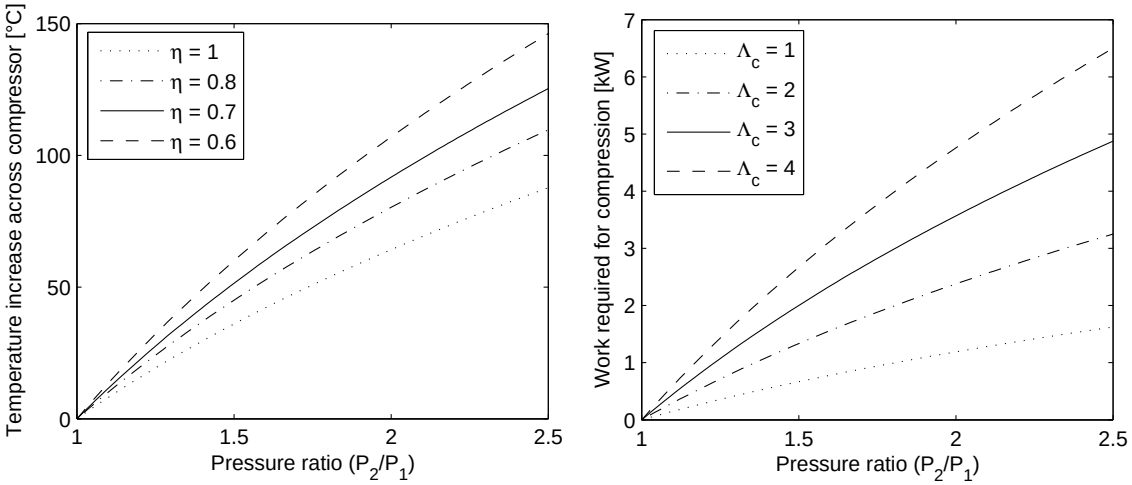

(a) Temperature increase across compressor

(b) Work required for compression

Figure 3.10: Temperature increase and work required for compression at different isentropic efficiencies and stoichiometries

To represent the transient delay of the compressor in achieving a desired flow rate with changes in current demand, a first order transfer function has been included with a time constant of 0.75 seconds. This is shown in equation 3.74, where $\dot{m}_{comp,target}$ is the requested flow rate and $\dot{m}_{comp}$ is the actual flow rate. The time constant is selected to give transient behaviour in line with the Department of Energy (DOE) 2020 targets for compressor performance of fuel cell vehicles [68].

$$\dot{m}_{comp} = \frac{1}{0.75s + 1}\dot{m}_{comp,target} \tag{3.74}$$

3.8.2 Manifolds

When the current density of the stack is changed, the flow rates into the anode and cathode must be modified to maintain a constant stoichiometry. The process of increasing the com-

pressor flow rate and seeing an increase in mass flow in the stack is not instantaneous. In reality the air takes time to travel between the compressor and stack and through the inlet manifold to the cells. Similarly, changes to the back pressure valve position will not instantaneously effect the pressure and exit flow rate of the stack because of the mass stored in the exit manifold. To account for these manifold dynamics two additional volumes have been included in the model, one between the compressor and cathode inlet, and one between the cathode exit and back pressure valve, illustrated in figure 3.11. The manifolds are assumed to be adiabatic and well mixed. Manifold effects on the anode side have not been considered since mass flow rate is lower and the hydrogen content in the anode is high, meaning fast changes in current demand will have a lesser effect.

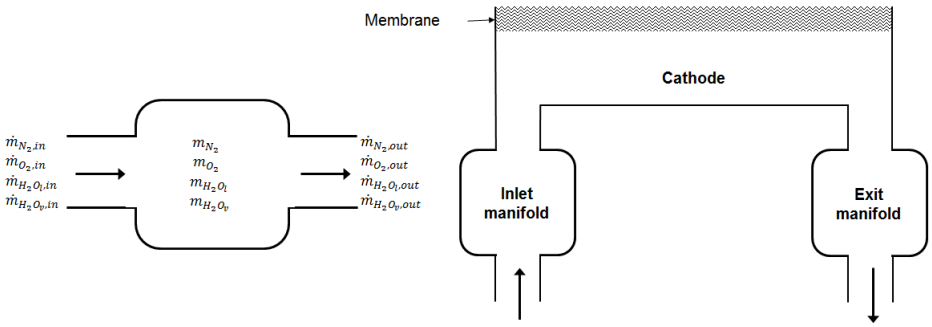

Figure 3.11: Mass conservation of manifolds

Mass balance within the manifolds are based on the same first order differentials used in the cathode mass conservation model in section 3.4, however since no mass transfer occurs within the volume, several of the terms can be omitted. The species mass conservation equations for the manifolds are defined in equations 3.75-3.77 where subscript m denotes either the inlet or outlet manifold.

$$\frac{dm_{O_2,m}}{dt} = \dot{m}_{O_2in} - \dot{m}_{O_2out} \tag{3.75}$$

$$\frac{dm_{N_2,m}}{dt} = \dot{m}_{N_2in} - \dot{m}_{N_2out} \tag{3.76}$$

$$\frac{dm_{H_2O,m}}{dt} = \dot{m}_{H_2Oin} - \dot{m}_{H_2Oout} \tag{3.77}$$

For the inlet manifold $\dot{m}_{O_2in}$, $\dot{m}_{N_2in}$ and $\dot{m}_{H_2Oin}$ are determined from mass fractions of the air flow leaving the compressor ($\dot{m}_{air}$). Gas exit flow rates are determined using the

linearised nozzle equation with a fixed manifold coefficient (k_{im}) and cross sectional area (A_{im}), shown in equation 3.78 where subscript im represents inlet manifold.

$$\dot{m}_{im,out} = A_{im} k_{im} \left(P_{im} - P_{ca} \right) \tag{3.78}$$

From the total gas exit flow rate, species flow rates are determined from mass fractions within the manifold. The exit from the inlet manifold feeds directly into the cathode volume, meaning $\dot{m}_{N_2,out}$ from the inlet manifold (equation 3.76) is equal to $\dot{m}_{N_2,in}$ for the cathode (equation 3.25) . Since liquid water is added in the stack volume, after the inlet manifold the presence of liquid water has not been considered.

For the exit manifold, equations 3.75-3.77 also apply. The inlet is fed directly from the cathode outlet or condenser and the exit vents to atmospheric pressure across a controllable valve which is used to regulate system back pressure. At high levels of back pressure, the pressure ratio between the exit manifold and environment will exceed the limits over which the linearised nozzle equation is valid. Instead the non-choked nozzle equation [69] shown in equation 3.79 has been used. Where C_n represents the nozzle coefficient, A_t the nozzle cross sectional area and (P_2/P_1) the ratio of atmospheric to exhaust manifold pressure. The non-choked nozzle equation is valid up to the critical pressure ratio, which is 0.53 for air [69]. This equates to an exit manifold pressure of 1.9bar.a for air flow with an atmospheric pressure of 1.0bar.a. A target back pressure within the system is achieved by changing the cross sectional area of the back pressure valve A_t in equation 3.79 using a proportional integral derivative (PID) controller; the change in cross sectional area represents the amount by which the valve is opened. Similarly to the anode, actuator transients are represented using a first order transfer function with a one second time constant, saturation limits (0-0.015m^2 for a 50kW stack) are used to prevent unrealistic cross sectional areas and integrator anti-windup used. Controller gains are manually tuned to provide good transient response for step changes in fuel cell flow rates. The influence of target back pressure on the performance of an evaporatively cooled fuel cell is discussed in chapter 6. Liquid water accumulation within the exit manifold is not considered, instead liquid flow rate from the cathode exhaust is equal to liquid flow rate from the exit manifold. This assumption is deemed reasonable since there is no water formation or heat transfer within the manifold and pressure drop from the cathode to exit manifold volume is small.

$$\dot{m}_{c,out} = \frac{C_n A_t P_1}{\sqrt{R_0 T}} \left(\frac{P_2}{P_1} \right)^{\frac{1}{\gamma}} \left[\frac{2\gamma}{\gamma - 1} \left(1 - \left(\frac{P_2}{P_1} \right)^{\frac{\gamma-1}{\gamma}} \right) \right]^{\frac{1}{2}} \tag{3.79}$$

The influence of both compressor and manifold transient effects on oxygen concentration

within the cathode are demonstrated in figure 3.12. For a step change from 1.0-0.25A/cm^2 at 5 seconds a spike in cathode stoichiometry can be seen due to excess oxygen in the cathode. For the reverse step change (0.25-1.0A/cm^2) oxygen fraction is reduced due to increased consumption leading to an increase in mass concentration losses.

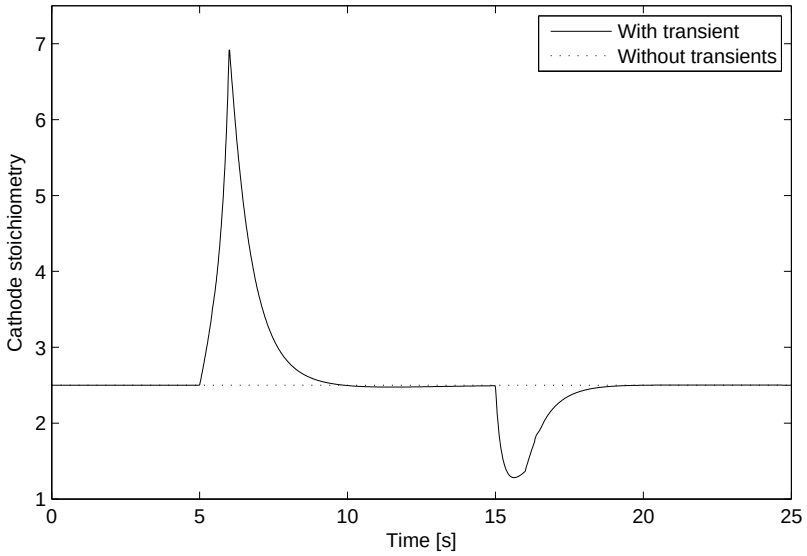

Figure 3.12: Influence of transients on cathode stoichiometry during step current change

3.8.3 Humidifier (Liquid cooled only)

Unlike the evaporatively cooled system, the liquid cooled system is unable to add water internally within the fuel cell stack. In cases where the product water alone is not sufficient to achieve a desired level of humidification additional humidification is provided to the inlet stream by recycling water vapour from the cathode exhaust. In the liquid cooled model a simple vapour exchange system has been used which allows the transfer of water vapour from the cathode exhaust to the cathode inlet, post compressor. Water vapour can be transferred from the exhaust stream to the inlet stream either up to a desired humidity or until the vapour molar concentrations are equal, this represents the best case exchange humidifier without the use of additional heat exchangers.

Equations 3.80 to 3.85 show the mass balance equations used in the humidifier, both Nitrogen and Oxygen are unchanged. Given a desired humidity (RH_{target}), the required water vapour mass flow is determined from equation 3.84. The maximum water vapour flow rate at the humidifier exit occurs when the concentrations of the cathode exhaust

and humidifier exit are equal, calculated using equation 3.85. In certain circumstances the requested vapour transfer may exceed the maximum allowable water vapour transfer, this is accounted for in equation 3.83.

$$\dot{m}_{N_2,hum} = \dot{m}_{N_2,comp} \tag{3.80}$$

$$\dot{m}_{O_2,hum} = \dot{m}_{O_2,comp} \tag{3.81}$$

$$\dot{m}_{H_2Ov,hum} = \dot{m}_{H_2Ov,comp} + \dot{m}_{H_2Ov,trans} \tag{3.82}$$

$$\dot{m}_{H_2Ov,trans} = \max\left[0, \min\left(\dot{m}_{H_2Ov,hum,max}, \dot{m}_{H_2Ov,hum,target}\right) - \dot{m}_{H_2Ov,comp}\right] \tag{3.83}$$

$$\dot{m}_{H_2Ov,hum,target} = \frac{M_{H_2O}}{M_{O_2}x_{O_2} + M_{N_2}\left(1 - x_{O_2}\right)} \frac{P_{sat}RH_{target}}{P_{comp} - P_{sat}RH_{target}} \left(\dot{m}_{N_2,hum} + \dot{m}_{O_2,hum}\right) \tag{3.84}$$

$$\dot{m}_{H_2Ov,hum,max} = \dot{m}_{H_2Ov,ca,out} \frac{\dot{m}_{N_2,hum}M_{O_2} + \dot{m}_{O_2,hum}M_{N_2}}{\dot{m}_{N_2ca,out}M_{O_2} + \dot{m}_{O_2ca,out}M_{N_2}} \tag{3.85}$$

The transfer of mass from the cathode exhaust stream to the cathode inlet stream also changes the thermal energy in the humidifier. The new thermal energy of the humidifier exit is determined from equation 3.86, assuming phase change does not take place. The new cathode inlet stream temperature is then found using equation 3.87.

$$\begin{aligned}\dot{Q}_{hum} = \left(\dot{m}_{N_2,hum}C_{p,N_2} + \dot{m}_{O_2,hum}C_{p,O_2} + \dot{m}_{H_2Ov,comp}C_{p,H_2Ov}\right)\left(T_{comp} - T_0\right) \\ + \dot{m}_{H_2Ov,trans}C_{p,H_2Ov}\left(T_s - T_0\right)\end{aligned} \tag{3.86}$$

$$T_{hum} = \frac{\dot{Q}_{hum}}{\dot{m}_{N_2hum}C_{p,N_2} + \dot{m}_{O_2hum}C_{p,O_2} + \dot{m}_{H_2Ov,hum}C_{p,H_2Ov}} + T_0 \tag{3.87}$$

The change in temperature within the humidifier will also influence the saturation pressure, maximum vapour flow rate and relative humidity. In the case of a temperature increase this would give a humidity or vapour flow rate into the cathode lower than that requested. To account for such changes in temperature equations 3.80 to 3.87 are repeated at the new exit

temperature, this process is repeated until the temperature change in successive iterations is less than 0.01°C.

3.9 Vehicle model

To translate vehicle speed from common drive cycles into power demands which can then be passed to the fuel cell stack, a model of the vehicle is required. For this work a backwards facing driveline model is used. The model input is a vehicle speed time trace, such as a standard drive cycle, and the output is the power required by the powertrain to achieve the speed time trace. Since it is desired to study thermal and water management, an additional model is also required to determine the airflow across the vehicle radiator relative to the specified forward speed, considering the impediments of vehicle under bonnet geometry. These models are discussed below.

3.9.1 Tractive effort

The tractive effort F_t required by the vehicle to achieve a desired forward velocity V is shown in equation 3.88. From left to right, the terms considered in calculating F_t are the acceleration forces, aerodynamic drag, static tyre friction, dynamic tyre friction and road gradients. Where m represents vehicle mass, ρ air density, C_D vehicle drag coefficient, A_f vehicle frontal area, a_{tyre} and b_{tyre} tyre friction coefficients and θ the road gradient.

$$F_T = m\frac{dV}{dt} + \frac{1}{2}\rho C_D A_f V^2 + mga_{tyre} + Vb_{tyre} + mgsin(\theta) \tag{3.88}$$

Tractive effort is then equated to power requirement by multiplying by vehicle speed $W = F_T V$. The net power output of the fuel cell stack is then matched to the required road load using a proportional integral (PI) controller to regulate the stack current demand. The controller was manually tuned to achieve the desired current response and maintain the error between power demanded by the vehicle and power supplied by the fuel cell stack to less than 1%. To prevent the request for negative fuel cell currents during deceleration the required road load is restricted to positive values only, during braking the power demanded by the vehicle model becomes zero.

Total transmission efficiency is 85%, based on typical efficiencies for the DC/DC converter and motor taken from [10]. In practice the power electronics will introduce a small high frequency oscillation on the fuel cell load causing a small fluctuation in the stack voltage. Provided sufficient liquid water is supplied to maintain humidity within the gas flow channels, the high frequency perturbations of the power electronics will have a minimal ef-

fect on the overall stack temperature and system net water flow.

The vehicle model used assumes that the fuel cell is the only power source, in practice the fuel cell is often hybridised with either a battery or super-capacitor to smooth transient load profiles. A hybrid system has not been modelled since the hybrid control strategy would increase the number of variables to be considered in the study of transient water balance and remove the focus of the study from the thermal and water management subsystems.

3.9.2 Vehicle air flow

The air velocity experienced by the radiator is not the same as the speed of the vehicle because of the restrictions to flow of the under bonnet geometry and the possible operation of a fan. The air flow across the radiator is of critical importance in a fuel cell thermal management system since it is the primary method of removing waste heat from the system. Figure 3.13 shows a simplified diagram of the under bonnet cooling geometry of a typical passenger vehicle with a fully fan shrouded radiator. Eight separate points are considered, these are: (1) Ram air, (2) Radiator grille, (3) Expansion behind grille, (4) Contraction before fan, (5) Radiator fan, (6) Expansion after fan, (7) Radiator, (8) Air exit.

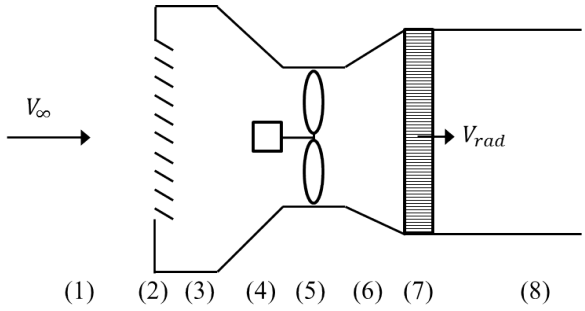

Figure 3.13: Simplified underbonnet cooling geometry

A pressure coefficients method has been used to equate radiator air speed to vehicle speed, this method is based on the work of Ap [32] with modifications to include the influence of a radiator fan. The same method may be used if the fan is positioned in front of or behind the vehicle radiator. The pressure coefficient of each component within the under bonnet flow system ($k_{p,i}$) can be expressed as the local pressure drop divided by the dynamic pressure using the local velocity (V_i), shown in equation 3.89. Pressure loss through each section of the under bonnet geometry can be found and then summed to give the internal flow pressure loss using equation 3.90.

$$k_{p,i} = \frac{\Delta P_i}{\frac{1}{2}\rho V_i^2} \tag{3.89}$$

$$\Delta P_{internal} = \frac{1}{2}\rho \sum_{i=1}^{8} k_{p,i} V_i^2 \tag{3.90}$$

Assuming that no air flow leaves the system, the volume flow rate will remain the same at each of the eight sections, therefore the local speed of each component can be expressed in terms of the radiator velocity and ratio of areas using equation 3.91. Combining equation 3.91 with 3.90, the internal flow pressure drop can be expressed in terms of radiator velocity (equation 3.92).

$$V_i A_i = V_{rad} A_{rad} \quad \rightarrow \quad V_i = V_{rad} \frac{A_{rad}}{A_i} \tag{3.91}$$

$$\Delta P_{internal} = \frac{1}{2}\rho \left(V_{rad} A_{rad}\right)^2 \sum_{i=1}^{8} \frac{k_{p,i}}{A_i^2} \tag{3.92}$$

The operation of a radiator fan seeks to reduce the overall pressure loss through the system and increase the air flow rate across the radiator. In a traditional IC engine the fan is typically only utilised at low vehicle speeds or when stationary where the cooling air flow is not sufficient to remove the waste heat. The pressure increase of the fan is modelled using the empirical method of [26], shown in equation 3.93 where N_{fan} is fan speed in revolutions per minute (rpm), $c_1 = -8.02 \times 10^{-6}$, $c_2 = -0.005231$ and $c_3 = 327.8$.

$$\Delta P_{fan} = c_1 \left(V_{rad} A_{rad}\right)^2 + c_2 \left(V_{rad} A_{rad}\right) \left(\frac{N_{fan}}{2100}\right) + c_3 \left(\frac{N_{fan}}{2100}\right)^2 \tag{3.93}$$

The total pressure loss of the system can then be using equation 3.94, ΔP_{fan} is negative since it acts to reduce the pressure drop.

$$\Delta P_{total} = \Delta P_{internal} - \Delta P_{fan} \tag{3.94}$$

Using the same method as equation 3.89 the pressure loss of the total under bonnet geometry can be expressed in terms of vehicle speed (V_∞) using equation 3.95.

$$\Delta P_{total} = \frac{1}{2} k_{p,t} \rho V_\infty^2 \tag{3.95}$$

Equating equations 3.95 and 3.94 for a known vehicle speed gives a quadratic equation (3.96), which when solved gives the radiator air velocity.

$$0 = \left[A_{rad}^2 \left(\frac{1}{2}\rho \sum_{i=1}^{8} \frac{k_{p,i}}{A_i^2} + c_1\right)\right] V_{rad}^2 + \left[c_2 A_{rad} \left(\frac{N_{fan}}{2100}\right)\right] V_{rad} + \left[c_3 \left(\frac{N_{fan}}{2100}\right)^2 - \frac{1}{2} k_{p,t} \rho V_\infty^2\right] \tag{3.96}$$

The pressure coefficient and cross sectional area values used for the different under bonnet flow components are shown in Table 3.2. Figure 3.14 shows how vehicle forward velocity relates to radiator air velocity at different radiator fan speeds. Parasitic fan power is calculated by the same method as the compressor, using the work formula for non-isentropic compression (equation 3.73). Exit pressure (P_2) is determined as inlet pressure (P_1) plus ΔP_{fan} from equation 3.93; fan efficiency is taken to be 35%. For a stationary vehicle the fan parasitic load at 1000rpm and 2000rpm is 147W and 585W respectively.

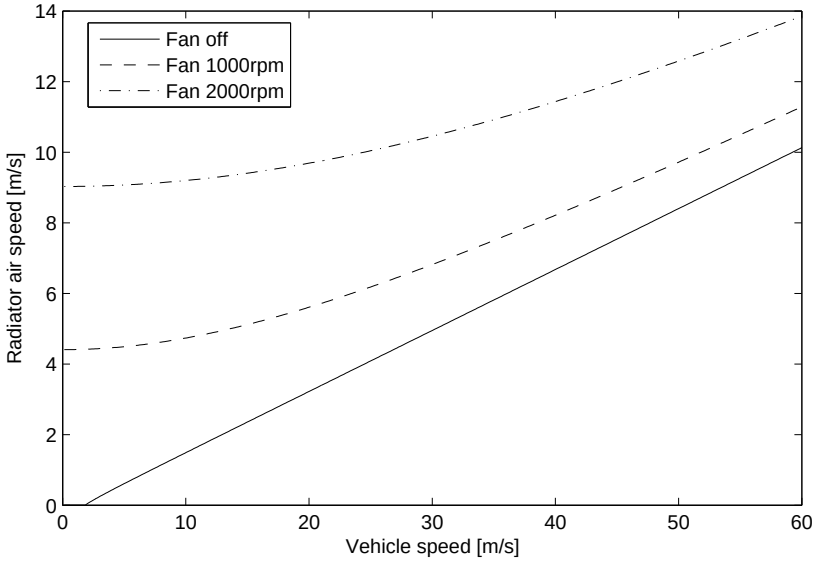

Figure 3.14: Radiator air speed vs. vehicle speed for different fan operations

3.10 Computation

The model was implemented using MATLAB Simulink with the variable step ODE45 Runge-Kutta solving method. Excluding integral controllers and compressor transient transfer function the model has 12 states. Three in each of the cathode inlet manifold, cathode and cathode exit manifolds, two in the Anode and one for stack temperature. Fuel cell parameters and initial values for each state are determined by an initialisation file prior to running the Simulink simulation. An electronic copy of the model is available on request.

Location	$k_{p,i}$	**Cross sectional area (A_i) (m^2)**
Ram air (1)	1.0	0.5
Grille (2)	2.0	0.5
Expansion behind grille (3)	1.0	0.5
Contraction for fan (4)	0.2	0.13 (400mm diameter fan)
Radiator fan (5)	-	-
Expansion after fan (6)	1.0	Variable with radiator geometry
Radiator (7)	4.0	Variable with radiator geometry
Air exit (8)	1.0	1.5
Whole system (relative to V_∞)	0.2	-

Table 3.2: Underbonnet pressure coefficients

Initial species mass for all the cathode side volumes are calculated for air at ambient conditions using equations 3.97-3.99 where i represents the volume (i.e inlet/exit manifold or cathode) and all values are evaluated at ambient conditions. It is assumed that the anode contains only hydrogen gas on start up, and no water vapour is present ($\dot{m}_{H_2O,a}|_{t=0} = 0$), hydrogen mass is then calculated using the ideal gas law. The initial stack temperature is equal to ambient temperature, although this can be changed to simulate a warm start.

$$\dot{m}_{N_2,i}|_{t=0} = \frac{M_{N_2} V_i \left(1 - x_{O_2}\right) \left(P_a - P_{sat} RH\right)}{R_0 T_a} \tag{3.97}$$

$$\dot{m}_{O_2,i}|_{t=0} = \frac{M_{O_2} V_i x_{O_2} \left(P_a - RH P_{sat}\right) RH}{R_0 T_a} \tag{3.98}$$

$$\dot{m}_{H_2Ov,i}|_{t=0} = \frac{M_{H_2O} V_i P_{sat} RH}{R_0 T_a} \tag{3.99}$$

Figure 3.15 shows the transient start up time for a 30kg thermal mass stack with a 3.5kJ/kgK heat capacity operating at 0.75A/cm^2. Increasing pressure is seen to elevate stack temperature, this occurs since at constant humidity the partial pressure of water vapour is fixed, increasing pressure therefore reduces the mass fraction of water in the exhaust. To maintain thermal balance at the same flow rate the saturation pressure, and hence temperature must increase to reject sufficient heat through the system. The temperature regulation of evaporatively cooled fuel cells is discussed in section 6. The increase with temperature, along with the increased reactant concentration reduces the fuel cell voltage losses, shown in figure 3.16a. However, the higher pressure ratio increases the work required in compression, reducing the system net efficiency. This is shown in figure 3.16b where efficiency is seen to be higher for the lowest operating pressure.

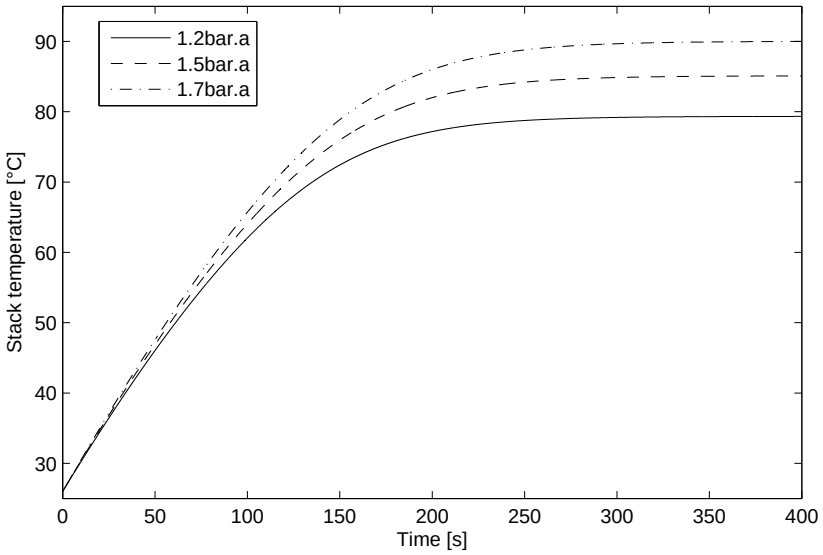

Figure 3.15: Influence of pressure on stack warm up (i=0.75A/cm^2)

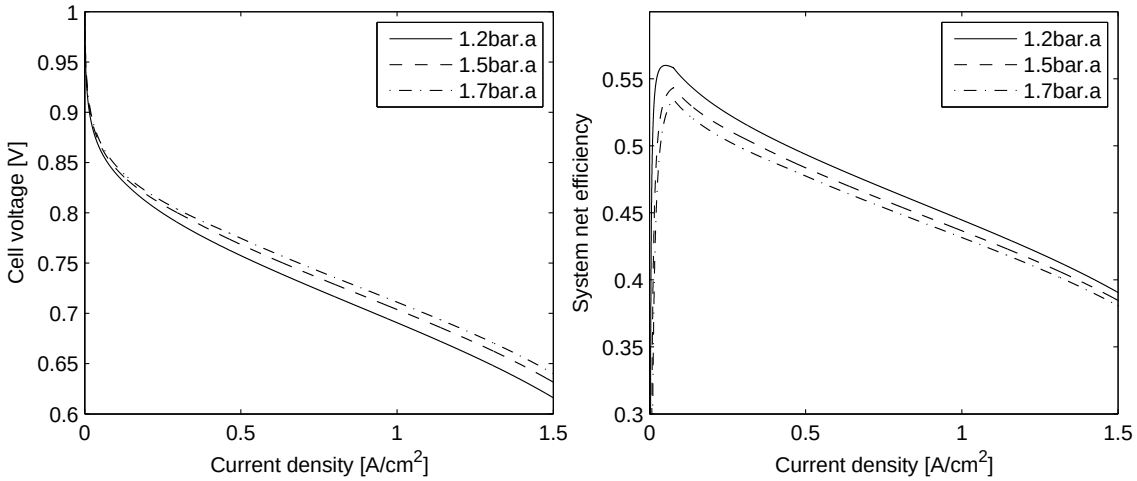

(a) Cell voltage at different pressures

(b) Net efficiency at different pressures

Figure 3.16: Influence of system pressure on voltage and efficiency

Figure 3.17 demonstrates how changing the target cathode humidity influences the cell polarisation curve. A reduction in relative humidity increases the resistance to proton transport across the membrane, increasing the ohmic overpotential (equation 3.10). A detailed analysis of the modelling results, including the quantitative evaluation of water balance of transient drive cycles is presented in chapter 6.

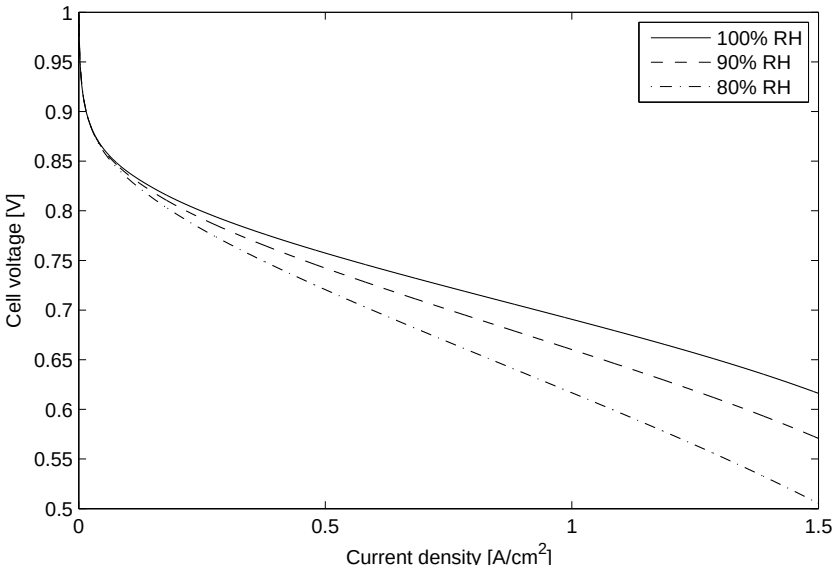

Figure 3.17: Influence of humidity on cell voltage

3.11 Chapter summary

In this chapter, a lumped parameter model has been put forward for an evaporatively cooled fuel cell stack and balance of plant components, validation of the fuel cell stack model has been performed using third party experimental data. The model is capable of predicting both stack temperature and cell voltage over steady state and transients with a high computational efficiency. Considerations have also been made to allow direct comparison to liquid cooling. When combined with the heat exchanger models of section 5 this will allow a quantitative study of water balance in an evaporatively cooled fuel cell vehicle to be performed, along with a direct comparison to liquid cooling.

Several assumptions were made in simplifying the model for the study of transient behaviour. Treating the anode and cathode as single volumes does not consider the issue of temperature, humidity and concentration profiles throughout the cell from inlet to outlet. This will have implications on the current density throughout the cell and the ideal rate and location of the injected liquid water. Furthermore, the influence of liquid water on cell performance and the presence of a gas diffusion layer have not been considered. To address these issues a one-dimensional cell model is required which will account for these variations during steady state operation, this model is presented in chapter 4.

Chapter 4

Segmented model of an evaporatively cooled fuel cell

4.1 Introduction

In the previous chapter, a lumped parameter model of an evaporatively cooled fuel cell was presented. The model is capable of calculating stack temperature, cell voltage and water addition rate required for operation over transient drive cycles for use in water balance studies. However, by treating the anode and cathode flow channels as lumped volumes to improve computational efficiency the effects of spatial variation along the flow channel are ignored. In this chapter, a one dimensional, non-isothermal, steady state model of an evaporatively cooled fuel cell is detailed, the model considers variation of current density and species concentration along the flow channel. Mass transfer resistances of product and reactant transport through the gas diffusion layer are also considered, including the presence of liquid water. The model is used to study liquid water addition profiles for evaporative cooling and observe how spatial variation of both temperature and current density effect the performance of the cell compared to the lumped volume assumptions of chapter 3.

4.2 Segmented flow channel

Spatial distribution along the flow channel is considered by splitting the length of the flow channel into multiple sections of equal length from inlet to outlet for a co-flow single cell, shown in figure 4.1. All properties are assumed constant across each section and re-evaluated on segment exit, feeding into the next section. Each section consists of five separate elements;

cathode flow channel, cathode gas diffusion layer, membrane, anode gas diffusion and anode flow channel.

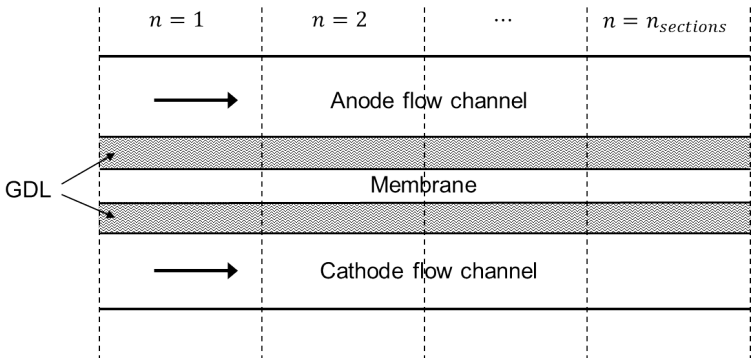

Figure 4.1: Segmented flow channel model diagram

4.3 Section voltage

Voltage is calculated individually for each section as the reversible voltage and sum of key voltage losses (overvoltages) for a known current density. Equation 4.1 is used to determine the voltage in section n for a liquid product, the causes of the different overvoltages are explained in section 3.2. An additional empirical term for the mass transport overvoltage is not required in the one dimensional model since this will be accounted for due to the change in reactant concentration both along the flow channel and through the gas diffusion layer. Exchange current density (i_{oc}) is found using equation 4.2, section resistivity (Ω) is calculated from membrane water activity (section 4.7) using the method described in section 3.3.3 .

$$V_{sec}(n) = -\frac{\Delta\hat{h} - T(n)\,\Delta\hat{s}}{2F} + \frac{R_0 T(n)}{2F} ln\left(\frac{P_{H_2}(n)\,(P_{O_2}(n))^{\frac{1}{2}}}{1}\right) - \frac{R_0 T(n)}{2\alpha F} ln\left(\frac{i(n) + i_n}{i_{oc}(n)}\right) - \Omega(n)\,i(n) \tag{4.1}$$

$$i_{oc}(n) = i_{oc,0}\left(\frac{P_{O_2}(n)}{P_0 x_{O_2,0}}\right)^{\psi} exp\left[-\frac{E_c}{R_0 T(n)}\left(1 - \left(\frac{T(n)}{T_0}\right)\right)\right] \tag{4.2}$$

Once the potential for every section in the model has been calculated, the variation in potential between sections is used to modify the current density for the next iteration. Further iterations are conducted until the variation in section potential is below a specified

threshold, the method for determining the revised current density profile for each iteration is discussed in section 4.10.

4.4 Mass balance

Product and reactant flow rates into and out of each section are considered, including transport through the gas diffusion layers and cell membrane. Unlike the lumped parameter model of chapter 3, the segmented model is steady state and mass accumulation is not considered. Therefore flux of species into each section is equal to species flux leaving the previous section (including flux consumed or liberated from the electrochemical reaction). Figure 4.2 shows the flux of species into or out of a single section, the exit of one section is equal to the inlet of the next section. For simplicity all species flows are expressed in moles per second.

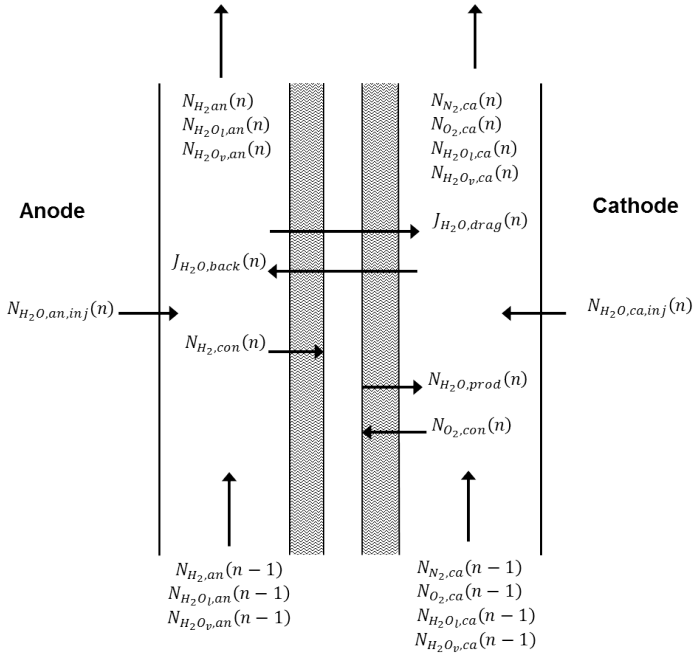

Figure 4.2: Molecular flux in single section

Based on the assumption of steady state operation, the molar flow rates of Hydrogen and Oxygen at the exit of section n can be expressed in terms of the section current density ($i\,(n)$) and molar flows from section $n-1$ using equations 4.3 and 4.4 respectively. Since Nitrogen is not consumed in the electrochemical reaction the molar flow rate in each section of the fuel cell is equal.

$$N_{H_2,an}(n) = N_{H_2,an}(n-1) - \frac{i(n) A_{sec}}{2F} \tag{4.3}$$

$$N_{O_2,ca}(n) = N_{O_2,ca}(n-1) - \frac{i(n) A_{sec}}{4F} \tag{4.4}$$

$$N_{N_2,ca}(n) = N_{N_2,ca}(n) \tag{4.5}$$

Molar flow rate of water in the anode and cathode flow channels also requires knowledge of the liquid water addition rates ($N_{H_2O,an,inj}$ and $N_{H_2O,ca,inj}$) calculated in section 4.5 and net membrane water transport ($J_{H_2O,net}A_{sec}$) calculated in section 4.7. Equations 4.6 and 4.7 are used to determine the molar flow rate of water in the anode and cathode respectively.

$$N_{H_2O,an}(n) = N_{H_2O,an}(n-1) + N_{H_2O,an,inj}(n) + J_{H_2O,net}(n) A_{sec} \tag{4.6}$$

$$N_{H_2O,ca}(n) = N_{H_2O,ca}(n-1) + N_{H_2O,c,inj}(n) - J_{H_2O,net}(n) A_{sec} + \frac{i(n) A_{sec}}{2F} \tag{4.7}$$

Water flow in the anode and cathode is further split into water vapour and liquid water. The maximum flow rate of water vapour within a section is calculated as a function of temperature from the saturation pressure using equations 4.8 and 4.9 for the anode and cathode respectively.

$$N_{H_2O,v,an,max}(n) = \frac{P_{sat}(n)}{P_{an} - P_{sat}(n)} N_{H_2,an}(n) \tag{4.8}$$

$$N_{H_2O,v,ca,max}(n) = \frac{P_{sat}(n)}{P_{ca}(n) - P_{sat}(n)} \left(N_{O_2,ca}(n) + N_{N_2,ca}(n)\right) \tag{4.9}$$

In the lumped parameter model it was assumed that any liquid water would evaporate up to the saturation point. This assumption was deemed reasonable since the length of the flow channel is several orders of magnitude larger than the cross sectional dimensions giving sufficient time and conditions for evaporation to occur. However, by splitting the flow channel into multiple sections of equal length this assumption may lead to inaccuracies. For example, if the liquid water is added into a flow channel with a 2m/s gas velocity and section length of 5mm, evaporation would need to occur in less than 2.5ms for all the water to be in vapour form at the section exit. To represent the maximum rate at which liquid water can evaporate the simplified method based on kinetic theory from [70] has been used in this work, shown in equation 4.10. The area A_{sec} in equation 4.10 represents the area over

which the liquid water is added, this is chosen to be the area of the flow channel opposite to the GDL/membrane assembly, shown in figure 4.3 and is equal to the flow channel width multiplied by the section length.

$$N_{H_2O,evap} = A_{sec}\left(\frac{1}{2\pi M_{H_2O} R_0 T_{sec}}\right)^{\frac{1}{2}} (P_{sat} - P_v) \tag{4.10}$$

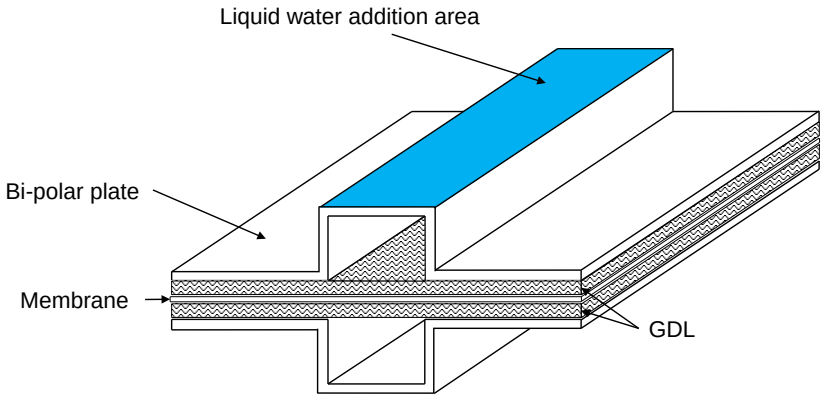

Figure 4.3: Flow channel area for liquid addition A_{sec}

The flow rate of water vapour leaving a section is therefore determined as the minimum value of; total water flow, maximum flow at saturation or inlet vapour flow plus maximum evaporation. Liquid water in the flow channel is then the difference between the total water flow in the section flow channel and vapour flow, shown in equations 4.11 to 4.14 for both the anode and cathode.

$$N_{H_2Ov,ca}(n) = \min\left[N_{H_2O,ca}(n), N_{H_2Ov,max}, N_{H_2Ov}(n-1) + N_{H_2O,evap}\right] \tag{4.11}$$

$$N_{H_2Ol,ca}(n) = N_{H_2O,ca}(n) - N_{H_2Ov,ca}(n) \tag{4.12}$$

$$N_{H_2Ov,an}(n) = \min\left[N_{H_2O,an}(n), N_{H_2Ov,max}, N_{H_2Ov}(n-1) + N_{H_2O,evap}\right] \tag{4.13}$$

$$N_{H_2Ol,an}(n) = N_{H_2O,an}(n) - N_{H_2Ov,an}(n) \tag{4.14}$$

4.5 Liquid water addition

Four different methods of calculating the rate of liquid water addition are explored in this model, in each case water can be added to either the anode or cathode. In the literature review on evaporative cooling both wicking and injection methods were discussed, to simulate these methods would require extensive two phase modelling of the both the liquid addition process and transport into the flow channel. Such a simulation would need to be three dimensional and the additional complexity required would likely prohibit the simulation of a full flow channel. Such study is therefore left as further work, in this study it is assumed that the liquid water is added directly into the flow channel mixture. The four methods of calculating the rate of liquid water addition are detailed below.

4.5.1 Method I - Target channel humidity

Liquid water is added to the flow channel of each section independently at a rate sufficient to obtain a desired relative humidity in the flow channel. The target channel relative humidity is specified at the start of the simulation, the rate of water addition required to obtain the desired humidity is determined from the section saturation pressure and species flow rates. The water vapour volume fraction in the cathode at the target relative humidity is obtained using equation 4.15. The target water vapour molar flow rate ($N_{H_2O,ca,target}$) is composed of the existing water vapour flow rate and the additional water vapour required to achieve the desired relative humidity. Combining equations 4.15 and 4.16 the cathode liquid water addition rate ($N_{H_2O,ca,inj}$) required to obtain a desired relative humidity (RH_{target}) is found using equation 4.17.

$$x_{H_2O,ca,target}(n) = \frac{P_{sat}(n)\, RH_{target}}{P_{ca}(n)} = \frac{N_{H_2O,ca,target}(n)}{N_{N_2,ca} + N_{O_2,ca}(n) + N_{H_2O,ca,target}(n)} \tag{4.15}$$

$$N_{H_2O,ca,target}(n) = N_{H_2O,ca}(n) + N_{H_2O,ca,inj}(n) \tag{4.16}$$

$$N_{H_2O,ca,inj}(n) = \frac{\frac{P_{sat}(n)\, RH_{target}}{P_{ca}(n)} \left(N_{N_2,ca}(n) + N_{O_2,ca}(n) + N_{H_2O,ca}(n)\right) - N_{H_2O,ca}(n)}{1 - \frac{P_{sat}(n)\, RH_{target}}{P_{ca}(n)}} \tag{4.17}$$

Similarly, equation 4.18 is used to find the required addition rate for a desired anode relative humidity.

$$N_{H_2O,an,inj}(n) = \frac{\frac{P_{sat}(n)\,RH_{target}}{P_{an}(n)}\left(N_{H_2,an}(n) + N_{H_2O,an}(n)\right) - N_{H_2O,an}(n)}{1 - \frac{P_{sat}(n)\,RH_{target}}{P_{an}(n)}} \tag{4.18}$$

In calculating the rate of liquid water addition it was assumed that the water would evaporate into the gas stream. Section 4.4 showed there was an upper limit on rate of evaporation, which if lower than the rate at which liquid water is added to the cell could lead to flooding. In practice the limiting evaporation rate predicted by kinetic theory [70] is significantly higher than the rate at which liquid water is added, however in certain conditions this may lead to the liquid water addition flooding the cathode.

4.5.2 Method II - Target interface humidity

Liquid water is added to the flow channel of each section independently at a rate sufficient to obtain a desired relative humidity at the interface between the gas diffusion layer and membrane. The rate at which liquid water is added is determined as the difference between the actual and desired relative humidity multiplied by an arbitrary fixed gain τ.

$$N_{H_2O,ca,inj}(n) = \tau_{ca}\left(RH_{target} - RH_{ca,i}(n)\right) \tag{4.19}$$

$$N_{H_2O,an,inj}(n) = \tau_{an}\left(RH_{target} - RH_{an,i}(n)\right) \tag{4.20}$$

Maintaining a target interface activity allows the ionic resistance of the membrane to be minimised. Furthermore, controlling the water activity at the cathode interface can be used to reduce the risk of flooding at high current densities when the concentration gradient across the gas diffusion layer must be higher to remove the additional water generated. The target interface humidity method does not consider the ability to physically measure relative humidity at the interface position inside a real test cell, but is used to determine the water injection profiles required to achieve such conditions.

4.5.3 Method III - Vapour partial pressure

Liquid water is added to the flow channel at a rate proportional to the difference between the saturation pressure and gas channel vapour partial pressure within the section multiplied by a constant β. This method is representative of the behaviour exhibited by a wicking material where the rate of water entering the flow channel is proportional to the difference between existing and saturated conditions. At low humidity the rate of water addition is high, but as

the humidity increases the vapour partial pressure approaches the saturation pressure and water addition reduces. Such a method is seen to self regulate the humidity within the flow channel to prevent excessive flooding.

$$N_{H_2O,ca,inj}(n) = \beta\left(P_{sat}(n) - P_{ca,v}(n)\right) \tag{4.21}$$

$$N_{H_2O,an,inj}(n) = \beta\left(P_{sat}(n) - P_{an,v}(n)\right) \tag{4.22}$$

Variation in the constant β can be used to qualitatively represent different wicking material properties, a higher value of β represents a more effective wicking material than a lower value. Experimental tests or more detailed numerical simulations would be required to quantitatively relate this parameter to physical material properties.

4.5.4 Method IV - Constant rate

The previous methods have assumed the rate of liquid water added to each section can be varied. In practice this may be impractical, particularly with method I and method II which both require knowledge of localised relative humidity within the cell. A more practical method for water addition, particularly relating to liquid injection, is to add liquid water at a constant rate across the cell. This is represented by adding the same amount of liquid water to every section in the model. The rate of water addition can either be determined from the cell operating conditions (feedforward control) or from the exhaust relative humidity (feedback control). Both methods can be easily implemented in practice using existing commercially available sensors.

$$N_{H_2O,ca,inj}(n) = \zeta_{ca} \tag{4.23}$$

$$N_{H_2O,an,inj}(n) = \zeta_{an} \tag{4.24}$$

4.6 Gas diffusion layer model

The role of the gas diffusion layer (GDL) is to provide a pathway for products and reactants to travel between the gas flow channel and membrane, remove liquid water from the membrane GDL interface and provide low electronic resistance between the membrane and bi-polar plate. The GDL is usually constructed from either carbon fibre papers or woven carbon fibre fabrics, forming a porous structure with a PTFE coating to provide some degree of hydrophobicity for liquid water removal [9]. To reach the membrane interface, reactant

gas must diffuse through the pathways between the carbon fibres. Liquid product water will either evaporate and diffuse across the GDL to the flow channel, or remain in the liquid phase and be transported through capillary pressure to the flow channel. The presence of liquid water in the GDL blocks potential diffusion paths, reducing the effective diffusivity and hence reduces reactant concentration at the membrane interface. This is one of the main causes of mass transport voltage loss at high current density, due to an increased rate of both water production and reactant consumption. Figure 4.4 illustrates the non-direct diffusion paths taken by products and reactants across the GDL.

The diffusion of multi-component gas species from an area of higher to lower gas concentration is described using the Stefan-Maxwell equation, shown in equation 4.25 it describes the concentration gradient of species i across the GDL thickness z in the presence of a known number of other gases j.

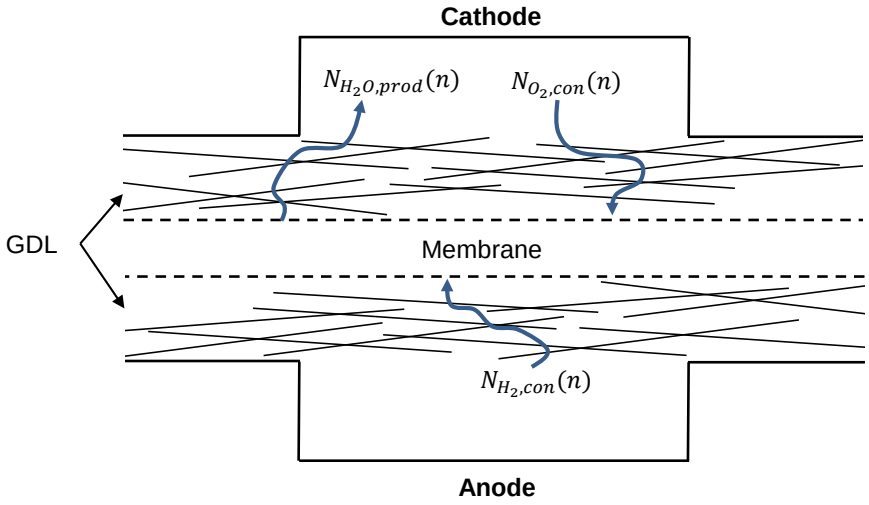

Figure 4.4: Gas diffusion layer diagram

$$\frac{dx_i}{dz} = R_0 T \sum_{j=1}^{n} \frac{x_i N_j - x_j N_i}{P D_{i-j}^{eff}} \tag{4.25}$$

The pressure diffusivity PD_{i-j} is calculated from equation 4.26 [71]. Constants a and b are taken for each species from [52], critical temperatures and pressures are taken from [72], values used are shown in table 4.1

$$PD_{i-j} = a \left(\frac{T}{\sqrt{T_{c_r i} T_{c_r j}}} \right)^b (P_{c_r i} P_{c_r j})^{\frac{1}{3}} (T_{c_r i} T_{c_r j})^{\frac{5}{12}} \left(\frac{1}{M_i} + \frac{1}{M_j} \right)^{\frac{1}{2}} \tag{4.26}$$

Parameter	Value	Source
a_{H_2} , a_{O_2} , a_{N_2}	2.75×10^{-4}	[52]
b_{H_2} , b_{O_2} , b_{N_2}	1.832	[52]
a_{H_2O}	3.64×10^{-4}	[52]
b_{H_2O}	2.334	[52]
T_{H_2O}	647.3K	[72]
T_{H_2}	33.2K	[72]
T_{O_2}	154.8K	[72]
T_{N_2}	126.3K	[72]
P_{H_2O}	221.3atm	[72]
P_{H_2}	13.2atm	[72]
P_{O_2}	50.9atm	[72]
P_{N_2}	34.0atm	[72]

Table 4.1: Constants and critical values used to determine pressure diffusivity

The presence of carbon fibres used to construct the GDL inhibit the transport of gas from the flow channel to the membrane interface creating longer diffusive paths. Furthermore, as the volume of liquid water within the GDL increases, diffusive paths become blocked, reducing the diffusivity compared to that predicted by equation 4.26. To correct for these effects in the Stefan-Maxwell equation the pressure diffusivity is corrected to take into account the porosity (ϵ) and tortuosity (τ) of the GDL along with the liquid water void fraction (s) within the GDL, giving the effective pressure diffusivity, shown in equation 4.27.

$$PD_{i-j}^{eff} = PD_{i-j} f(\epsilon, \tau)\, g(s) \tag{4.27}$$

By assuming the tortuosity can be approximated by the inverse square root of porosity ($\tau = \epsilon^{-1/2}$) the correction for both porosity and tortuosity can be represented using the Bruggeman correction factor [52, 73–75], shown in equation 4.28. Water void fraction s is the ratio of liquid water volume to total void space within the GDL ($s = V_l/V_t$) [73], the influence of liquid water on diffusivity is considered using the normalised form void fraction of equation 4.29. The power 2 is derived from the work of [76], although the authors indicate that the power used will increase significantly for contact angles greater than 90°.

$$f(\epsilon, \tau) = \frac{\epsilon}{\tau} = \epsilon^{1.5} \tag{4.28}$$

$$g(s) = (1 - s)^2 \tag{4.29}$$

The final form for effective pressure diffusivity is then expressed using equation 4.30

$$PD_{i-j}^{eff} = PD_{i-j} \epsilon^{1.5} (1 - s)^2 \tag{4.30}$$

The Stefan-Maxwell equations for each species interaction can then be expressed in the form of two state space equations with no external input, equations 4.31 and 4.32 for the cathode and anode respectively. The corresponding A matrices are shown in equations 4.33 and 4.34. Since the model assumes steady state operation the molar fluxes are equal to the rate of consumption or production from the electrochemical reaction, excluding the water vapour flux which also includes the net membrane water transport. As Nitrogen is not involved in the electrochemical reaction, there is no molar flux across the GDL and corresponding terms from the Stefan-Maxwell equation are removed in calculating A_{ca}.

$$\frac{d}{dz}\begin{bmatrix} x_{N_2} \\ x_{O_2} \\ x_{H_2O_v} \end{bmatrix} = R_0 T \left[A_{ca}\right] \begin{bmatrix} x_{N_2} \\ x_{O_2} \\ x_{H_2O_v} \end{bmatrix} \tag{4.31}$$

$$\frac{d}{dz}\begin{bmatrix} x_{H_2} \\ x_{H_2O_v} \end{bmatrix} = R_0 T \left[A_{an}\right] \begin{bmatrix} x_{H_2} \\ x_{H_2O_v} \end{bmatrix} \tag{4.32}$$

$$\left[A_{ca}\right] = \begin{bmatrix} \left(\frac{N_{H_2O,v}}{PD^{eff}_{N_2-H_2O}} + \frac{N_{O_2}}{PD^{eff}_{N_2-O_2}}\right) & 0 & 0 \\ -\frac{N_{O_2}}{PD^{eff}_{O_2-N_2}} & \frac{N_{H_2Ov}}{PD^{eff}_{O_2-H_2O}} & -\frac{N_{O_2}}{PD^{eff}_{O_2-H_2O}} \\ -\frac{N_{H_2O,v}}{PD^{eff}_{H_2O-N_2}} & -\frac{N_{H_2Ov}}{PD^{eff}_{H_2O-O_2}} & \frac{N_{O_2}}{PD^{eff}_{H_2O-O_2}} \end{bmatrix} \tag{4.33}$$

$$\left[A_{an}\right] = \begin{bmatrix} \frac{N_{H_2Ov}}{PD^{eff}_{H_2-H_2O}} & -\frac{N_{H_2}}{PD^{eff}_{H_2-H_2O}} \\ \frac{-N_{H_2Ov}}{PD^{eff}_{H_2O-H_2}} & \frac{N_{H_2}}{PD^{eff}_{H_2O-H_2}} \end{bmatrix} \tag{4.34}$$

The state space equations can then be solved using the state transition matrix solution for a linear time-invariant system with no external input [77], shown in equation 4.35. z_0 refers to the GDL/flow channel interface at which point the distance is taken to be zero, $x\left(z_0\right)$ refers to the concentrations this point, which are assumed to be the same as the bulk flow channel concentrations. The solution to equation 4.35 at the point $z = t_{GDL}$ gives the concentrations at the GDL/membrane interface.

$$x(z) = exp\left(\left[A_{ca}\right]\left(z - z_0\right)\right) x(z_0) \tag{4.35}$$

In the case where the concentration of water vapour at the GDL membrane interface is equal to the saturation limit it is not possible for either the product water, or net water transported across the membrane to evaporate. In this situation the corresponding water

vapour transport term $N_{H_2O_v}$ in equation 4.33 or 4.34 (depending on which GDL is saturated) becomes zero and all water is transported across the GDL in liquid form through capillary pressure. The capillary pressure within the GDL is determined from equation 4.36 [73], where σ is the liquid water surface tension, θ the contact angle and K the permeability. $j(s)$ represents the Leverett J-function, an empirical relationship used in determining the capillary pressure in a porous solid, shown in equation 4.37 [78]. Although used extensively in fuel cell modelling [73, 75, 76], the original Leverett J-function was based on liquid water transport through soil via capillary pressure as a function of the liquid water void fraction. More detailed empirical functions can be used to describe the capillary pressure, such as [79] which takes into consideration PTFE loading and compressed porosity, although such correlations are specific to the type of GDL used.

$$P = \sigma cos\left(\theta\right)\left(\frac{\epsilon}{K}\right)^{\frac{1}{2}} j(s) \tag{4.36}$$

$$j(s) = \begin{cases} 1.417\left(1-s\right) - 2.120\left(1-s\right)^2 + 1.263\left(1-s\right)^3 & \text{if } \theta < 90^\circ \\ 1.417s - 2.120s^2 + 1.263s^3 & \text{if } \theta \geq 90^\circ \end{cases} \tag{4.37}$$

Capillary pressure is related to water flux using equation 4.38. κ_{rl} is the relative permeability, defined as the ratio of permeability in the liquid phase at a specific saturation relative to the total permeability of the porous medium, the relationship $\kappa_{rl} = s^3$ has been used in this work [73].

$$N_{H_2O_l} = -\frac{\kappa_{rl} K \rho}{M_{H_2O}\mu}\left(\frac{dP}{ds}\right)\left(\frac{ds}{dz}\right) \tag{4.38}$$

Substituting in the differential of equation 4.36 with respect to liquid void fraction s gives equation 4.39 where $\nabla j(s)$ is the differential of the Leverett function with respect to s.

$$N_{H_2O_l} = \frac{-\kappa_{rl} K \rho \sigma}{M_{H_2O}\mu} cos\left(\theta\right)\left(\frac{\epsilon}{K}\right)^{\frac{1}{2}}\left(\frac{ds}{dz}\right)\nabla j(s) \tag{4.39}$$

By re-arranging equation 4.39, integrating $\kappa_{rl} j(s)$ with respect to s and the remaining constants with respect to z a sixth order polynomial is produced, shown in equation 4.40 for a hydrophobic GDL ($\theta > 90^\circ$). Solving for the sensible positive real root of the polynomial ($0 < s < 1$) yields the water void fraction in the GDL for a given liquid water flux $N_{H_2O_l}$. Constant C is equal to zero, since at $s = 0$ liquid water flux $N_{H_2O_l}$ is also zero. The calculated liquid void fraction is in turn used to determine the effective diffusivity, the calculation procedure for $N_{H_2O_l}$ is discussed in section 4.10.

$$\frac{N_{H_2O_l} M_{H_2O} \mu}{(\epsilon K)^{1/2} \rho cos(\theta)} z + C = s^4 \left(0.35423 - 0.8480s + 0.6135s^2\right) \tag{4.40}$$

Using equations 4.25-4.35 the mole fraction profiles for Oxygen and water vapour in the cathode GDL are shown in figure 4.5 for a 300μm thick GDL with a 72.5% porosity [77]. The flow channel boundary conditions were 80% relative humidity, 70°C at 1.2bar.a pressure, simulations were performed at different current densities assuming zero net water transport. The plots demonstrate that as current increases, water vapour fraction at the membrane interface increases due to the additional product water and Oxygen fraction decreases due to oxygen consumption.

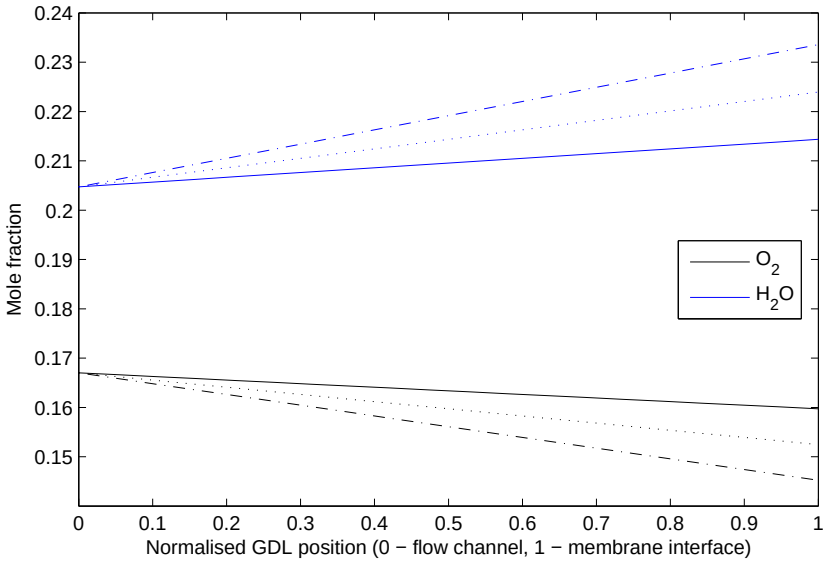

Figure 4.5: Gas mole fraction through the GDL at 0.5A/cm^2 (solid), 1.0A/cm^2 (dashed) and 1.5A/cm^2 (dash-dot)

In figure 4.5 the water vapour fraction did not exceed the saturation limits and liquid water did not form in the GDL. Further increasing the current density leads to higher water vapour fractions at the membrane interface and eventually saturation will occur. Figure 4.6 shows the current density at which liquid water forms as a function of gas channel humidity for the same conditions as figure 4.5 except the porosity is varied. Results show that at high gas channel humidity, the onset current density for liquid formation is low, especially in the less porous GDL. At the point immediately prior to saturation the water content of the membrane will be high, giving a high ionic conductivity and good cell performance. Exceeding saturation will result in liquid water formation within the GDL, reducing the product and reactant diffusive paths and increasing the mass transfer voltage loss.

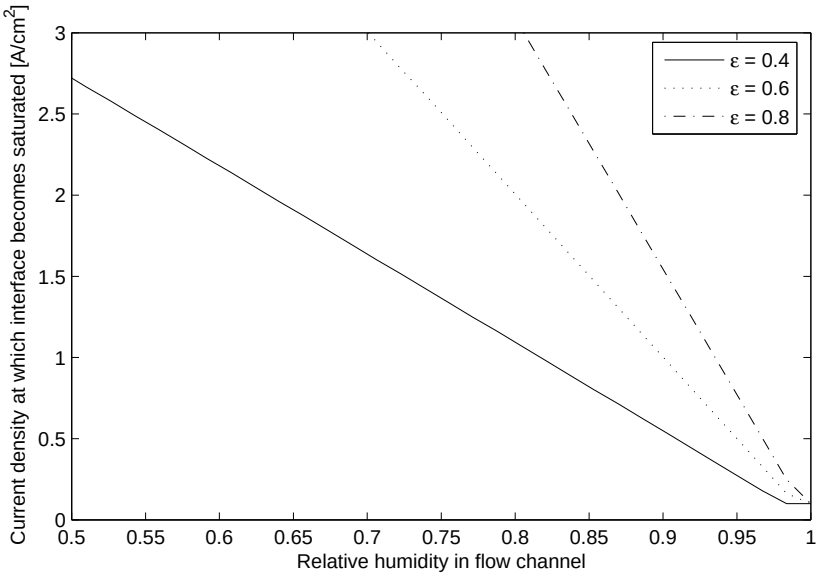

Figure 4.6: Current density for onset of liquid water formation in the GDL at different flow channel humidities

4.7 Water transport

Water transport across the membrane is calculated separately for each section of the model. The same method as described in section 3.3 is used, based on the empirical correlations of [52]. Both electro-osmotic drag and back diffusion are considered, assuming a linear water content gradient across the membrane. Water content at the anode and cathode is evaluated from the water activity at the interface between the membrane and gas diffusion layer. Since the water activity used to determine the membrane hydration is itself a function of the net water transport an iterative method is required to solve for both interface water activity and membrane net water transport simultaneously. This is achieved in the model by manually selecting a range of net water transport rates and using these in the gas diffusion layer model of section 4.6, along with the flow channel boundary conditions to determine the water activity at the interface. The water activity can then be used to calculate the actual membrane net water transport and section membrane resistivity for the given input conditions. The point at which the input and calculated net water transport rates are equal represents the steady state operating conditions for that section of the cell.

4.8 Energy balance

Energy balance is performed for each section of the model, since the model operates at steady state the sum of all energy flows in each section must sum to zero. Similarly to section 3.5, energy balance is performed considering inlet and exit enthalpies, heat release of the electrochemical reaction and electrical energy. Heat release to the environment through natural convection is not considered since the edge area exposed to the atmosphere on a single cell is small. Equation 4.41 shows the energy balance for section n of the one-dimensional fuel cell model, $\dot{Q}_{error}$ represents the error in the energy balance for a chosen exit temperature, progressive iterations are performed until $\dot{Q}_{error}$ is less than a specified tolerance.

$$\dot{Q}_{error}(n) = \dot{Q}_{ca}(n-1) - \dot{Q}_{ca}(n) + \dot{Q}_{an}(n-1) - \dot{Q}_{an}(n) + \dot{Q}_{reac}(n) - \dot{Q}_{elec}(n) + \dot{Q}_{cd}(n) \tag{4.41}$$

Heat release through the electrochemical reaction is determined from the current across the section area though equation 4.42, electrical energy for each section is calculated from equation 4.43.

$$\dot{Q}_{reac}(n) = -\Delta\hat{h}\frac{i(n)\,A_{sec}}{2F} \tag{4.42}$$

$$\dot{Q}_{elec}(n) = V_{sec}(n)\,A_{sec}\,i(n) \tag{4.43}$$

Enthalpy for the anode or cathode exit of section n is determined separately using equation 4.44. The left hand term calculates the enthalpy of vapourisation of the water vapour, the right hand term calculates the sensible heat of the single phase species. For the cathode this includes Nitrogen, Oxygen, liquid water and the sensible heat of the water vapour; for the anode only Hydrogen, liquid water and water vapour need to be considered. Enthalpy of vapourisation and specific heat capacity are evaluated as a function of temperature using data from [66].

$$\dot{Q}(n) = N_{H_2Ov}(n)\,M_{H_2O}\Delta H_v(n) + \sum_{j=1}^{n} N_j(n)\,M_j C_{pj}(n)\,(T_{sec}(n) - T_0) \tag{4.44}$$

An additional term Q_{cd} is included in equation 4.41 for the one-dimensional model, this term accounts for the case where in certain situations water vapour may be transported from an under-saturated anode to a saturated cathode through electro-osmotic drag causing condensation to occur. This consideration is required due to the presence of significant water

concentration gradients across gas diffusion layer at high current densities. In such cases the rate of heat release from the condensing vapour is determined using equation 4.45, for all other cases where the cathode is not saturated or the anode is saturated $Q_{cd} = 0$.

$$\dot{Q}_{cd}(n) = J_{H_2O,net}(n) M_{H_2O} A_{sec} \Delta H_v \quad if \quad RH_{ca} = 1 \quad \& \quad RH_{an} < 1 \tag{4.45}$$

4.9 Pressure drop

Pressure drop across each section of the model is calculated for the cathode flow channel using the Darcy-Weisbach equation. Flow is assumed laminar across all operating conditions, friction factor is determined analytically for a smooth pipe from equation 4.46 [44]. Viscosity of the multicomponent mixture is determined using the method of Wilke [80], the influence of liquid water on pressure drop is ignored.

$$f = \frac{64}{Re} \qquad Re \leq 2100 \tag{4.46}$$

$$\Delta P = \frac{-f L \rho V^2}{2 d_h} \tag{4.47}$$

Since the anode is modelled as being dead ended with time averaged purging, the gas flow rate is small and it is reasonable to assume the pressure is uniform throughout.

4.10 Computation

The one dimensional fuel cell model is implemented using MATLAB, an electronic copy of the model is available on request. The model inputs are inlet properties of the anode and cathode flow channels (operating in co-flow), mean current density, liquid water addition method and cell flow channel geometry. Once the conditions within the flow channels of the first section are established the cathode pressure drop and molar flow rates of the electrochemical reaction are established. Next an iterative procedure is carried out, described in section 4.7, to determined the steady state net water flow across the membrane, gas diffusion layer concentrations and membrane hydration. The section reversible open circuit voltage and irreversible voltage are then determined, along with the flow channel exit enthalpies and residual heat transfer Q_{error}. The section temperature is then varied iteratively until $Q_{error} < 1 \times 10^{-4}$W; cell voltage, liquid water addition rate and exit enthalpies are recalculated for each iteration. The exit properties of section n then feed into the input of section $n + 1$, this process is repeated until the total number of sections is reached, 5000 sections

have been used for the modelling results discussed in this work. This number was determined based on a sensitivity study performed at a low mean current density ($0.1\mathrm{A/cm^2}$) where the model was seen to be most sensitive to change in the number of sections due to lower gas flow rates. The variation in gas channel exit temperature with the number of sections is shown in figure 4.7 for a 1.1bar.a, 40°C, 90% relative humidity inlet and a 99% target cathode gas channel relative humidity. Increasing the number of sections above 5000 yields changes in exit temperature less than 0.001°C at the expense of computational load.

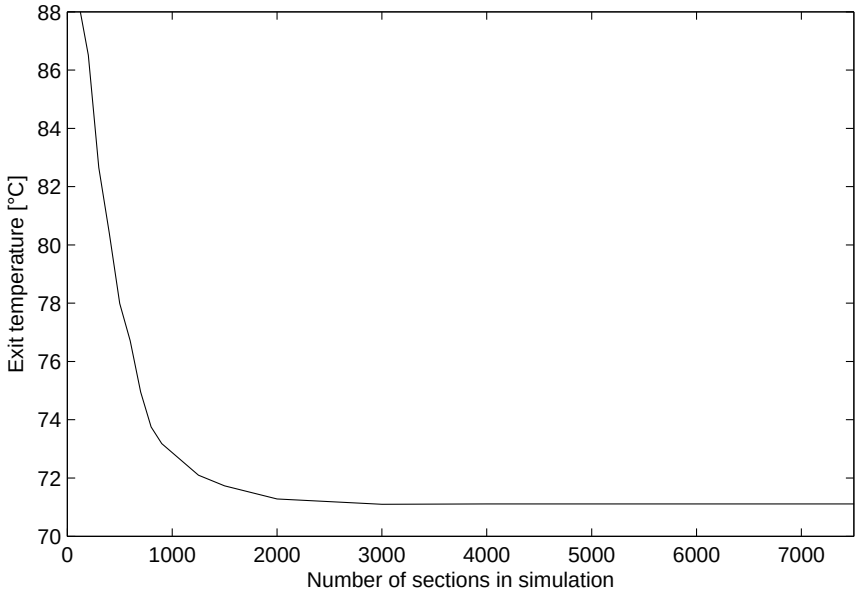

Figure 4.7: Influence of number of sections on gas channel exit temperature

Once the properties along the whole flow channel have been determined for a given current density, the cell voltage in each section is compared to the mean cell voltage. The difference between the section voltage and mean cell voltage is then used to modify the current density input for each section, shown in equation 4.48, where m represents the iteration number and n_{cell} the total number of sections in the cell. For sections where the voltage is less than the mean, the current density is lowered, increasing the voltage. Whereas for sections were the voltage is greater than the mean the current density is increased, decreasing the voltage. Progressive iterations are performed, recalculating the properties along the flow channel in each iteration until the variation between section voltage and mean cell voltage is less than 1mV.

$$i\left(n,m+1\right)=i\left(n,m\right)+\left[V_s\left(n,m\right)-\frac{\sum_{n=1}^{n_{cell}}V_s\left(n,m\right)}{n_{cell}}\right] \tag{4.48}$$

The calculation procedure for the model is illustrated graphically in the flow chart of figure 4.8.

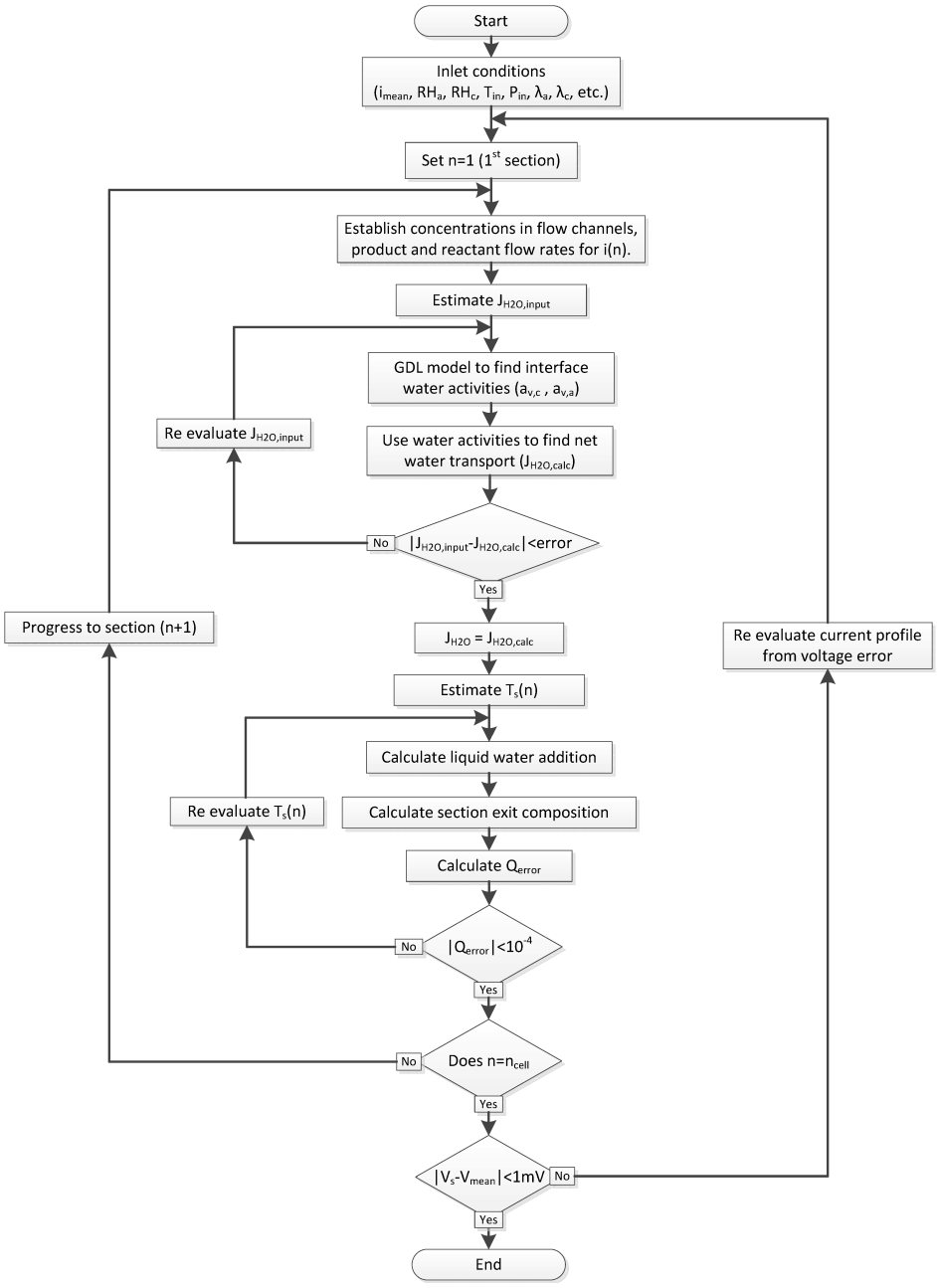

Figure 4.8: Segmented model flow chart

4.11 Validation

The segmented fuel cell model was validated using experimental data from the evaporatively cooled fuel cell stack of [12]. A comparison of the polarisation curve of [12] and the voltage predicted by the model is shown in figure 4.9, the values of $i_{oc,0}$ and i_n used are shown in table 4.2.

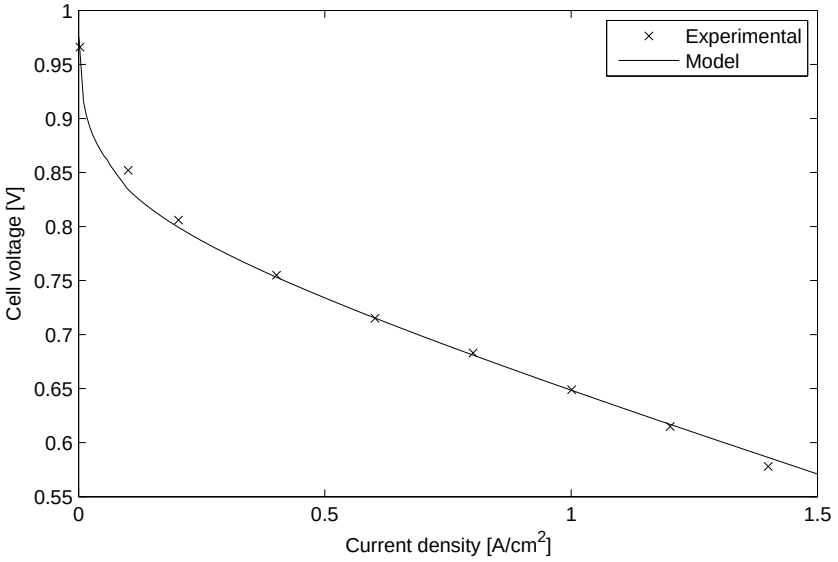

Figure 4.9: Comparison of One-dimensional model voltage to experimental data of [12]

Parameter	**Value**
Internal current density (i_n)	3.0×10^{-4}A/cm^2
Exchange current density at STP ($i_{oc,0}$)	6.8×10^{-8}A/cm^2

Table 4.2: Segmented model cell voltage parameters

Comparing the cell voltage predicted by the model to the experimental data of [12] demonstrates that the model agrees well at an overall cell level. The model fit is best in the linear 'ohmic' operating region between 0.2A/cm^2 and 1.2A/cm^2, a slight deviation is seen at low operating current densities (<0.2A/cm^2) where the activation and fuel crossover overvoltages are dominant. At high current densities (>1.2A/cm^2) where mass concentration losses dominate, the segmented model voltage is higher than the final experimental data point. This is the opposite case to the lumped parameter model detailed in chapter 3 where the model under predicts the final experimental data point. The difference between the two models is caused by the use of an empirical exponential function to simulate mass concen-

tration loss in the lumped parameter model. This is not required in the segmented model since both mass consumption along the flow channel and reactant concentration gradients across the gas diffusion layer are considered. The properties of the gas diffusion layer in the segmented model have been inferred from the literature as they are not available for the experimental work of [12]. Differences in gas diffusion layer thickness, porosity and contact angle will influence the behaviour of the cell in the mass concentration region, possibly leading to the discrepancies seen. To provide a better validation of the polarisation performance in this region, experimental data points at higher current densities are required where the voltage drop due to mass concentration is more significant.

The cell level polarisation curve used in figure 4.9 does not validate the internal mechanisms and spatial distributions within the model. To validate the internal mechanisms, an experimental method which considers spatial distribution throughout the cell is required, a segmented fuel cell is a possible method of achieving this. In a segmented cell, the current collector is separated into multiple sections across the membrane active area to allow the study of current density distribution at multiple points within the cell. Segmented fuel cells have been used widely in the literature, reviewed by [81], but to date none of these techniques have been applied to evaporatively cooled fuel cells and therefore existing data is not suitable to further validate this model. The measurement of current density at different sections of the flow channel in an evaporatively cooled cell would allow the spatial distribution of the present model to be validated. Furthermore, electrochemical impedance spectroscopy (EIS) of the separate segments will also allow a more detailed study of the localised voltage loss mechanisms. The development of a segmented evaporatively cooled fuel cell is therefore a key area for further work, results from such a cell would increase the validity of the current model if a good agreement can be demonstrated.

4.12 Chapter summary

In this chapter, a steady state, one dimensional, along the flow channel model of a co-flow evaporatively cooled fuel cell has been produced. The model allows for the study of temperature and species profiles throughout the length of the flow channel including the influence of the gas diffusion layers. Four different methods are presented for determining the rate of liquid water addition into the cell required to maintain sufficient humidity and thermal balance. The results obtained using the one-dimensional model are presented and analysed in chapter 6.

Chapter 5

Heat exchanger models and experiments

5.1 Introduction

The models developed in the previous chapters are capable of determining the water addition requirements and operating conditions of evaporatively cooled fuel cells, as well as the cathode exhaust conditions. In this chapter, the heat exchangers and associated models used to condense water from the cathode exhaust mixture are detailed. This completes the fuel cell system layout discussed in chapter 2, allowing the water balance of the system to be calculated.

Three heat exchanger models are presented in this chapter, the first is a conventional louvred fin and tube radiator with ambient air cold side and liquid hot side. This model, used in both the liquid cooled system (figure 2.4) and evaporatively cooled system with intermediate condenser and liquid cooling loop (figure 2.8), is presented in section 5.2. The second, also a louvred fin and tube radiator, has an ambient air cold side and cathode exhaust mixture hot side. This is used in the evaporatively cooled system with the condensing radiator (figure 2.7) and is described in section 5.4. The final heat exchanger model, described in section 5.6, is a compact plate condenser with chevron flow enhancements, the cold side is liquid coolant and the hot side is the cathode exhaust mixture. This represents the intermediate condenser used in the evaporatively cooled system with the liquid cooling loop (figure 2.8). Section 5.5 also details the experimental work conducted on this heat exchanger.

5.2 Liquid radiator model

The liquid cooled radiator has been modelled as a one dimensional cross flow heat exchanger with both fluids unmixed, the hot side of the heat exchanger is the water glycol mixture of the vehicle cooling loop and the cold side is forced air flow at ambient temperature from the underbonnet geometry of section 3.9.2. Figure 5.1 shows, a typical louvered fin radiator, illustrating how the louvered fins disturb the air flow and increase heat transfer area. The geometry notation used for the louvered fin radiator model is shown in figure 5.2, geometry used is taken from [82] and detailed in table 5.1.

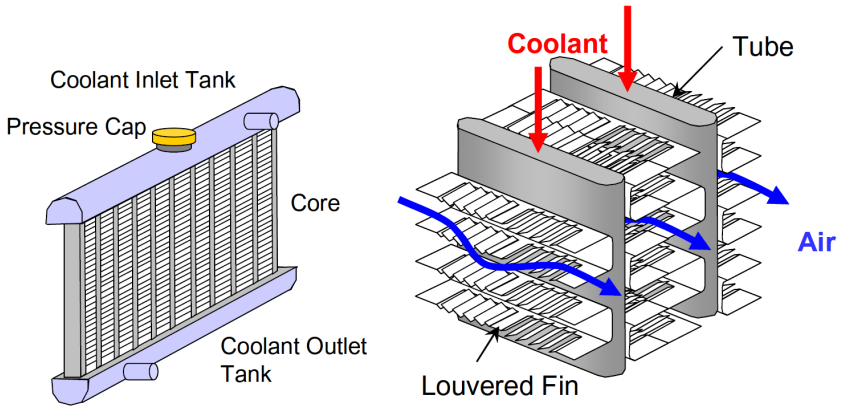

Figure 5.1: Diagram of a typical louvered fin radiator. Image from [82], Reprinted with permission from SAE paper 2006-01-0726 Copyright ©2006 SAE international. Further use or distribution is not permitted without permission from SAE

Parameter	**Value**
Fin pitch (F_p)	2.5mm
Louvre pitch (L_p)	1.14mm
Fin length (F_l)	8.59mm
Tube height (T_h)	2.5mm
Tube depth (T_d)	21.58mm
Tube thickness (T_t)	0.32mm
Louvre length (L_l)	6.74mm
Fin thickness (F_t)	0.10mm
Louvre height (L_h)	0.32mm
Louvre angle (θ)	28°

Table 5.1: Tube and fin geometry for a standard radiator [82]

Radiator heat transfer is calculated using the effectiveness number of transfer units method (ϵ-NTU) with semi-empirical relationships for the convective heat transfer coef-

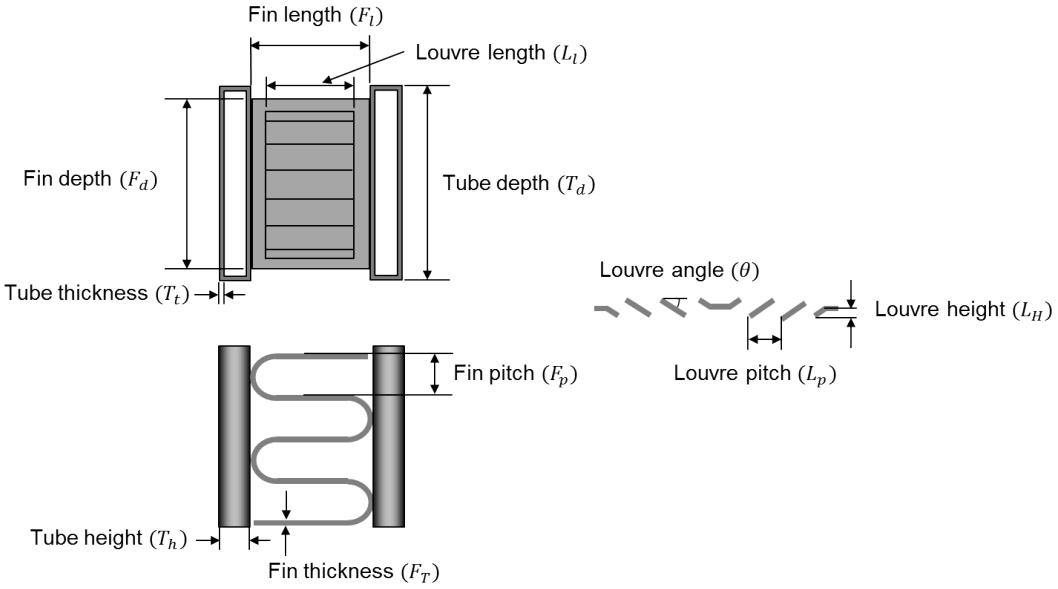

Figure 5.2: Geometry of louvered fin radiator

ficients. It is assumed that the coolant manifold is sufficient in distributing flow evenly across the different cooling tubes and that air flow maldistribution across the face of the radiator is negligible [83]. The radiator can therefore be represented as a single tube and fin arrangement with results scaled up across the radiator, this is illustrated in figure 5.3 which shows a single coolant tube and fin arrangement. The coolant tube is split into multiple sections equal to the fin spacing to consider the change in coolant composition with temperature, producing a one dimensional model. The airflow through each of the fins is equal across the face of the radiator. The following sections detail how the hot side and cold side heat transfer coefficients are calculated.

5.2.1 Hot side

Based on the assumption that the flow in each coolant tube is the same, the coolant mass flow rate and Reynolds numbers are determined from equations 5.1 and 5.2 respectively. Where n_{tubes} is the number of parallel coolant tubes in the radiator, $d_{h,tube}$ the hydraulic diameter, $A_{CSA,tube}$ the cross sectional area of a single coolant tube and subscript h refers to the coolant mixture.

$$\dot{m}_{h,tube} = \frac{\dot{m}_h}{n_{tubes}} \tag{5.1}$$

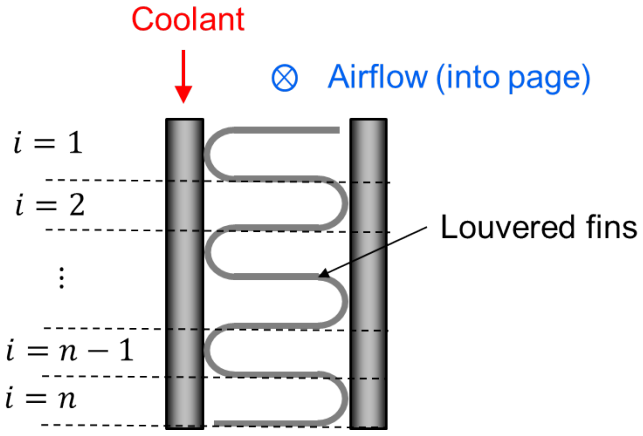

Figure 5.3: Single radiator tube and fins

$$Re_{h,tube} = \frac{\dot{m}_{h,tube} d_{h,tube}}{A_{CSA,tube} \mu_h} \tag{5.2}$$

Hot side Nusselt number is then calculated using the Dittus-Boelter empirical correlation for cooling turbulent flow in circular pipes [44] (equation 5.3). Hot side convective heat transfer coefficient is then found from equation 5.4, coolant thermal conductivity k_h is evaluated as a function of temperature.

$$Nu_h = 0.023 Re^{0.8} Pr^{0.3} \tag{5.3}$$

$$h_h = \frac{Nu_h k_h}{d_{h,tube}} \tag{5.4}$$

5.2.2 Cold side

To model the convective heat transfer coefficient of the cold side, the geometry of the louvred fin needs to be taken into consideration. Chang and Wang [84] used experimental data from 91 louvred fin radiators with different geometry. Producing a correlation for Colburn number (c) as a function of geometry, shown in equation 5.5 using geometry notation from figure 5.2. Mean deviation between measured and predicted Colburn number was shown to be 7.55% across the different geometries. Louvre Reynolds number is calculated assuming all air flow travels evenly through the louvre cross sectional area.

$$c = Re_l^{-0.49} \left(\frac{\theta}{90}\right)^{0.27} \left(\frac{F_p}{L_p}\right)^{-0.14} \left(\frac{T_d}{L_p}\right)^{-0.23} \left(\frac{L_l}{L_p}\right)^{0.68} \left(\frac{T_p}{L_p}\right)^{-0.28} \left(\frac{T_t}{L_p}\right)^{-0.05} \tag{5.5}$$

Convective heat transfer coefficient is then calculated from the Colburn number using equation 5.6

$$h_{air} = \frac{c\dot{m}_{air,fin} C_{p,air}}{A_{CSA,fin} Pr_{air}^{\frac{2}{3}}} \tag{5.6}$$

Conductive resistance along the fin causes the mean temperature difference between the fin and air to reduce. To account for this a fin efficiency (η_{fin}) is included which is defined as the ratio of actual heat transfer to maximum heat transfer assuming no temperature drop across the fin. The fin efficiency is determined from the convective heat transfer coefficient, fin geometry and fin material using equations 5.7 and 5.8 [44]. Where P_{fin} is the fin perimeter, A_{fin} the fin cross sectional area an k_t the fin/tube thermal conductivity.

$$\eta_{fin} = \frac{tanh\left(m_{fin} F_l/2\right)}{m_{fin} F_l/2} \tag{5.7}$$

$$m_{fin} = \sqrt{\frac{h_{air} P_{fin}}{k_t A_{fin}}} \tag{5.8}$$

5.2.3 Heat transfer

Heat transfer in each section is calculated using the effectiveness number of transfer units (ϵ-NTU) method. The ϵ-NTU method allows heat transfer to be calculated without prior knowledge of the exit temperatures based on the maximum possible heat transfer and a heat exchanger effectiveness (equation 5.9).

$$\dot{Q}_n = \epsilon C_{min} \left(T_{h,i} - T_{c,i}\right) \tag{5.9}$$

C_{min} is the minimum heat capacity of either the hot or cold side, similarly C_{max} represents the maximum heat capacity. The method of determining the heat exchanger effectiveness depends on the heat exchanger arrangement, the effectiveness for a single pass cross flow with both fluids unmixed is shown in equation 5.11 [44]. Where C_r is the heat capacity ratio and NTU the dimensionless number of transfer units defined from equations 5.12 and 5.13 respectively.

$$\begin{aligned} C_{min} &= \min\left(\dot{m}_{h,tube} C_{p,h}, \dot{m}_{air,fin} C_{p,air}\right) \\ C_{max} &= \max\left(\dot{m}_{h,tube} C_{p,h}, \dot{m}_{air,fin} C_{p,air}\right) \end{aligned} \tag{5.10}$$

$$\epsilon = 1 - exp\left[\left(\frac{1}{C_r}\right) NTU^{0.22} \left(exp\left[-C_r NTU^{0.78}\right] - 1\right)\right] \tag{5.11}$$

$$C_r = \frac{C_{min}}{C_{max}} \tag{5.12}$$

$$NTU = \frac{UA_n}{C_{min}} \tag{5.13}$$

From knowledge of the hot and cold side heat transfer coefficients the overall heat transfer coefficient UA_n is found using equation 5.14, where r_h is the internal hydraulic radius and $L_{tube,n}$ the coolant tube length in a single section.

$$UA_n = \left[\frac{1}{h_h \pi d_h L_{tube,n}} + \frac{ln\left(\frac{r_h + t_{tube}}{r_h}\right)}{2\pi L_{tube,n} k_{tube}} + \frac{1}{\eta_{fin} h_{air} A_{fin}} \right]^{-1} \tag{5.14}$$

Once heat transfer for each section is evaluated from equations 5.9-5.14 coolant exit conditions are found using equation 5.15. This process is repeated for each section from hot side in to hot side out, re-evaluating the coolant thermal properties at each step.

$$T_{h,out} = T_{h,in} - \frac{\dot{Q}_n}{\dot{m}_{h,tube} C_{p,hot}} \tag{5.15}$$

5.2.4 Validation

The radiator model was validated using experimental data from [82], shown in figure 5.4. For a range of hot and cold side flow rates the model was seen to predict heat rejection with a 1.71% mean absolute error. Error was seen to increase with a reduction in the coolant flow rate, possibly due to the turbulent assumptions made in calculation of the hot side Nusselt number over predicting heat transfer. However this error is both small and outside of the main operating conditions of the radiator which will experience flow rates in the region of 40-80 lpm for the majority of operating conditions.

Figure 5.5 shows the coolant temperature profiles throughout the radiator for three different coolant flow rates. Temperature change is highest for the lowest flow rate because of the reduced heat capacity. As flow rate increases the temperature drop reduces, raising the mean temperature difference between hot and cold sides, increasing heat transfer. Increasing the coolant flow rate is seen to have a diminishing effect at higher flow rates. Figure 5.5 was produced using a 600mm×600mm core size, 5m/s air velocity and 20°C ambient temperature.

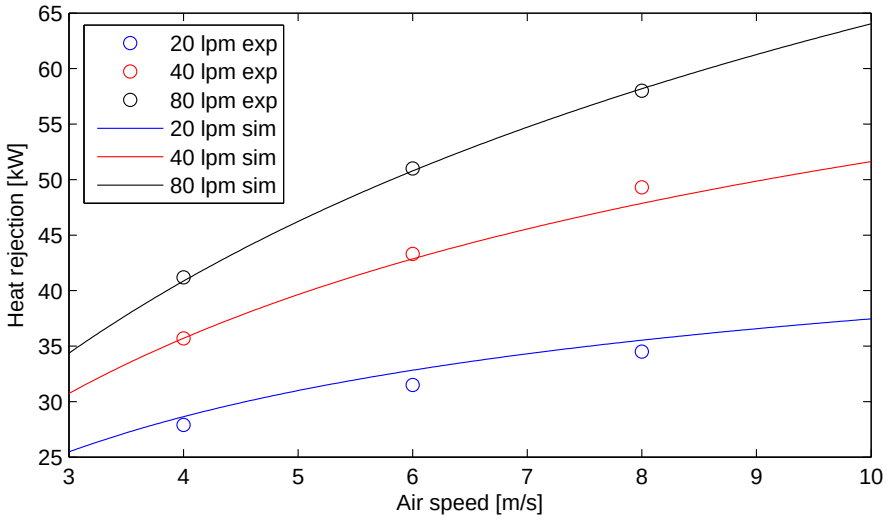

Figure 5.4: Liquid radiator validation, experimental data from [82]

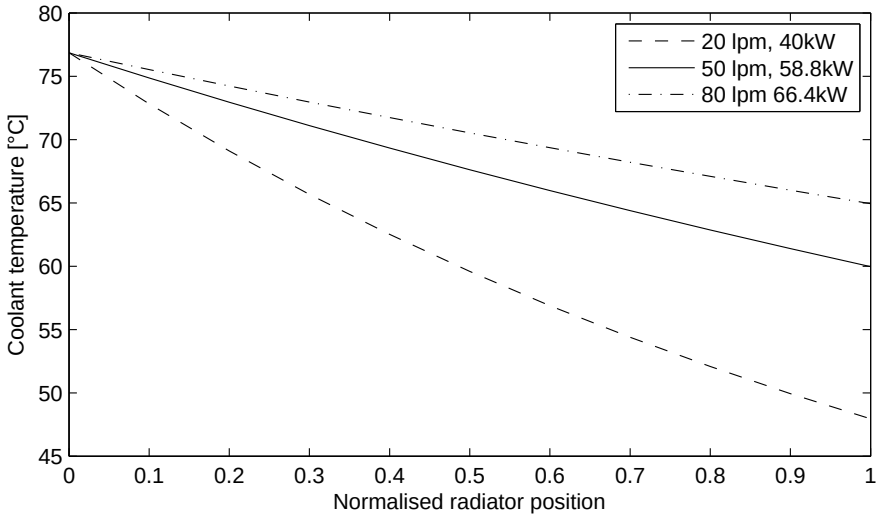

Figure 5.5: Coolant temperature profiles at different flow rates

5.3 Condensation in the presence of non-condensables

Unlike the liquid cooled radiator discussed in section 5.2, where the hot side is liquid coolant, the hot side of the condensing radiator and compact plate condenser is the outlet from the cathode of the fuel cell stack. The cathode exhaust of a PEM fuel cell is a mixture of water vapour, Nitrogen, Oxygen and possibly liquid water. To extract enough liquid water to replenish the amount used in humidifying and cooling the cell, some of the water vapour must be condensed.

During condensation of a pure vapour, the vapour turns to liquid when it meets a surface, such as a heat exchanger wall, below the dew point temperature. Heat equal to the enthalpy of vapourisation is released to the wall, which is usually then removed by cooling on the other side of the wall. As more liquid water condenses, a thin film forms on the wall, further condensation occurs on the interface between the film and the vapour and heat released is transferred through the film and wall to the cooling fluid. This is shown in figure 5.6a.

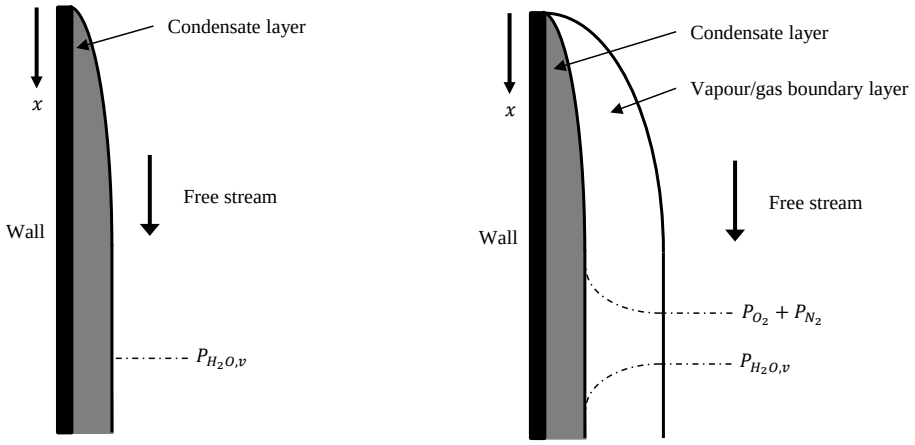

(a) Pure condensation

(b) Non-condensable boundary layer

Figure 5.6: Diagrams of pure condensation and condensation in the presence of non-condensable gases

When the condensing vapour is mixed with a gas which does not condense at the same temperature (such as water vapour and air), the problem becomes more complex. As the water vapour condenses on the wall surface, the non-condensable gas is left behind, as more vapour condenses and a liquid film forms, more non-condensable gas is left behind. The vapour condensing out from the mixture at the film surface leaves behind a region where the mass fraction of non-condensable gas will be higher than in the bulk mixture. This region of higher non-condensable mass fraction forms a second boundary layer on top of the condensate film layer and is referred to as a double boundary layer, shown in figure 5.6b. Once the double boundary layer is established, for vapour in the bulk mixture to condense at the liquid film interface it must first diffuse through the non-condensable boundary layer. The mass transfer resistance to this diffusion significantly reduces the amount of heat transfer compared to the pure condensation rate. Analytical studies by Sparrow *et al.* [85] showed reductions in forced convection heat transfer by up to 50% due to only a 10% mass fraction

of non-condensable gas. For comparison, the exhaust of a typical PEM fuel cell with a 75°C, 1.2bar.a exhaust has a 77% mass fraction of non-condensable gases.

Despite the significant effect on heat transfer, most previous studies of fuel cell system water balance have not considered the influence of non-condensable gases on heat transfer. The water balance study of Ito *et al.* only looked at thermal loads by performing an energy balance and excluded the influence of heat exchanger sizing. Heat exchanger sizing was considered by [40, 41] and [86]. Haraldsson *et al.* [41] and Haraldsson and Alvfors [40] assumed a constant heat transfer coefficient for the condenser hot side, this assumption is invalid since the experimental work of Siddique [87] and others demonstrate up to an order of magnitude change on hot side heat transfer coefficient from inlet to outlet. Izenson and Hill [86] used the logarithmic mean temperature difference (LMTD) method to predict the product of overall heat transfer coefficient and area for fuel cell condensers. However the LMTD method assumes both a constant heat capacity and heat transfer coefficient, neither of which are true of heat transfer with phase change [44].

Bao *et al.* [38] conducted the only PEM fuel cell water balance study to consider the influence of non-condensable gas in their condenser model. Based on the outlet conditions required for water balance the heat transfer area was calculated. Whilst the LMTD method was still used, it was applied to individual sections of the condenser over which the temperature change was small so the change in heat capacity and heat transfer coefficient were smaller. Because the condenser outlet conditions were required prior to the calculation, this model is not suitable for transient studies. Therefore a new model is required to study water balance across transient drive cycles whilst considering the effects of non-consensable gas on heat transfer.

Modelling the influence of non-condensable gases on condensation has received significant attention in other academic fields, notably the nuclear and power generation industries. Colburn and Hougen [88] were the first to produce such a model, using an iterative approach to find the interface temperature between the condensate film and non-condensable boundary layer. Key experimental work was later undertaken by Siddique [87] and Vierow and Schrock [89], both conducting separate tests for air/water condensation in vertical tubes, suitable for use in nuclear power plants. Siddique produced a Nusselt number correlation for the hot side flow based on the Reynolds number, mass fraction of non-condensable gases in the bulk flow and at the wall temperature and Jakob number (ratio of sensible to phase change heat), shown in equation 5.16. Vierow and Schrock [89] produced a similar correlation for heat transfer coefficient, based on the Nusselt 'pure condensation' heat transfer coefficient

multiplied by a 'degradation factor' based on the mass fraction of non-condensables and the bulk Reynolds number, shown in equation 5.17. More recent experimental correlations were compared to those of [87, 89] by Kuhn *et al.* [90].

$$Nu = a \times Re^b \left(\frac{W_{nc,w} - W_{nc,b}}{W_{nc,w}} \right)^c \times Ja^d \tag{5.16}$$

$$h = a \times Re^b \times W_{nc}^c \times h_N \tag{5.17}$$

Since the works discussed above were applied to simplified boiling water reactors (SBWR), the geometry and inlet conditions were not similar to those seen in automotive fuel cell applications. The experimental set-up of Siddique [87] used a 2.54m long 46mm internal diameter tube with inlet temperatures up to $140°C$. For comparison, the automotive radiator modelled by Jung *et al.* [82] had tube length of 382mm and hydraulic diameter of 3.4mm. Krishnaswamy *et al.* [91] conducted the only published experimental study into the influence of non-condensable gas on the condensation of water vapour for geometry and inlet conditions similar to those seen in fuel cell vehicles. The experimental set-up consisted of a horizontal ovalized tube 1m in length with a 3mm hydraulic diameter, a hot side mixture of air and vapour was forced through the tube, the cold side was liquid water in an annular tube run in counterflow. Inlet conditions ranged from sub 100°C high humidity to above 160°C low humidity, a full set of results can be seen in [92]. Krishnaswamy [92] also produced a model to predict condensate rates in such heat exchangers with the intended application of fuel cell exhausts, the model is shown to agree well with the experimental results, however application to other results, such as those of [87] shows under prediction of condensate rate. It is believed that the model does not perform as well when the bulk stream is saturated, possibly due to the method used to calculate the section exit properties.

Based on the current literature there is a need for validated models of condensers suitable for PEM fuel cell vehicles which consider the influence of non-condensable gas and can be used for the study of water balance in fuel cell vehicles. The following sections detail two such models, the first being validated using the experimental work of [92], and the second, which uses a more complex geometry, validated using the experimental set-up detailed in section 5.5.

5.4 Condensing radiator model

5.4.1 Hot side

The calculation of hot side heat transfer is primarily based on the iterative model proposed by No and Park [93], with modifications to account for superheated sections, low relative humidities, pressure drop and different oxygen molar fractions. The model represents downward forced internal flow in a tube with a cooled wall and is based on the double boundary layer discussed in section 5.3. The addition of a second boundary layer creates both a partial pressure and temperature profile between the condensate layer/gas interface and the bulk flow. Since knowledge of the interface properties are required to calculate heat transfer, an iterative method has been used in this model. Whilst non-iterative methods do exist, such as those also detailed by No and Park [93], prior knowledge of wall temperature is required. Since wall temperature is also unknown, iteration would still be required with these models.

The model Hot side heat flux is found using a total heat transfer coefficient h_t which combines separate coefficients from both the sensible and condensation heat transfer from the gas to the interface as well as the film side thermal resistance (equation 5.18). Where h_t is expressed from its components in equation 5.19

$$q_t{}' = h_t \left(T_b - T_{w,h}\right) \tag{5.18}$$

$$\frac{1}{h_t} = \frac{\delta}{k} + \frac{1}{h_{cd} + h_{cv}} \tag{5.19}$$

The condensation heat transfer coefficient (h_{cd}) is found from the mass flux of water vapour transferred from the bulk to the condensate layer, which is calculated from the mass transfer coefficient and concentration gradient between the bulk and interface, shown in equations 5.20 to 5.22

$$h_{cd} \left(T_b - T_i\right) = \dot{m}'_{cd} H_{vap} \tag{5.20}$$

$$\dot{m}'_{cd} = -G \frac{W_{v,i} - W_{v,bulk}}{1 - W_{vi}} = -GB \tag{5.21}$$

$$h_{cd} = G \Delta H_v \frac{W_{v,i} - W_{v,b}}{\left(1 - W_{vi}\right)\left(T_i - T_b\right)} \tag{5.22}$$

Mass fraction of vapour in the bulk mixture is known from the species mass flow rate (equation 5.23). Mass fraction at the interface is evaluated for saturated conditions at the

interface temperature shown in equation 5.24. Saturation pressure is determined as a function of temperature using a look-up table, M_{nc} refers to the molar mass of the Nitrogen, Oxygen non-condensable mixture.

$$W_{v,b} = \frac{\dot{m}_{v,b}}{\dot{m}_{v,b} + \dot{m}_{N_2,b} + \dot{m}_{O_2,b}} \tag{5.23}$$

$$W_{v,i} = 1 - \frac{P_b - P_{i,sat}}{P_b - \left(1 - \left(\frac{M_v}{M_{nc}}\right)\right) P_{i,sat}} \tag{5.24}$$

Next the thickness of the condensate layer is calculated, knowledge of this is required to determine the interface friction factor and blowing parameters used in equations 5.38 and 5.41 respectively. The approximate method of Muñoz-Cobo [94] is used to calculate the condensate thickness (δ), shown in equation 5.25. Where δ_N^* is the Nusselt condensate thickness for conventional condensation, l_i and m_i are defined functions of the flow conditions, δ_p is the approximate condensate layer thickness neglecting the influence of interfacial shear stress τ_i at the interface.

$$\delta = \frac{1.259\left(\delta_N^*\right)^{4/3}}{\left(\delta_p\left(2 - \frac{28}{15}x - \frac{1}{3}x^2\right) + l_i\left(\frac{4}{3} - 2x + \frac{8}{15}x^2 + \frac{1}{3}x^3\right) + m_i\delta_p\left(\frac{1}{2} - \frac{8}{15}x\right)\right)^{1/3}} \tag{5.25}$$

$$\delta_N^* = \left(\frac{4k_f\mu_f\left(T_b - T_i\right)z}{g\Delta H_v\rho_f\left(\rho_f - \rho_b\right)}\right)^{1/4} \tag{5.26}$$

$$l_i = \frac{2\tau_i}{\left(\rho_f - \rho_b\right)g} \tag{5.27}$$

$$\tau_i = \frac{f\rho_b V_b^2}{2} \tag{5.28}$$

$$m_i = \frac{360 f\rho_b\left(V_b - V_f\right)^2}{\left(\rho_f - \rho_b\right)g d_{h,h}} \tag{5.29}$$

$$x = \frac{2\delta_p}{d_{h,h}} \tag{5.30}$$

$$\delta_p = \frac{1.189\delta_N^*}{\left(1 - \frac{4}{5}x_N - \frac{4}{3}x_N^2\right)^{1/4}} \tag{5.31}$$

$$x_N = \frac{2\delta_N^*}{D_{h,hot}} \tag{5.32}$$

Convective heat transfer coefficient and mass transfer coefficient are both calculated from the Stanton number using the mass and heat transfer coefficient analogy. The Dipprey correlation for a rough tube is used in this model, shown in equation 5.33 for heat transfer and 5.34 for mass transfer, where relative roughness is represented by equation 5.35. Friction factor for a smooth tube is found using equation 5.36 for laminar flow and the Petukhov correlation (equation 5.37) for turbulent flow. From which the friction factor at the interface is found using the correlation of Wallis for interfacial friction in vertical annular flow (equation 5.38) [70].

$$St_{ht} = \frac{\frac{f_i}{2}}{1 + \sqrt{\frac{f_i}{2}}\left(5.19\left(Re_b\sqrt{\frac{f_i}{2}}\frac{\epsilon_s}{d}\right)^{0.2} Pr_b^{0.44} - 8.48\right)} = \frac{Nu}{Re_b Pr_b} \tag{5.33}$$

$$St_{mt} = \frac{\frac{f_i}{2}}{1 + \sqrt{\frac{f_i}{2}}\left(5.19\left(Re_b\sqrt{\frac{f_i}{2}}\frac{\epsilon_s}{d}\right)^{0.2} Sc_b^{0.44} - 8.48\right)} = \frac{G}{\rho_b V_b} \tag{5.34}$$

$$\frac{\epsilon_s}{d} = exp\left(3 - \frac{0.4}{\sqrt{\frac{f_i}{2}}}\right) \tag{5.35}$$

$$f = \frac{64}{Re_b} \qquad Re_b \lesssim 2100 \tag{5.36}$$

$$f = \frac{1}{\left(0.790\ln\left(Re_b\right) - 1.64\right)^2} \qquad 3000 \lesssim Re_b \lesssim 5 \times 10^6 \tag{5.37}$$

$$f_i = f\left(1 + 300\frac{\delta}{d_{h,h}}\right) \tag{5.38}$$

Convection Nusselt number is found directly from the heat transfer Stanton number. The mass transfer conductance is found from the mass transfer Stanton number which is then used to calculate the condensation heat transfer coefficient in equation 5.22. Using equation 5.39 the condensation Nusselt number is found.

$$Nu \equiv \frac{hd_h}{k} \tag{5.39}$$

The mass transfer of vapour from the bulk to the interface causes a flux of vapour towards the wall, perpendicular to the direction of forced convection. The motion of this flux causes

thinning and waviness of the condensate layer, promoting heat transfer; this is referred to as 'blowing' and will increase heat transfer at high vapour mass fractions. Blowing is accounted for in the model using the blowing parameter defined in [93] to calculate the modified Stanton number in equation 5.40, blowing parameter is calculated using equation 5.41.

$$St_b = St\frac{b_h}{exp\,(b_h) - 1} \tag{5.40}$$

$$b_h = \frac{\dot{m}'_{cd}}{\dot{m}'_b St} = -\frac{JaNu_{cd}}{StPr_bRe_b}\frac{Nu_f}{Nu_f + (Nu_{cv} + Nu_{cd})\,\frac{k_b}{k_f}} \tag{5.41}$$

$$Ja = \frac{C_{p,b}\,(T_b - T_{w,h})}{\Delta H_v} \tag{5.42}$$

Both condensation and convection Stanton numbers are corrected for blowing effects and revised Nusselt numbers are obtained. A second correction is then made to account for increased heat transfer close to the tube inlet due to the establishing boundary layer, the empirical method of Bonilla has been used, shown in equation 5.43 [93].

$$Nu_e = \begin{cases} 1.5\left(\dfrac{x}{d_h}\right)^{-0.16} Nu & \text{if } \dfrac{x}{d_h} < 12 \\ Nu & \text{if } \dfrac{x}{d_h} \geq 12 \end{cases} \tag{5.43}$$

Using the condensation and convection Nusselt numbers corrected for blowing and entrance effects, the corrected heat transfer coefficients are found using equation 5.39. This is combined with the film thermal resistance to give the overall hot side heat transfer coefficient which will be used in section 5.4.4.

In certain operating conditions such as a high wall temperature or low bulk humidity the mass fraction of vapour at the interface (assuming saturation) may be higher than the mass fraction of vapour in the bulk. In such circumstances the bulk gas is said to be superheated and condensation will not occur until either the bulk or wall temperature is reduced. Heat transfer in a superheated section occurs directly between the bulk flow and hot wall since there is no condensation or film layer interface. Convective heat transfer coefficient is determined using equations 5.33 and 5.39 with friction factor for a smooth pipe. Blowing effects are not present during sensible heat transfer but the correction for entrance effects are still considered. Hot side heat transfer is then calculated using equation 5.44.

$$q_t{}' = h_{cv}\,(T_{bulk} - T_{wall,h}) \tag{5.44}$$

5.4.2 Cold side

Cold side heat transfer coefficient is found using the same method as the liquid cooled radiator discussed in section 5.2.2. Colburn factor is determined using the empirical method of [84] and fin efficiency considered using equation 5.7. The cold side heat transfer coefficient and fin efficiency are used in section 5.4.4 to find the overall heat transfer.

5.4.3 Pressure loss

Hot side pressure loss in each section is determined from the friction factor calculated in equation 5.38 (equation 5.36/5.37 if superheated). The pressure loss gradient is found using equation 5.45. This method does not consider two phase pressure loss behaviour, however existing two phase pressure drop prediction methods suitable for this application are unreliable [72], and given the small section length it is reasonable to assume single phase flow for the prediction of pressure loss.

$$\frac{dP}{dx} = \frac{f_i \rho_b V_b^2}{2\left(d_{h,h} - 2\delta\right)} \tag{5.45}$$

5.4.4 Heat transfer

With both hot and cold side heat transfer coefficients known from sections 5.4.1 and 5.4.2 respectively, the overall heat transfer coefficient is found using equation 5.46 where $r_{h,h}$ is the hot side hydraulic radius.

$$UA_n = \left(\frac{1}{\left(h_{cd} + h_{cv}\right) \pi d_{h,h} L} + \frac{\ln\left(\frac{r_{h,h}}{r_{h,h} - \delta}\right)}{2\pi L k_f} + \frac{\ln\left(\frac{r_{h,h} + T_t}{r_{h,h}}\right)}{2\pi L k_{tube}} + \frac{1}{\eta_{fin} h_{air} A_{cell}} \right)^{-1} \tag{5.46}$$

Overall heat transfer is then found using equation 5.47, from which the hot and cold side wall temperatures can be found from equations 5.48 and 5.49 respectively.

$$q_t = UA_n \left(T_b - T_a\right) \tag{5.47}$$

$$T_{w,h} = T_i - \frac{q_t \ln\left(\frac{r_{h,h}}{r_{h,h} - \delta}\right)}{2\pi L k_f} \tag{5.48}$$

$$T_{w,c} = T_{w,h} - \frac{q_t \ln\left(\frac{r_{h,h} + t_t}{r_{h,h}}\right)}{2\pi L k_{tube}} \tag{5.49}$$

If condensation has occurred, heat transfer through the condensate film (equation 5.50) can be compared to heat transfer between the bulk and interface (equation 5.51). Equations 5.50 and 5.51 should be equal since heat cannot accumulate at the interface, if this is not the case a new interface temperature should be calculated using equation 5.52 and equations 5.22 through 5.51 repeated until $|1 - q_f{}'/q_b{}'| \leq 10^{-5}$ at which point the solution is deemed to have converged.

$$q_f{}' = h_f \left(T_i - T_{w,h}\right) \tag{5.50}$$

$$q_b{}' = \left(h_{cd} + h_{cv}\right)\left(T_b - T_i\right) \tag{5.51}$$

$$T_i = T_{w,h} + \frac{q_b}{h_f} \tag{5.52}$$

In the case that the bulk fluid is superheated and no condensation occurs then iteration occurs to find the correct wall temperature comparing heat transfer between the bulk and wall to heat transfer across the tube wall.

5.4.5 Exit conditions

Once the total heat transfer for a section is known, the hot side exit properties are calculated. The calculation procedure is different depending on if the bulk mixture is saturated at the exit.

In the case where the bulk flow is not saturated yet condensation still occurs due to saturation at the tube wall, mass and energy balance is used to obtain the bulk exit temperature. Using the derivation from inlet and outlet enthalpies in [92], modified for reduced variable oxygen concentration, the hot side exit temperature is found using equation 5.53. Where n refers to the condenser section and q_{gas} refers to the sensible heat transfer from the bulk to the interface (i.e. calculated using only h_{cv}).

$$T_{b,n+1} = \frac{\left(\dot{m}_{N_2} C_{p,N_2} + \dot{m}_{O_2} C_{p,O_2} + \dot{m}_{v,n} C_{p,v}\right) T_{b,n} - q_{gas} - \dot{m}_{cd} C_{p,v} T_{i,n}}{\dot{m}_{N_2} C_{p,N_2} + \dot{m}_{O_2} C_{p,O_2} + \dot{m}_{v,n+1} C_{p,n}} \tag{5.53}$$

$$q_{gas} = h_{cv}\pi d_{h,h}L\left(T_{b,n} - T_{i,n}\right) \tag{5.54}$$

$$\dot{m}_{cd} = -G\frac{W_{v,i} - W_{v,b}}{1 - W_{v,i}}\pi d_{h,h}L \tag{5.55}$$

$$\dot{m}_{v,n+1} = \dot{m}_{v,n} - \dot{m}_{cd} \tag{5.56}$$

$$\dot{m}_{l,n+1} = \dot{m}_{l,n} + \dot{m}_{cd} \tag{5.57}$$

$$\dot{m}_{N_2,n+1} = \dot{m}_{N_2,n} \tag{5.58}$$

$$\dot{m}_{O_2,n+1} = \dot{m}_{O_2,n} \tag{5.59}$$

The above method does not consider the upper limit placed on vapour flow due to saturation which can lead to relative humidities greater than 100%. For saturated flow an alternative method is used based on the flow enthalpy at saturation. When saturated, the enthalpy of the hot side flow can be found using equations 5.60 to 5.62. For a given inlet flow rate of nitrogen, oxygen, vapour and liquid water the enthalpy is a function of pressure and temperature, this is used to create a two dimensional map of enthalpy for the given inlet conditions for each combination of possible pressure and temperature.

$$\dot{m}_{v,max} = \frac{M_{H_2O}}{M_{nc}}\frac{P_{sat}}{P_b - P_{sat}}\left(\dot{m}_{N_2} + \dot{m}_{O_2}\right) \tag{5.60}$$

$$\dot{m}_l = \dot{m}_{l,in} + \left(\dot{m}_{v,in} - \dot{m}_{v,max}\right) \tag{5.61}$$

$$H_h = f\left(T,P\right) = \left(\dot{m}_{N_2}C_{p,N_2} + \dot{m}_{O_2}C_{p,O_2} + \dot{m}_l C_{p,l}\right)\left(T - T_0\right) + \dot{m}_{v,max}\left(\Delta H_v + C_{p,v}\left(T - T_0\right)\right) \tag{5.62}$$

If the hot side inlet enthalpy, and heat transfer are known, the exit enthalpy can be found from equation 5.63. From knowledge of the exit pressure the hot side exit temperature associated to the exit enthalpy is then found from equation 5.62. The exit mass flow rates associated to the calculated exit pressure and temperature are then found from interpolation of the two dimensional enthalpy map.

$$H_{out} = H_{in} - q_t \tag{5.63}$$

5.4.6 Computation

The model is computed using MATLAB and can be embedded into the fuel cell vehicle model proposed in section 3. A flow chart detailing the calculation procedure of determining heat transfer is shown in figure 5.7.

5.4.7 Validation

There is no experimental data available in the literature for a cross-flow louvred fin radiator with a condensing hot side in the presence of a non-condensable gas, therefore the hot and cold sides have been validated separately. Krishnaswamy *et al.* [92] conducted tests on condensation from air-water vapour mixtures across a range of relative humidities (including wall superheating) in a non-circular tube with dimensions representative of those seen in automotive radiators. The tube was horizontal with annular counterflow of liquid coolant. Inlet conditions and wall temperature along the length of the tube was measured and an exponential curve fitted. Comparison of the proposed model to the experimental results of Krishnaswamy *et al.* shows a mean absolute heat transfer error of 10.1% and condensate flow error of 8.2% across 19 experimental tests. A comparison of measured and predicted heat transfer and condensate rates is shown in figure 5.8. Some of the contribution towards the error is likely due to the estimation of the cold side heat transfer coefficient.

The cold side correlation was obtained by [84] using a set of 91 different radiator geometries. Mean deviation between the Colburn factor estimated by the correlation and measured by experiment was 7.55% with 89.28% of the results fitting within ±15% deviation. The correlation has been extensively used and compared to experimental heat transfer data of radiators from other sources [82]. The model has been simulated for liquid coolant hot side and compared to the experimental heat transfer of [82], giving an average error of less than 5% across a variety of coolant and air flow rates.

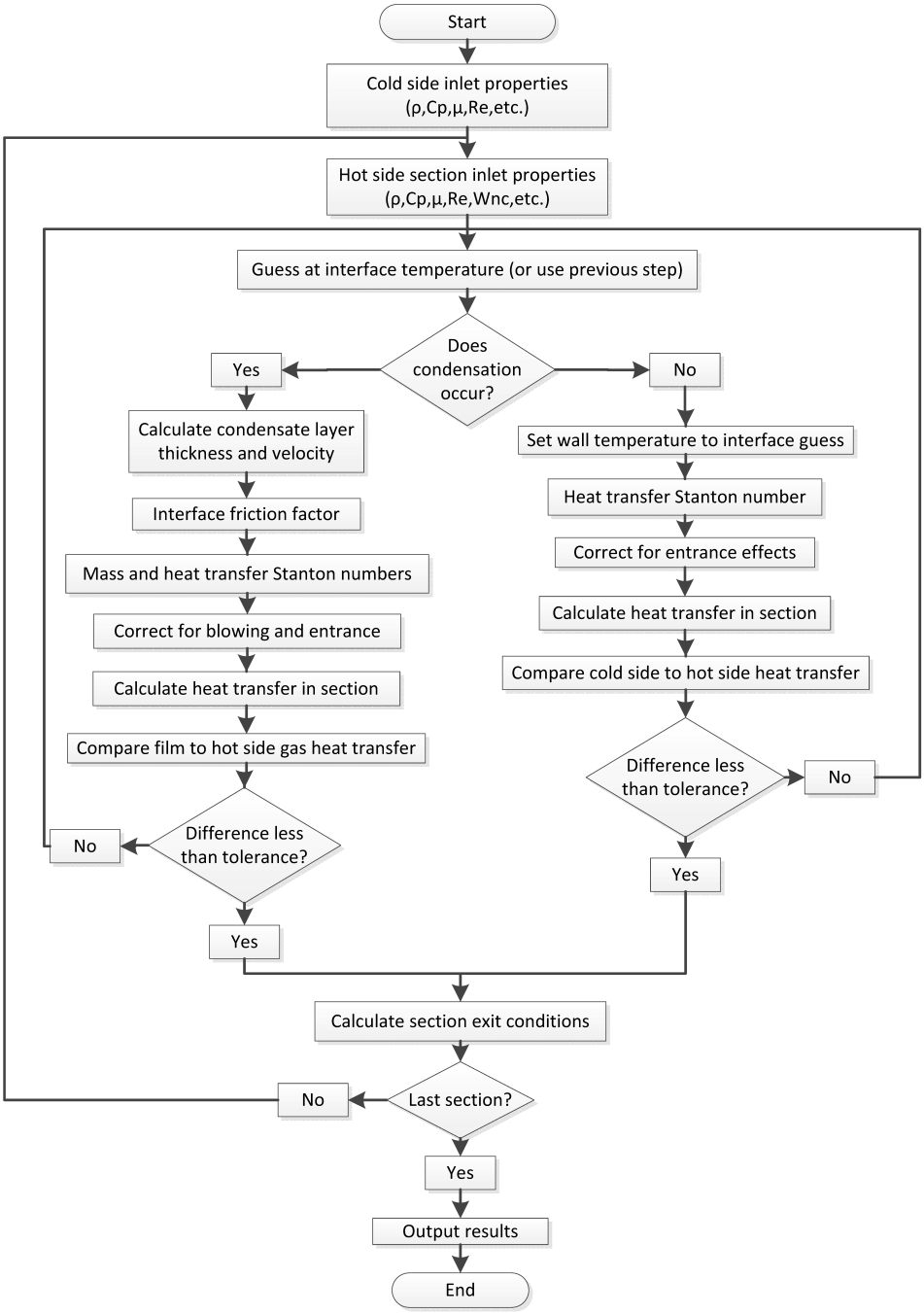

Figure 5.7: Condenser model flow chart

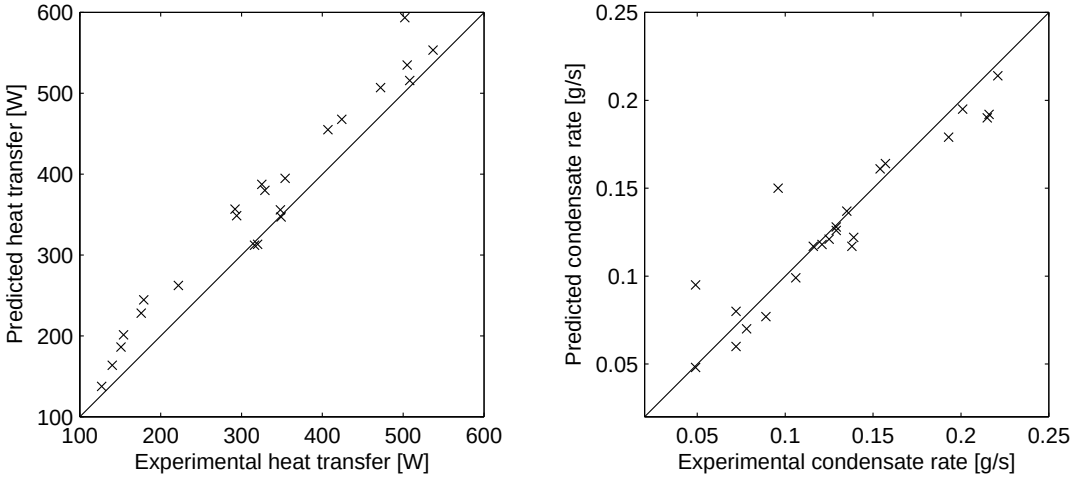

(a) Measured vs. predicted heat transfer

(b) Measured vs. predicted heat transfer

Figure 5.8: Comparison of condensing radiator model results with experimental work of Krishnaswamy *et al.* [92]

5.5 Compact plate condenser testing

The evaporatively cooled fuel cell layout with the intermediate cooling loop, shown in figure 2.8, requires a heat exchanger to transfer the thermal energy of the cathode exhaust to the vehicle cooling loop. Compact plate heat exchangers are suitable for such an application due to having a high volume to heat transfer area ratio and being commonly manufactured from materials compatible for use with de-ionised water. A compact plate heat exchanger consists of multiple pressed plates stacked on top of one another, the plates often have chevron or 'herringbone' patterns within the pressing to both control the plate spacing and promote turbulent flow. The hot and cold side fluids pass through the channels between alternating plates giving a high heat transfer area in a small volume.

Single phase heat transfer, pure condensation and pure evaporation in compact plate heat exchangers have all received significant attention in the literature. Numerous single phase heat transfer correlations for different geometries and flow conditions have been produced, a review of 28 such correlations for Nusselt number and pressure drop was provided by Ayub [95]. Because of their applications in the process and refrigerant industries many two-phase correlations for compact plate heat exchangers also exist. Longo *et.al* [96] produced correlations for both condensation and evaporation of R-22 in compact plate heat exchangers with varying amounts of surface enhancement. Han *et.al* [97] conducted experiments on the condensation heat transfer coefficient of refrigerants R410A and R22 under different plate

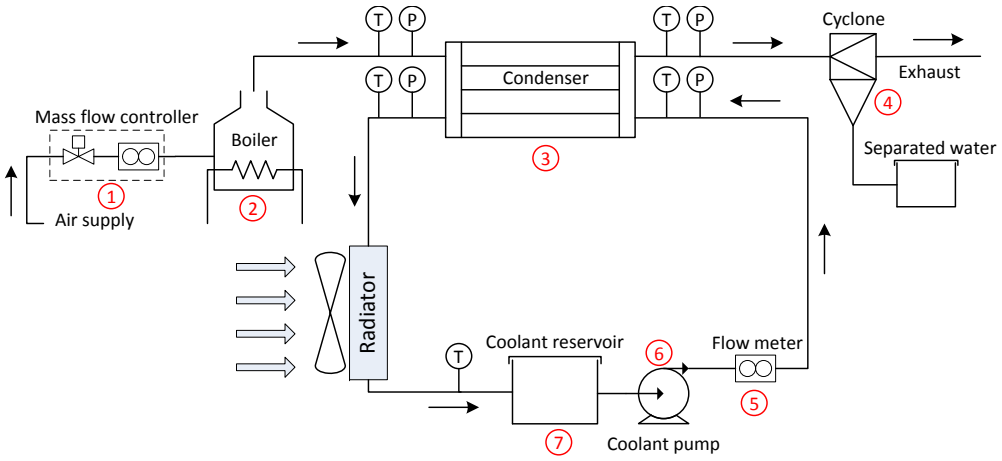

Figure 5.9: Experimental set-up diagram

chevron angles, whilst Yan *et al.* [98] produced a correlation for R-134a. A comparison of five different correlations, including the ones of [97] and [98] can be found in [99]. However, limited information is available on condensation with non-condensable gas present in compact plate heat exchangers. Both Chang and Huang [100] and Vlasogiannis *et al.* [101] used visualisation techniques to study air/water flow regimes in compact plate heat exchangers, however, neither considered the effects of condensation.

Based on the existing gaps in the literature, and the need for a validated heat exchanger model, an experimental set-up was produced to study the influence of non-condensable gas on condensation inside compact plate heat exchangers. With specific focus given to the conditions typically seen in a PEM fuel cell exhaust.

5.5.1 Experimental set-up

A diagram of the experimental set-up is shown in figure 5.9. The cold side closed loop consists of a variable speed coolant pump, paddle flow meter, inlet and outlet pressure and temperature measurements and a radiator with variable fan speed. The hot side open loop consists of compressed air from a building supply regulated using a mass flow controller (0-200 slpm). The air is then bubbled through a 3kW electric boiler with variable power supply before entering the condenser, a cyclone is used post condenser to separate and measure condensate flow rate. A picture of the experimental rig is shown in figure 5.10 with key visible components numbered with respect to figure 5.9.

The condenser used in the tests was a SWEP M10 gasketed compact plate heat exchanger,

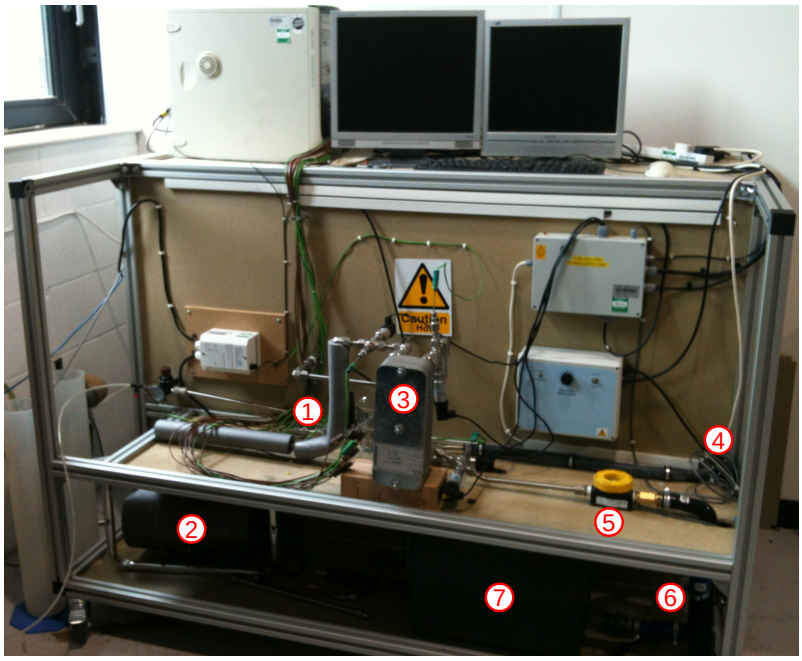

Figure 5.10: Experimental rig photo

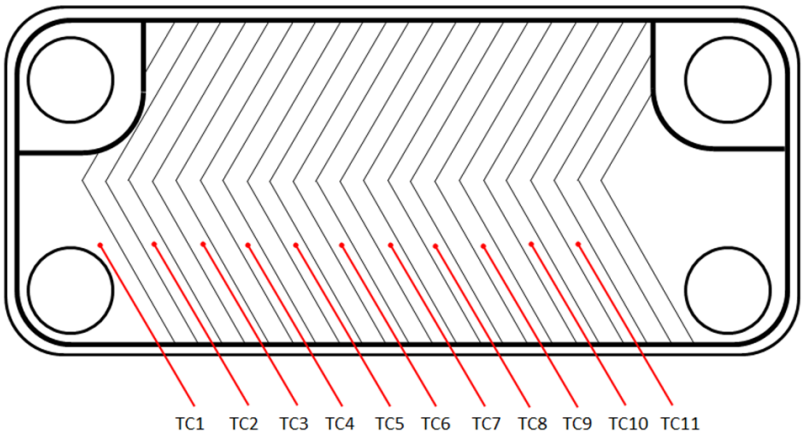

Figure 5.11: Hot side thermocouple positions

with external plate dimensions 116x287mm, 2mm pressing depth and a 22° chevron angle. Unless otherwise specified all tests were conducted with one hot side and one cold side plate, connected in a counterflow arrangement. Since the vapour quality and mass fraction of non-condensable gas will vary considerably with temperature inside the condenser, eleven type-T thermocouples were placed in the hot side plate, attached with silicon sealant to measure fluid bulk temperature. Figure 5.11 shows the location of the thermocouples within the hot plate.

Both data capture and system control were achieved using a LabVIEW compact Field-Point data logger, variation to boiler power allowed condenser inlet temperature to be controlled within ±0.5°C. The system was then run until a steady-state was achieved, at which point condensate flow rate samples were taken. A list of key components used and a detailed experimental procedure is shown in appendix B, a copy of the LabVIEW data acquisition file used is available on request.

5.5.2 Results

After commissioning, initial tests were run with a liquid to liquid set up using mains water supply to first establish a correlation for single phase heat transfer. Once the cold side correlation was obtained (section 5.5.3), the layout was reverted back to that shown in figure 5.9 with the vapour/air hot side. Multiple runs were conducted, varying inlet air flow rate between 10-130 slpm and the saturated air inlet temperature between 70-95°C, this provided non-condensable mass fractions ranging from 0.40-0.97. For each test run the heat exchanger was allowed to reach steady state then values were averaged over a 90 second period, during which time the separated liquid condensate was collected. Collected liquid condensate was compared to that predicted from the measured temperatures and air flow rates assuming saturation. Cold side heat transfer was obtained from coolant flow rate and temperature change, this was compared to hot side heat transfer predicted from a saturated inlet. Results which showed good correlation between both measured and predicted condensate flow and hot to cold side heat transfer ratio (>90%) were used in the analysis. Measurements with higher errors occurred either at low air flow rates or low overall heat transfer where the thermocouple accuracy had a significant influence on the predicted heat transfer and condensate rates.

5.5.3 Cold side correlation

The modified Wilson plot, described in [102], has been used to obtain the cold side heat transfer correlation, since the wall temperature is not known. Based on similar correlations

for compact plate condensers and the Dittus-Boelter correlation for turbulent flow in smooth tubes, power coefficients of 4/5 and 1/3 were chosen for the Reynolds and Prandtl numbers respectively. Giving the relationship of equation 5.64, where C_1 is the coefficient to be determined from the modified Wilson plot.

$$h_c = C_1 Re^{4/5} Pr^{1/3} \tag{5.64}$$

Data from 16 sets of time averaged steady state experimental data for liquid to liquid heat transfer were used to obtain the correlation, varying only the cold side flow rate. Overall thermal resistance was calculated from the measured heat transfer and log mean temperature difference and plotted against the inverse of equation 5.64 with constant C_1 removed. The corresponding Wilson plot and linear regression fit can be seen in figure 5.12, where constant C_1 is equal to the inverse of the gradient (16.15).

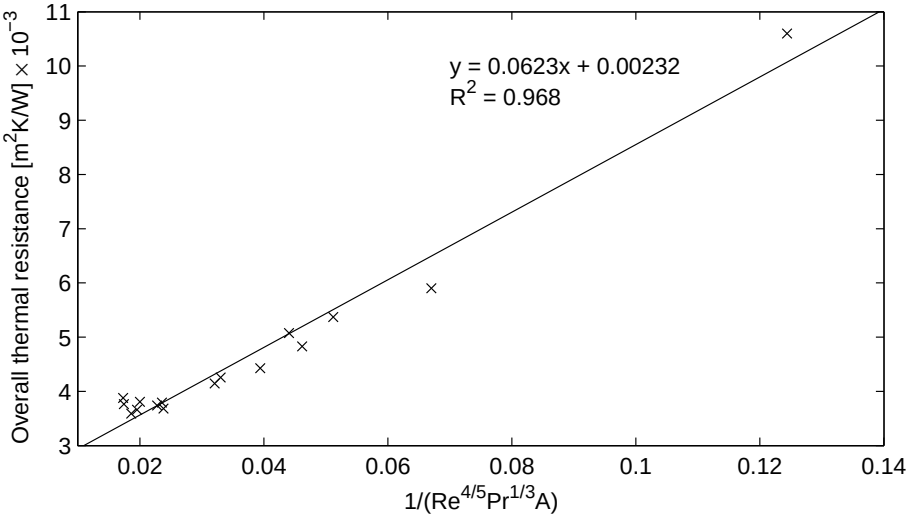

Figure 5.12: Modified Wilson plot for liquid/liquid heat transfer

The Wilson plot provides a correlation for the heat transfer coefficient, however it is more desirable for the correlation to be in the non-dimensionalised Nusselt number form. This can be achieved using equation 5.65 where thermal conductivity evaluated at the mean water temperature.

$$Nu \equiv \frac{h d_h}{k} \tag{5.65}$$

The final form of the cold side Nusselt correlation is given in equation 5.66. A comparison to other correlations in the literature for compact plate heat exchangers, detailed in [95], is shown in figure 5.13, demonstrating good agreement. The increase in Nusselt number

compared to a smooth tube (Dittus-Boelter) can also be seen. The variation between the different compact plate correlations is likely due to the difference in geometries between the heat exchanger where the correlation was originally obtained and the current heat exchanger. For example, the correlation of Wanniarachchi, which shows the largest discrepancy from the experimental work, does not consider how the change in chevron angle influences the Nusselt number. Further geometry variations such as the plate aspect ratio and pressing depth which will also influence the Nusselt number are not considered by the existing correlations, contributing to the differences seen in figure 5.13.

$$Nu = 0.103 Re^{4/5} Pr^{1/3} \tag{5.66}$$

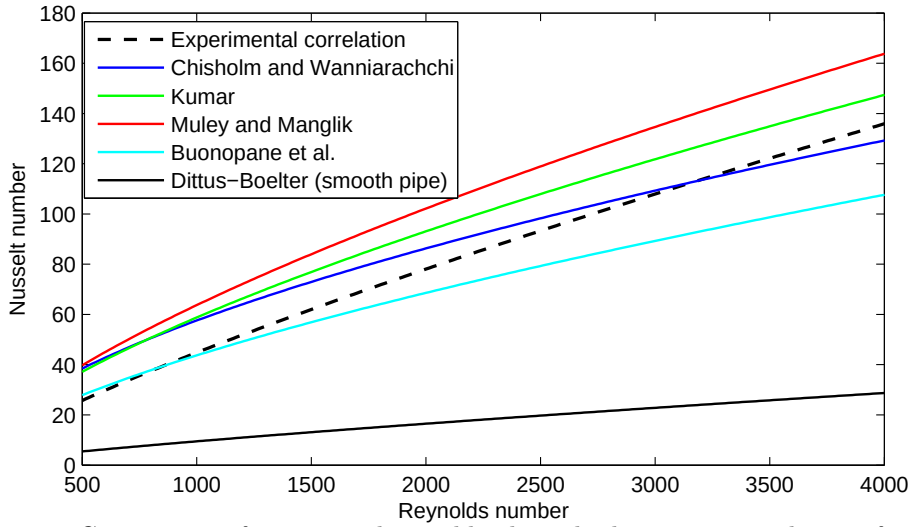

Figure 5.13: Comparison of compact plate cold side with alternative correlations from [95]

5.5.4 Hot side correlation

During the vapour/air experiments variations were observed in the measured temperature profiles, this is because of complex flow distribution within the plate and small hydraulic diameter relative to the size of the thermocouple. To allow for a more reliable calculation of the hot side heat transfer profile a second order polynomial was fitted to the experimental data, shown in figure 5.14 for a 95°C hot side inlet test. Across all the tests conducted the mean coefficient of determination across all polynomial fits was 95.3%.

It was assumed that the hot side inlet was saturated in all cases, this assumption was validated by comparing the hot side heat transfer assuming saturation to the measured cold

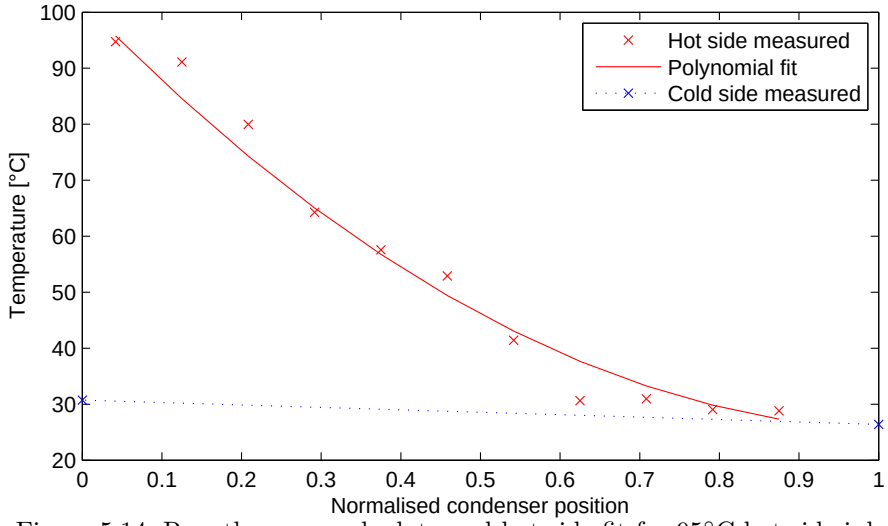

Figure 5.14: Raw thermocouple data and hot side fit for 95°C hot side inlet

side heat transfer, good agreement was seen across all tests. Based on the hot side flow rate into the condenser with known pressure, the enthalpy and flow composition at each point in the condenser can be found from the temperature. The enthalpy change between two points is equal to the heat transferred from the hot side to the cold side. Splitting the condenser into ten sections, the heat transfer profile is used to calculate the cold side temperature profile between inlet and outlet. Using the correlation of equation 5.66, the wall temperatures can then be determined, from which the hot side heat transfer coefficient is found using equation 5.67. Fluid temperature at this point is taken from the centre of the section.

$$h_h = \frac{\dot{Q}}{A\left(T_h - T_w\right)} \tag{5.67}$$

Viscosity of the air/vapour mixture is found using the method of Wilke described in [103], which in turn is used to establish the gas mixture Reynolds number at each test section in the condenser, which was seen to range between 300-4000 for the flow rates studied. Heat transfer coefficient was seen to increase with Reynolds number and decrease with increasing non-condensable mass fraction (figure 5.15), showing the same qualitative trends observed by [87] and [89] except at higher non-condensable mass fractions. An experimental correlation for the heat transfer coefficient was determined from a non-linear least squares fit, shown in Equation 5.68. Figure 5.16 compares predicted to measured heat transfer coefficient.

$$h_h = 66.67 Re^{0.76} \left(1 - W_{nc}\right)^{0.80} \tag{5.68}$$
$$300 < Re < 4000$$
$$0.4 < W_{nc} < 0.97$$

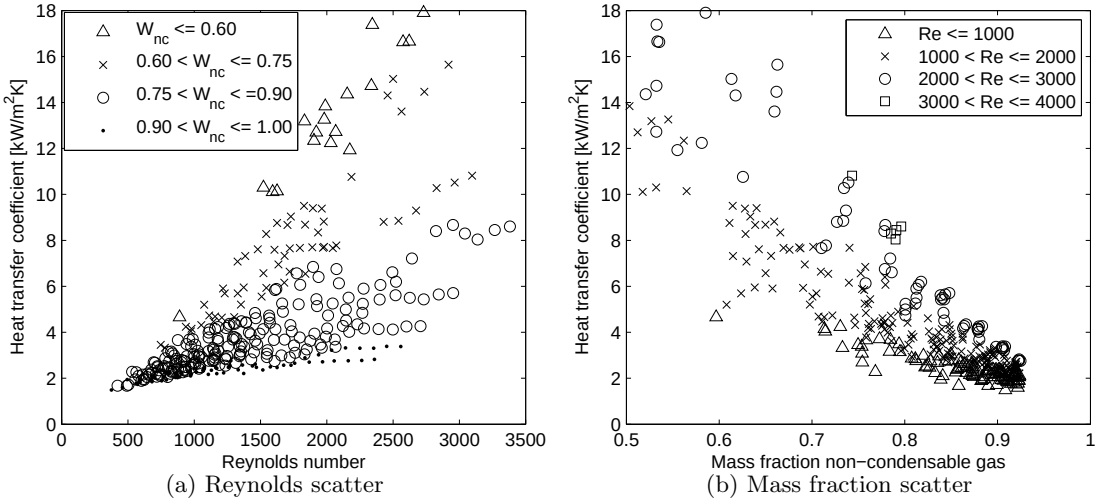

(a) Reynolds scatter (b) Mass fraction scatter

Figure 5.15: Experimental heat transfer coefficients

The measured heat transfer coefficients are significantly higher than those predicted using the Nusselt correlations of figure 5.13 for single phase flow due to the presence of phase change. Comparison of the correlation in equation 5.68 to the correlation obtained by Vierow and Schrock [89] (equation 5.17), which was derived for annular pipe flow at lower non-condensable mass fractions, is shown in figure 5.17. Hot side inlet temperature and pressure are fixed at 80°C 1.2bar.a, the saturated air flow rate is varied to give different Reynolds numbers. It can be seen that as Reynolds number increases the deviation from the pipe flow correlation also increases, the heat transfer coefficient predicted by the current study was up to 4.7 times greater than that predicted for smooth pipe flow. This would suggest the enhanced turbulence of the chevron flow pattern is reducing the build up of a non-condensable boundary layer, leading to reduced mass transfer resistance and increased heat transfer coefficients. At higher Reynolds numbers the discrepancy between the Vierow and Schrock correlation and the correlation from the present work is similar to the degradation factor ($a \times Re^b \times W_{nc}^c$) in equation 5.17 and the heat transfer coefficient approaches that predicted for pure Nusselt condensation.

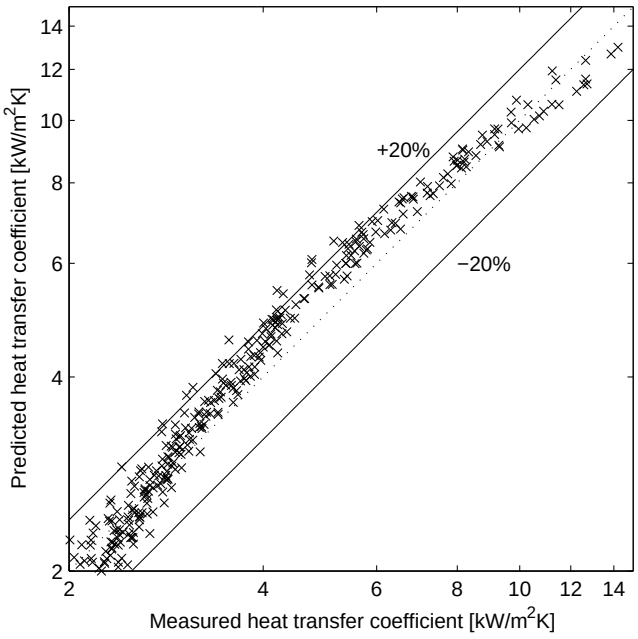

Figure 5.16: Measured vs. predicted heat transfer coefficients

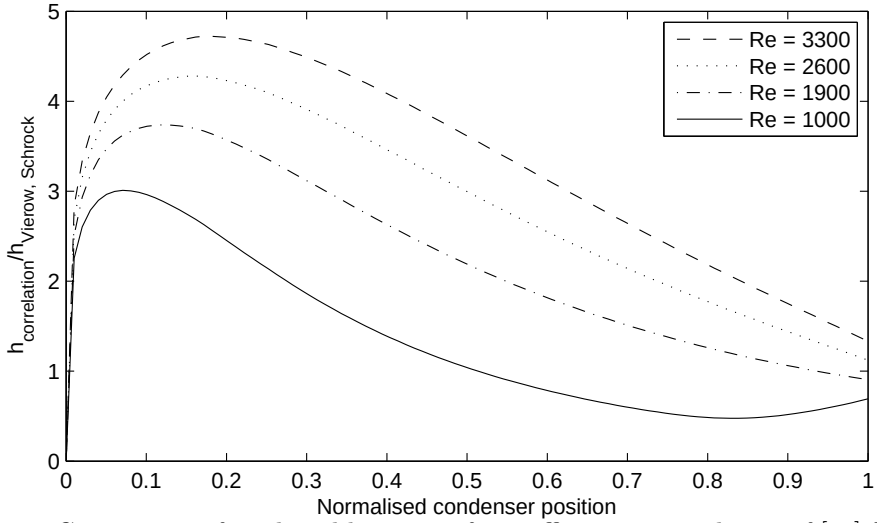

Figure 5.17: Comparison of predicted heat transfer coefficient to correlation of [89] for 80°C inlet

5.6 Compact plate condenser model

Based on the correlations developed in section 5.5, a simplified model has been developed to predict condensation in compact plate heat exchangers with high mass fractions of non-condensable gases present. The model also accounts for variations in the composition of air, so is suitable for fuel cell cathode exhausts where the oxygen content is reduced. Hot side inputs are mass flows of each species, temperature and pressure, cold side inputs are mass flow rate and temperature. To consider the non linear variation of heat transfer coefficient throughout the heat exchanger due to condensation in the hot side, the model is separated into multiple sections so that temperature change between sections can be assumed linear; fluid properties and heat transfer are evaluated separately for each section and outlet conditions are found from mass and energy balances. Heat transfer is calculated using the effectiveness number of transfer units (ϵ-NTU) method.

Hot side heat transfer coefficient is determined from equation 5.68. Whilst this method does not consider the physical phenomena of a non-condensable boundary layer and associated interface properties, it does provide a simple method to predict heat transfer without having to address the flow behaviour between the plates of the heat exchanger. Non-condensable gas mass fraction is expressed using equation 5.69, where the saturated mass flow rate of water vapour is found using equation 5.70, where M_{nc} is the molar mass of the de-oxygenated air stream.

$$W_{nc} = \frac{\dot{m}_{O_2} + \dot{m}_{N_2}}{\dot{m}_{O_2} + \dot{m}_{N_2} + \dot{m}_{H_2Ov}} \tag{5.69}$$

$$\dot{m}_{H_2Ov} = \frac{P_{sat}}{P_h - P_{sat}} \frac{M_{H_2O}}{M_{nc}} \left(\dot{m}_{N_2} + \dot{m}_{O_2}\right) \tag{5.70}$$

$$M_{nc} = \frac{\dot{m}_{N_2} + \dot{m}_{O_2}}{\frac{\dot{m}_{O_2}}{M_{O_2}} + \frac{\dot{m}_{N_2}}{M_{N_2}}} \tag{5.71}$$

To obtain the number of transfer units and exit temperatures, the heat capacity of the hot side must be known. For sensible heat transfer this is the product of mass flow rate and specific heat, whereas for pure phase change the heat capacity is infinite since no temperature change occurs. For a combination of both sensible and latent heat transfer an effective heat capacity has been used, which is defined as the enthalpy change for a specified drop in temperature ΔT.

From knowledge of the hot side inlet conditions it is possible to express the enthalpy as a function of temperature, shown in equation 5.72 where the water mass flow composition,

specific heats and enthalpy of vapourisation are also functions of temperature. By evaluating this function the heat transfer required for a specified temperature drop can be found. Provided the heat transfer and temperature drop across each discreatized section remains small, it is reasonable to assume the effective heat capacity remains constant for each section. Should the flow not be saturated in a section, the mass flow of water will remain unchanged causing the latent heat contributions of equation 5.73 to cancel and return to conventional, sensible heat capacity.

$$H_h(T) = \left(\dot{m}_{O_2} C_{pO_2}(T) + \dot{m}_{N_2} C_{pN_2}(T) + \dot{m}_{H_2Ol}(T) C_{p,H_2Ol}(T)\right)(T - T_0) + \dot{m}_{H_2Ov}(T)\left(C_{p,H_2Ov}(T)(T - T_0) + \Delta H_v(T)\right) \quad (5.72)$$

$$C_h(T_h) = \frac{H_h(T_h) - H_h(T_h - \Delta T)}{\Delta T} \quad (5.73)$$

Once the heat transfer for a section is known from equation 5.79 the section outlet enthalpy can be determined from 5.74, from which the associated temperature is evaluated from 5.72.

$$H_{h_{out}} = H_{h_{in}} - Q_{sec} \quad (5.74)$$

Cold side heat transfer coefficient is determined using the Nusselt correlation from equation 5.13, converting to heat transfer coefficient from equation 5.65. Overall heat transfer coefficient for each section is then found using equation 5.75.

$$UA = \frac{A_{sec}}{\frac{1}{h_h} + \frac{t_w}{k_w} + \frac{1}{h_c}} \quad (5.75)$$

Heat exchanger effectiveness is found using the method from Incropera, Dewitt [44] for a counterflow heat exchanger, equation 5.76.

$$\epsilon = \frac{1 - exp\left(-NTU\left(1 - C_r\right)\right)}{1 - C_r exp\left(-NTU\left(1 - C_r\right)\right)} \quad (5.76)$$

$$C_r = \frac{C_{min}}{C_{max}} \quad (5.77)$$

$$NTU = \frac{UA}{C_{min}} \quad (5.78)$$

$$Q_{sec} = \epsilon C_{min} \left(T_{h,i} - T_{c,i}\right) \tag{5.79}$$

Heat transfer in each section is then found using equation 5.79, where $T_{h,i}$ is the section hot side inlet temperature and $T_{c,i}$ is the cold side inlet temperature. Recalling that the heat exchanger is counter flow, the cold side inlet temperature is dependant on the heat transfer which occurs in the next section, which is yet to be calculated. To solve for both hot and cold side temperature profiles the model must iterate. For the first iteration it is assumed that all sections in the cold side have temperature equal to the coolant inlet temperature, heat transfer in each section is then calculated and the new cold side temperature profile evaluated. This process is repeated until the mean temperature difference between the cold side temperature profiles is within a specified tolerance of 0.5°C.

5.6.1 Validation

The model was validated using the test rig described in section 5.5.1 . A set of tests, separate to those used in the correlation fit, were conducted. The hot and cold side inputs were used as the model boundary conditions and the predicted temperature profile compared to the measured profile. The temperature profile predicted by the model, closely matched that observed during the experimental runs. Figure 5.18 compares results for a single run at 80°C inlet. The overall heat transfer predicted by the model was compared to that measured experimentally based on the hot side temperature change, results for all of the tests conducted are shown in figure 5.19. The mean error across the tests was 3.8%, increasing with higher flow rates. Further tests were performed with increased number of plates to observe the influence of heat transfer area on model accuracy. Throughout the tests the model error remained within the mean 3.8% error, demonstrating its suitability for being scaled up with more plates to achieve the thermal load required for evaporatively cooled fuel cell vehicles.

5.7 Liquid water separation

To maintain water balance in an evaporatively cooled fuel cell system the liquid water at the condenser hot side exit is separated from the gas flow, collected and re-used in humidifying the fuel cell stack. The most common method for separating the liquid water from the gas flow is through the use of a cyclone. The liquid and gas mixture is added tangential to a conical container at a velocity suitable for separation to occur, as the cone diameter reduces, the higher density liquid has too much inertia to follow the curvature of the air flow and meets the cyclone wall where gravity forces it out the lower cyclone exit. The less

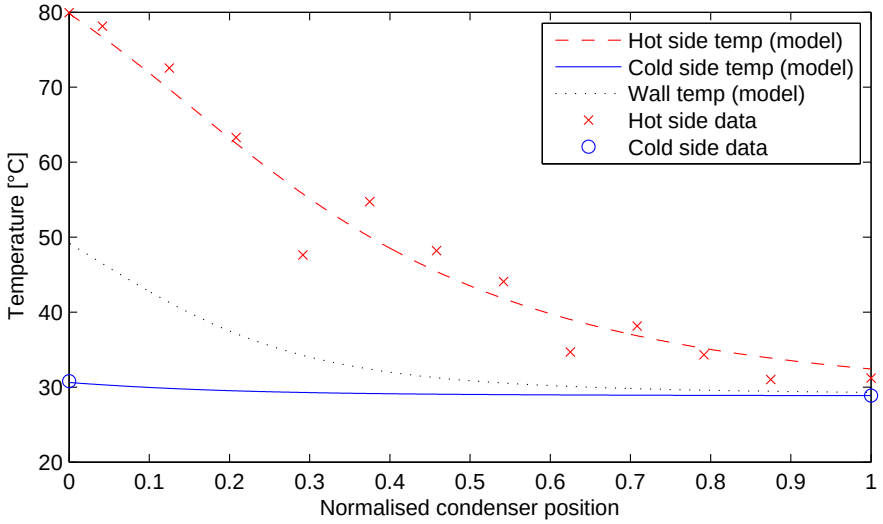

Figure 5.18: Model temperature profile validation

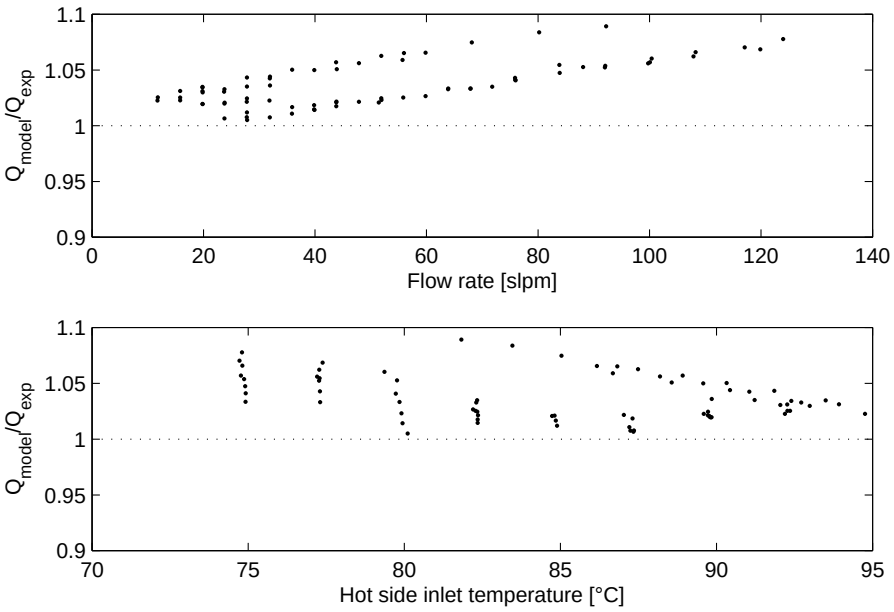

Figure 5.19: Measured vs. predicted heat transfer coefficients

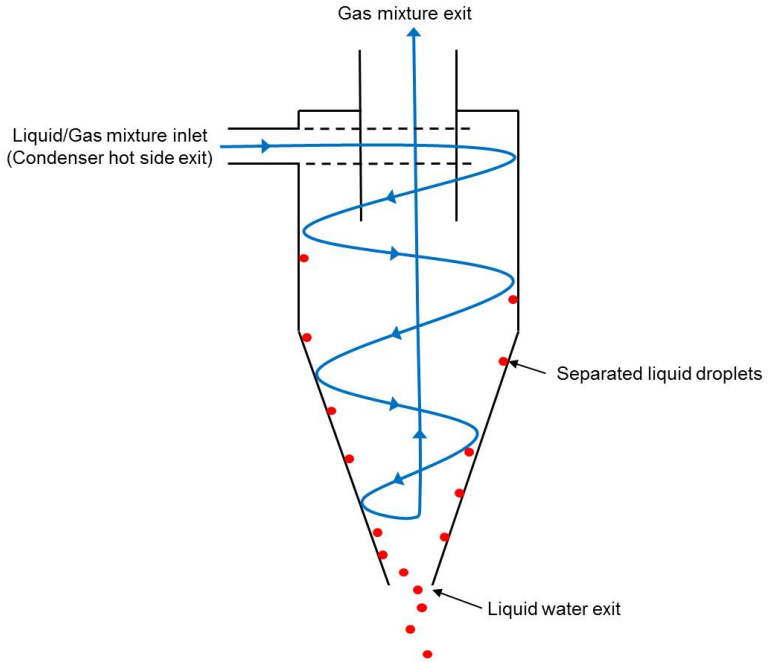

Figure 5.20: Diagram of a cyclone separator

dense gas mixture follows a vortex pattern inside the cyclone and is forced out the upper exit of the cyclone. Figure 5.20 illustrates the operation of a cyclone separator. Numerical models of the fluid behaviour inside cyclones require extensive computational power and are highly dependant on the cyclone geometry and flow conditions [104]. To remove additional complexity in the system modelling of water balance, a constant cyclone efficiency has been used in this work. The separation efficiency (or collection efficiency) refers the the fraction of liquid water which can be separated from the mixture. The separation efficiency of liquid water from saturated air using a cyclone is not extensively documented in the existing literature, Kurokawa and Ohtaki [105] conducted experimental tests on such conditions, demonstrating separation efficiencies in the region of 95.0-99.8%. The influence of variation in separation efficiency on system water balance is discussed in chapter 6.

5.8 Chapter summary

In this chapter, the influence of non-condensable gas on condensation has been discussed, and models have been presented for the condensation of water in the presence of de-oxygenated air. The first condensation model details a radiator, utilising the conventional fin and tube heat exchanger used in automotive radiators, replacing the liquid coolant in the tube with

the air/water vapour mixture. The hot and cold sides of the model have been validated separately using experimental data in the literature. This layout represents the simplest form of evaporatively cooled system where the fuel cell exhaust feeds directly into the vehicle radiator and liquid water collects and the exit. However this method is often not suitable due to the purity requirements of condensed water and thermal loads of other components. In such cases an additional intermediate heat exchanger is required, such as a compact plate condenser.

An additional model of a compact plate condenser with a liquid cold side, air/vapour mixture hot side and chevron flow pattern has also been developed. Due to the complex internal geometry, empirical correlations for the heat transfer coefficients have been used. An experimental set-up was developed and series of tests conducted to obtain the correlations which were used in the model and showed good agreement with experimental results from a separate series of tests.

In the next chapter, the models detailed in this chapter, along with the fuel cell models developed in chapters 3 and 4 are used to quantitatively study water balance in an evaporatively cooled PEM fuel cell vehicle.

Chapter 6

Analysis

6.1 Introduction

In this chapter, the models put forward in the previous chapters are used to analyse the behaviour of an evaporatively cooled fuel cell system. Section 6.2 uses the lumped parameter fuel cell vehicle model from chapter 3, and the heat exchanger models from chapter 5, to study the performance of an evaporatively cooled fuel cell vehicle across steady state and transient conditions. Section 6.5 uses the one dimensional cell model of chapter 4 to study the effects of spatial distribution across a single evaporatively cooled fuel cell.

6.2 Evaporatively cooled fuel cell vehicle model

By combining the models presented in this thesis a thermally oriented model of an evaporatively cooled fuel cell vehicle can be produced which is capable of simulating either the condensing radiator or intermediate cooling loop system architectures presented in section 2. Figures 6.1 and 6.2 illustrate the model architecture and interaction of sub models used to construct the condensing radiator and intermediate cooling loop models respectively. The manifold dynamics, hydrogen supply and water addition are included in the fuel cell section, the numbers refer to the chapter and section of this thesis where the model is described. The models are populated with parameters to represent a typical passenger vehicle powered by a 50kW evaporatively cooled fuel cell stack, 50kW was chosen since it provides sufficient power to achieve common drive cycles and has been commercially demonstrated for an evaporatively cooled system by [49]. A full list of the model parameters is shown in appendix A, key parameters are replicated in table 6.1. Unless otherwise specified, all simulations in

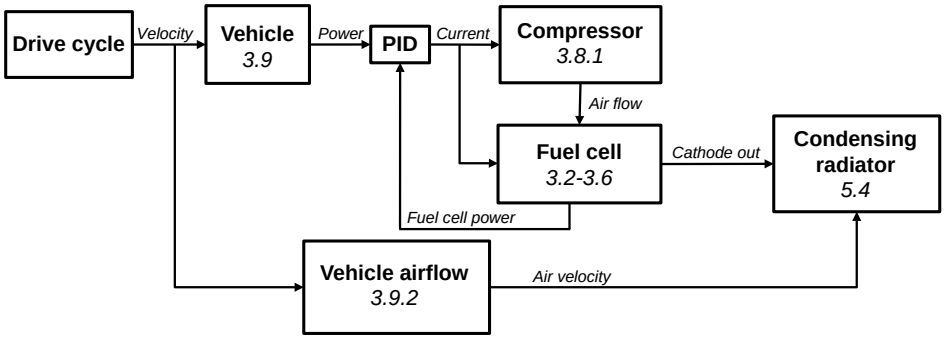

Figure 6.1: Diagram of sub model interaction for evaporatively cooled system with condensing radiator

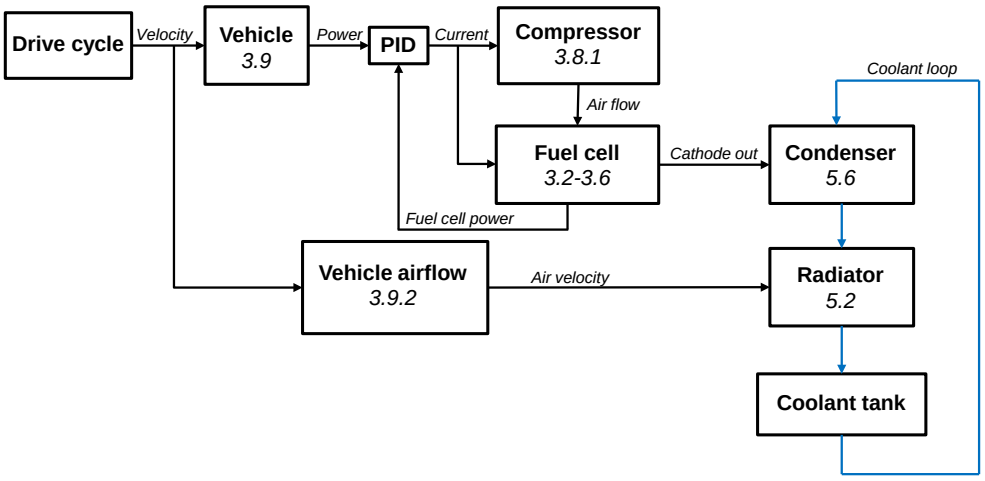

Figure 6.2: Diagram of sub model interaction for evaporatively cooled system with cooling loop

this section use the base operating conditions given in appendix A, electronic copies of the models are available on request.

6.2.1 Temperature

The steady state variation in stack temperature with current density is shown in figures 6.3 and 6.4 for different cathode pressures and stoichiometries respectively. In both cases liquid water is added to the cathode to achieve 100% relative humidity in the exhaust. To maintain a constant stoichiometry, the air flow into the fuel cell increases linearly with current. This also increases the amount of water vapour which can be evaporated within the stack, increasing the potential heat rejection. The direct link between heat generation (through current

Parameter	Value
Fuel cell	
Fuel cell rated power	50kW
Maximum system efficiency (LHV)	56%
System efficiency @ 50% load	50%
Number of cells	360
Cell active area	200cm^2
Membrane thickness (z)	100μm
Cathode stoichiometry	2.5
Anode stoichiometry	1.03
Target cathode humidity	100%
Vehicle	
Vehicle mass (m)	1500kg
Vehicle frontal area (A_f)	2.2m^2
Drag coefficient (C_d)	0.33
Heat exchangers	
Coolant flow rate	60 lpm
Condenser heat transfer area	1.0m^2
Radiator core size	600mm×600mm
Ambient temperature	25°C

Table 6.1: Key parameters used in fuel cell vehicle model (unless otherwise specified)

density) and heat rejection (through air flow rate) means that the temperature increase across the operating range of the fuel cell is small, without the need for active temperature control. For example, the temperature increase between 0.2-1.2A/cm^2 is 3.14°C at 1.1bar.a pressure, 2.5 cathode stoichiometry despite a 731% increase in heat generation.

The increase in temperature with current density across the operating range is caused by the increase in irreversibilities (voltage loss) with current density, giving a non-linear increase in heat generation. Since the exhaust gas flow rate varies linearly with current density (constant stoichiometry), the temperature of the stack must increase to match heat generation to heat rejection. Raising the stack temperature both increases the sensible heat rejection, but more importantly increases the water vapour saturation pressure, allowing more water to be evaporated for the same relative humidity. The non-linear increase in saturation pressure with temperature means that the temperature increase is limited and the evaporatively cooled fuel cell stack will self regulate temperature within reasonable limits, provided humidity is maintained through sufficient liquid water addition.

The observed steeper reduction in stack temperature at low current densities in figures 6.3 and 6.4 are caused by the compressor minimum set-point. At current densities below

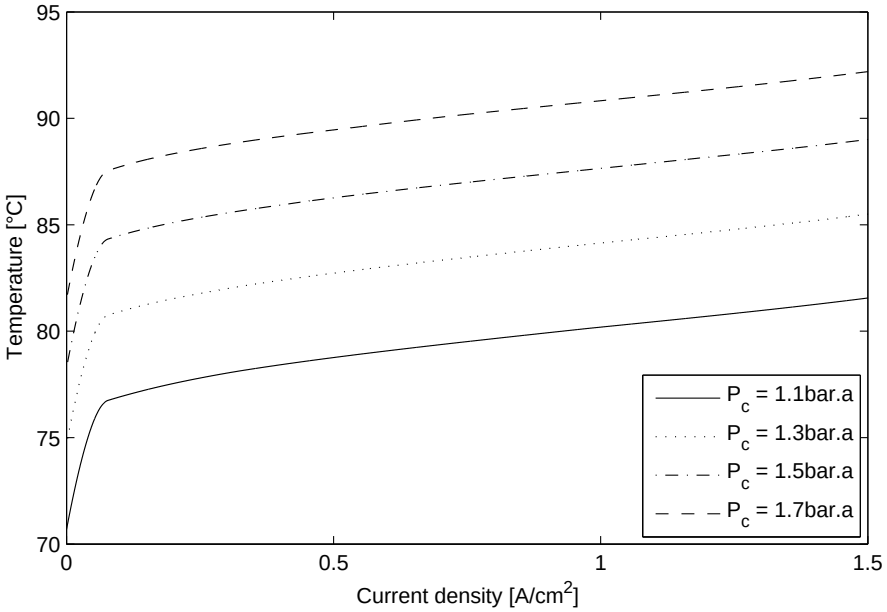

Figure 6.3: Steady state temperature at different pressures ($\Lambda_c = 2.5$)

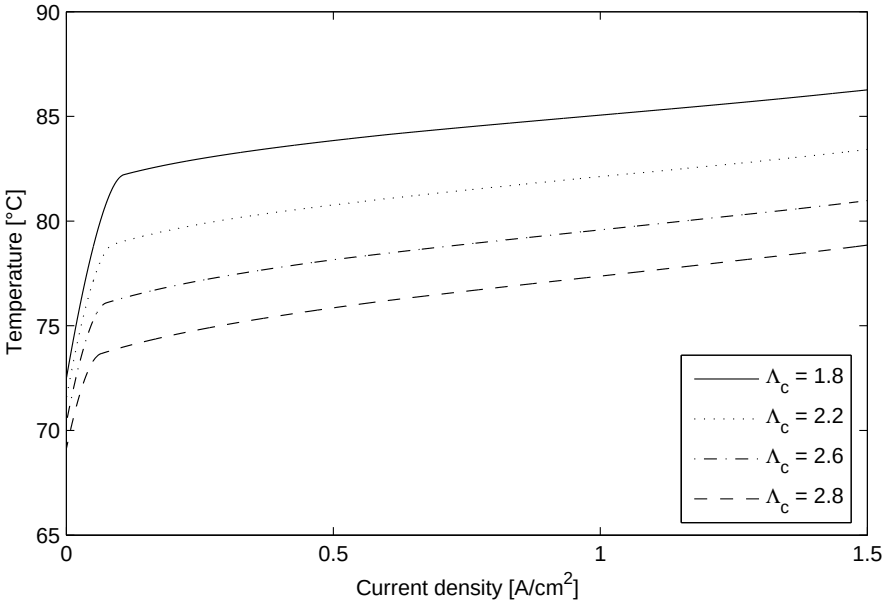

Figure 6.4: Steady state temperature at different stoichiometry ($P_c = 1.2bar.a$)

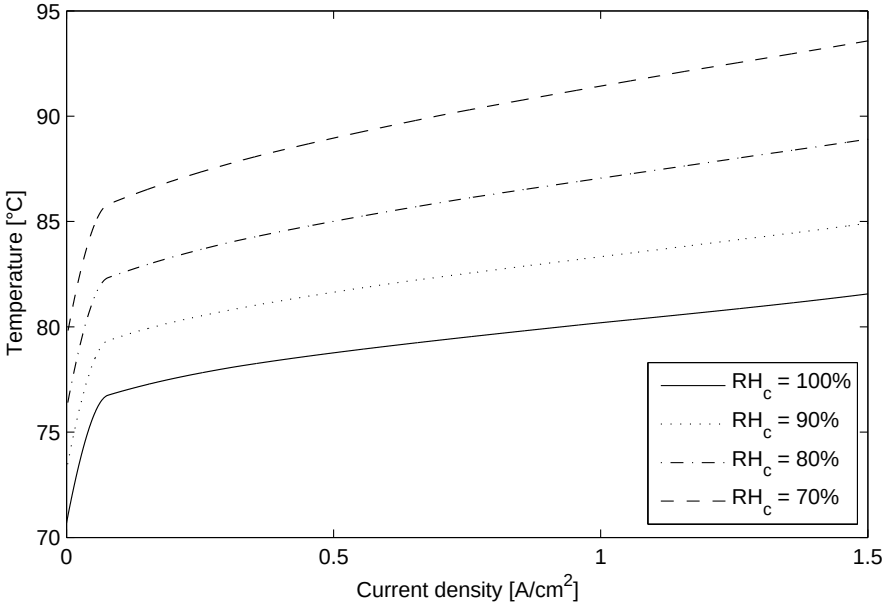

Figure 6.5: Steady state temperature at different target relative humidities

$0.1 A/cm^2$ the compressor cannot continue to maintain the requested stoichiometry since the required airflow rate is outside the operating range of the compressor. Below this value, the minimum compressor flow rate corresponds to an increase in stoichiometry and heat rejection, reducing temperature until the point where heat generation again equals heat rejection.

Figure 6.3 demonstrates that the fuel cell stack operating temperature is elevated at higher pressures. As pressure increases, the mass fraction of water vapour in the exhaust is reduced. To maintain the same rate of evaporation the vapour partial pressure and hence stack temperature must increase. For an evaporatively cooled system the maximum operating pressure will be limited by the operating temperature range of the membrane, whereas in liquid cooled systems higher pressures are possible due to a separate method of heat removal. At higher cathode stoichiometries the stack operating temperature is seen to decrease, shown in figure 6.4. As the air mass flow rate increases, the vapour partial pressure required for thermal balance is reduced and the operating temperature is subsequently lowered.

The influence of cathode relative humidity on steady state stack temperature is shown in figure 6.5, reductions in the relative humidity are seen to increase the operating temperature. This occurs for two reasons, firstly because of the reduction in vapour partial pressure at equal temperature, and secondly because the reduced membrane hydration increases protonic resistance, reducing cell voltage and increasing heat generation. Further reductions in

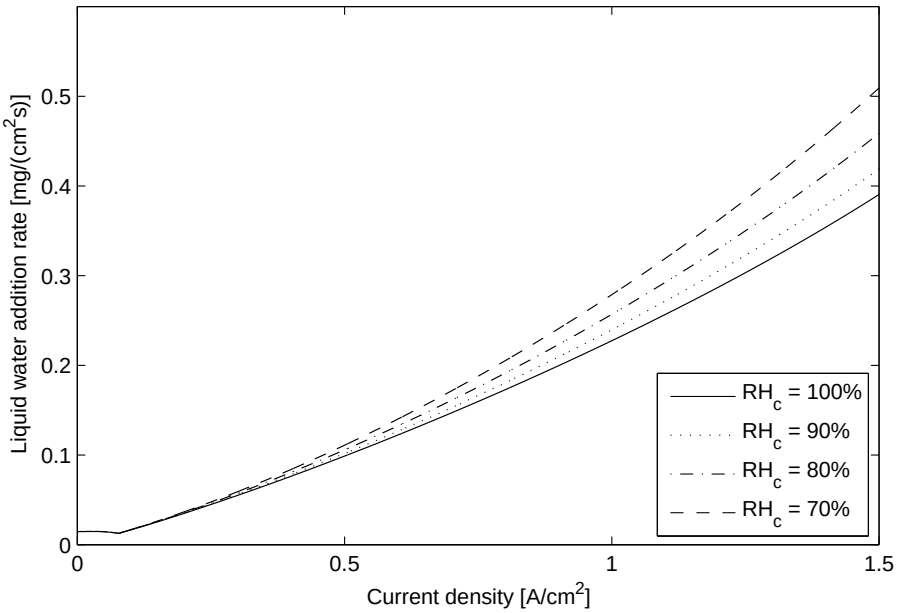

Figure 6.6: Liquid water addition required for thermal balance at different humidities

humidity will likely exceed the operating constraints of the membrane, causing permanent damage to the cell. It is therefore essential that the method of liquid water addition be suitable to maintain the relative humidity within acceptable limits. Figure 6.6 shows the rate of liquid water addition required to maintain thermal balance at different humidities. The least humid case requires the most water addition, whereas the most humid case requires the least water addition. The increase in water addition with a reduction in relative humidity is due to the additional heat generated from the additional membrane resistive losses, demonstrating that water consumption can be minimised through efficient operation.

The model response to a transient step change in current is shown in figure 6.7. Current density is increased from 0.3-0.8A/cm^2 at 250s and later reduced back to the original current density at 550s. The stack temperature is seen to increase by approximately 1.5°C with the increase in current with no overshoot. The temperature increase takes approximately 150s whereas the time to return to the original temperature after the current has been decreased is significantly longer at around 450s. The rapid increase in current initially causes some drying of the anode and cathode sides of the membrane, the liquid water addition PID controller is quick to respond and restore the cathode water content to saturation. Steady state anode water content is lower during the higher current density operation due to increased electro-osmotic drag. To maintain water balance within the cell, the water content gradient for back diffusion is increased, reducing the anode side membrane water content.

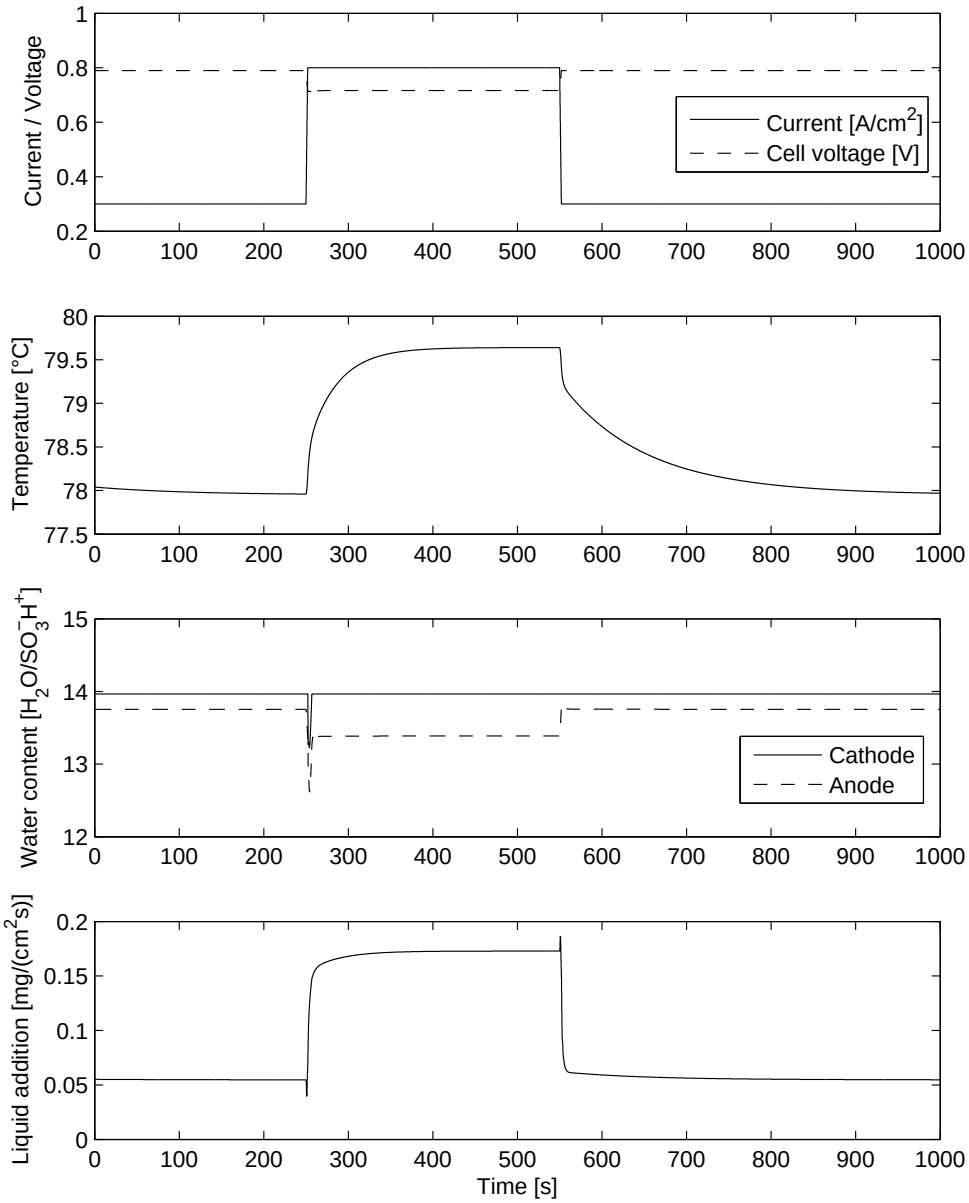

Figure 6.7: Stack response for step current change

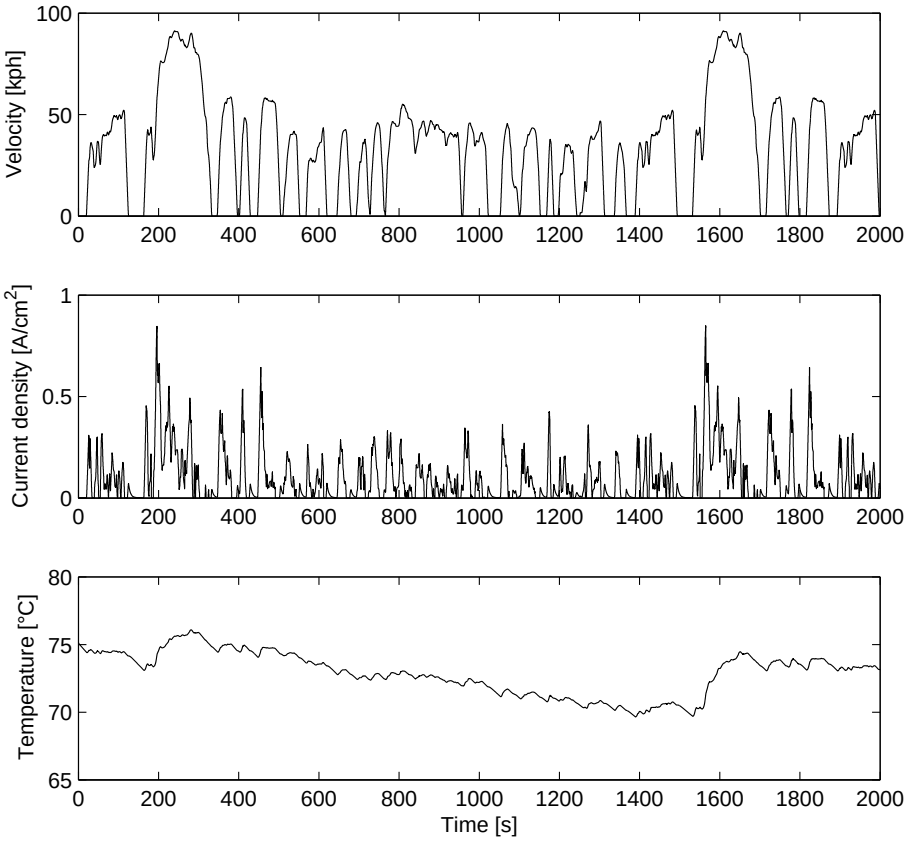

Figure 6.8: Temperature variation across the Federal Test Procedure drive cycle

The transient temperature of the fuel cell stack across a Federal Test Procedure (FTP) drive cycle, where the fuel cell stack is the sole power source, is shown in figure 6.8. The significant changes in current density create variation in the stack operating temperature. At low loads the compressor operates at the minimum set point, cooling the stack. During rapid acceleration the current density increases, raising the stack temperature. Total variation across the cycle was 6.5°C, this variation may be reduced through either the hybridisation of the powertrain, allowing the load profile to be smoothed, or through variation of the pressure ratio or stoichiometry to achieve a desired target temperature.

6.2.2 Water balance

System water balance in an evaporatively cooled fuel cell system is defined as the difference between liquid water separated from the exhaust stream post condenser and liquid water added to the stack for cooling, shown in equation 2.3. A positive net water flow implies the

system is gaining water, a negative net water flow implies the system is losing water and the stored water level is being depleted. The following section studies how different operating parameters influence the ability of the system to maintain water balance.

The maximum net water flow of an evaporatively cooled fuel cell system using a conventional radiator and 100% ambient humidity is equal to the product water of the electrochemical reaction. For this to occur, the condenser must cool the cathode exhaust down to ambient temperature, at which point both the product water and water evaporated to cool the stack will be in the liquid phase. Assuming all the liquid water can be collected the net water flow will be equal to the product water. In reality, the actual net water flow will be less than the product water due to restrictions in heat exchanger performance and liquid water separation efficiency. Figure 6.9 shows the net water flow as a function of current density at different ambient temperatures for the condensing radiator layout (figure 2.7). Vehicle speed is 25m/s which corresponds to a radiator air speed velocity of 4.1m/s. At low current densities the cathode exhaust flow rate is low and the condensing radiator is able to cool the exhaust close to ambient, meaning the net water flow is close to the theoretical maximum. As current density increases, the heat flow also increases and the effectiveness of the heat exchanger is reduced. The efficiency of collection compared to the theoretical maximum is reduced, however the overall net water flow increases because of the increase in product water. As current density increases further, the effectiveness of the condenser reduces and the actual net water flow deviates further from the theoretical maximum. For each set of operating conditions a point of maximum net water flow will occur, at this point further increase in current density will lead to a decrease in net water flow. If current density continues to increase, the system will transition from net water gain to net water loss, meaning the system is unable to reclaim all of the water added to the stack for cooling.

Increasing the ambient temperature is seen to decrease the net water flow rate. At 20°C the transition current density (change from net water gain to loss) occurs at 1.5A/cm^2, increasing ambient temperature to 40°C reduces the transition current density to 1.0A/cm^2. Increasing the ambient temperature reduces the driving temperature for heat rejection and hence the amount of water which can be condensed. For an 80°C stack temperature, the increase in ambient temperature from 20-40°C reduces the driving temperature difference for heat rejection by 33%.

Ambient temperature is not the only operational parameter to significantly influence the system net water flow, figure 6.10 shows how the target cathode relative humidity influences the overall net water flow of the condensing radiator system for a fixed vehicle

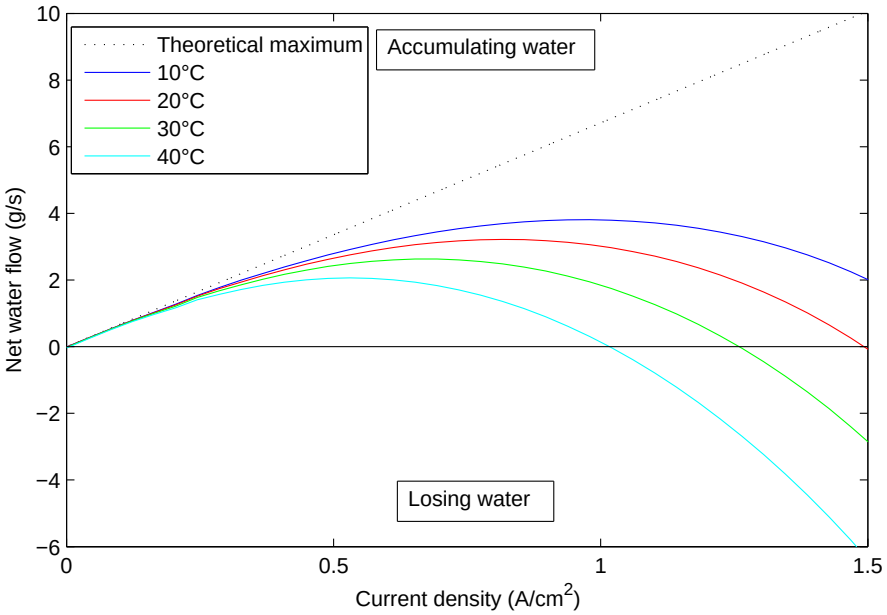

Figure 6.9: Steady state system net water flow at different ambient temperatures.

speed of 25m/s. Lower humidities are seen to give a lower net water flow, this is despite the higher operating temperatures shown in figure 6.5. Referring back to figure 6.6 the reason for improved net water flow at higher humidities is due to a lower liquid water addition rate because of higher efficiencies. Furthermore at higher humidities the amount of superheating is reduced and more of the heat exchanger can be used for condensation.

It was shown in figure 6.3 that increasing operating pressure raises the stack temperature through a reduced exhaust water vapour mass fraction. This creates a larger temperature difference between the condenser hot side and ambient, increasing the net water flow for an equivalent current density. However, elevated pressures also increase the parasitic load of the compressor (equation 3.73) meaning a higher current density is required to achieve an equivalent net work output at higher temperatures. Figure 6.11 shows the net water flow as a function of net power (fuel cell power minus compressor power) for different operating pressures for a fixed vehicle speed of 25m/s. The model results demonstrate that despite the increased parasitic load and reduced electrical efficiency, increasing pressure improves net water flow because of elevated operating temperatures. At 50kW net power, increasing the operating pressure from 1.1bar.a to 1.7bar.a increases the system net water flow by 82% due to a 11.4°C increase in fuel cell stack temperature. The improvement in system net water flow at higher operating pressures comes at the expense of increased compressor power consumption and reduced overall fuel efficiency. At 50kW net power, fuel consumption

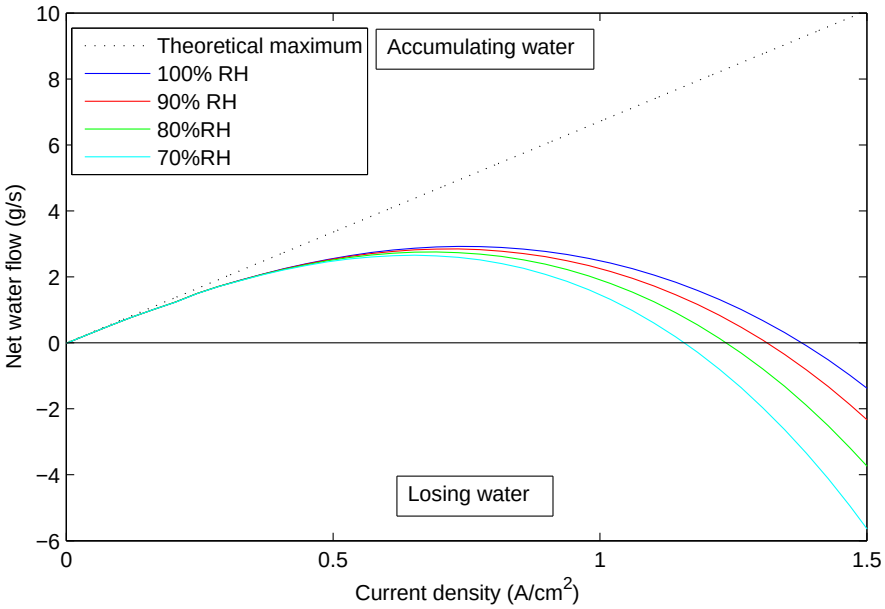

Figure 6.10: Steady state system net water flow at different cathode relative humidities.

is increased 4.7% by increasing the operating pressure from 1.1bar.a to 1.7bar.a. Both fuel efficiency and system net water flow should therefore be considered when selecting an appropriate operating pressure, this is especially important if a variable pressure strategy is used. Such a controller would operate at low pressure (high efficiency) during normal operation and higher pressure (increased net water flow) when the stored water tank level becomes low. This multi objective control problem would be well suited to the use of optimal control strategies using cost functions to determine the ideal operating pressure, this is a possible area for future work.

Figures 6.9 to 6.11 have all used the same vehicle speed of 25m/s, which with the under bonnet geometry parameters chosen gives an air velocity across the radiator of 4.1m/s. Figure 6.12 demonstrates the influence of the radiator air velocity on net water flow for the condensing radiator system. At low radiator air velocities water balance becomes increasingly difficult at higher powers, this condition is representative of a stationary application with a low fan speed, a vehicle accelerating from rest or a heavily laden vehicle travelling up a steep incline. Higher air velocities both increase the heat transfer coefficient through higher Reynolds numbers and increase the mean temperature difference between the hot and cold sides. The benefit of further increases in air velocity are progressively reduced as the incremental increase in net water flow with air velocity saturates. At low current densities increasing radiator air velocity has little effect on net water flow, activating a radiator fan

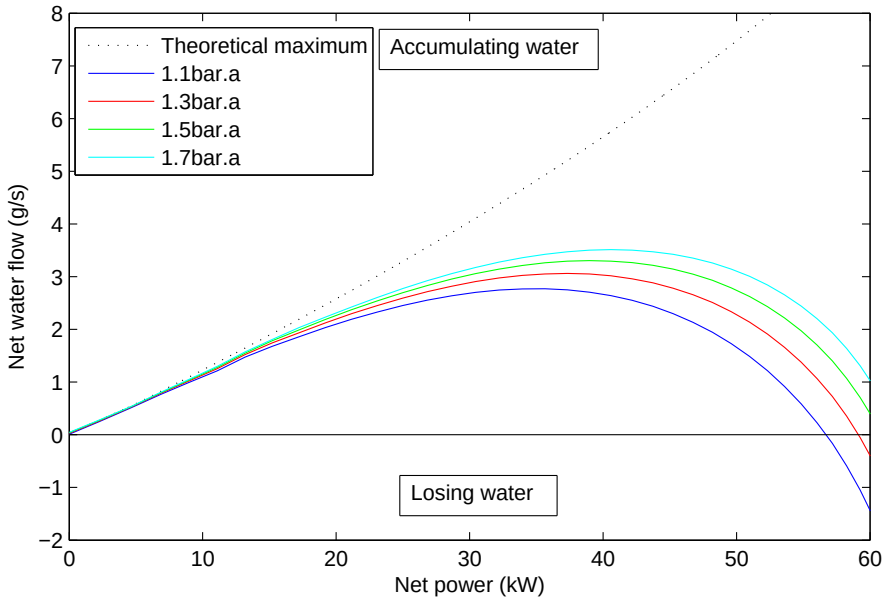

Figure 6.11: Steady state system net water flow at different cathode pressures.

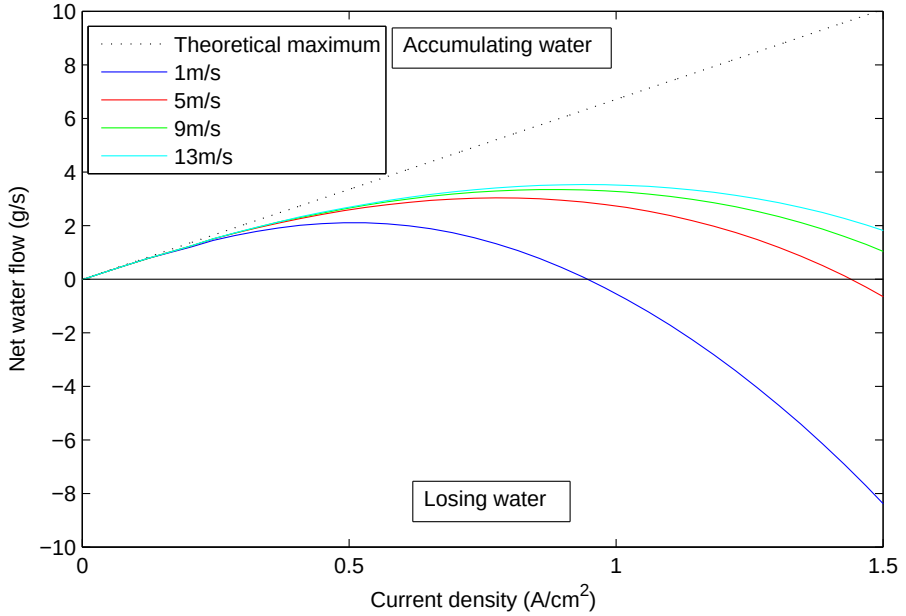

Figure 6.12: Steady state system net water flow at different radiator air velocities

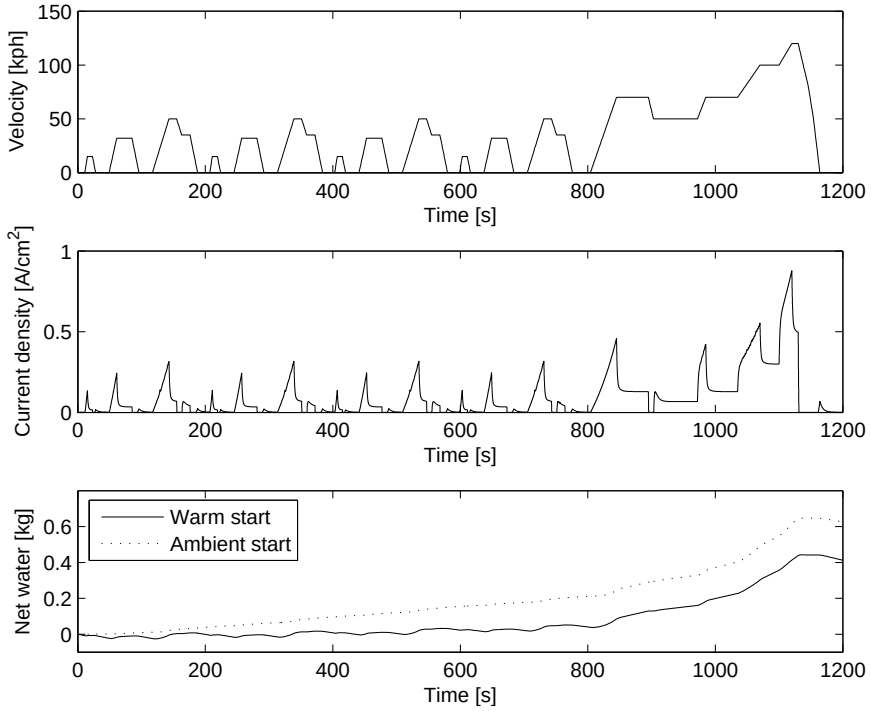

Figure 6.13: Velocity, current and stored water mass for automatic NEDC

in this region will therefore have very little influence on net water flow at the expense of increased power consumption. Alternatively it is more beneficial to activate the radiator fan during periods of high power to maximise the benefits of increased air flow across the radiator. This opposes the conventional strategy for fan operation in both internal combustion engines and liquid cooled fuel cells where fan operation when stationary is used to reduce coolant temperature and prevent overheating.

Figure 6.13 shows the cumulative net water flow of the condensing radiator system over the transient New European Drive Cycle (NEDC) at an ambient temperature of 35°C. Two cases were simulated, a warm start with an initial stack temperature of 75°C and an ambient start where the initial stack temperature was equal to ambient. In both cases the system produced a positive net water change over the drive cycle with the majority of the gain occurring in the latter extra urban section (>800s), where both current density and cooling air flow are higher. The net water gain from an ambient start was greater than from the warm start, this result contradicts the findings of Harraldsson *et al.* [40, 41] who showed the opposite for a liquid cooled system. The difference between the two works is that the model of Harraldsson *et al.* did not consider the collection of liquid water present at the fuel cell exit,

only vapour condensed in the heat exchanger. At low operating temperatures the product water will exist in liquid form at the stack exit, and can therefore be collected for future use in cooling the system through evaporation. During the warm start (75°C) case, short periods of net water loss can be observed in the urban section (<800s) when accelerating from rest. Figure 6.13 demonstrates that it is more difficult to maintain water balance across low speed stop/start operation than for higher speed operation at higher current densities. In a battery hybrid powertrain arrangement water balance could be improved if the battery acted as the main power source during stop/start operation, and was recharged by the fuel cell during higher speed driving when water balance is easier to maintain.

6.3 Condensing radiator layout

The previous discussion on water balance has focused on the condensing radiator system shown in figure 2.7. However, as discussed in section 2, such a layout may not be possible due to packaging or radiator material constraints. An alternative is to use a liquid cooled condenser in a conventional cooling loop with a liquid cooled radiator, shown in figure 2.8. The addition of a cooling loop creates several additional parameters including coolant flow rate and coolant tank temperature. Figure 6.14 illustrates the steady state relationship between stack temperature and coolant tank temperature as a function of current density for an evaporatively cooled system with a vehicle speed of 25m/s and ambient temperature of 25°C. At low current densities the coolant temperature approaches ambient, as current density increases the coolant tank temperature increases up to 62°C at full power. For a balanced ratio of condenser to radiator heat transfer capabilities, the coolant temperature should be half-way between the stack temperature and ambient temperature at full power. From figure 6.14 it can be seen that the tank temperature is slightly above this value, indicating that increasing the radiator heat transfer area would have greater effect than increasing the condenser heat transfer area. Comparing the condenser coolant exit temperature (radiator inlet temperature) to the stack temperature it can be seen that the presence of an additional heat exchanger reduces the radiator inlet temperature and hence driving temperature difference for heat rejection compared to the condensing radiator case.

The system net water flow of the evaporatively cooled system with the intermediate cooling loop is shown in figure 6.15 for different combinations of condenser heat transfer area and radiator frontal area for a constant 0.75A/cm^2 current density. Net water flow is strongly dependant on condenser heat transfer area for areas below 0.2m^2. Above 0.2m^2 the increase in net water flow with additional condenser area begins to saturate for the chosen conditions, implying the condenser is over specified for the radiator core size. The same

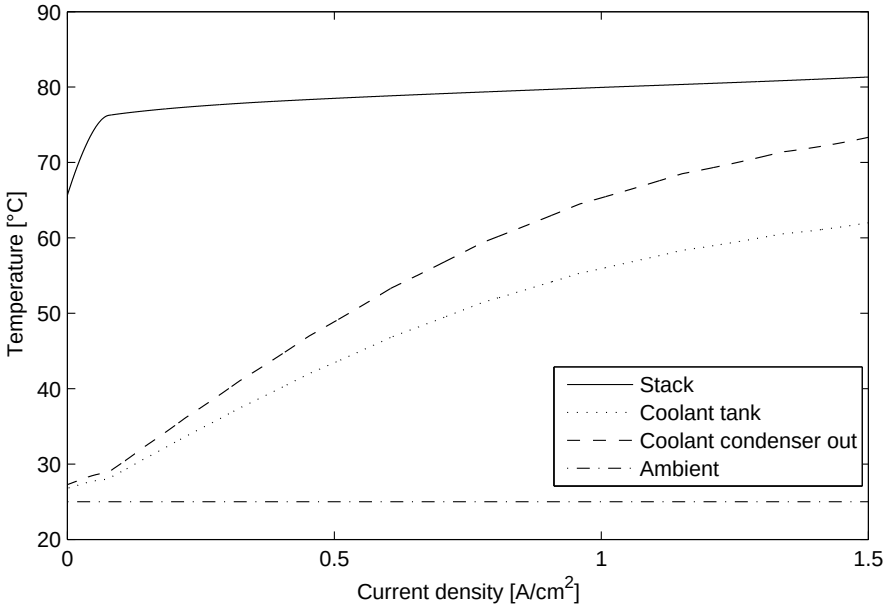

Figure 6.14: Fuel cell stack and coolant tank temperatures for intermediate condenser system layout

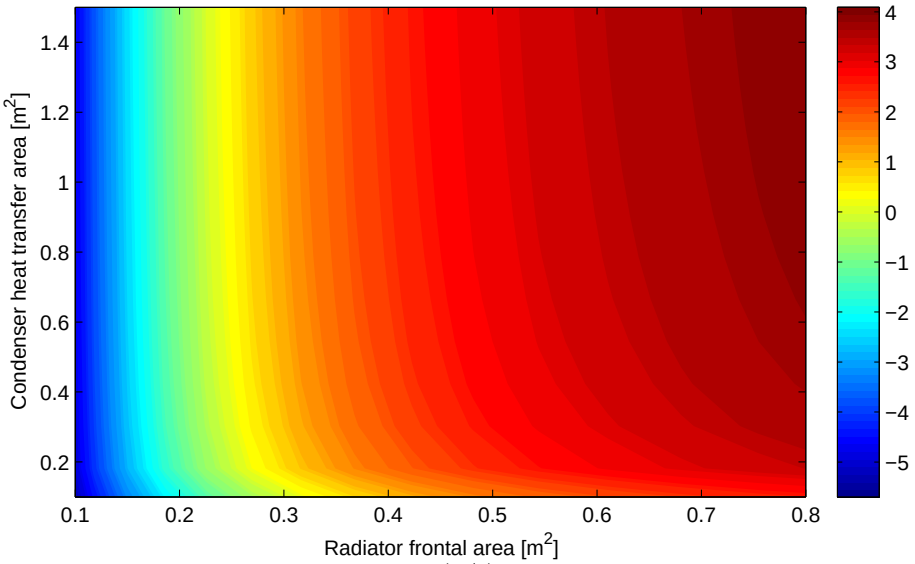

Figure 6.15: Sensitivity of net water flow (g/s) to radiator and condenser heat exchange areas at $0.75\mathrm{A/cm}^2$

strong saturation effect cannot be seen by changing the radiator frontal area for the same simulation parameters. Further increases in frontal area yield an increase in net water flow up to the maximum value of 0.8m^2 simulated. The decision on the respective sizing of both heat exchangers when designing such a system will also take into account the packaging constraints and material cost of both heat exchangers. Unlike the radiator, the condenser has the benefit of not requiring location at the front of the vehicle making packaging easier. However, the incremental cost of increasing the condenser area will likely be higher than the radiator because of lower production volumes and more material constraints.

6.3.1 System layout comparison

By using the model structures of figures 6.1 and 6.2 it is possible to quantitatively compare the condensing radiator layout to the intermediate cooling loop layout across steady state and transients for identical fuel cell operation and radiator core size. Figure 6.16 compares the steady state net water flow of both systems as a function of current density. System operating pressure was 1.3bar.a, vehicle speed 25m/s and liquid coolant flow rate 60 lpm. Results show that when using aluminium radiators, the condensing radiator performs significantly better than the system with the intermediate condenser, the difference being more pronounced at higher current densities. The transition from net water gain to net water loss occurs at a 32% higher current density when using the condensing radiator compared to the intermediate condenser and liquid cooling loop. Since the water addition into the stack is identical, the difference in net water flow between layouts is solely due to the heat exchangers. One reason for the higher net water flow in the condensing radiator layout is the higher radiator hot side inlet temperature, improving heat transfer and vapour condensation rate. Referring to figure 6.14, at the transition current density of 1.04A/cm^2 the radiator inlet temperature was 14°C lower for the system with the intermediate cooling loop than for the condensing radiator layout, representing a 34% reduction in driving temperature difference.

A further reason for the difference in net water flow between the two system layouts is the different radiator hot side fluids. In the layout with the intermediate cooling loop the radiator hot side fluid is a liquid water/glycol mix (pure water is used in the simulations for simplicity). Whereas in the condensing radiator layout, the hot side fluid is a mixture of de-oxygenated air and water vapour from the cathode exhaust. The presence of phase change in the condensing radiator produces much higher heat transfer coefficients. As the gas mixture cools inside the condenser the condensation rate drops, and the primary source of heat transfer becomes sensible cooling at a much lower heat transfer coefficient. A comparison of the hot side heat transfer coefficients inside the radiator from hot side inlet to hot side exit for different operating conditions are shown in figure 6.17. The heat transfer

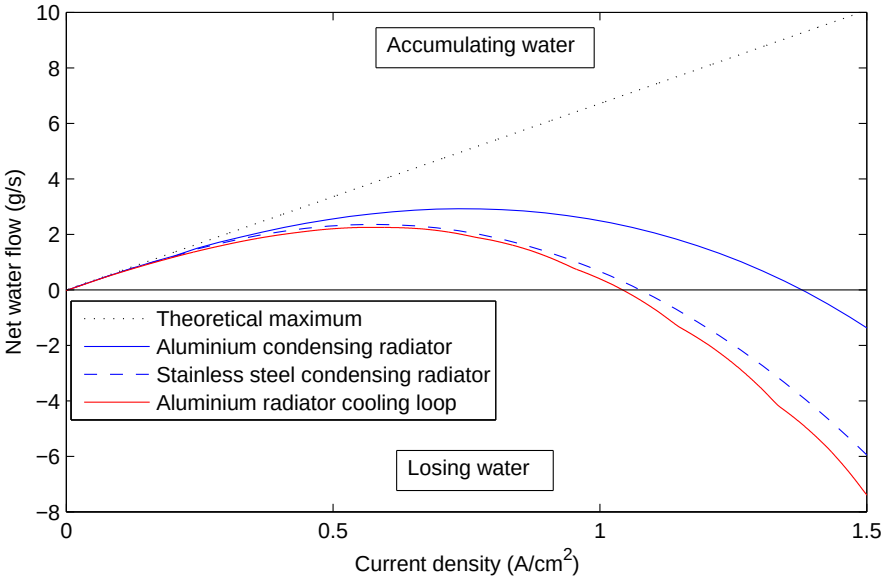

Figure 6.16: Steady state system net water flow for different layouts

coefficient of the condensing radiator varies significantly, both across the profile of the heat exchanger due the reduction in vapour mass fraction, and with current density due to the change in gas velocity and mixture heat capacity. At low current densities the heat transfer coefficients in the condensing radiator are lower than for the liquid cooling loop, however the lower inlet temperature of the liquid coolant and low heat loads give similar net water flows. As current density increases, so do the heat transfer coefficients of the condensing radiator. Both higher Reynolds numbers and marginally increased temperatures give higher inlet heat transfer coefficients. The increased heat capacity also means more water is condensed from the mixture before the vapour mass fraction, and hence heat transfer coefficient, reduces. It is possible to increase the liquid cooled radiator hot side heat transfer coefficient through increasing flow rate, although the high pressure losses in the compact plate condenser will increase the parasitic load.

Figure 6.16 also considers the case where an aluminium condensing radiator cannot be used because of possible aluminium ion contamination of the collected liquid water, instead stainless steel is used as the radiator material. This change is simulated by changing the radiator material thermal conductivity from 237W/mK (Pure aluminium [44]) to 15.1W/mK (AISI 302 [44]), the wall thickness and other geometry are not changed. The resulting change shows a significant drop in net water flow to the point where the intermediate cooling loop and condensing radiator performances are comparable across all current densities. The thermal resistance of the stainless steel radiator could be lowered by reducing the wall thickness,

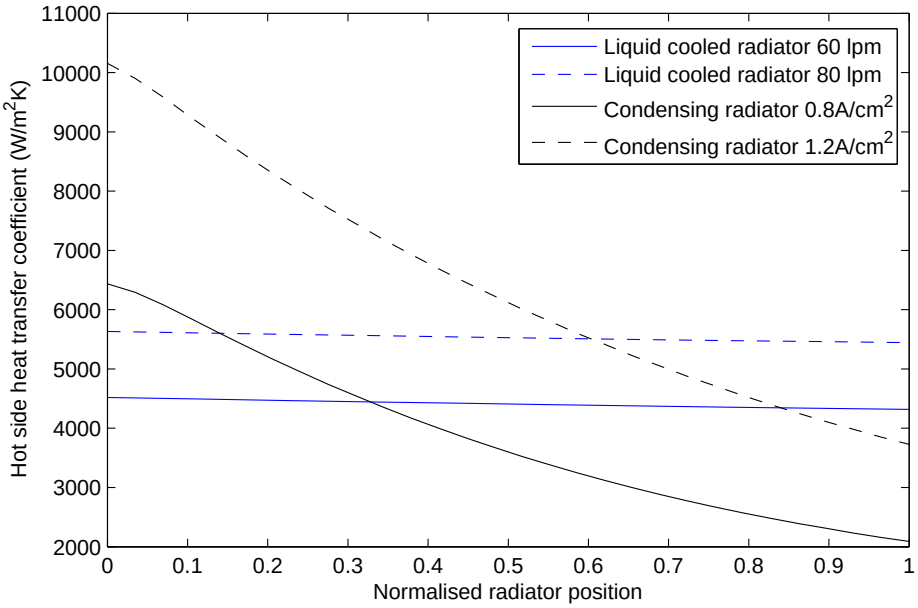

Figure 6.17: Comparison of Radiator hot side heat transfer coefficients

although not likely to the point where performance is restored to that of the aluminium radiator. Potential methods of improving net water flow whilst maintaining water quality include covering the internal tubes with a thin durable coating to prevent contact between aluminium and de-ionised water. Alternatively aluminium can still be used for the radiator fins, provided a suitable material is used for the tubes. This would give the same fin efficiency as an aluminium radiator negating some of the difference but at the added expense of cost and construction complexities relating to electrolytic corrosion.

The addition of a liquid coolant loop and tank in the intermediate condenser layout adds an additional thermal transient to the system. Condenser and radiator thermal loads are balanced through the coolant tank temperature, the time taken to achieve steady state will depend on the coolant thermal mass. Figure 6.18 compares the transient net water flow of both system layouts for a step change in current density. A step increase in current density at 250 seconds creates a short increase in net water flow for both layouts. This is due to the back pressure controller and compressor giving a slight increase in pressure and reduction in stoichiometry as the stack transitions from one operating point to the other. Likewise, when the current density reduces at 550s a temporary increase in cathode stoichiometry and decrease in pressure causes a drop in net water flow before steady state is achieved. Comparing the two system layouts, the aluminium condensing radiator gives a higher net water flow throughout the current profile, increasing net water flow at the elevated current

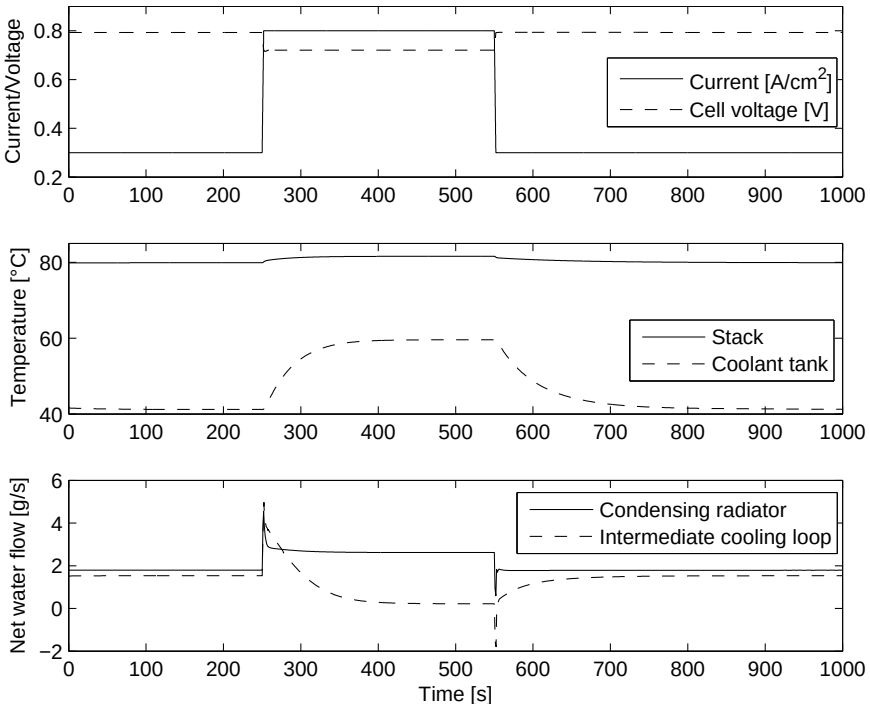

Figure 6.18: Transient system net water flow for different layouts

density, whereas the intermediate cooling loop system net water flow decreases. Immediately after the increase in current density (252-275 seconds) the net water flow of the intermediate cooling loop layout was higher than for the condensing radiator. This short term higher flow rate is due to the thermal inertia of the coolant mass. When heat generation is originally increased, the coolant temperature is low so the heat transfer in the condenser is high and the majority of vapour is condensed. The low coolant temperature means the radiator cannot reject sufficient heat and the coolant temperature rises, lowering the condensation rate. The opposite can be seen when the current density is reduced, the coolant temperature takes time to cool to its steady state value at the lower current density, giving a reduced net water flow for a period in comparison to the steady state value.

6.4 Evaporative vs. liquid cooling

The literature review identified multiple studies detailing both thermal and water balance in liquid cooled fuel cell systems and several publications discussing the operation of evaporatively cooled fuel cell systems. This section seeks to quantitatively compare the two methods of fuel cell cooling by using the fuel cell model of chapter 3 and heat exchangers of chapter 5.

6.4.1 Liquid cooled system

A schematic of the liquid cooled fuel cell system used in this study is shown in figure 2.4. Liquid coolant is forced through circular channels between the cells, transferring waste heat from the stack to the coolant so that it can be rejected to the environment through the vehicle radiator. Section 3.6.2 details the method of calculating heat transfer between the stack and coolant.

Stack temperature in the liquid cooled system requires active control, this is achieved using a PID controller to regulate the radiator by-pass valve to achieve a target stack temperature. During low thermal load the by-pass valve is predominantly open, allowing coolant to by-pass the radiator, during high thermal load the by-pass valve closes directing all flow through the radiator. The coolant flow rate is also varied using a PID controller to minimise both parasitic load and thermal gradients across the stack with a target temperature difference between stack coolant inlet and outlet of 5°C. Both controllers have fixed saturation points, the by-pass valve being restricted between 0 (by-pass open) and 1 (by-pass closed) and flow rate between 10 lpm and 80 lpm. In both cases anti-windup has been used and controller gains have been manually tuned.

The steady state temperatures and corresponding actuator positions of the liquid cooled system are shown in figure 6.19 for an operating pressure of 1.3bar.a, 10°C ambient temperature and 25m/s vehicle speed. As current density increases, so to do both the coolant flow rate and fraction of coolant flowing through the radiator. Above 0.71A/cm^2 further increases in heat generation yield coolant temperature increases across the stack of greater than 5°C at 80 lpm flow rate. Above 1.54A/cm^2 the heat rejection rate is not sufficient and the fuel cell stack overheats, for operation above this point the heat rejection capabilities of the system need to be improved.

The transient temperature regulation of the liquid cooled system is shown in figure 6.20, for the same step change as figure 6.7 except at 1.3 bar cathode pressure and 10°C ambient temperature. Temperature regulation through feedback control of the radiator by-pass is

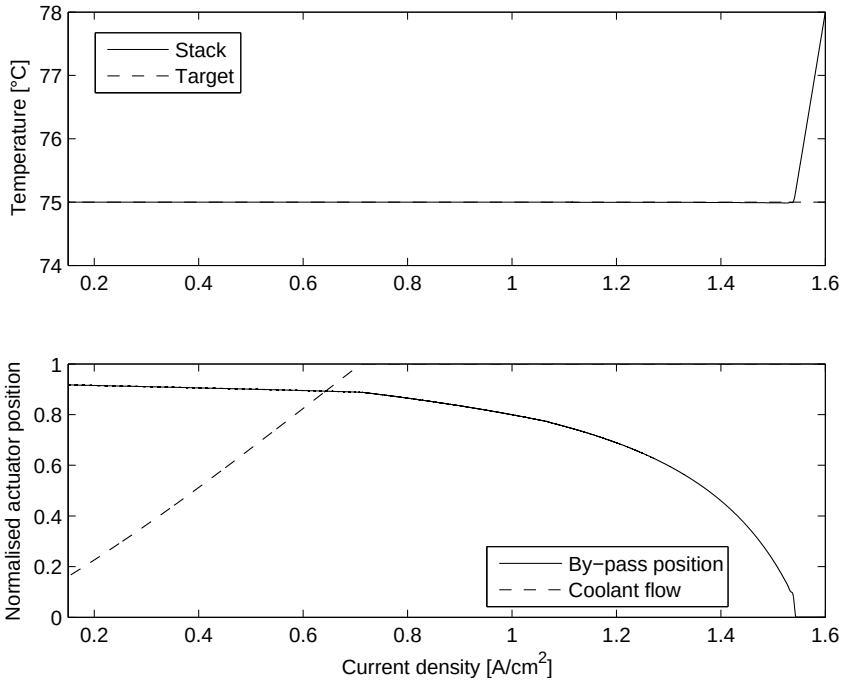

Figure 6.19: Steady state temperature regulation of liquid cooled fuel cell system

able to control stack temperature to within $\pm 1.1°C$ of the target temperature across the step increase and decrease in current density.

6.4.2 Steady state

Before a quantitative comparison of heat exchanger requirements between evaporative and liquid cooling can be performed, the basis for such a comparison must first be detailed. In the liquid cooled system the purpose of the heat exchangers are to maintain water balance, whereas in the liquid cooled system the heat exchangers maintain thermal balance. Furthermore, in the evaporatively cooled system the stack temperature is passively controlled based on the operating parameters, whereas the liquid cooled system aims to achieve a specified target temperature within operation limits. To perform a fair comparison, the heat exchanger requirements for water balance of the evaporatively cooled system are compared to the heat exchanger requirements for thermal balance of the liquid cooled system. The target stack temperature of the liquid cooled system is equal to the mean operating temperature of the evaporatively cooled stack across the same current density profile.

Figure 6.21 shows the required radiator frontal area of the two evaporatively cooled lay-

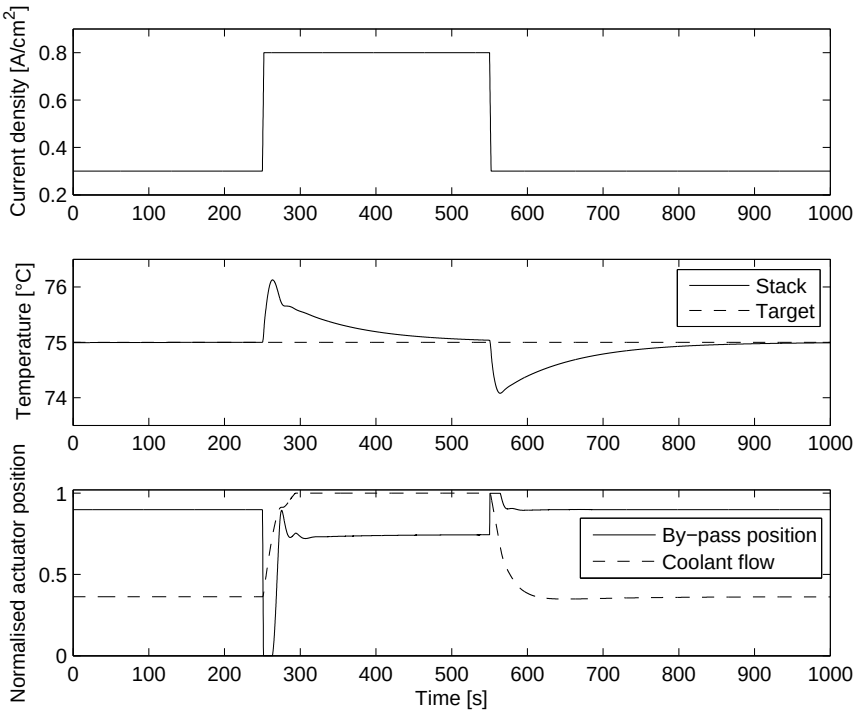

Figure 6.20: Liquid cooled stack response for step current change

outs and the liquid cooled system as a function of ambient temperature for a fixed 1.0A/cm^2 current density, 1.3 bar cathode pressure and 4m/s radiator air velocity. Across the range of ambient temperatures the evaporatively cooled system with aluminium condensing radiator requires the smallest frontal area, followed by the liquid cooled system, and then by the evaporatively cooled system with the intermediate cooling loop. The lower frontal area requirement of the condensing radiator is due to both increased heat transfer coefficients in the presence of phase change and higher radiator inlet temperatures. The liquid cooled system requires a smaller radiator frontal area compared to the evaporatively cooled system with the intermediate cooling loop because of both higher coolant flow rate and higher coolant radiator hot side inlet temperature. At 35°C ambient temperature the frontal area requirement of the evaporatively cooled system with the condensing radiator is 12.3% less than the liquid cooled system and 39.4% less than the evaporatively cooled system with intermediate cooling loop. At 1.25A/cm^2 the difference in frontal area changes to 39.2% for the liquid cooled system and 61.8% for evaporatively cooled system with intermediate cooling loop. This improved reduction in frontal area is due to both higher flow rates in the radiator tube and reduced non-condensable mass fraction from the small increase in stack temperature.

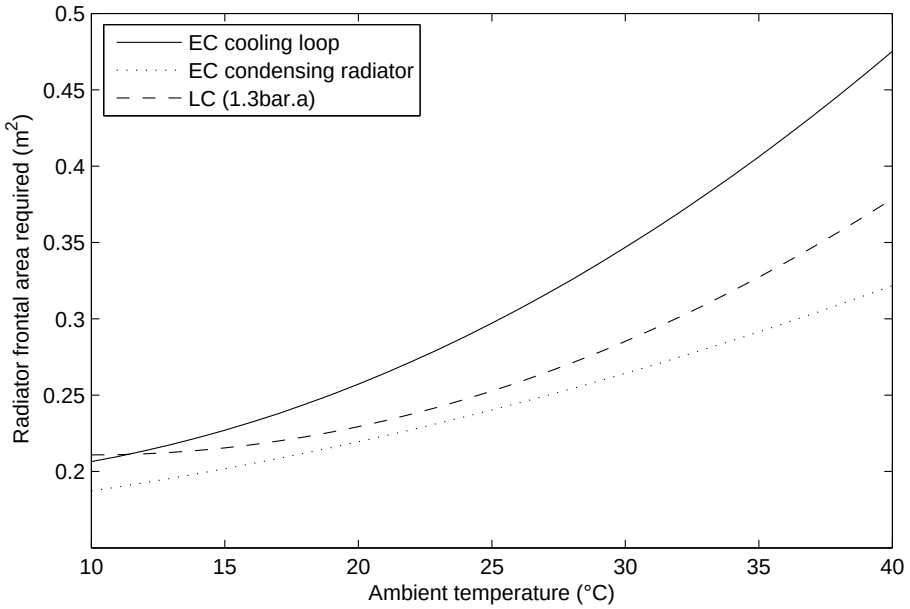

Figure 6.21: Radiator size required for different layouts and ambient temperatures at 1.0A/cm^2

At lower ambient temperatures (<15°C) the frontal area requirement of the liquid cooled system does not decrease at the same rate as the evaporatively cooled system; this is due to the reduced vapour content of the inlet air stream. At lower ambient temperatures both the water vapour in the compressor inlet air flow and compressor exit temperature are lower, reducing the amount of water vapour which can enter the stack. As ambient temperature continues to decrease, the humidity of the stack inlet stream is not sufficient to maintain a high humidity within the stack, causing the membrane resistance and hence heat generation to increase. The liquid cooled stack humidity could be improved in these conditions by increasing the operating pressure, this would both reduce the vapour concentration required for the same humidity and increase the temperature of the air entering the humidifiers.

Another method of comparing the different cooling methods is to look at the maximum current density at which water or thermal balance can be achieved for a fixed radiator frontal area at different ambient temperatures. This is referred to as the a 'de-rate' curve since the power output of the system is restricted to the maximum current density. Figure 6.23 shows the de-rate curve for both evaporatively cooled system layouts and the liquid cooled system for a 0.36m^2 radiator frontal area, 1.3bar.a operating pressure and 25m/s vehicle speed. These values were chosen to represent a typical radiator frontal area and fuel cell system

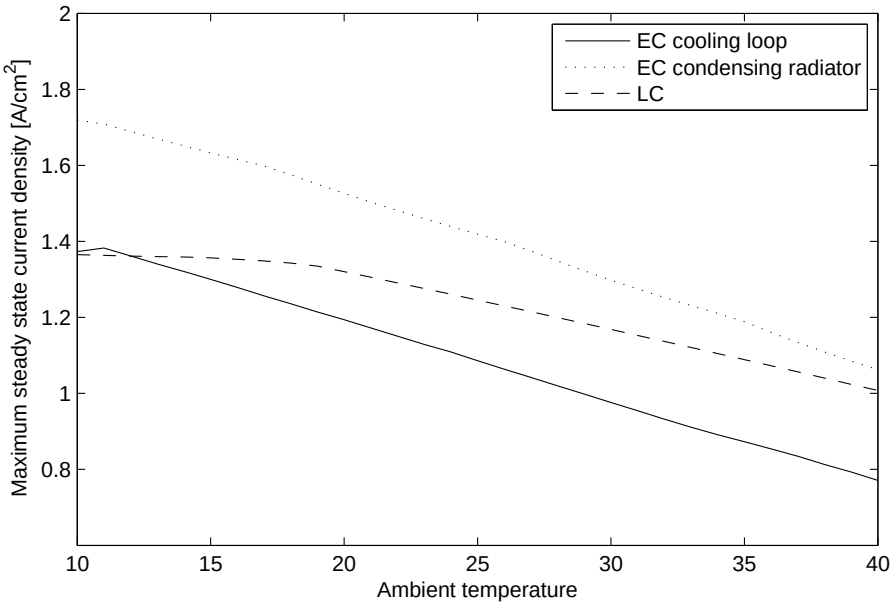

Figure 6.22: Maximum current density obtainable from a 600mmx600mm radiator for different cooling methods

operating pressure at a steady cruise velocity. The evaporatively cooled system with the aluminium condensing radiator is again seen to give the best performance over a wide range of ambient temperatures, followed by the liquid cooled system and finally the evaporatively cooled system with the intermediate cooling loop. As ambient temperature increases the difference between the maximum rated current densities of the evaporatively cooled system with the condensing radiator and the liquid cooled system reduce. This occurs because as maximum current density reduces with increasing ambient temperature, both the flow rate and vapour mass fraction in the condensing radiator reduce. At elevated ambient temperatures the maximum current density at which water balance can be achieved is reduced to the point where the performance of the condensing radiator is similar to that of the radiator in the liquid cooled system. However for the system modelled this does not occur until ambient temperatures in excess of 40°C.

All of the previous results presented have assumed that 100% of the liquid water at the condenser exit can be collected and re-used, in practice the actual collection efficiency will be slightly less than 100%, typically in the region of 95.0-99.8% [105]. A reduction in collection efficiency means additional water must be condensed to maintain water balance, increasing the condenser heat load and lowering the condenser hot side exit temperature. The relationship between collection efficiency and radiator frontal area required for water balance

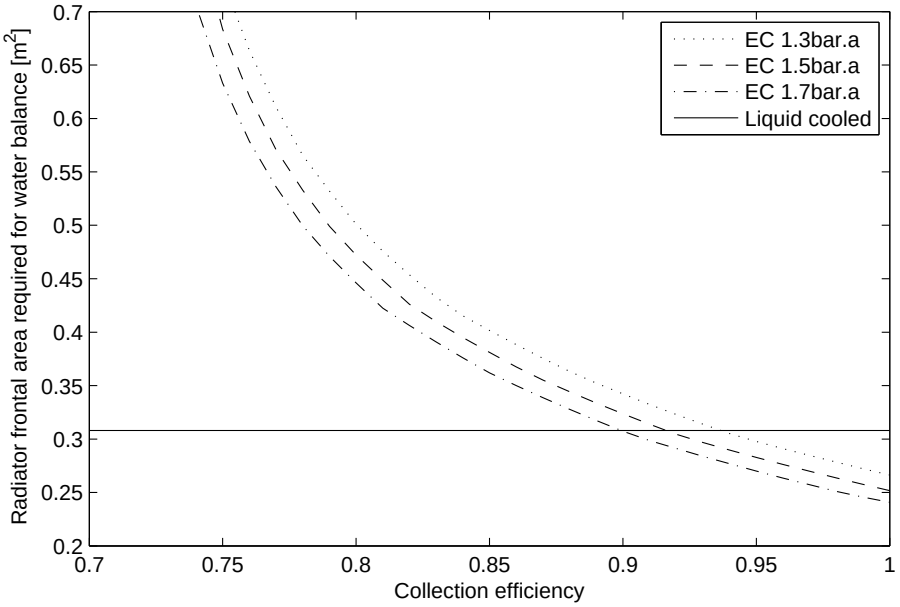

Figure 6.23: Influence of collection efficiency on required radiator frontal area

is shown in figure 6.23 for the evaporatively cooled system with an aluminium condensing radiator. Simulations were run at a constant current density of 1.25A/cm^2, 7m/s radiator air velocity and 35°C ambient temperature to represent high power output at cruising speed in a hot climate. At 100% collection efficiency the evaporatively cooled system requires a smaller radiator frontal area than the liquid cooled system. As collection efficiency decreases the radiator frontal area requirement of the evaporatively cooled system increases at a non-linear rate. As the collection efficiency reduces, the condenser outlet temperature required for water balance reduces at a rate proportional to the mixture water vapour content. Since the vapour saturation pressure is non-linear, further reductions in the collection efficiency require larger reductions in condenser outlet temperature to achieve the required liquid condensate flow rate, causing the non-linear increase in frontal area seen in figure 6.23. Increasing the operating pressure of the evaporatively cooled system allows for a lower collection efficiency for the same radiator frontal area due to increased operating temperatures. A 0.31m^2 radiator frontal area was used for the liquid cooled system, this gives a stack temperature equal to that of the evaporatively cooled stack at 1.3bar.a operating pressure. Above 93.5% collection efficiency the evaporatively cooled system requires a smaller radiator frontal area whereas for collection efficiencies below this value the liquid cooled system requires the smaller radiator. If collection efficiency were to reduce to 73% then the radiator frontal area required would be in excess of 1m^2. This demonstrates the importance of efficient water separation in evaporatively cooled fuel cell systems.

6.4.3 Transients

The temperature regulation abilities of evaporatively cooled and liquid cooled systems across a transient current profile are shown in figure 6.24. Both cooling methods demonstrate a good ability to regulate stack temperature within a narrow region, the liquid cooled system by using regulation of the radiator coolant by-pass valve and the evaporatively cooled system by maintaining humidity within the stack. Comparing the coolant tank temperatures of the liquid cooled and evaporatively cooled (with intermediate cooling loop) systems, it can be seen that the evaporatively cooled tank temperature is significantly lower than the liquid cooled system. This occurs because in the liquid cooled system the coolant tank temperature is directly linked to the stack temperature through the rate of heat removal. The by-pass valve indirectly controls the coolant tank temperature as means of regulating the stack temperature. Since the evaporatively cooled system does not have this restriction, the coolant tank temperature is free to change depending on the difference between condenser and radiator thermal loads. The lower temperature of the evaporatively cooled system is advantageous when considering the cooling of ancillaries such as the drive motors and power electronics with the same cooling loop, since the lower coolant temperature will improve heat transfer. However, as shown in figure 6.21 this advantage may be offset by increased radiator frontal area requirements of the evaporatively cooled system with intermediate cooling loop compared to the liquid cooled system. The evaporatively cooled fuel cell stack with the condensing radiator has not been considered here since the cathode exhaust feeds directly into the radiator, meaning a separate system is required for ancillary thermal loads.

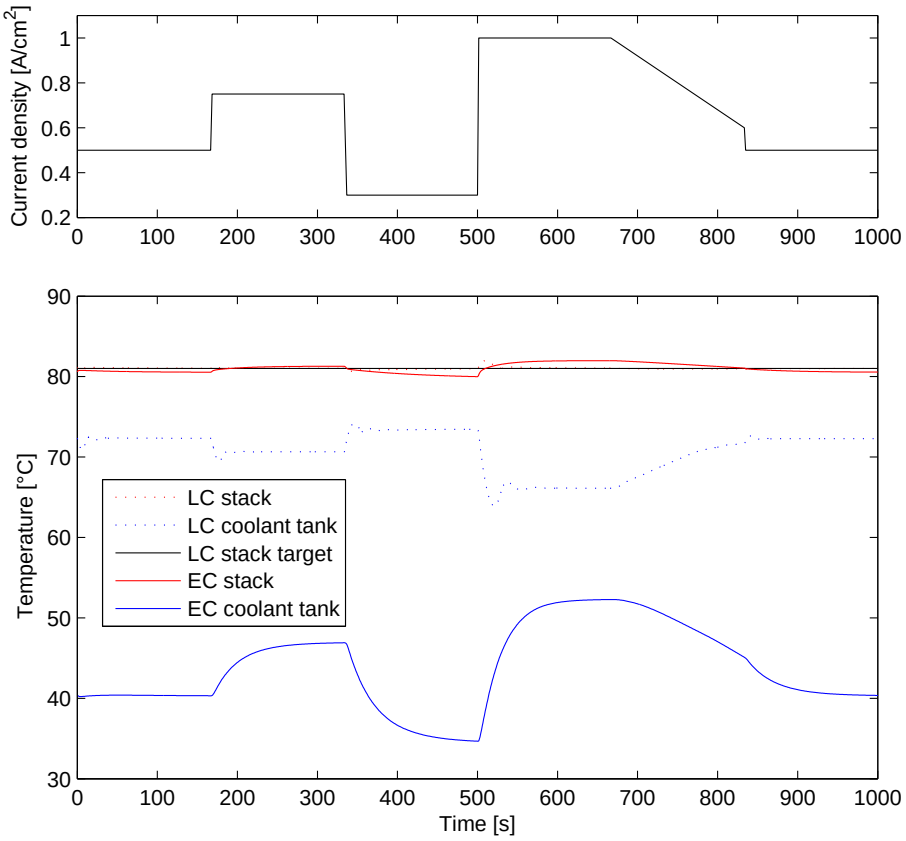

Figure 6.24: Comparison of temperatures in evaporatively cooled and liquid cooled system

6.5 1D fuel cell model

Sections 6.2 to 6.4 have looked at temperature regulation and system level water balance using a lumped parameter evaporatively cooled fuel cell stack model. The use of single lumped volumes for the anode and cathode does not consider the influence of spacial distribution inside the fuel cell. This section uses the model described in chapter 4 to study the spacial distribution along the flow channel of a co-flow evaporatively cooled fuel cell. The fuel cell parameters used in the one-dimensional study are detailed in full in table A.4, key parameters are shown in table 6.2 for convenience. Parameter values have been chosen from the literature to represent a typical PEM fuel cell.

Parameter	**Value**
Cell active area	100cm^2
Membrane thickness	100μm
Gas diffusion layer thickness	300μm
Gas diffusion layer contact angle	80°
Gas diffusion layer porosity [77]	0.725

Table 6.2: Key parameters for one dimensional simulation

The model was run using the solution procedure described in figure 4.8. The following sections analyse the one dimensional, along the flow channel, behaviour of an evaporatively cooled fuel cell. Four different liquid water addition methods are studied, these are described in detail in section 4.5.

6.5.1 Temperature profile

The lumped parameter study assumed the gas channel temperature was uniform across the fuel cell, in reality the gas temperature will change from the inlet to the outlet temperatures along the flow channel. This will effect the open circuit voltage, water content, and membrane diffusivity amongst other parameters within the cell. The gas channel temperature profile within the cell from inlet (0) to outlet (1) is shown in figure 6.25 for different current densities, using liquid water addition method I (target channel humidity) to achieve a target cathode humidity of 99%. Inlet conditions were 40°C, 80% Relative humidity and 1.1bar.a. The gas channel temperature is seen to increase at a non-linear rate from inlet to outlet, at 0.9A/cm^2 the total gas channel temperature increase was 39.2°C, 70% of this increase occurred in the first half of the flow channel. The uneven increase in temperature is primarily due to the non-linear water vapour saturation pressure increasing the water content of the gas stream, and hence heat capacity, at higher temperatures. Comparing the different mean

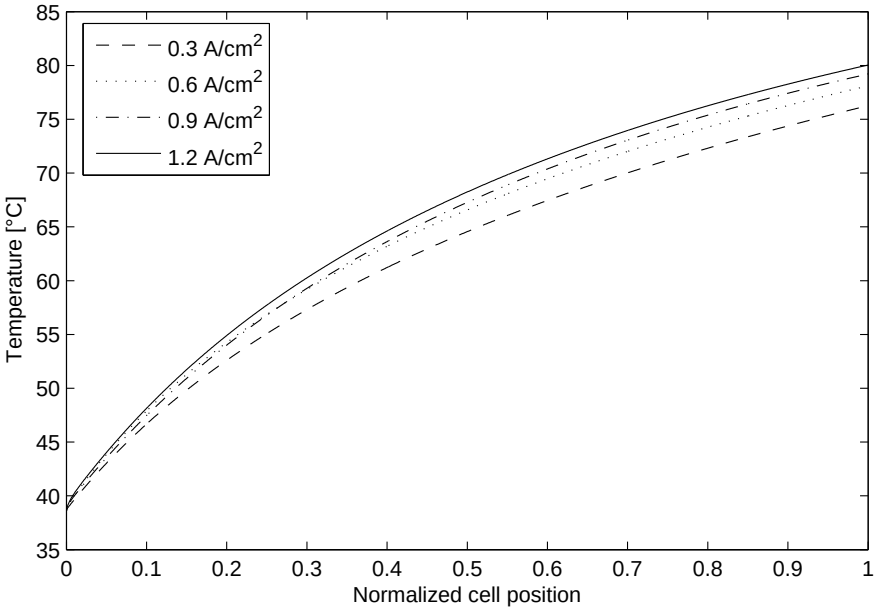

Figure 6.25: Gas channel temperature profiles (addition method I)

current densities in figure 6.25 it can be seen that the localised position in the flow channel has a much greater effect on temperature than the mean cell current density. This occurs because the gas channel flow rate, and hence water vapour capacity, increases linearly with current at constant stoichiometry. An increase in current therefore equates to an equal increase in heat removal through evaporation, provided humidity is maintained. The increase in temperature with mean current density observed in figure 6.25 is due to additional voltage loss and associated heat generation caused by increasing the mean current density. It is also apparent that the gas channel temperature in the initial stages of the cell are at times higher for lower mean current densities, this is due to the unequal distribution of heat generation within the cell. Since the potential is the same across the cell, and the change in open circuit voltage is small, heat generation varies linearly with local current density. At high cell current densities, electro-osmotic drag lowers the anode humidity close to the inlet, increasing membrane resistance. To maintain the the same potential across the cell, the localized current density, and hence heat generation, reduces close to the inlet at higher currents, causing the results seen in figure 6.25. The localized distribution for a 0.9A/cm^2 mean cell current density is shown in figure 6.28.

The gas flow channel exit temperatures predicted by the one-dimensional model are compared to those predicted by the lumped parameter model at different current densities and pressures in figure 6.26. Both models were run with the same inlet conditions of 40°C, 90%

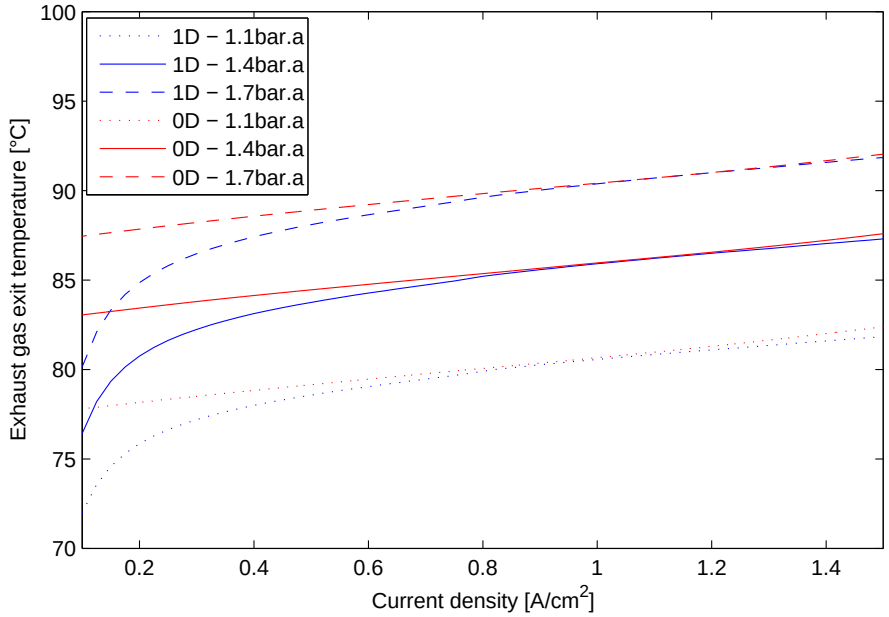

Figure 6.26: Cell gas exit temperatures (addition method I) compared to lumped parameter model

relative humidity and a cathode target relative humidity of 90%. Both models demonstrate that the cell temperature is self regulating within a narrow temperature band provided humidity is maintained within the cell. The two models show excellent agreement in gas channel exit temperature at higher current densities, however at lower current densities the gas channel exit temperature prediction of the one dimensional model is lower than that of the lumped parameter model. The lower temperature of the one dimensional model is due to reduced heat generation at lower current densities through increased cell voltage. The higher cell voltage of the one dimensional model at low currents is due to the assumptions made in the lumped parameter model when calculating the open circuit voltage (equation 3.3) and exchange current density (equation 3.5). Both of these terms will vary depending on the value of the reactant partial pressure. In the lumped parameter model the partial pressures are taken at the cell inlet, whereas in the one dimensional model the open circuit voltage and exchange current density vary along the gas channel with changes in partial pressure. Since the lumped parameter performs these calculations based on the inlet values, increasing the stoichiometry will have a minimal influence on the cell voltage. In comparison, increasing the stoichiometry of the one dimensional model will raise the reactant partial pressure in the latter regions of the cell increasing performance.

Both models were validated using the same polarisation data [12] at 1.67 cathode stoi-

chiometry, the comparison of temperature in figure 6.26 was performed at a cathode stoichiometry of 2.5. This increase in stoichiometry would have little influence on the lumped parameter model since inlet partial pressures would remain similar. However, the one dimensional model cell voltage would increase due to higher partial pressures in the latter stages of the cell, reducing heat generation and causing the trend seen in figure 6.26. The difference between the two calculation procedures is evident at low current densities since this is where the changes to open circuit voltage and exchange current density are most prevalent. At higher current densities protonic resistance of the membrane will become a significant loss, which will be similar for both models. Also the influence of the gas diffusion layer included in the one dimensional model only will begin to impede performance at higher currents through liquid water formation. The difference in temperature seen at low current densities justifies the additional complexity of the one-dimensional model and demonstrates the inaccuracies caused by assuming a uniform reactant pressure across the cell.

6.5.2 Current density distribution

The localised current density will vary along the fuel cell flow channel due to changes in reactant concentration and temperature to achieve a uniform potential between the anode and cathode. In the model, the localised current density is determined through an iterative process using equation 4.48. Figure 6.27 shows the localised current density to achieve a desired mean current density in the cell. Simulations were conducted with a 90% relative humidity, 40°C inlet at 1.1bar.a pressure, liquid water was added to maintain a 99% relative humidity in the gas flow channel using addition method I. At low mean current densities the local current density distribution is relatively uniform, the current density is slightly above the mean value close to the inlet since reactant partial pressure is higher. Heat generation is therefore fairly uniform across the cell. At high current densities the local current density is less evenly distributed with a reduced current density close to the inlet, increasing towards the middle of the cell and again reducing close to the cell exit. The reduced performance close to the inlet occurs due to increased electro-osmotic drag at higher current densities reducing the anode side humidity and increasing protonic resistance of the membrane. Further along the flow channel, both net water flow from cathode to anode and consumption of hydrogen gas help to restore the anode humidity, reducing losses and increasing the local current density. In the final stages of the cell the reduction in reactant partial pressure leads to a drop in the cell performance, this later loss is seen across all mean current densities. It is possible to reduce the mass concentration loss by operating higher stoichiometries to increase the reactant partial pressure, however this will increase compressor load and reduce cell temperature.

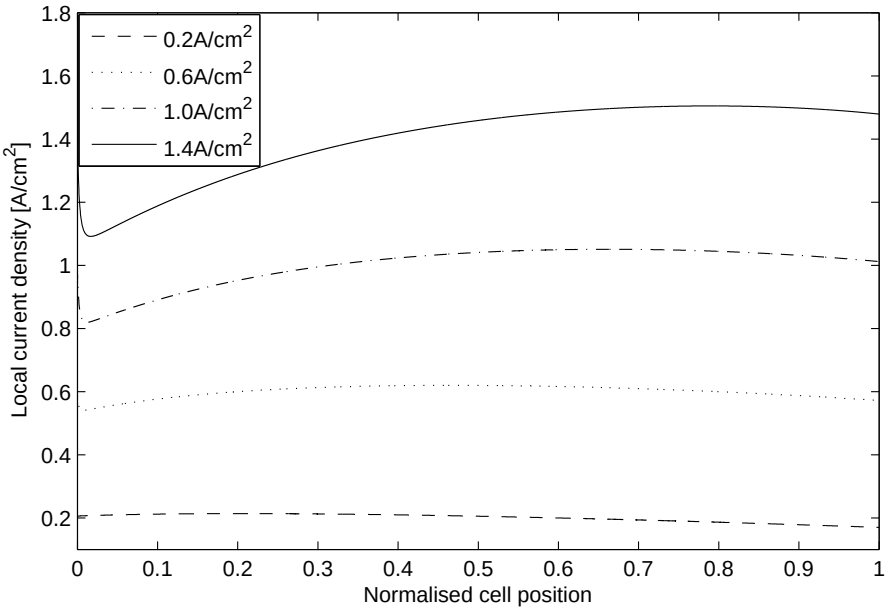

Figure 6.27: Cell current density distribution at different mean current densities, (addition method I)

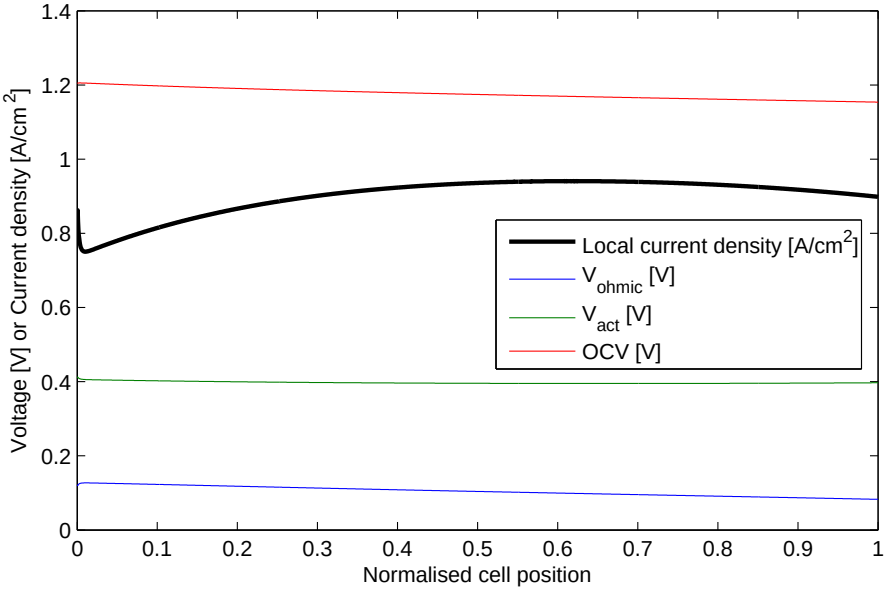

Figure 6.28: Cell current distribution ($i_{mean} = 0.9\text{A/cm}^2$, addition method I)

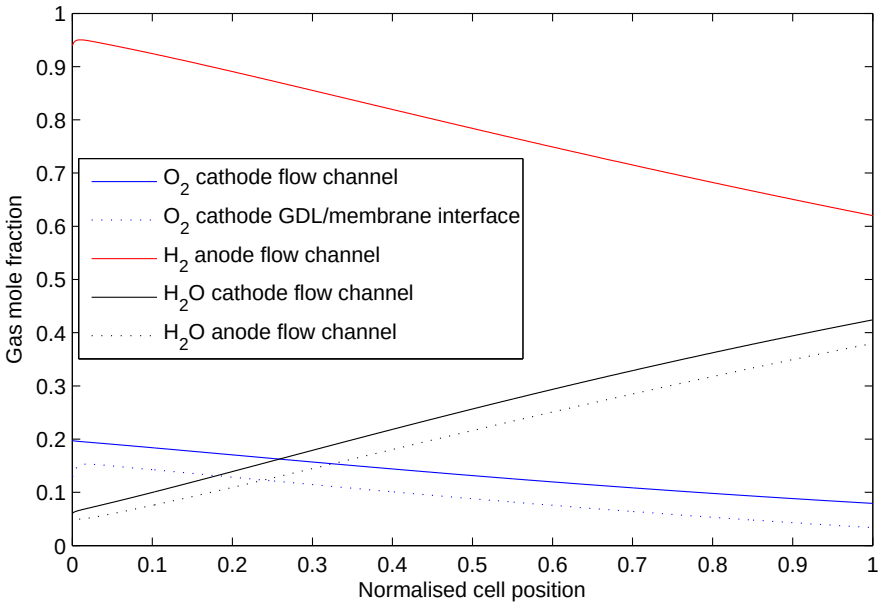

Figure 6.29: Gas mole fractions at ($i_{mean} = 1.2\text{A/cm}^2$, addition method I).

Figure 6.28 shows the changes in current distribution, open circuit voltage and overvoltages for a mean current density of 0.9A/cm^2 and the same inlet conditions as figure 6.27. The reversible open circuit voltage (OCV) (first two terms on the right hand side of equation 4.1) is seen to decrease slightly throughout the cell, again due to a reduction in reactant concentration. This reduction in reversible open circuit voltage is offset by the reduction in the ohmic resistance overvoltage, caused by an increase in membrane hydration. The sum of the activation and fuel crossover overvoltages remains relatively constant throughout the cell; the reduction in reactant partial pressure is offset by the increase in temperature, increasing the exchange current density and reducing the loss. The sum of the three overvoltages (equation 4.1) is equal across the cell with a 1mV mean error.

The variation of partial pressure within the cell for a high mean current density of 1.2A/cm^2 is shown in figure 6.29 for the same inlet conditions as figure 6.27. The influence of mass transfer resistance within the gas diffusion layer can be clearly seen, lowering the oxygen content at the membrane interface compared to the gas flow channel. Furthermore, the gradient in water content between the anode and the cathode can also be seen. The size of these differences will further increase with higher mean current densities.

6.5.3 Liquid water addition

Providing the correct amount of liquid water for evaporation and cooling within the cell is essential to maintain a high membrane water content and good cell performance. The liquid water should also be added in the correct location within the cell to prevent flooding of the gas diffusion layer. Of the different liquid water addition methods discussed in section 4.5, so far only liquid water addition method I (gas flow channel humidity regulation) has been considered. Figure 6.30 shows the local liquid water addition profile for different mean current densities using liquid water addition method I to maintain a 99% relative humidity in the cathode gas flow channel. Inlet conditions for the anode and cathode were 90% humidity at 40°C and 1.1bar.a pressure. Similar to the distribution of localised current density, the distribution of liquid water is less even at higher mean current densities.

The overall liquid flow rate is observed to increase non-linearly with mean current density due to a reduction in cell voltage and increase in heat generation. At a localised level, liquid injection rates were highest at the entrance of the cell due to the inlet cathode humidity being less than the target humidity, reaching the arbitrary limit set at 1.0mg/cm^{2}s. The required liquid water addition rate was then observed to quickly reduce after inlet as the cathode gas channel humidity was established. At low current densities the rate of water addition remains close to constant throughout the cell, representing an even heat distribution. At high current densities the rate of liquid water addition increases throughout the cell, because as discussed previously, heat generation is biased towards the second half of the cell due to a higher localised current density.

An advantage of using evaporative cooling is that it removes the requirement for external humidification of the cathode inlet stream, meaning the compressor or blower outlet feeds directly into the fuel cell stack. Depending on the pressure ratio and ambient conditions this could mean the cathode inlet has a high temperature and low relative humidity. The following figures demonstrate the performance of the different liquid water addition methods given a representative input from a 75% efficient compressor with a 1.3 pressure ratio. Using the non-isentropic compression equations from section 3.8.1 with 20°C, 1.0bar.a and 80% relative humidity ambient conditions, the cathode inlet conditions are 50°C, 1.3bar.a at a relative humidity of 20%. Anode temperature and pressure were set to be equal to the cathode, humidity was 80% at the anode inlet.

Figure 6.31 shows the relative humidity and liquid water addition profiles within the cell for the given input conditions at a 1.0A/cm^2 mean current density and 99% gas channel target humidity. The high initial rate of liquid water addition means that the cathode gas

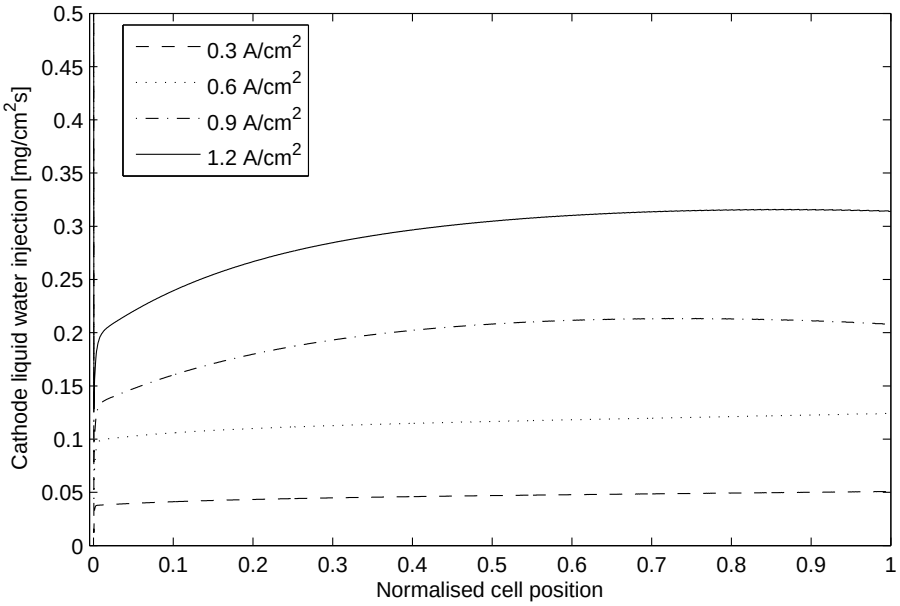

Figure 6.30: Cathode liquid water injection profiles (addition method I)

channel humidity reaches the target humidity close to the channel inlet, the target gas channel humidity is maintained throughout the length of the flow channel. Despite the low inlet humidity of the cathode gas channel the cathode GDL/membrane interface humidity remains high due to a net water flow from the anode to cathode through electro-osmotic drag. The high cathode interface humidity prevents back diffusion from occurring and the anode humidity drops from its initial value to 75%, slowly increasing to above 90% at the exit. As discussed previously, the reduced anode humidity will lower the membrane hydration and decrease the cell performance, most noticeably at high current densities when electro-osmotic drag is highest. To reduce this effect, some liquid may be added to the anode inlet, this is discussed further in section 6.5.4.

For maximum efficiency the GDL/membrane interface humidity should be high to decrease membrane resistance, yet not become saturated since the presence of liquid water within the GDL blocks potential diffusion paths, decreasing the effective diffusivity. By regulating the gas channel humidity the interface humidity is not controlled, during high current density operation or during high rates of net water transport from anode to cathode the cathode GDL may become saturated. During the simulation shown in figure 6.31 the maximum saturation (water void fraction) in the cathode GDL was 5.24% using liquid water addition method I. By using liquid water addition method II to regulate the interface humidity the level of saturation within the cathode GDL may be controlled, the humidity

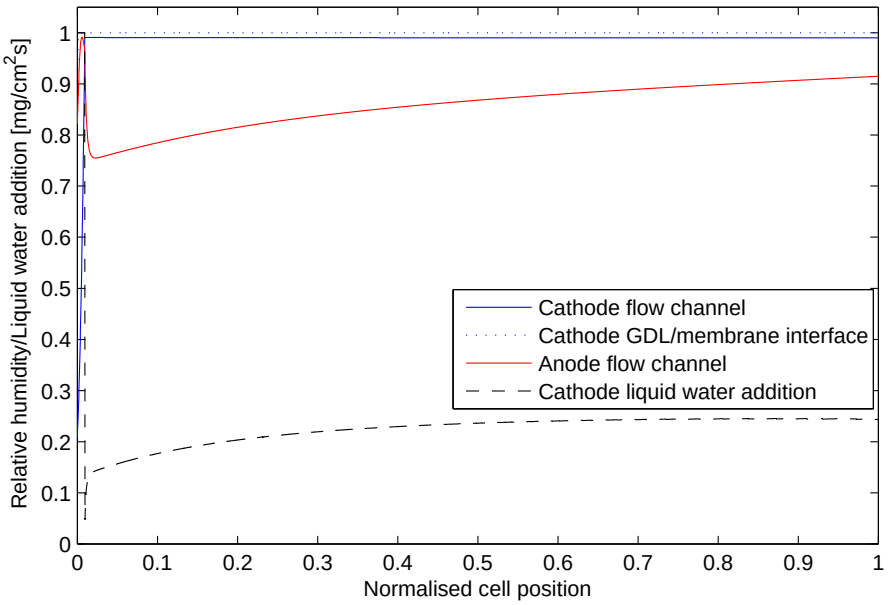

Figure 6.31: Humidity and liquid water addition profiles for addition method I

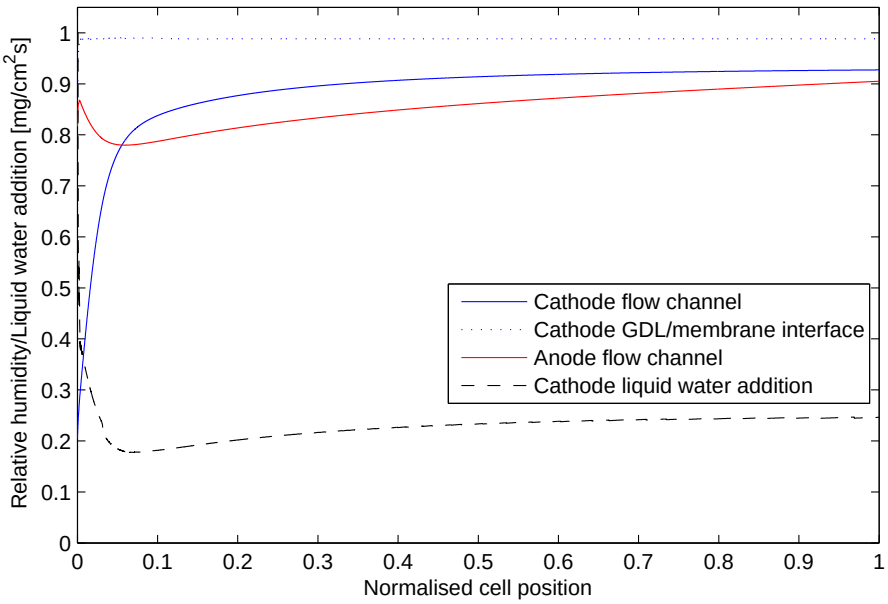

Figure 6.32: Humidity and liquid water addition profiles for addition method II

profiles using liquid water addition method II are shown in figure 6.32 for the same model inputs as figure 6.31. The interface is seen to maintain a desired 95% relative humidity while the cathode gas channel humidity increases from the inlet condition at a slower rate than method I, reaching 93% at exit. By regulating the interface humidity the GDL does not become saturated, increasing the reactant partial pressure and reducing heat generation. This results in a 0.87% reduction in liquid water addition and a 0.60% increase in cell voltage.

Methods I and II provide a useful insight into the liquid water addition profiles required to achieve a desired humidity within the cell, however their dependence on the knowledge of the humidity within the cell flow channels, or at the interface, makes them impracticable for use with existing physical sensors. Liquid water addition methods III and IV do not require measurement of the humidity within the cell making them easier to implement. Method III utilises the difference in vapour partial pressure to add water to the flow channel whereas method IV adds water evenly across the cell the maintain a desired exit humidity which can be easily measured using a conventional humidity sensor. Figure 6.33 shows the humidity and liquid water addition profiles using liquid water addition method III for the same inlet conditions used to compare the two previous methods. Close to the inlet the rate of liquid water addition is high due to a large difference between the vapour partial pressure and saturation pressure. As the gas channel humidity increases, the rate of liquid water added to the gas channel reduces. The cathode gas channel exit humidity was 97.6% and the interface was saturated throughout. Reducing the value of β in equation 4.21 would reduce the rate of liquid water addition throughout the cell, along with the GDL saturation. In practice the value of β would be influenced by the porosity of the wicking material used to add liquid water to the flow channel.

Figure 6.34 shows the humidity and water addition profiles for the same input conditions using liquid water addition method IV. Water is supplied at a rate of 0.30mg/cm^{2}s, the minimum rate required to achieve a cathode exit relative humidity greater than 95%. Unlike the three other methods the water addition rate is not higher close to the inlet, this leads to a reduction in the interface humidity reducing cell performance close to the inlet. As water addition continues along the fuel cell flow channel, both the cathode gas channel and interface become saturated and remain so until the cell exit. Since the rate of water addition is uniform across the cell, a compromise must be met between the high addition rate required at the inlet and the lower addition rate required close to the exhaust, this results in increased water consumption compared to the other cases where water addition rates can be varied.

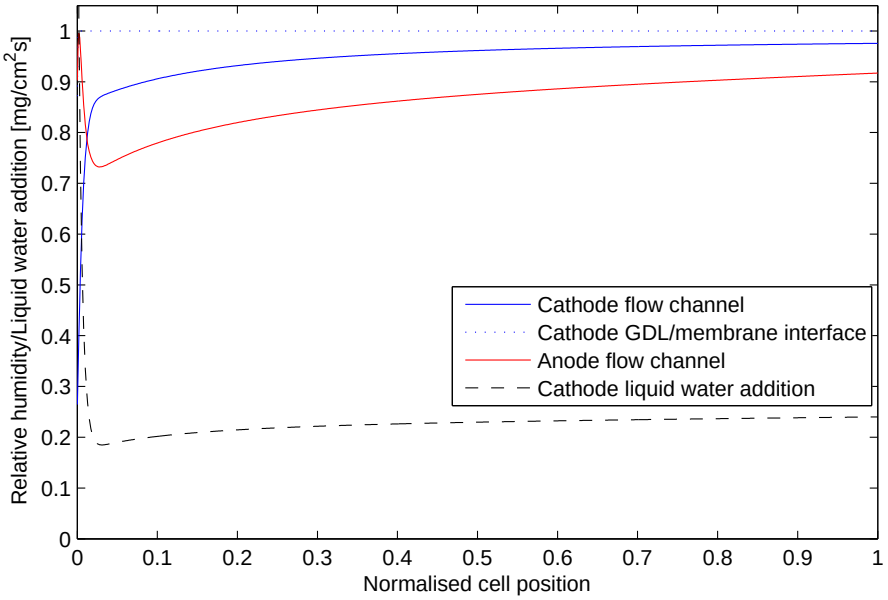

Figure 6.33: Humidity and liquid water addition profiles for addition method III

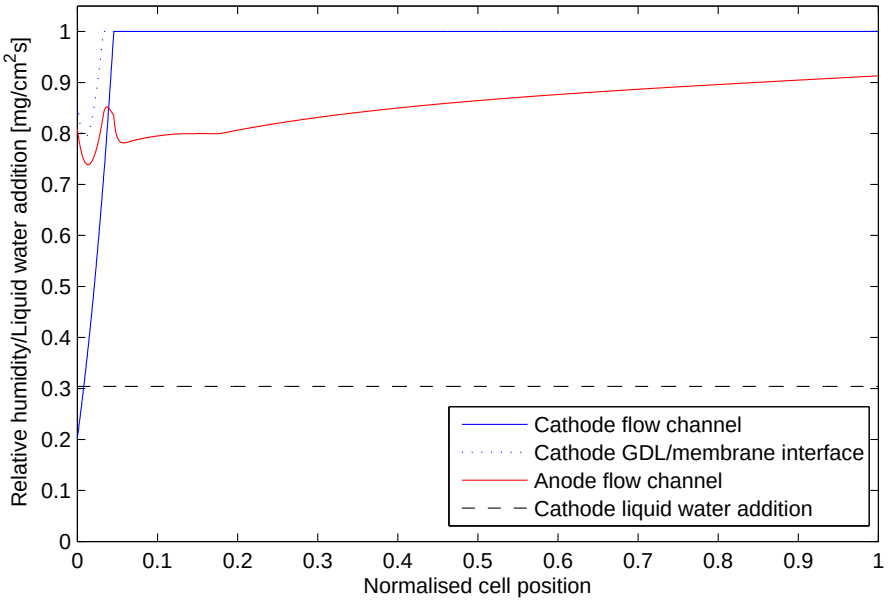

Figure 6.34: Humidity and liquid water addition profiles for addition method IV

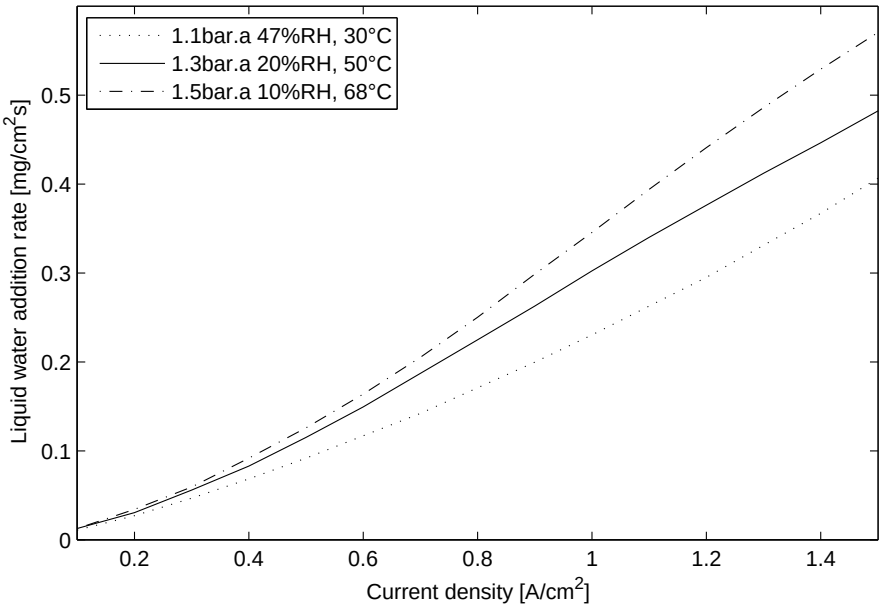

Figure 6.35: Constant liquid water addition rates (addition method IV)

The uniform liquid water addition rates required to obtain at least 95% cathode gas channel exit humidity as a function of mean current density for different inlet conditions are shown in figure 6.35. Despite the disadvantage of increased water consumption compared to the other methods, figure 6.35 demonstrates that sufficient membrane hydration and thermal balance can be obtained through either feedforward control based on knowledge of the inlet conditions and current density, feedback control based on a measured exhaust humidity or a combination of the two.

Numerical comparison of the different liquid water addition methods discussed in figures 6.31 to 6.34 are shown in table 6.3. Method II is seen to give the best performance with the highest cell voltage and lowest rate of liquid water required. Conversely method IV (constant rate addition) gives the equal lowest voltage and requires 32.8% more water than method II, creating an additional load on the thermal management system and increasing the required radiator frontal area.

6.5.4 Anode water addition

In the previous discussion, water was added into the cathode gas flow channel to provide both cooling and humidification. In this configuration the anode is humidified through back diffusion across the membrane and the water vapour present in the hydrogen inlet stream. At high mean current densities this can lead to drying of the anode and a reduction in per-

Addition method	Voltage (V)	Liquid added (mg/s)	Max GDL saturation (%)
I - Target channel humidity	0.666	23.1	5.24
II - Target interface humidity	0.670	22.9	0.00
III - Vapour partial pressure	0.665	23.1	5.22
IV - Constant rate	0.665	30.4	3.62

Table 6.3: Numerical comparison of different liquid water addition methods at 1.0A/cm^2 mean current density

formance close to the cell inlet due to increased electro-osmotic drag, as shown in figure 6.31. By adding some liquid water to the anode the reduction in humidity due to electro-osmotic drag can be reduced, although at the expense of additional system complexity. This section looks at how adding liquid water to the anode to achieve a desired anode gas channel humidity influences the overall cell performance. Four different cases are considered; no anode humidity regulation, 85% target gas channel humidity, 90% target gas channel humidity and 95% target gas channel humidity. In each case liquid water is still added to the cathode gas flow channel to maintain a 99% target humidity using liquid water addition method I. The reactant inlet conditions are the same as figure 6.31; 50°C, 1.3bar.a, 20% relative humidity at the cathode inlet and 50°C, 1.3bar.a, 80% humidity at the anode inlet.

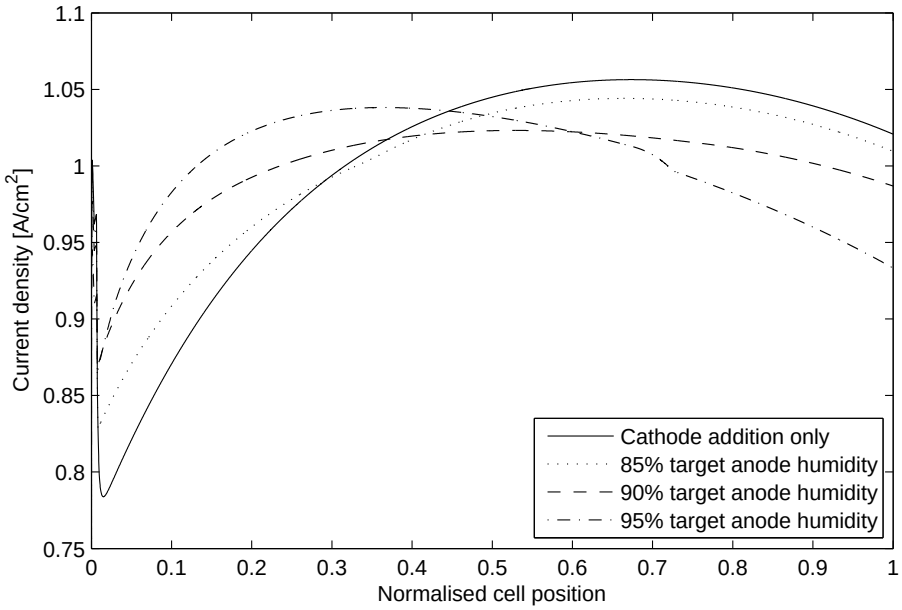

Figure 6.36: Current density distribution for different anode addition rates (i_{mean} = 1.0A/cm^2)

The influence of anode liquid water addition on cell current density distribution along

the flow channel is shown in figure 6.36 for the four cases specified above at a mean cell current density of 1.0A/cm^2. The simulated results show that as the anode target humidity increases, the reduction in performance close to the gas channel inlet is reduced. The minimum localised current density increases from 0.78A/cm^2 with no anode liquid water addition to 0.87A/cm^2 at 95% anode gas channel humidity target. Some reduction in performance at the inlet is still seen despite the increased anode humidity, this is due to both lower gas channel temperatures and higher liquid saturation fractions in the cathode gas diffusion layers. Close to the gas channel exit the localised current density decreases with increasing anode target humidity. This is primarily because the more even current density distribution at higher anode target humidities allows the localised current density to operate closer to the mean cell current density since it does not have to offset the reduced performance close to the inlet. At high anode target humidities (>90%) the humidity in the gas channel will exceed that from cathode liquid water addition alone (figure 6.31), leading to a reduced hydrogen concentration and therefore reduced performance. However given the small change in anode water vapour between 90-100% humidity this effect will be small.

The variation in current density along the length of the flow channel can be quantitatively compared using the current density uniformity (I_u), defined in equation 6.1. Where $i\,(n)$ is the local current density, i_{mean} the mean current density (1.0A/cm^2) and n_{cell} the total number of sections in the simulation. Without anode liquid water addition (cathode only) the current density uniformity was 0.943, increasing to a maximum of 0.979 when both anode and cathode liquid water addition were used (90% anode humidity target), a 62.5% reduction in local current density variation.

$$I_u = 1 - \frac{\sum_{n=1}^{n_{cell}} |i\,(n) - i_{mean}|}{n_{cell}} \tag{6.1}$$

The amount of liquid water added to the anode gas flow channel to achieve different target humidities is shown in figure 6.37. As the anode target humidity increases so to does the length of the flow channel where liquid water is added and the rate at which water is added. To achieve a 95% gas channel humidity liquid water is added across the whole of the anode flow channel. After an initial increase close to the inlet the rate of anode liquid water addition reduces significantly throughout the cell. This occurs due to the consumption of hydrogen in the electrochemical reaction increasing the concentration of water vapour at the anode. The same does not occur at the cathode since the oxygen reactant is diluted in air and a higher stoichiometry is used (2.5 at the cathode compared to 1.05 at the anode).

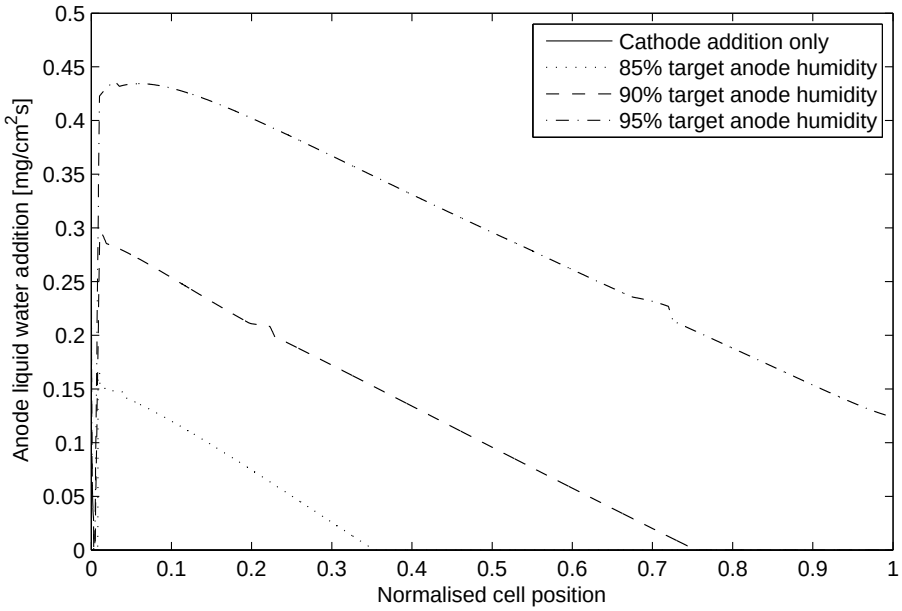

Figure 6.37: Anode liquid water addition rates for different gas channel humidity targets ($i_{mean} = 1.0\text{A/cm}^2$)

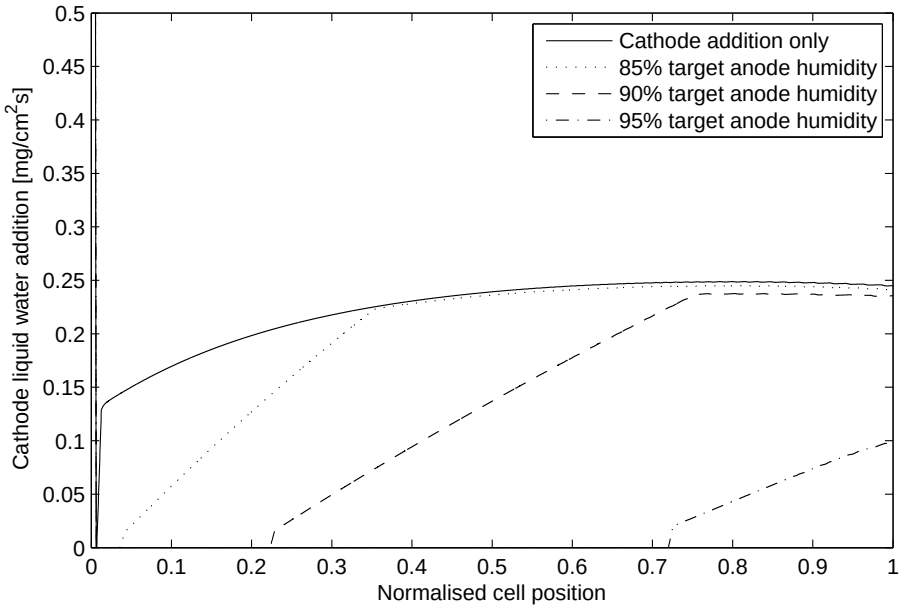

Figure 6.38: Cathode water addition required to maintain desired cathode gas channel humidity at different anode humidities ($i_{mean} = 1.0\text{A/cm}^2$)

Increasing the humidity of the anode gas flow channel also increases the anode side membrane water content, reducing the amount of back diffusion from cathode to anode meaning more of the product water remains within the cathode. The localised rate of cathode gas channel liquid water addition corresponding to the different anode liquid water addition cases is shown in figure 6.38. As the rate of anode water addition increases, the liquid water added to the cathode to maintain the desired cathode humidity reduces. At 95% anode gas channel humidity the majority of the cathode gas flow channel is saturated, with hydration requirements met by water transport from the anode and the electrochemical product water. The point at which the cathode gas flow channel drops below saturation and cathode liquid water addition is required can be seen on both the liquid water addition profiles of figures 6.37 and 6.38. For the 95% anode gas channel humidity case this point occurs at 0.72 of the normalised flow channel length.

The total rate of localised liquid water addition (anode and cathode combined) is shown in figure 6.39 for the different cases studied. Higher anode humidity targets lead to higher localised rates of liquid water addition close to the inlet of the cell and higher overall liquid water consumption. Maintaining the anode close to saturation eliminates the concentration gradient for back diffusion of water from the cathode leading to increased water flux from anode to cathode through electro osmotic drag. This combined with the water produced at the cathode catalyst layer during the electrochemical reaction leads to liquid water accumulation in the cathode gas flow channel, causing potential blockages to gas flow and reducing potential diffusion paths through the gas diffusion layer. It is therefore recommended that if anode liquid water addition is present that the target humidity be sufficient to provide adequate cooling and membrane hydration, yet not excessively high since this will prevent back diffusion and cause liquid water formation within the cathode.

The net water flux ratio across the membrane for the four anode target humidity cases studied is shown in figure 6.40. Net water flux ratio (ω_w) is defined as the number of moles of water transferred across the membrane ($J_{H_2O,net}$) per mole of hydrogen consumed at the anode ($N_{H_2,cons}$), shown in equation 6.2 where flux is positive from anode to cathode.

$$\omega_w\left(n\right) = \frac{J_{H_2O,net}\left(n\right)}{N_{H_2,cons}\left(n\right)} = \frac{J_{H_2O,net}\left(n\right) \times 2F}{i\left(n\right)} \tag{6.2}$$

Without anode liquid water addition the net water flux is primarily negative (cathode to anode) except for a significant positive flux close to the inlet due to the low cathode gas inlet humidity, a negative net water flux implies that back-diffusion is dominant. As the humidity target of the anode increases, the magnitude of net water flux reduces, eventually changing

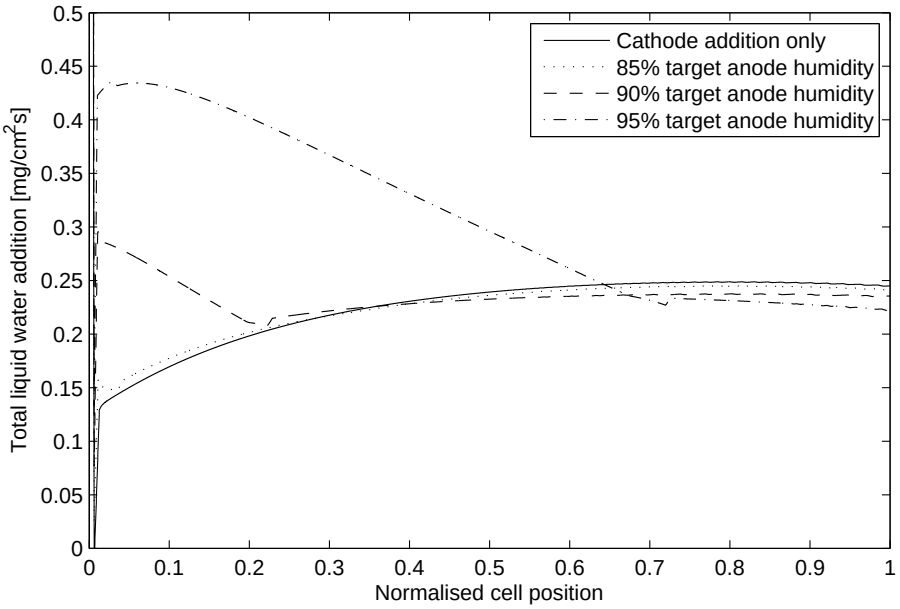

Figure 6.39: Total water addition (anode and cathode) for 99% cathode gas channel humidity and varying anode gas channel humidity ($i_{mean} = 1.0\text{A/cm}^2$)

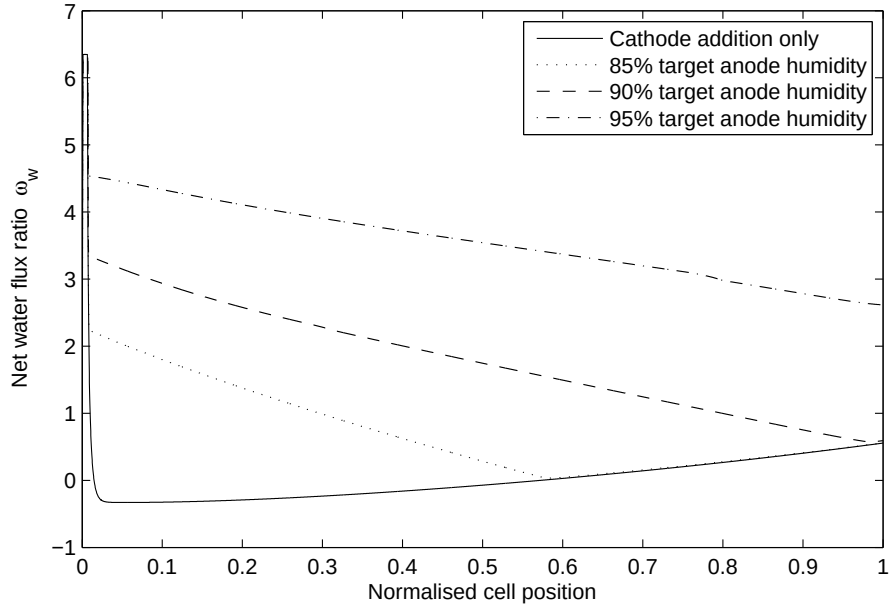

Figure 6.40: Net water flux ratio (positive anode to cathode) for different target anode humidities ($i_{mean} = 1.0\text{A/cm}^2$)

to positive (anode to cathode), implying that electro-osmotic drag is dominant. Referring back to the calculation of electro-osmotic drag in section 3.3.1, at full saturation 2.5 water molecules are dragged from anode to cathode with each proton. Therefore the maximum net water flux ratio from electro-osmotic drag alone is 5.0 (2 protons in H_2), values above this are due to both electro-osmotic drag and back diffusion working together in the same direction.

6.6 Chapter summary

In this chapter, a detailed analysis has been performed using the validated models produced in chapters 3-5. The potential advantages of evaporative cooling have been demonstrated in terms of temperature regulation, water balance and heat exchanger requirements. Potential drawbacks of evaporative cooling have also been presented, such as system layout restrictions, radiator material constraints and dependence on high liquid water separation efficiencies. Four different methods of liquid water addition distribution for humidification and cooling have been demonstrated and quantitatively evaluated. The work conducted in this analysis represents the first numerical comparison of evaporatively cooled and liquid cooled fuel cell thermal management, along with the first published study into spacial variation along the flow channel of an evaporatively cooled fuel cell.

Chapter 7

Conclusions and further work

7.1 Conclusions

The objective of this work was to develop the current understanding of evaporatively cooled fuel cells, specifically relating to how water and thermal management are influenced by different operating conditions. This has been achieved at both cell level and system level through the use of the validated component models presented in this thesis. The key conclusions of this work are summarised below:

7.1.1 Fuel cell

- A lumped parameter transient model and one dimensional steady state model of an evaporatively cooled fuel cell has been produced and validated using published polarisation curves and cathode exhaust temperatures from experimental data. This work represents the first published one dimensional, along the flow channel, model of an evaporatively cooled fuel cell.

- The passive temperature regulation ability of evaporatively cooled fuel cells have been demonstrated in both the lumped parameter and one-dimensional models. Provided liquid water is added to maintain a sufficient humidity in the flow channel the temperature change with current density will be small; $\pm 1.6°C$ for operation in the ohmic loss region (0.2-1.0A/cm^2) with no temperature overshoot during step load changes. Fuel cell temperature change across transient drive cycles was shown to be similar to conventional liquid cooled systems without the need for active temperature control provided extended periods of low load ($<$0.1A/cm^2) do not occur. The influence of operating parameters such as pressure and stoichiometry on fuel cell temperature has

also been investigated, demonstrating that maximum operating pressure is restricted by the temperature limitations of the membrane in an evaporatively cooled cell. For a 95°C maximum permissible membrane temperature at full load, the cell operating pressure should not exceed 1.8bar.a at 2.5 cathode stoichiometry for the conditions simulated in this work.

- Through using a one-dimensional model it has been shown that an evaporatively cooled fuel cell can operate with low humidity (20%) cathode inlet conditions, typical of those seen at the compressor exit without the need for an external humidifier, simplifying the system architecture. At high current density operation, some liquid water may need to be added to the anode to replace water lost to the cathode through electro-osmotic drag.

- Four different methods for determining the rate of liquid water addition into the cell flow channel have been simulated. To both maximise efficiency and minimise water consumption, liquid water should be added to the cathode flow channel at a rate sufficient to maintain a high humidity at the interface of the cathode gas diffusion layer and membrane. This results in a variation of the required liquid flow rate throughout the cell; at 1.0A/cm^2 mean current density the liquid addition rate to maintain a 95% interface humidity reduced from 0.50mg/cm^{2}s at the inlet to 0.25mg/cm^{2}s at the exit for a 20% cathode inlet humidity. A constant rate of liquid water addition through the cell was seen to give a similar cell voltage whilst consuming up to 32.8% more water. Using the simpler constant rate method it is possible to manage cell humidity based only on exhaust humidity value, without requiring knowledge of the local relative humidity within the cell.

- At high current densities some liquid water addition to the anode gas flow channel can reduce anode side membrane drying caused by increased electro-osmotic drag compared to cathode only water addition. By maintaining a target 90% relative humidity in the anode gas flow channel variation in local current density across the length of the flow channel was reduced 62.5% compared to using cathode water addition alone at 1.0A/cm^2 mean current density.

7.1.2 Heat exchangers

- Three heat exchanger models are presented and validated which can be used to assemble different layouts of fuel cell systems to explore thermal management.

- A heat exchanger model suitable for the simulation of condensation of water vapour from a fuel cell cathode exhaust in a fin and tube radiator was presented. The hot side

of the model uses a semi-empirical double boundary layer method to account for the presence of non-condensables in the gas stream. The hot side has been validated using existing published experimental data, the cold side uses an empirical heat transfer coefficient correlation based on a wide range of experimental data covering a broad range of geometries. This model represents the first fixed geometry fin and tube heat exchanger model suitable for use with a PEMFC cathode exhaust hot side that considers the presence of non-condensable gases. Calculated hot side heat transfer coefficient was seen to vary extensively with both location within the heat exchanger and operating current density due to changes in both Reynolds number and mass fraction of non-condensable gas. For the base simulation parameters used, localised heat transfer coefficient at 1.2A/cm^2 was 10.1kW/m^{2}K at the inlet, reducing to 3.8kW/m^{2}K at the exit. In comparison a hot side heat transfer coefficient of 4.5kW/m^{2}K was calculated for a single phase radiator at 60 lpm liquid flow rate.

- An experimental correlation has been produced for condensation of water vapour in the presence of a non-condensable gas (air) in a compact plate condenser with chevron surface enhancements. The correlation predicts the hot side heat transfer coefficient as a function of Reynolds number and mass fractional of non-condensable gas, the R-squared value of the experimental fit was 93.5%. This represents the first study of such a mixture in a compact plate heat exchanger and one of only a few studies to measure the internal temperature profile in a compact plate condenser. A semi-empirical model built around the experimental correlation was produced, which showed less than 10% error in overall heat transfer rate estimation compared to a separate set of experimental data in which the heat transfer area was varied.

7.1.3 Fuel cell system

- Two alternative models of an evaporatively cooled fuel cell vehicle have been presented, representing two different system architectures. One consisting of the fuel cell cathode exhaust connected directly to a condensing radiator, and another consisting of a fuel cell cathode exhaust connected to a compact plate condenser. In the latter system heat is transferred from the condenser to a liquid cooled radiator via an intermediate liquid cooling loop. These are the first published thermal models of an evaporatively cooled fuel cell system.

- The concept of net water flow was introduced for an evaporatively cooled system and the impact of system operating parameters on it studied. It was identified that for each set of operating conditions a current density for maximum net water flow exists. Knowledge of this value along with the point the system transitions to net water loss

can be used further to develop control strategies for net water flow in evaporatively cooled systems. It was shown that increasing the system operating pressure improves the rate of water collection for comparable net power despite the increased compressor load due to higher stack operating temperatures. At 50kW net load and base simulation parameters, increasing the operating pressure from 1.1-1.7bar.a resulted in a 82% increase in system net water flow.

- System net water flow over transient drive cycles was studied, results showed a reduced net water flow at low speed start/stop operation compared to constant speed motorway cruise. This is primarily due to reduced product water generation at low fuel cell load and not due to lower cooling air flow across the radiator. In an evaporatively cooled system without a liquid cooling loop it is therefore ineffective to operate the radiator fan at low fuel cell loads.

- The heat exchanger requirements and temperature regulation abilities of evaporatively cooled and liquid cooled systems were compared. The simulated results showed that radiator frontal area reductions of up to 39.2% can be obtained by using an evaporatively cooled system with a condensing radiator compared to a liquid cooled system due to higher heat transfer coefficients in the presence of phase change. Any gain in heat exchanger performance is subject to using a radiator material which has both a high thermal conductivity and will not ionise the condensed water.

- The ability to separate the liquid water from the exhaust gas stream post condenser (collection efficiency) was seen to have a significant influence on the system heat exchanger sizing. Collection efficiencies in excess of 90% are required to make evaporative cooling beneficial in terms of radiator frontal area compared to liquid cooled systems. At collection efficiencies below 70% it becomes impossible to achieve a positive net water flow regardless of radiator frontal area.

7.2 Further work

Whilst the literature on liquid cooled fuel cell systems is relatively mature, there is significant scope to further develop the current knowledge of evaporatively cooled fuel cells. One such area were additional research is required is in the modelling at a single cell level. The one-dimensional model presented in this thesis has provided a useful insight into the amount of liquid water required for humidification, but the model does not address the physical method of adding the liquid water into the flow channel. Numerical simulations using computational fluid dynamic (CFD) solution methods would allow for more detailed two-phase study into the interaction between the water addition method (injection or wicking), gas flow channel

and fuel cell assembly. Furthermore, the cell model presented in this work assumed a uniform temperature across each section of the cell (anode to cathode), considering the spacial distribution of temperature through the profile of the cell would influence the localised water management and should be considered in any future models. Further attention should be given to the operating conditions close to the gas channel entrance, where high rates of water flux across the membrane were observed, this may be reduced through operating the flow channels in counterflow, however this is not possible based on the current model assumptions.

The current evaporatively cooled fuel cell models have been validated based on literature polarisation curves and experimental cathode exit temperatures. Additional experimental work to evaluate temperature profiles within the fuel cell would help to increase confidence in the model. Further experimental work could also be used to study different liquid water addition methods and flow rates.

At a system level, the current work has presented a model suitable of simulating thermal transients which may be used to predict system level water balance. Further development in this area should look into the development of control algorithms to ensure water balance is maintained over transient drive cycles. This may be achieved through a combination of changing the stack operating conditions and radiator fan speed whilst maximising system efficiency, this type of control problem would be well suited to model based or optimal control techniques.

References

[1] IPCC, "Climate change 2014: Synthesis report. contribution of working groups i, ii and iii to the fifth assessment report of the intergovernmental panel on climate change," tech. rep., IPCC, 2014.

[2] IEA, "CO_2 emissions from fuel combustion," tech. rep., International Energy Agency, 2014.

[3] J. A. Adams, W. chul Yang, K. A. Oglesby, and K. D. Osborne, "The development of Ford's P2000 fuel cell vehicle," *SAE technical paper*, pp. 2000–01–1061, 2000.

[4] B. McCormick and E. Schubert, "Fuel cells at General Motors," *SAE technical paper*, pp. 2002–21–0072, 2002.

[5] Y. Sando, "Research and development of fuel cell vehicles at Honda," *ECS Transactions*, vol. 25, pp. 211–224, 2009.

[6] W. Sung, Y.-I. Song, K.-H. Yu, and T.-W. Lim, "Recent advances in the development of Hyundai & Kia's fuel cell electric vehicles," *SAE Int.J.Engines*, vol. 3, pp. 768–772, 2010.

[7] K. Kojima and S. Shinobu, "Development of fuel cell hybrid vehicle in Toyota," *SAE technical paper*, pp. 2011–05–17, 2011.

[8] O. Berger, S. Schmitz, and K. Go, "Optimization of a fuel cell cooling system for automotive transportation at Volkswagen," in *2008 Fuel Cell Seminar and Exposition, Phoenix, USA*, 2008.

[9] F. Barbir., *PEM Fuel Cells*. US: Academic Press, 2nd ed., 2013.

[10] J. Larminie and A. Dicks, *Fuel Cell Systems Explained*. Wiley, 2nd ed., 2006.

[11] M. H. Fronk, D. L. Wetter, D. A. Masten, and A. Bosco, "PEM fuel cell system solutions for transportation," *SAE technical paper*, pp. 2000–01–0373, 2000.

[12] J. P. Meyers, R. M. Darling, C. Evans, R. Balliet, and M. L. Perry, "Evaporatively-cooled PEM fuel-cell stack and system," in *Proton Exchange Membrane Fuel Cells 6 - 210th Electrochemical Society Meeting, Cancun, Mexico*, pp. 1207–1214, Electrochemical Society Inc, 2006.

[13] A. Warburton, D. Mossop, B. Burslem, P. Rama, P. Adcock, J. Cole, J. Edwards,

D. Ninan, and M. Provost, "Development of an evaporatively cooled hydrogen fuel cell system and its vehicle application," *SAE technical paper*, pp. 2013–01–0475, 2013.

[14] J. Wu, X. Z. Yuan, J. J. Martin, H. Wang, J. Zhang, J. Shen, S. Wu, and W. Merida, "A review of PEM fuel cell durability: Degradation mechanisms and mitigation strategies," *Journal of Power Sources*, vol. 184, pp. 104–119, 2008.

[15] U. Soupremanien, S. LePerson, M. Favre-Marinet, and Y. Bultel, "Tools for designing the cooling system of a proton exchange membrane fuel cell," *Applied Thermal Engineering*, vol. 40, pp. 161–173, 2012.

[16] G. Zhang and S. G. Kandlikar, "A critical review of cooling techniques in proton exchange membrane fuel cell stacks," *International Journal of Hydrogen Energy*, vol. 37, pp. 2412–2429, 2012.

[17] A. P. Sasmito, E. Birgersson, and A. S. Mujumdar, "Numerical evaluation of various thermal management strategies for polymer electrolyte fuel cell stacks," *International Journal of Hydrogen Energy*, vol. 36, pp. 12991–13007, 2011.

[18] M. Odabaee, S. Mancin, and K. Hooman, "Metal foam heat exchangers for thermal management of fuel cell systems, an experimental study," *Experimental Thermal and Fluid Science*, vol. 51, pp. 214–219, 2013.

[19] D. Ryan, J. Shang, C. Quillivic, and B. Porter, "Performance and energy efficiency testing of a lightweight FCEV hybrid vehicle," *European electric vehicle congress (EEVC)*, 2014.

[20] K. Ikeya, K. Hirota, Y. Takada, T. Eguchi, K. Mizutani, and T. Ohta, "Development and evaluation of air-cooled fuel cell scooter," *Society of Automotive Engineers in Japan (JSAE)*, pp. 2011–32–0644, 2011.

[21] J.-C. Shyu, K.-L. Hsueh, F. Tsau, and F.-L. Chen, "Modification of the liquid cooling channel of PEMFCs for their operation with dry reactant gases," *Energy Conversion and Management*, vol. 52, pp. 125–135, 2011.

[22] F. C. Chen, Z. Gao, R. O. Loutfy, and M. Hecht, "Analysis of optimal heat transfer in a PEM fuel cell cooling plate," *Fuel Cells*, vol. 3, pp. 181–188, 2003.

[23] S. Kang, K. Min, F. Mueller, and J. Brouwer, "Configuration effects of air, fuel, and coolant inlets on the performance of a proton exchange membrane fuel cell for automotive applications," *International Journal of Hydrogen Energy*, vol. 34, pp. 6749–6764, 2009.

[24] A. P. Sasmito, J. C. Kurnia, and A. S. Mujumdar, "Numerical evaluation of various gas and coolant channel designs for high performance liquid-cooled proton exchange membrane fuel cell stacks," *Energy*, vol. 44, pp. 278–291, 2012.

[25] S. Yu and D. Jung, "Thermal management strategy for a proton exchange membrane fuel cell system with a large active cell area," *Renewable Energy*, vol. 33, pp. 2540–2548,

2008.

[26] S. Yu and D. Jung, "A study of operation strategy of cooling module with dynamic fuel cell system model for transportation application," *Renewable Energy*, vol. 35, pp. 2525–2532, 2010.

[27] Y. Saygili, I. Eroglu, and S. Kincal, "Model based temperature controller development for water cooled PEM fuel cell systems," *International Journal of Hydrogen Energy*, vol. 40, pp. 615–622.

[28] R. T. Meyer and B. Yao, "Control of a PEM fuel cell cooling system," *ASME International Mechanical Engineering Congress and Exposition, Chicago, USA*, pp. 289–296, 2006.

[29] P. Hu, G.-Y. Cao, X.-J. Zhu, and M. Hu, "Coolant circuit modeling and temperature fuzzy control of proton exchange membrane fuel cells," *International Journal of Hydrogen Energy*, vol. 35, pp. 9110–9123, 2010.

[30] J.-W. Ahn and S.-Y. Choe, "Coolant controls of a PEM fuel cell system," *Journal of Power Sources*, vol. 179, pp. 252–264, 2008.

[31] C. Panos, K. I. Kouramas, M. C. Georgiadis, and E. N. Pistikopoulos, "Modelling and explicit model predictive control for PEM fuel cell systems," *Chemical Engineering Science*, vol. 67, pp. 15–25, 2012.

[32] N.-S. Ap, "A simple engine cooling system simulation model," *SAE technical paper*, pp. 1999–01–0237, 1999.

[33] C. Vermillion, J. Sun, and K. Butts, "Modeling, control design, and experimental validation of an overactuated thermal management system for engine dynamometer applications," *IEEE Transactions on Control Systems Technology*, vol. 17, pp. 540–551, 2009.

[34] S. Rogg, M. Höglinger, E. Zwittig, C. Pfender, W. Kaiser, and T. Heckenberger, "Cooling modules for vehicles with a fuel cell drive," *Fuel Cells*, vol. 3, pp. 153–158, 2003.

[35] R. K. Ahluwalia and X. Wang, "Fuel cell systems for transportation: Status and trends," *Journal of Power Sources*, vol. 177, pp. 167–176, 2008.

[36] H. Zhang, Z. Qian, D. Yang, and J. Ma, "Design of an air humidifier for a 5kW proton exchange membrane fuel cell stack operated at elevated temperatures," *International Journal of Hydrogen Energy*, vol. 38, pp. 12353–12362, 2013.

[37] T. Ito, J. Yuan, and B. Sunden, "Water recovery schemes and effects on the water/thermal balances for a 100kW PEMFC system, Irvine, USA," *ASME 4th International Conference on Fuel Cell Science, Engineering and Technology*, pp. 211–220, 2006.

[38] C. Bao, M. Ouyang, and B. Yi, "Analysis of the water and thermal management in proton exchange membrane fuel cell systems," *International Journal of Hydrogen Energy*, vol. 31, pp. 1040–1057, 2006.

[39] Z. M. Wan, J. H. Wan, J. Liu, Z. K. Tu, M. Pan, Z. C. Liu, and W. Liu, "Water recovery and air humidification by condensing the moisture in the outlet gas of a proton exchange membrane fuel cell stack," *Applied Thermal Engineering*, vol. 42, pp. 173–178, 2012.

[40] K. Haraldsson and P. Alvfors, "Effects of ambient conditions on fuel cell vehicle performance," *Journal of Power Sources*, vol. 145, pp. 298–306, 2005.

[41] K. Haraldsson, T. Markel, and K. Wipke, "An analysis of water management for a PEM fuel cell system in automotive drive cycles," in *ASME 2003 1st International Conference on Fuel Cell Science, Engineering and Technology, Rochester, USA*, p. 333, 2003.

[42] A. P. Silva, R. M. Galante, P. R. Pelizza, and E. Bazzo, "A combined capillary cooling system for fuel cells," *Applied Thermal Engineering*, vol. 41, pp. 104–110, 2012.

[43] P. T. Garrity, J. F. Klausner, and R. Mei, "A flow boiling microchannel evaporator plate for fuel cell thermal management," *Heat Transfer Engineering*, vol. 28, pp. 877–884, 2007.

[44] F. P. Incropera and D. P. Dewitt, *Introduction to heat transfer*. John Wiley and Sons, 4th ed., 2002.

[45] R. M. Darling and M. L. Perry, "Evaporatively cooled hybrid PEM fuel cell power plant assembly," 2011. US Patent 8048582 B2.

[46] S. G. Goebel, "Evaporative cooled fuel cell," 2005. US patent 6960404 B2.

[47] J. S. Matcham, N. Grange, P. A. Benson, S. Baird, A. Kells, J. Cole, P. Adcock, P. D. Hood, and S. E. Foster, "Water management in fuel cells," 2005. WO patent 2005064727 A2.

[48] P. Adcock, A. Kells, and C. Jackson, "PEM fuel cells for road vehicles," *EET-2008 European Ele-Drive Conference, Geneva, Switzerland*, 2008.

[49] H. Hardill, J. Edwards, and R. Clague, "Intelligent Energy's fuel cells in automotive range extender applications," *3rd International CTI Symposium, Suzhou, China*, 2014.

[50] M. Sulek, J. Adams, S. Kaberline, M. Ricketts, and J. R. Waldecker, "In situ metal ion contamination and the effects on proton exchange membrane fuel cell performance," *Journal of Power Sources*, vol. 196, pp. 8967–8972, 2011.

[51] C. Spiegel, *PEM Fuel Cell Modeling and Simulation Using MATLAB*. Elsevier, 1 ed., 2008.

[52] T. E. Springer, T. A. Zawodzinski, and S. Gottesfeld, "Polymer electrolyte fuel cell model," *Journal of the Electrochemical Society*, vol. 138, pp. 2334–2342, 1991.

[53] T. A. Zawodzinski, M. Neeman, L. O. Sillerud, and S. Gottesfeld, "Determination of water diffusion coefficients in perfluorosulfonate ionomeric membranes," *The Journal of physical chemistry*, vol. 95, pp. 6040–6044, 1991.

[54] D. M. Bernardi and M. W. Verbrugge, "Mathematical model of a gas diffusion electrode bonded to a polymer electrolyte," *AIChE Journal*, vol. 37, pp. 1151–1163, 1991.

[55] T. F. Fuller and J. Newman, "Water and thermal management in solid-polymer-electrolyte fuel cells," *Journal of the Electrochemical Society*, vol. 140, pp. 1218–1225, 1993.

[56] V. Gurau, H. Liu, and S. Kakaç, "Two-dimensional model for proton exchange membrane fuel cells," *AIChE Journal*, vol. 44, pp. 2410–2422, 1998.

[57] J. C. Amphlett, R. F. Mann, B. A. Peppley, P. R. Roberge, and A. Rodrigues, "A model predicting transient responses of proton exchange membrane fuel cells," *Journal of Power Sources*, vol. 61, pp. 183–188, 1996.

[58] J. T. Pukrushpan, A. G. Stefanopoulou, and H. Peng, "Control of fuel cell breathing," *Control Systems, IEEE*, vol. 24, pp. 30–46, 2004.

[59] A. Kells and O. Jackson, "Simulation of a fuel cell hybrid London taxi," *The 24th International battery, hybrid and fuel cell electric vehicle symposium and exhibition, Stavanger, Norway*, 2009.

[60] J. H. M.Schultze, "A control oriented simulation model of an evaporation cooled polymer electrolyte membrane fuel cell system," *18th International federation of automatic control world congress, Milan, Italy*, pp. 14790–14795, 2011.

[61] R. O'Hayre, S.-W. Cha, W. Colella, and F. B. Prinz, *Fuel Cell Fundamentals*. John Wiley and Sons, 2nd ed., 2009.

[62] W. Dai, H. Wang, X.-Z. Yuan, J. J. Martin, D. Yang, J. Qiao, and J. Ma, "A review on water balance in the membrane electrode assembly of proton exchange membrane fuel cells," *International Journal of Hydrogen Energy*, vol. 34, pp. 9461–9478, 2009.

[63] A. Husar, A. Higier, and H. Liu, "In situ measurements of water transfer due to different mechanisms in a proton exchange membrane fuel cell," *Journal of Power Sources*, vol. 183, pp. 240–246, 2008.

[64] T. A. Zawodzinski, C. Derouin, S. Radzinski, R. J. Sherman, V. T. Smith, T. E. Springer, and S. Gottesfeld, "Water uptake by and transport through Nafion® 117 membranes," *Journal of The Electrochemical Society*, vol. 140, pp. 1041–1047, 1993.

[65] J. T. Pukrushpan, H. Peng, and A. G. Stefanopoulou, "Control-oriented modeling and analysis for automotive fuel cell systems," *Journal of Dynamic Systems, Measurement, and Control*, vol. 126, pp. 14–25, 2004.

[66] W. M. Haynes, *CRC Handbook of Chemistry and Physics*. 93rd ed., 2012.

[67] A. Rabbani and M. Rokni, "Effect of nitrogen crossover on purging strategy in PEM fuel cell systems," *Applied Energy*, vol. 111, pp. 1061–1070, 11 2013.

[68] W. Yu, X. Sichuan, and H. Ni, "Air compressors for fuel cell vehicles: An systematic review," *SAE Int.J.Alt.Power.*, vol. 4, pp. 115–122, 2015.

[69] J. T. Pukrushpan, "Modeling and control of fuel cell systems and fuel processors," *PhD Thesis, University of Michigan*, 2003.

[70] J. Collier and J. Thome, *Convective Boiling and Condensation.* Oxford University Press, 3rd ed., 1994.

[71] J. C. Slattery and R. B. Bird, "Calculation of the diffusion coefficient of dilute gases and of the self-diffusion coefficient of dense gases," *AIChE Journal*, vol. 4, pp. 137–142, 1958.

[72] G. Hewitt, G. Shires, and T. Bott, *Process Heat Transfer.* CRC Press, 1st ed., 1994.

[73] U. Pasaogullari and C. Y. Wang, "Liquid water transport in gas diffusion layer of polymer electrolyte fuel cells," *Journal of the Electrochemical Society*, vol. 151, pp. A399–A406, 2004.

[74] C. Bao and W. G. Bessler, "Two-dimensional modeling of a polymer electrolyte membrane fuel cell with long flow channel. part i. model development," *Journal of Power Sources*, vol. 275, pp. 922–934, 2015.

[75] Y. Wang, "Modeling of two-phase transport in the diffusion media of polymer electrolyte fuel cells," *Journal of Power Sources*, vol. 185, pp. 261–271, 2008.

[76] J. H. Nam and M. Kaviany, "Effective diffusivity and water-saturation distribution in single and two-layer PEMFC diffusion medium," *International Journal of Heat and Mass Transfer*, vol. 46, pp. 4595–4611, 2003.

[77] Y.-S. Chen and H. Peng, "A segmented model for studying water transport in a PEMFC," *Journal of Power Sources*, vol. 185, pp. 1179–1192, 2008.

[78] M. Leverett, "Capillary behavior in porous solids," *Transactions of the AIME*, vol. 142, 1941.

[79] E. C. Kumbur, K. V. Sharp, and M. M. Mench, "Validated leverett approach for multiphase flow in PEFC diffusion media: iii. temperature effect and unified approach," *Journal of The Electrochemical Society*, vol. 154, pp. B1315–B1324, 2007.

[80] D. F. Fairbanks and C. R. Wilke, "Diffusion coefficients in multicomponent gas mixtures," *Industrial and Engineering Chemistry*, vol. 42, pp. 471–475, 1950.

[81] L. C. Pérez, L. Brandão, J. M. Sousa, and A. Mendes, "Segmented polymer electrolyte membrane fuel cellsa review," *Renewable and Sustainable Energy Reviews*, vol. 15, pp. 169–185, 2011.

[82] D. Jung and D. N. Assanis, "Numerical modeling of cross flow compact heat exchanger with louvered fins using thermal resistance concept," *SAE technical paper*, pp. 2006–01–0726, 2006.

[83] E. Y. Ng, P. W. Johnson, and S. Watkins, "An analytical study on heat transfer performance of radiators with non-uniform airflow distribution," *Proceedings of the Institution of Mechanical Engineers, Part D: Journal of Automobile Engineering*, vol. 219,

pp. 1451–1467, 2005.

[84] Y.-J. Chang and C.-C. Wang, "A generalized heat transfer correlation for louver fin geometry," *International Journal of Heat and Mass Transfer*, vol. 40, pp. 533–544, 1997.

[85] E. M. Sparrow, W. J. Minkowycz, and M. Saddy, "Forced convection condensation in the presence of noncondensables and interfacial resistance," *International Journal of Heat and Mass Transfer*, vol. 10, pp. 1829–1845, 12 1967.

[86] M. G. Izenson and R. W. Hill, "Water and thermal balance in PEM and direct methanol fuel cells," *Journal of Fuel Cell Science and Technology*, vol. 1, pp. 10–17, 2004.

[87] M. Siddique, "The effects of noncondensable gases on steam condensation under forced convection conditions," *PhD thesis: Massachusetts Institute of Technology*, 1992.

[88] A. P. Colburn and O. A. Hougen, "Design of cooler condensers for mixtures of vapors with noncondensing gases," *Industrial and Engineering Chemistry*, vol. 26, pp. 1178–1182, 1934.

[89] K. Vierow and V. E. Schrock, "Condensation in a natural circulation loop with noncondensable gases part i - heat transfer," *Proc. of International Conference on Multiphase Flow, Tsukuba, Japan*, p. 183, 1991.

[90] S. Z. Kuhn, V. E. Schrock, and P. F. Peterson, "An investigation of condensation from steam & gas mixtures flowing downward inside a vertical tube," *Nuclear Engineering and Design*, vol. 177, pp. 53–69, 1997.

[91] S. Krishnaswamy, H. S. Wang, and J. W. Rose, "Condensation from gas & vapour mixtures in small non-circular tubes," *International Journal of Heat and Mass Transfer*, vol. 49, pp. 1731–1737, 2006.

[92] S. Krishnaswamy, "Filmwise condensation inside a non-circular tube in the presence of forced convection and a non-condensing gas," *PhD thesis: Queen Mary University of London*, 2004.

[93] H. C. No and H. S. Park, "Non-iterative condensation modeling for steam condensation with non-condensable gas in a vertical tube," *International Journal of Heat and Mass Transfer*, vol. 45, pp. 845–854, 2002.

[94] J. L. Munoz-Cobo, L. Herranz, J. Sancho, I. Tkachenko, and G. Verdú, "Turbulent vapor condensation with noncondensable gases in vertical tubes," *International Journal of Heat and Mass Transfer*, vol. 39, pp. 3249–3260, 1996.

[95] Z. H. Ayub, "Plate heat exchanger literature survey and new heat transfer and pressure drop correlations for refrigerant evaporators," *Heat Transfer Engineering*, vol. 24, pp. 3–16, 2003.

[96] G. A. Longo, A. Gasparella, and R. Sartori, "Experimental heat transfer coefficients

during refrigerant vaporisation and condensation inside herringbone-type plate heat exchangers with enhanced surfaces," *International Journal of Heat and Mass Transfer*, vol. 47, pp. 4125–4136, 2004.

[97] D. Han, K. Lee, and Y. Kim, "The characteristics of condensation in brazed plate heat exchangers with different chevron angles," *Journal of Korean Physical Society*, vol. 43, p. 66, 2003.

[98] Y.-Y. Yan, H.-C. Lio, and T.-F. Lin, "Condensation heat transfer and pressure drop of refrigerant R-134a in a plate heat exchanger," *International Journal of Heat and Mass Transfer*, vol. 42, pp. 993–1006, 1999.

[99] J. R. García-Cascales, F. Vera-García, J. M. Corberán-Salvador, and J. Gonzlvez-Maciá, "Assessment of boiling and condensation heat transfer correlations in the modelling of plate heat exchangers," *International Journal of Refrigeration*, vol. 30, pp. 1029–1041, 2007.

[100] S. W. Chang and B.-J. Huang, "Thermal performance improvement by injecting air into water flow," *International Journal of Heat and Mass Transfer*, vol. 57, pp. 439–456, 2013.

[101] P. Vlasogiannis, G. Karagiannis, P. Argyropoulos, and V. Bontozoglou, "Air & water two-phase flow and heat transfer in a plate heat exchanger," *International Journal of Multiphase Flow*, vol. 28, pp. 757–772, 2002.

[102] J. Fernández-Seara, F. J. Uhía, J. Sieres, and A. Campo, "A general review of the Wilson plot method and its modifications to determine convection coefficients in heat exchange devices," *Applied Thermal Engineering*, vol. 27, pp. 2745–2757, 2007.

[103] B. E. Poling, J. M. Prausnitz, J. P. O'Connell, and R. C. Reid, *The properties of gases and liquids*. McGraw-Hill Professional, 5th ed., 2000.

[104] K. U. Bhaskar, Y. R. Murthy, M. R. Raju, S. Tiwari, J. K. Srivastava, and N. Ramakrishnan, "CFD simulation and experimental validation studies on hydrocyclone," *Minerals Engineering*, vol. 20, pp. 60–71, 2007.

[105] J. Kurokawa and T. Ohtaki, "Gas-liquid flow characteristics and gas-separation efficiency in a cyclone separator," *ASME Gas Liquid Flows*, vol. 225, pp. 51–57, 1995.

Appendix A

Simulation parameters

Table A.1: Heat exchanger parameters (unless otherwise specified)

Parameter	**Value**
Compact plate condenser	
Coolant flow rate	60 lpm
Number of plates	50
Plate length	180mm
Plate height	100mm
Plate thickness	1mm
Surface enlargement factor	1.12
Hydraulic diameter (per plate)	4mm
Condenser heat transfer area	$1m^2$
Radiator	
Aluminium thermal conductivity	237W/mK
Fin pitch	2.5mm
Louvre pitch	1.14mm
Fin length	8.59mm
Tube height (liquid)	2.5mm
Tube height (condensing)	5.0mm
Tube depth	21.58mm
Tube thickness	0.32mm
Louvre length	6.74mm
Fin thickness	0.1mm
Louvre height	0.315mm
Coolant tank capacity	10l

Table A.2: Lumped parameter model fuel cell parameters (unless otherwise specified)

Parameter	**Value**
Fuel cell rated power	50kW
Maximum system efficiency (LHV)	56%
System efficiency @ 50% load	50%
Number of cells	360
Cell active area	200cm^2
Cathode stoichiometry	2.5
Anode stoichiometry	1.03
Stack mass (m_s)	30kg
Stack specific heat (C_{ps})	3.5kJ/kgK
Cathode volume	0.01m^3
Anode volume	0.01m^3
Manifold volumes	0.01m^3
Cathode cross sectional area (A_{ca})	0.04m^2
Stack dimensions (EC)	$20 \times 20 \times 60$cm
Inlet manifold/cathode/anode orifice constant	5×10^{-5}kg/(sPa)
Ambient humidity	80%
Membrane thickness (z)	100μm
Charge transfer coefficient (α)	0.5
Internal current density (i_n)	1.5×10^{-4}A/cm^2
Mass transport coefficient (a_{trans})	3×10^{-4}
Mass transport coefficient (b_{trans})	3.0
Exchange current density at STP	3.2×10^{-8}A/cm^2
Stack surface heat transfer coefficient	5W/m^{2}K
Water entrainment constant (δ)	2.0
Molar mass membrane [77] (M_{mem})	1.1 kg/mol
Dry density membrane [73] (ρ_{dry})	1.98g/cm^3
Cathode activation energy [9] (E_c)	66kJ/mol
Cooling tubes per plate	50
Number cooling plates	358
Cooling tube diameter	2mm
Coolant plate thickness	2.5mm
Coolant plate thermal conductivity	15.1W/mK
Stack cooling heat transfer area	5m^2
Compressor efficiency	70%
Liquid water collection efficiency	100%

Table A.3: Vehicle parameters (unless otherwise specified)

Parameter	**Value**
Vehicle mass (m)	1500kg
Static tyre friction coefficient	0.01
Dynamic tyre friction coefficient	0.01
Vehicle frontal area (A_f)	2.2m^2
Drag coefficient (C_d)	0.33
Rolling radius	0.325m

Table A.4: One dimensional simulation parameters (unless otherwise specified)

Parameter	**Value**
Cell active area	100cm^2
Gas channel width	3.0mm
Gas channel height	3.0mm
Gas channel length	0.5m
Cathode stoichiometry	2.5
Anode stoichiometry	1.05
Gas channel inlet pressure	1.2bar.a
Membrane thickness	100μm
Gas diffusion layer thickness	300μm
Gas diffusion layer contact angle	80°
Exchange current density at STP	6.8×10^{-8}A/cm^2
Internal current density	3.0×10^{-4} A/cm^2
Charge transfer coefficient (α)	0.5
Gas diffusion layer porosity [77]	0.725
Surface tension [73]	0.0625N/m
GDL permeability [73]	6.88×10^{-13}m^2
Dry membrane density [73]	1.98g/cm^3
Molar mass membrane [77]	1.1g/mol
Activation energy [9]	66kJ/mol
Interface humidity control gain (τ)	8×10^{-5}mol

Appendix B

Experimental procedure

Table B.1 shows the key components and sensors used for the experimental set up of section 5.5. Figure B.1 details the procedure used to operate and obtain data from the experimental set up.

Component	**Description**
Boiler	Earlex LCS270 2.75kW 240V
Condenser	SWEP M10 plate heat exchanger
Mass flow controller	Teledyne HFC-203 0-200 slpm air
Coolant pump	Davis Craig ewp115 electric water pump
Flow meter	Omega liquid flow transmitter FPR204P-PC
Pressure sensor	GE Druck guage pressure sensor 0-4bar.g
Thermocouples	Type K 100m, 310 stainless steel sheath, 3mm diameter
Thermocouples (condenser)	Type T, 150mm, 321 stainless steel sheath, 0.5mm diameter
Data logger	National Instruments cFP-2000

Table B.1: Components used in experimental rig

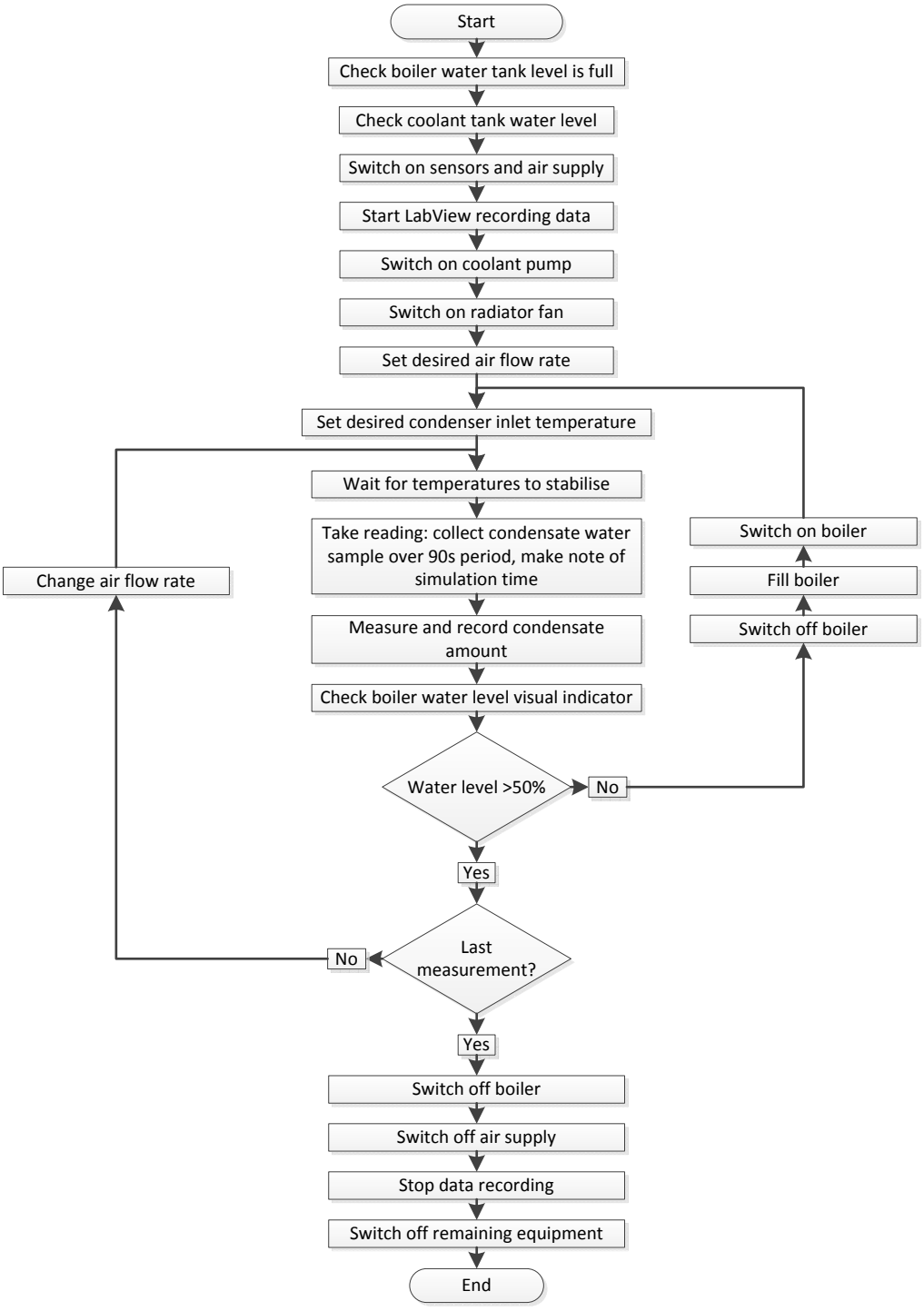

Figure B.1: Experimental procedure flow chart

Appendix C

Experimental results

A sample set of experimental results, obtain using the set up detailed in section 5.5, is shown in table C.1. The definition and units of the columns are detailed below:

P_{in}	Pressure measured at condenser inlet (mbar.g)
T_{in}	Temperature measured at condenser inlet (°C)
Air flow	Air volume flow rate measured into condenser (slpm)
W_{nc}	Mass fraction of non-condensable gas based on temperature and pressure
Coolant flow	Liquid coolant volume flow rate measured (lpm)
a,b,c	Hot side temperature profile coefficients for $0 < x < 1$ ($T = ax^2 + bx + c$)
P_{out}	Pressure measured at condenser exit (mbar.g)
T_{out}	Temperature measured at condenser exit (°C)
Heat transfer: Hot	Heat transfer in condenser based on hot side enthalpy change (W)
Heat transfer: Cold	Heat transfer in condenser based on measured cold side temperature change (W)
$\dot{m}_c$: Measured	Mean rate of collected water over 90 second period (g/s)
$\dot{m}_c$: Predicted	Liquid water flow predicted based on hot side temperature and pressures (g/s)

Table C.1: Reduced data sample from experimental tests

Run	Hot in				Cold in		Hot temp profile			Hot out			Cold out	Heat transfer		$\dot{m}_c$	
	P_{in}	T_{in}	Air flow	W_{nc}	T_{in}	Coolant flow	a	b	c	P_{out}	T_{out}	W_{nc}	T_{out}	Hot	Cold	Measured	Predicted
1	134	87.3	27.8	0.559	30.6	6.84	88.9	-142.5	88.3	122	33.1	0.971	33.2	1112	1225	0.61	0.52
2	193	87.2	51.8	0.590	30.0	6.72	58.1	-111.5	89.4	126	35.1	0.968	34.1	1808	1911	0.98	0.85
3	160	84.9	35.9	0.619	30.3	6.84	74.4	-124.8	85.0	122	33.3	0.971	33.0	1114	1250	0.66	0.51
4	202	84.8	51.9	0.638	30.3	6.76	61.2	-111.1	86.4	125	35.1	0.968	33.8	1468	1637	0.83	0.68
5	215	84.7	55.9	0.644	29.7	6.76	58.6	-108.6	86.3	126	34.9	0.968	33.4	1541	1710	0.90	0.71
6	226	84.8	59.8	0.646	28.7	6.74	56.4	-107.0	86.4	127	34.0	0.970	32.6	1643	1808	0.96	0.76
7	181	82.4	43.8	0.670	30.3	6.86	63.1	-109.4	81.0	122	33.9	0.970	32.8	1076	1205	0.65	0.49
8	247	82.3	67.9	0.693	30.9	6.76	47.8	-91.6	82.2	127	36.8	0.965	34.4	1467	1626	0.88	0.67
9	256	82.3	71.4	0.695	30.5	6.77	48.6	-92.4	82.3	128	36.8	0.965	34.1	1526	1679	0.87	0.70
10	270	82.2	75.9	0.700	29.9	6.77	47.9	-91.6	82.2	129	36.7	0.965	33.6	1588	1747	0.93	0.73
11	283	82.3	80.1	0.703	29.0	6.71	46.5	-90.7	82.1	130	35.7	0.967	32.9	1663	1820	1.02	0.76
12	287	79.8	83.9	0.737	30.8	6.76	45.8	-86.0	79.2	129	37.2	0.964	34.2	1436	1561	0.92	0.65
13	298	79.7	87.9	0.740	30.6	6.71	43.0	-83.0	78.9	131	37.3	0.964	34.0	1480	1595	0.91	0.67
14	319	79.8	95.9	0.744	29.7	6.68	41.2	-81.2	78.7	133	37.0	0.965	33.3	1583	1675	0.97	0.72
15	331	79.7	100.6	0.748	28.9	6.69	41.4	-81.2	78.4	134	36.4	0.966	32.6	1632	1720	1.01	0.74

Appendix D

Publications

Fly A. and Thring R. H. Temperature regulation of an evaporatively cooled PEMFC stack, *International Journal of Hydrogen Energy*, vol. 40, pp. 11976-11982, 2015

Fly A. and Thring R. H. Model based investigation of liquid water injection strategies for evaporatively cooled PEM fuel cells, *Proceedings of ASME 13th Fuel Cell Science, Engineering, and Technology Conference*, 2015, San Diego, USA,

Fly A. and Thring R. H. Condensation of water from saturated air in a compact plate condenser with application to water balance in proton exchange membrane fuel cell systems, *Proceedings of the 15th International Heat Transfer Conference (IHTC-15)*,2014, Kyoto, Japan,

Fly A. and Thring R. H. System thermal and water balance in an evaporatively cooled PEM fuel cell vehicle, *Vehicle Thermal Management Systems (VTMS11)*,p.267, 2013, Coventry, UK

Whiteley M., Fly A., Leigh J., Dunnett S., Jackson L. Advanced reliability analysis of Polymer Electrolyte Membrane Fuel Cells using Petri-Net analysis and fuel cell modelling techniques, *International Journal of Hydrogen Energy*, vol. 40, pp. 11550-11558, 2015